UNIVERSITY OF OKLAHOMA

GRADUATE COLLEGE

A MOBILE RADAR BASED CLIMATOLOGY OF SUPERCELL TORNADO STRUCTURES AND DYNAMICS

A DISSERTATION

SUBMITTED TO THE GRADUATE FACULTY

in partial fulfillment of the requirements for the

Degree of

DOCTOR OF PHILOSOPHY

By

CURTIS R. ALEXANDER
Norman, Oklahoma
2010

A MOBILE RADAR BASED CLIMATOLOGY OF
SUPERCELL TORNADO STRUCTURES AND DYNAMICS

A DISSERTATION APPROVED FOR THE
SCHOOL OF METEOROLOGY

BY

_____
Dr. Frederick Carr, Chair

_____
Dr. Michael Biggerstaff

_____
Dr. Sheena Murphy

_____
Dr. Alan Shapiro

_____
Dr. Louis Wicker

_____
Dr. Joshua Wurman

Acknowledgements

I would first like to thank my doctoral committee Frederick Carr, Michael Biggerstaff, Sheena Murphy, Alan Shapiro, Louis Wicker and my principle research advisor Joshua Wurman for their helpful comments, suggestions and feedback during this work. I would also like to recognize important contributions from David Dowell who provided helpful comments and suggestions both as a friend and colleague in keeping me focused on my objectives as well as helping to fund my studies.

Considerable time and effort was involved in the collection of mobile radar data in tornadoes by the Doppler On Wheels (DOWs) team over the past decade. Countless faculty, staff, students and other interested persons helped contribute to the collection of this data, and far too many to list here. However, several people including Joshua Wurman, Herb Stein, David Dowell, Scott and Yvette Richardson, Swarndeep Gill, Stephen McDonald, and Brian Pereria all helped immensely during the many field campaigns to keep the radar trucks operating and collecting data.

I would also like to thank Josh's wife, Ling Chan, for her kind words and help with logistical arrangements whether it be shipping of radar data or making flight reservations. I would like to thank the School of Meteorology staff including Celia Jones, Marcia Pallutto, and Nancy Campbell for their help with paperwork related to graduation deadlines and degree requirements.

Finally, and last but certainly not least, I would like to thank my parents Jeannie and Richard Alexander along with my sister Denise and my wife Anneliese in their support throughout my years as a graduate student.

The prototype Doppler On Wheels (DOW1) was developed jointly by the University of Oklahoma with support from the School of Meteorology, the College of Geosciences, the Graduate College, the Center for the Analysis and Prediction of Storms (sponsored by the National Science Foundation)], the National Center for Atmospheric Research (sponsored by the National Science Foundation), and the National Severe Storms Laboratory (part of the National Oceanic and Atmospheric Administration). This work was supported in part by National Science Foundation (NSF) grants AGS-0801041 and 0437505. The Doppler On Wheels (DOW) radars are supported through NSF grant AGS-0734001 and operated by the Center for Severe Weather Research (CSWR).

Table of Contents

Section	Page
Acknowledgements	iv
Table of Contents	vi
List of Tables	viii
List of Figures	ix
Abstract	xx
Chapter 1: Introduction	1
Chapter 2: Literature Review	8
2.1 Theories of Tornado Structure	8
2.1.1 Scale of Tornadoes	8
2.1.2 Maximum Horizontal Wind Speeds	9
2.2 Models of Tornado Dynamics	11
2.2.1 Laboratory Simulations of Vortex Breakdown	11
2.2.2 Numerical Simulations of Corner Flow Region	13
2.2.3 Numerical Simulations of Tornadogenesis	20
2.3 Observations of Tornadoes	25
2.3.1 Damage Survey Climatologies	25
2.3.2 In-situ Near Surface Measurements	29
2.3.3 Photogrammetry	31
2.3.4 Single-Doppler Radar	35
2.3.5 Dual-Doppler Radar	53
2.4 Key Issues	59
Chapter 3: Data	61
3.1 Doppler On Wheels Radar Observations	61
3.2 Navigation Procedures	67
3.2.1 Date/Time and Lat/Lon Corrections	68
3.2.2 Ranging Corrections	69
3.2.3 Pointing Angle Corrections	69
3.2.4 Rotation to Ground-Relative Position	70
3.3 Quality Control Procedures	73
3.3.1 Normalized Coherent Power Thresholding	74
3.3.2 Removal of Low-NCP Speckles	74
3.3.3 Removal of Staggered Pulse Repetition Period Velocity Glitches	74
3.3.4 Dealiasing of Doppler Velocity	75
3.3.5 Removal of Ground Clutter	76
3.3.6 Removal of Radar Velocity	76
3.4 Analysis Algorithms	77
3.4.1 Tornado Detection	77
3.4.2 Tornado Isolation	80

3.4.3 Tornado Tracking 81
3.4.4 Patch Extraction 81
3.4.5 Cross-Section Extraction (1-D) 82
3.4.6 Single-Doppler Velocity Retrieval Extraction (2-D) 84
3.4.7 Single-Doppler Velocity Retrieval Extraction (3-D) 85

Chapter 4: Analysis 87
4.1 Kinematic Tornado Structures 87
4.1.1 Data Sampling Statistics 87
4.1.2 Tornado Intensity Distribution 89
4.1.3 Kinematic Distributions 90
4.1.4 Rates Of Change 94
4.1.5 Vertical Profiles 98
4.1.6 Horizontal Profiles 95
4.2 Comparison with 88D Observations 99
4.2.1 Comparison with 88D Algorithms 100
4.2.2 Simulated Observations 101
4.3 Tornado Evolution 103
4.3.1 Vortex Scale Contraction 103
4.3.2 Angular Momentum Evolution 104

Chapter 5: Discussion and Conclusions 108
5.1 Discussion of Analysis Results 108
5.1.1 Tornado Intensity Distribution 108
5.1.2 Tornado Diameter and Divergence Distribution 113
5.1.3 Kinematic Distributions 115
5.1.4 Horizontal and Vertical Profiles 116
5.1.5 Scale Contraction 117
5.1.6 Angular Momentum Evolution 118
5.2 Conclusions 119
5.3 Future Work 120

References 123
Tables 134
Figures 139

List of Tables

Table		Page
Table 1.1.	Characteristics of the Doppler On Wheels (DOWs) mobile radar systems when scanning in convection during VORTEX and ROTATE (Wurman et al. 1997). Each radar maintained the same hardware configuration throughout the entire climatology except where noted in the table.	134
Table 1.2.	History of DOW radar sampling characteristics including maximum unambiguous velocity and minimum attainable 3-dB sample volume dimensions in azimuth, elevation and range for features at three distances from the radars.	134
Table 1.3.	History of DOW radar typical data collection strategies including temporal updates and distance between nearest data points in azimuth, elevation and range for features at three distances from the radars.	135
Table 2.1.	Fujita Scale used for estimating tornado intensity, defined as the fastest quarter-mile of wind at 10 m AGL, and based upon observed damage to structures.	136
Table 2.2.	Enhanced Fujita Scale used for estimating tornado intensity, defined as the fastest three-second gust at 10 m AGL, and based upon maximum degree of damage to one or more damage indicators.	136
Table 3.1	Order of magnitude estimates for variables relevant to ground-relative coordinate transformation.	137
Table 3.2.	Kinematic quantities computed from the Doppler velocity observation patches.	137
Table 4.1.	List of strong or violent DOW-observed tornado cases including the available WSR-88D level II or III data. All radar data is classified by the height above ground level of the lowest beam in the tornado or parent mesocyclone. The * indicates ground-based Doppler velocity estimates of the tornado intensity where the official damage survey is either unavailable or indicates a weaker intensity due to a lack of damage descriptors.	138

List of Figures

Figure		Page
Figure 1.1.	The WSR-88D radar network across the ROTATE domain of operations approximating regions of 88D radar coverage below 0.5 km AGL within green circles, below 1 km AGL within yellow circles and below 2 km AGL within the outermost red circles.	139
Figure 1.2.	The locations of all mesocyclonic tornadoes observed by the DOWs from 1995 through 2001 and color-coded by storm-reported intensity (F0 = purple, F1 = blue, F2 = green, F3 = orange, F4 = red, F5 = black).	140
Figure 1.3.	Frequency of dates when either (a) VORTEX or ROTATE field projects were conducted from 1995 through 2003 or (b) when DOW-observed tornadoes were present.	141
Figure 2.1.	Change of vortex structure with increasing swirl ratio S in a vortex chamber. (a) At low S, the inflow boundary later separates and a confined vortex forms aloft. (b) As S increases, the boundary layer flow attaches and the vortex intensifies. There is vortex breakdown aloft which terminates the laminar core. (c) For S > critical value, the vortex breakdown has descended to the surface, the vortex intensity has decreased, and a downdraft penetrates into the turbulent core. (d) At high S, the downdraft has penetrated to the lower surface (Fiedler and Rotunno 1986).	142
Figure 2.2.	Conceptual model of a supercell thunderstorm including horizontal streamlines, regions of ascending air (UP) and descending air in the forward flank downdraft (FFD) and rear flank downdraft (RFD), and the location often associated with mesocyclone produced tornado (T) in a plan view (a) (Lemon and Doswell 1979) and in three dimensions (b) (Rasmussen et al. 1994).	143
Figure 2.3.	Vortex scale contraction conceptual models including the downward-building dynamic pipe effect (DPE) in (a) and (b) as opposed to simultaneous contraction in (c) (Trapp and Davies-Jones 1997).	144
Figure 2.4.	An example of a DOW radar observation showing the 1.4° elevation scan of the Spencer, SD tornado including Doppler velocities (m s^{-1}) on left and reflectivity (dB) on	145

right. The tornado center is about 1.7 km from the radar (bottom center of each panel). A characteristic tornado rotational velocity couplet (left), and high-reflectivity disk are present.

Figure 3.1. The typical geometry for a single tornado vortex observation. All quantities derived from data in each tornado observation will be associated with a fixed height and time of the vortex center observation, where (θ) is the radar azimuth angle measured clockwise from the front of the radar truck, (ϕ) is the radar elevation angle measured upward from the truck bed, (φ) is the radar tuck heading measured clockwise from true north, (V_{DOW}) is the radar truck speed, (d) is the slant-path distance to a sample volume point in space, (D) is the horizontal projection of the slant-path distance, (z) is the vertical projection of the slant path distance, (B) is the 3-dB beamwidth of the radar, (d_c, θ_c , ϕ_c) are the radar position coordinates of the center of the tornado vortex, (α) is the horizontal position angle in the tornado vortex relative to true north, (β) is the heading of the tornado vortex center measured clockwise from true north, (C) is the translational speed of the tornado vortex center, (V_{max}) is the maximum axisymmetric tangential velocity, (R_{mv}) is the radius of the maximum axisymmetric tangential velocity relative to the center of the tornado vortex, (r) is the horizontal distance to any point from the center of the tornado vortex, (V_{din} and V_{dout}) are the observed maximum inbound and outbound Doppler velocities, and (r_{in}, r_{out}) are the radii of the maximum inbound and outbound Doppler velocities relative to the center of the tornado vortex. 146-147

Figure 3.2. The elevation angle correction used to account for partial beam blockage of the main radar lobe using the error function. The angle correction only impacts very low elevation angles where the reported elevation angle is less than about half a beamwidth (near 0.5 degrees) and the effective elevation angle reaches about 0.3 degrees in elevation for reported elevation angles at or just below zero degrees. 148

Figure 3.3. Example of automated quality control algorithms of Doppler velocity measurements (m s^{-1}) including (a) thresholding on NCP below 0.2 and two-pass despeckling within a 2-gate radius using 50% surrounding coverage minimum and (b) two-pass deglitching staggered-PRT 149

Doppler velocity values using Nyquist multiples of the individual PRTs as guesses to match the median value of surrounding gates by less than 20 m s^{-1}. Original Doppler velocity values appear on left and final quality controlled fields are on the right.

Figure 3.4. Example of automated quality control algorithms of Doppler velocity measurements (m s^{-1}) including the thresholding on NCP below 0.2, a two-pass despeckling within a 2-gate radius using 50% surrounding coverage minimum, and removal of radar platform motion including rotation to ground-relative orientation. Original Doppler velocity values appears on left and quality controlled fields are on the right. Note that standard velocity dealiasing must still be implemented on the right. 150

Figure 3.5. Example of tornado center identification showing a single DOW Doppler velocity field (m s^{-1}) through tornado at one degree elevation at about 3 km range. Cartesian tick marks are every 100 m. In the first step, the maximum Doppler velocity difference, at constant range from the radar, is identified and must be at least 40 m s^{-1} in magnitude over a horizontal distance of no more than 2 km. The Doppler velocity data point closest to the midpoint of the maximum inbound and outbound Doppler velocities (black circles), at constant rage, is the first-guess center point (hash mark on the line connecting the circles). The distance between the two maximum values is the first-guess core diameter (line connecting the circles). An intensive search domain is established using a sector of data that has dimensions in the azimuthal and radial directions that is twice the first-guess core diameter with a center point of the first-guess center (black polygon). 151

Figure 3.6. Example of tornado center identification showing a single DOW Doppler velocity field (m s^{-1}) through tornado at one degree elevation at about 3 km range. Cartesian tick marks are every 100 m. In the second step, the median velocity position (black circles) of the (a) lowest 10% of Doppler velocity values (magenta color) and (b) highest 10% of the Doppler velocity values (magenta color) in the intensive search domain (black polygon) are identified. 152

Figure 3.7. Example of tornado center identification showing a single DOW Doppler velocity field (m s^{-1}) through tornado at one 153

degree elevation at about 3 km range. Cartesian tick marks are every 100 m. In the third step, the Doppler velocity data point nearest the midpoint of the two median positions identified in step two (black circles) is classified as the refined tornado center point and used as the best-guess tornado center (the hatch through the line connecting the circles).

Figure 3.8. The aspect ratio correction factor used to account for reduction in Doppler velocity measurements when the radar beamwidth becomes large relative to the diameter of the tornado core. The correction factor is limited to a maximum value of 1.14 when the beamwidth reaches a quarter the inferred tornado diameter. The edge-case is reached when the beamwidth reaches half the diameter of the tornado and a gate-to-gate Doppler velocity signature results. 154

Figure 3.9. Example of tornado patch and cross-section extraction from the Doppler velocity field (m s^{-1}). The patch diameter in which attributes of the velocity field are collected and computed is set to three first-guess diameters (six radii) from the best-guess center point. The (a) azimuthal cross-section through the best-guess center to the edges of the patch are also extracted (black polygon) and (b) annuli (black dashed circles) in which axisymmetric tangential and radial components of the flow are retrieved relative to the best-guess center. 155

Figure 3.10. The sensitivity of the single-Doppler velocity retrieval technique to the selection of the vortex center point. The vortex center point is manually relocated 120 m in four directions from the refined center point and the resulting retrievals of axisymmetric tangential and radial velocities are compared with the retrieval from the algorithm identified center point (in bold black). The 120 m relocation represents a shift in center position by about 20% of the radius of maximum winds (700 m). 156

Figure 4.1. Frequency histogram of all DOW radar observations showing (a) number of observations for each DOW observed tornado at (a) all elevations and (b) all elevations below 500 m AGL. Observation counts less than 100 are expanded in (c) for all elevations and (d) all elevations below 500 m AGL. 157-158

Figure 4.2.	Frequency histogram of all DOW radar observations showing (a) horizontal range to the center of the vortex and (b) elevation of the vortex center observation AGL.	159
Figure 4.3.	Frequency histogram of all DOW radar observations showing (a) gate spacing at the center of the vortex, (b) beam spacing at the vortex center, (c) period between successive observations of the vortex center, (d) period between successive low-level (< 500 m AGL) observations of the vortex center, (e) ratio between beam spacing at the vortex center and detected core diameter and (f) ratio of gate-spacing at the vortex center and the detected core diameter.	160-162
Figure 4.4.	Frequency histogram of DOW observations (solid) containing the maximum ground-relative aspect-corrected velocity for each tornado observed as compared with OneTor tornado reports (hatched) for the same tornadoes using the (a) F-scale and (b) EF-scale mapping of the velocity. Frequency histogram of DOW observations (solid) containing the maximum ground-relative aspect-corrected velocity for each tornado that is not reported in OneTor and compared with OneTor tornado reports (hatched) not detected by the DOWs using the (c) F-scale and (d) EF-scale mapping of the velocity.	163-164
Figure 4.5.	Frequency histogram of DOW observations (solid) containing the maximum core-diameter of each tornado observed as compared with OneTor tornado reports (hatched) for (a) maximum DOW core width, (b) DOW core width at peak intensity and (c) DOW core width at peak intensity for EF2 or greater ratings.	165-166
Figure 4.6.	Frequency histogram of OneTor tornado reports in Texas, Oklahoma, Kansas and Nebraska during April-June of 1995-2003 showing (a) F-scale intensity classification and (b) F-scale intensity classification normalized by F0 reports.	167
Figure 4.7.	Frequency histogram of OneTor tornado reports in Texas, Oklahoma, Kansas and Nebraska during April-June of 1995-2003 for DOW-observed tornadoes showing (a) F-scale intensity classification and (b) F-scale intensity classification normalized by F0 reports.	168

Figure 4.8.	Box plots showing the distribution (minimum, 25th percentile, median, 75th percentile and maximum) of ground-relative aspect-corrected velocity for all DOW tornado observations below (a) 500 m AGL, (b) 200 m AGL, (c) 50 m AGL and (d) maximum value for each tornado below 500 m AGL. Sample sizes indicated for each distribution.	169-170
Figure 4.9.	Box plots showing the distribution (minimum, 25th percentile, median, 75th percentile and maximum) of maximum ground-relative aspect-corrected velocity for each DOW tornado observed below 500 m AGL when mapped to the (a) F-scale, (b) EF-scale, (c) EF-scale for observations within 10 km and (d) EF-scale for observations within 5 km. Sample sizes indicated for each distribution.	171-172
Figure 4.10.	Box plots showing the distribution (minimum, 25th percentile, median, 75th percentile and maximum) of (a) translational speed for all DOW tornado observations below 500 m AGL and (b) duration of tornado observation for all DOW scans. Sample sizes indicated for each distribution.	173
Figure 4.11.	Box plots showing the distribution (5th percentile, 25th percentile, median, 75th percentile and 95th percentile) of all DOW observations of vortex tilt angle with respect to the vertical for (a) all observations and (b) observations below 500 m AGL. Sample sizes indicated for each distribution.	174
Figure 4.12.	Box plots showing the distribution (minimum, 25th percentile, median, 75th percentile and maximum) of the velocity difference across the tornado core for all DOW tornado observations below (a) 500 m AGL, (b) 200 m AGL, (c) 50 m AGL and (d) maximum value for each tornado below 500 m AGL. Sample sizes indicated for each distribution.	175-176
Figure 4.13.	Box plots showing the distribution (minimum, 25th percentile, median, 75th percentile and maximum) of all DOW observations below (a) 500 m AGL, (b) 200 m AGL, (c) 50 m AGL and (d) diameter of maximum axisymmetric vertical vorticity below 500 m AGL. Sample sizes indicated for each distribution.	177-178

Figure 4.14. Box plots showing the distribution (5th percentile, 25th percentile, median, 75th percentile and 95th percentile) of all DOW observations below 500 m AGL for (a) axisymmetric vertical vorticity and (b) horizontal divergence across the core. Horizontal divergence is computed for tornado cores within (c) 200 m AGL, (d) 100 m AGL, (e) 50 m AGL and (f) 50 m AGL where observations with centripetal acceleration at core edge larger than 40 m s^{-2} are removed. Sample sizes indicated for each distribution. 179-182

Figure 4.15. Box plots showing the distribution (5th percentile, 25th percentile, median, 75th percentile and 95th percentile) of all DOW observations below 500 m AGL for (a) circulation at the radius of maximum Doppler velocity, (b) averaged angular momentum at the core radius and (c) centripetal acceleration at the edge of the core. Sample sizes indicated for each distribution. 183-184

Figure 4.16. Box plots showing the distribution (5th percentile, 25th percentile, median, 75th percentile and 95th percentile) of (a) acceleration and (b) deceleration in ground-relative aspect-corrected velocity below 500 m AGL, and (c) acceleration and (d) deceleration in ground-relative aspect-corrected velocity below 50 m AGL. Sample sizes indicated for each distribution. 185-186

Figure 4.17. Box plots showing the distribution (5th percentile, 25th percentile, median, 75th percentile and 95th percentile) of (a) acceleration and (b) deceleration in velocity difference across the tornado core below 500 m AGL, and (c) acceleration and (d) deceleration in velocity difference across the tornado core below 50 m AGL. Sample sizes indicated for each distribution. 187-188

Figure 4.18. Box plots showing the distribution (5th percentile, 25th percentile, median, 75th percentile and 95th percentile) of (a) expansion and (b) contraction in tornado core diameter for all observations below 500 m AGL, and (c) expansion and (d) contraction in tornado core diameter for all observations below 50 m AGL. Sample sizes indicated for each distribution. 189-190

Figure 4.19. Box plots showing the distribution (5th percentile, 25th percentile, median, 75th percentile and 95th percentile) of (a) strengthening and (b) weakening axisymmetric vertical 191-192

vorticity across the vortex core for observations below 500 m AGL and (c) strengthening and (d) weakening axisymmetric vertical vorticity across the vortex core for observations below 50 m AGL. Sample sizes indicated for each distribution.

Figure 4.20. Scatter plots showing correlation between all DOW observations of velocity difference across core and elevation of vortex center AGL below (a) 10000 m, (b) 1000 m, (c) 500 m, (d) 200 m, (e) 100 m and (f) 50 m AGL. The average velocity difference in each layer (solid line) along with one standard deviation from the average (dashed lines) is overlaid. The correlation coefficients for linear fits are shown. 193-196

Figure 4.21. Scatter plots showing correlation between all DOW observations of normalized velocity difference across core and elevation of vortex center AGL below (a) 10000 m, (b) 1000 m, (c) 500 m, (d) 200 m, (e) 100 m and (f) 50 m AGL. Velocity difference values are normalized relative to the maximum observed velocity difference for a given tornado. The average normalized velocity difference in each layer (solid line) along with one standard deviation from the average (dashed lines) is overlaid. The correlation coefficients for linear fits are shown. 197-200

Figure 4.22. Scatter plots showing correlation between all DOW observations of aspect-corrected ground-relative velocity below (a) 10000 m, (b) 1000 m, (c) 500 m, (d) 200 m, (e) 100 m and (f) 50 m AGL. The average ground-relative velocity in each layer (solid line) along with one standard deviation from the average (dashed lines) is overlaid. The correlation coefficients for linear fits are shown. 201-204

Figure 4.23. Scatter plots showing correlation between all DOW observations of normalized aspect-corrected ground-relative velocity below (a) 10000 m, (b) 1000 m, (c) 500 m, (d) 200 m, (e) 100 m and (f) 50 m AGL. Velocity values are normalized relative to the maximum observed aspect-corrected ground-relative velocity for a given tornado. The average normalized ground-relative velocity in each layer (solid line) along with one standard deviation from the average (dashed lines) is overlaid. The correlation coefficients for linear fits are shown. 205-208

Figure 4.24. Scatter plot showing correlation between all DOW observations of velocity difference across the core and core diameter for diameters between (a) 0-2000 m, (b) 0-700 m, and (c) 700-2000 m. The average velocity difference in each 100 m diameter bin (black solid line) along with one standard deviation from the average (black dashed lines) is overlaid. The diameter of the maximum averaged value is denoted (blue dashed vertical lines). The correlation coefficients for linear fits are shown. 209-210

Figure 4.25. Scatter plot showing correlation between all DOW observations of (a) difference in magnitude between maximum outbound and maximum inbound Doppler velocity and elevation AGL, (b) tornado heading relative to azimuth angle and elevation AGL, and (c) tornado heading relative to azimuth angle and elevation AGL only for observations where the radar was stationary and deployed. All positive (negative) angles measured clockwise (counterclockwise) from true north. The correlation coefficient for linear fit is shown. 211-212

Figure 4.26. Scatter plot showing the number of data points (gates) below/above the $10^{th}/90^{th}$ percentile within about two core radii of the vortex center when compared against the value of the $10^{th}/90^{th}$ percentile with respect to the maximum observed Doppler magnitude below 500 m ALG for (a) all observations and (b) maximum value for each tornado. Only Doppler magnitude values exceeding 40 m s^{-1} are shown. 213

Figure 4.27. Doppler velocity radial profiles for the peak intensity observation of each tornado observed below 500 m AGL. Radius position from the vortex center is normalized relative to the radius of maximum Doppler velocity and velocity values are normalized relative to the maximum Doppler velocity for each observation. The solid body interior (not well-resolved) and decay region profiles are shown for reference. The large number of observations below the profiles result from asymmetries between the inbound and outbound sides of individual tornado cross-sections that are composited for this figure. 214

Figure 4.28. Scatter plot showing correlation between DOW observations from 10 strong/violent tornadoes and the closest WSR-88D radar time-matched (a) Tornado Vortex Signature (TVS) maximum velocity difference, and DOW 215

velocity difference, (b) TVS shear vs DOW shear, and (c) mesocyclone shear vs DOW shear.

Figure 4.29. Line plots showing evolution of lowest-level DOW Doppler velocity difference observations (red/orange) from seven strong/violent tornadoes and the closest WSR-88D TVS algorithm maximum velocity difference (blue), lowest-level velocity difference (green) and average velocity difference (cyan) for tornadoes near (a) Spencer, SD 30 May 1998, (b) Moore, OK 03 May 1999, (c) Mulhall, OK 03 May 1999, (d) Alemena, KS 03 June 1999, (e) Oklahoma City, OK 09 May 2003, (f) Attica, KS 12 May 2004, and (g) Geary, OK 29 May 2004. 216-218

Figure 4.30. Doppler velocity fields for a tornado observed at (a) 1.8 km range from a DOW (left) and resampled using a Gaussian-weighted 0.5 azimuthal sampling with 250 m range gates (right). Resampling is then performed using 250 m range gates at increasing ranges in (b) including 10 km (upper-left), 30 km (upper-right), 60 km (lower-left) and 90 km (lower-right). Tick marks are spaced at 1 km intervals. 219

Figure 4.31. Time-height cross-sections of axisymmetric vertical vorticity across the vortex core for five cases where observations extend through at least the lowest 2 km AGL and capture tornadogenesis. Vorticity values are color-coded by magnitude where values less than 0.1 s^{-1} are blue, values 0.1 s^{-1} to 0.5 s^{-1} are green, values 0.5 s^{-1} to 1.0 s^{-1} are yellow, and values greater or equal to 1.0 s^{-1} are red. Cases include tornadoes observed near (a) Spencer, SD on 30 May 1998, (b) Tarzan, TX on 01 May 1999, (c) Thedford, NE on 04 June 1999, (d) Thedford, NE on 04 June 1999 and (e) Crowell, TX on 30 April 2000. 220-222

Figure 4.32. Retrieved horizontal profiles of axisymmetric (a) tangential velocity (b) radial velocity and (c) angular momentum for six weak tornadoes observed near Tulia, TX on 10 April 1997, Bridgeport, NE on 20 May 1998, Kremlin, OK on 21 April 1999, Tarzan, TX on 1 May 1999, Jericho, TX on 20 May 1999 and Pyote, TX on 26 May 1999. All radius values are normalized relative to the distance from the vortex center to the peak tangential velocity (1.0). All tangential velocities are normalized relative to the peak tangential velocity (1.0). All radial velocities are normalized relative to the peak radial velocity (1.0) with positive (negative) values indicating radial outflow 223-224

(inflow). All angular momentum values are normalized relative to the value at the radius of maximum axisymmetric tangential velocity. The composite profiles show the six weak tornadoes at their initial observation time.

Figure 4.33. Same as Figure 4.32 except for mature stage of weak tornadoes. 225

Figure 4.34. Same as Figure 4.32 except for the first observation time of six strong tornadoes observed near Dimitt, TX on 02 June 1995, Kellerville, TX on 08 June 1995, Spencer, SD on 30 May 1998, Moore, OK on 03 May 1999, Mulhall, OK on 03 May 1999 and Almena, KS on 03 June 1999. 226-227

Figure 4.35. Same as Figure 4.34 except for mature stage of strong tornadoes. 228

Figure 4.36. Same as Figure 4.35 except for last observation time of strong tornadoes. 229

Abstract

Fine-scale-resolution mobile radar observations of supercell tornadoes have been collected by the Doppler On Wheels (DOWs) platform between 1995 and 2010. The result of this ongoing effort is a large observational database spanning over 170 separate supercell tornadoes with a typical data spacing of O(50 m X 50 m X 50 m), updates every O(60 s) and measurements within 20 m of the surface extending to several km above the ground. The data used in this study span 1995-2001 and 69 tornadoes along with about four selected tornadoes from 2003-2004.

Stemming from this observational database is an effort to characterize both the structure and dynamics of the high wind speed environments in and near supercell tornadoes. To this end, a suite of algorithms was developed for and applied to the DOW radar observations for quality assurance along with detection, tracking and extraction of attributes associated with the tornadoes.

The integration of observations across tornado cases in the database produced tornado size and intensity distributions revealing a preferred scale and amplitude for tornadoes produced from mesocyclones of supercell thunderstorms while exhibiting a weak negative correlation between the horizontal scale of a tornado vortex core and the peak intensity. Two horizontal scales are apparent in the clustering of intensity observations with the strongest tornadoes on the smaller scale. The observed intensity distribution is contrasted with traditional damage derived intensity estimates of the same tornadoes from a storm report database to highlight the existing low-bias in supercell tornado intensity estimates.

The vertical structure of the DOW-observed tornadoes is characterized by a much larger variance of near-surface (within 200 m of the surface) tornado wind speeds compared to those associated with the larger scale mesocyclonic flow aloft (over 1 km above the surface) often observed by operational radars. Time and tornado averaged vertical profiles of intensity exhibit a nearly constant value with height in the lowest several hundred meters. Horizontal profiles of velocity and vorticity show a bias towards divergent tornado cores with vertical vorticity maxima in the interior of the tornado core and a departure from solid body rotation.

The evolution of vortex-scale vorticity in most of the tornadogenesis cases also revealed a dominant mode of simultaneous scale contraction through the lowest 1 km layer which has implications for the vertical structure of forcing associated with mesocyclone-associated tornado formation. Layer-averaged low-level (within 500 m of the surface) horizontal angular momentum profiles in weak and the decaying stage of strong tornadoes appear to have non-contracted angular momentum values remaining at larger radii but are removed through lateral advection away from the tornado and/or divergent flow.

Chapter 1

Introduction

Supercell tornado formation and structure have been a major focus of mesoscale atmospheric research for the past half-century. Pioneering observational work between the 1950s and the early 1990s in tornado damage surveys led by Fujita et al. (1970) and Fujita (1971, 1973, 1992) have been complemented by other visual observational analysis techniques including photogrammetry (Forbes 1976; Golden and Purcell 1977, 1978) and limited weather radar measurements (Zrnic and Doviak 1977; Zrnic and Istok 1980; Zrnic et al. 1985). Paralleling the observational studies were laboratory simulations of tornado-like vortices from Ward (1972), Church et al. (1977) and Church and Snow (1985). Laboratory simulations of the 1970s and 1980s yielded to the increasingly sophisticated numerical simulations of tornadoes and parent supercells (thunderstorms with persistent rotating updrafts called mesocyclones) in the 1980s, 1990s and 2000s from Rotunno (1977, 1979, 1984), Walko (1993), Wicker and Wilhelmson (1995), Trapp and Fiedler (1995), Nolan and Farrell (1999) and local eddy simulations by Lewellen et al. (1997, 2000). Theoretical contributions from Fujita et al. (1970) and Fiedler and Rotunno (1986) attempted to explain some characteristics of tornado structure.

During the 1980s and early 1990s several stationary and mobile weather radar systems were developed and deployed in the field including the Weather Surveillance Radar 1988 Doppler (WSR-88D). The high resolution continuous wave (CW) and W-band radar observations from Bluestein et al. (1993, 2003, 2004) contained some of the first detailed radar observations in a tornado vortex. Burgess (1993) and Wood and Brown (1997) discussed some attributes and limitations of sampling tornado and mesoscale vortices with WSR-88Ds. Field experiments including Verification of Rotation in Tornadoes EXperiment (VORTEX) 1994/5 incorporated airborne radar observations of tornadic supercells (Rasmussen et al. 1994).

During the second year of VORTEX 1995 a mobile radar system known as the Doppler On Wheels (DOWs) (Wurman et al. 1997) was first deployed in the field to collect high-resolution observations of tornadoes. Between 1995 and 2008 several additional DOWs were fielded to collect single and dual-Doppler observations of tornadoes during the field project known as Radar Observations of Tornadoes and Thunderstorms Experiment (ROTATE) (Wurman 1999, 2001; Wurman and Randall 2001).

The DOW 3 dB symmetric antenna beamwidth was 1.22 degrees in 1995 and 0.93 degrees from 1996-2008. DOW transmitters, receivers and signal processing systems permitted matched pulse widths and receiver sample spacings as small as 12.5 m by 1997 (Table 1.1). Furthermore, single processing of staggered pulse repetition periods (SPRTs) permitted unambiguous velocity measurements up to 128 m s^{-1} in some stronger tornado wind fields starting in 1999 (Table 1.2).

The DOWs are currently the only ground-based radar platform that has collected tornado-scale observations when stationary and while mobile which has almost tripled the number of available observations from the stationary data alone. The DOW platform was designed to resolve accurately 4Δx horizontal features on the scale of O(50 m) at 2 km range scaling to O(300 m) at 10 km range where Δx is the average horizontal data spacing (Table 1.3). Detection of 1Δx to 2Δx horizontal features on the scale of O(12-25 m) to O(75-150 m) at the respective 2 km and 10 km ranges are possible although amplitudes of such features are significantly reduced (Carbone et al. 1985). While the WSR-88D network does provide critical information to the operational community and the public pertaining to hazards associated with supercell thunderstorms, their typical range from such storms and their scanning strategies most often limit resolution of 4Δx features to O(1 km) or greater in horizontal scale. Even with proposed 0.5 degree sampling for WSR-88D radars, 4Δx reaches 1 km at a range of only about 29 km. It is

rare that tornadoes occur within 29 km of WSR-88D's. Only 3% of the ROTATE domain has 4Δx WSR-88D coverage of less than 1 km. This larger 1 km size is more characteristic of mesocyclones and does not resolve tornado-scale features at O(100 m) or even detects them in most cases. Another limitation with WSR-88D systems is the relatively small domain of coverage within 250 to 500 m AGL which is often the majority if not the entirety of the sub-cloud layer in tornadic supercell environments (Rasmussen and Blanchard 1998). In fact, only about 35% of the ROTATE domain has 88D observations below 1 km above ground level (AGL), which decreases to 12% below 500 m and only 3% below 250 m AGL (Fig. 1.1).

Over the past several decades efforts have been made to construct a climatology of tornadoes across the United States, with an attempt to characterize the spatial, temporal and frequency distribution of tornadoes as a function of intensity (Kelly et al. 1978; Grazulis 1984, 1993; Grazulis et al. 1993; Concannon et al. 2000; Brooks and Doswell 2001; Brooks et al. 2003; Dotzek et al. 2003; Feuerstein et al. 2005). However, the estimation of tornado intensity, and to a much more limited extent the width and track length, have all been inferred from observed damage to structures or vegetation. Therefore, this damage-based tornado intensity database has a high bias in both in intensity and frequency toward more populated areas (Schaefer and Galway 1982; Doswell and Burgess 1988). Furthermore, damage indicators result from the integrated effects of variations in structural integrity, upwind debris loads, duration of damaging winds, and proximity to the core-flow or multiple vortices, from which a single tornado intensity estimation is derived (Fujita 1971, 1973; McDonald and Marshall 1984; Marshall 1992, 2002). Finally, these damage indicators exist only near the ground and provide no information about the structure or intensity of the tornado and associated mesocyclone aloft.

It is no exaggeration to state that current knowledge does not permit even the most basic statistics concerning tornadoes to be known. *What is the average size and size distribution of tornadoes? What is the average and true distribution of tornado intensities? How does intensity correlate with size? What is the dependence of tornado windspeed on height?* Existing climatologies are also unable to provide statistical measures of more complex but important kinematics related to tornadoes and tornadogenesis. *What is the relationship between tornado intensity, size, duration-above-certain-intensity and mesocyclone strength? How does peak tornado intensity compare with total angular momentum in the tornado? How does scale contraction typically develop horizontally and vertically within a low-level mesoscyclone?*

DOWs have been fielded in project ROTATE nearly every year since 1995 between mid-April and mid-June. The ROTATE domain of operations was initially confined to the southern plains of the Unites States in Oklahoma and adjacent portions of Texas and Kansas. The operations domain was broadened after 1997 to include the remainder of the plains from North Dakota south to central Texas and eastern Colorado eastward into western Iowa (Fig. 1.2).

On average there are about 14 days of operations including radar data collection each season (Fig. 1.3a), and on about one-third of these days (34.5% of the time) one or more tornadoes are observed resulting in an average of about 5 tornado days each year with a standard deviation of about 3 days. This success rate is much lower for collection of observations in significant tornadoes (defined here as Doppler velocity observations exceeding 60 m s^{-1}) where only about 9% of operation days include data collection in significant tornadoes, or about 1.3 days each season with a standard deviation of 1.1 days. The most frequent days of tornado observations are 31 May and 12 June (Fig. 1.3b).

Efforts to collect radar observations of tornadoes from the DOWs during both the

VORTEX and ROTATE field projects have yielded a large database of quasi-horizontal scans comprising over 150 unique tornadoes produced by supercell mesocyclones with observed Doppler velocities as high as 135 m s^{-1} (Wurman and Gill 2000; Burgess et al. 2002; Wurman 2002; Alexander and Wurman 2005; Wurman and Alexander 2005; Wurman et al. 2007a,b,c; Marquis et al. 2008). Typical resolution in tornadoes from this dataset is on the order of 50 m X 50 m X 50 m (sometimes as fine as 12 m x 3 m x 3 m) with 60 s updates and observations usually extending below 100 m AGL and up to 3-5 km AGL.

Therefore, it is now possible to attempt a tornado climatology based upon high-resolution radar observations of actual tornado structure, rather than based on cruder measures of tornado intensity only near damaged structures at the ground (Alexander and Wurman 2006, 2007, 2008). Features on the scale of tornadoes located beyond 30 km range from a DOW have nearly identical resolution and horizon constraints as an 88D radar and these features are treated as undetected and not resolved. Although this analysis will be limited necessarily to supercell tornado observations within 30 km of a DOW in the ROTATE domain of the United States plains, it avoids the biases and limitations of damage-only based statistics. It is important to note that the DOWs observe about one percent of the annually reported tornadoes in the United States (Grazulis 1993; Brooks et al. 2003). This sampling rate is about two percent of the annually reported tornadoes over the United States plains.

Several analysis techniques have been developed to retrieve the three dimensional winds, pressure, and buoyancy in either single or dual-Doppler observations of mesoscale or stormscale phenomena including Gal-Chen (1978, 1982), Hane and Scott (1978), Sun and Cook (1994), Shapiro et al. (1995), Zhang and Gel-Chen (1996), Lee et al. (1994a,

1999), Lee and Marks (2000), and Gao et al. (2001). A single-Doppler velocity retrieval technique presented by Alexander in Dowell et al. (2005) has been specifically applied to DOW tornado observations for the purpose of estimating the axisymmetric rotational and convergent components of flow in a tornado as a function of radius from the vortex center.

Chapter 2 provides a historical background to the current state of knowledge regarding the distribution of kinematic structures and dynamics of supercell tornadoes based upon theoretical, modeling, and observational studies. Chapter 3 describes the radar data collected by the DOWs. A description of the quality control and analysis algorithms are provided including the techniques used to identify, isolate and track radar features associated with a tornado vortex along with the extraction of kinematic vortex attributes. The output from all the analysis algorithms is integrated to form a large tornado database in Chapter 4 where the distribution of tornado attributes such as peak velocities and core diameters are presented in comparison with damage-derived tornado intensity databases. Sampling biases in the DOW database are addressed in Chapter 5.

Several hypotheses are proposed related to the frequency distribution of tornado kinematics and dynamics produced from the storm-scale forcing associated with discrete supercell thunderstorms. A preferred horizontal scale and intensity of mesocyclonic tornadoes associated with the characteristic forcing is presented and supported by the DOW data. Furthermore, correlations between peak tornado intensity and intensity of the parent mesocyclone or scale of the tornado vortex are believed to be weak. Dynamical aspects of tornado vortex scale contraction in both the horizontal and vertical are presented in the context of existing conceptual models supported by DOW observations.

Chapter 5 provides a summary and discussion of the analysis presented in Chapter 4 and suggests more avenues of study related to this research.

Chapter 2

Literature Review

2.1 Theories of Tornado Structure

2.1.1 Scale of Tornadoes

Fujita (1965) used some limited observational evidence from three tornadoes and attempted to characterize typical tornado structure including size, wind speed, circulation, vorticity and angular momentum. *This work placed tornadoes on the scale between 10 and 100s of m with maximum wind speeds between 10 and 100s of m* s^{-1}. *Estimated mean vorticity and convergence values were both on the order of 0.01* s^{-1} *in the 1 km region surrounding the tornadoes. Circulation values in the same region were estimated around* $1x10^4$ m^2 s^{-1}. *The circulation values for the tornado scale itself were associated with the same order of magnitude, while vorticity values appeared to be about one or two orders of magnitude higher around 0.1 to 1.0* s^{-1}. Fujita speculated that mesocyclonic circulations conserved absolute circulation as they contracted (converged) to a tornado scale while absolute vorticity values increased. Fujita also speculated that the source of angular momentum and vorticity for mesocyclone and tornado formation must necessarily originate from large (macro) scale wind fields and along boundaries of storm (meso) scale features which are embedded in steady-state updrafts.

More recently, Nolan (2005) examined the scale associated with tornado vortices and based upon previous work determined that the radius of maximum tangential winds should occur where air, nearly conserving circulation and drawn in from a far field at or

beyond the radius of the convective updraft, has achieved a speed limit characteristic of the local convective environment (see section 2.1.2),

$$L = \frac{\Omega R^2}{U} \tag{2.1}$$

where L is the radius of the maximum tangential tornado winds, Ω and R are the far field angular rotation rate and radius respectively, and U is the local environment speed limit. *For typical values of the speed limit near 80 m s^{-1}, an updraft radius of 1 km (far field radius of 2 km) and an environmental rotation rate of 5x10^{-3} s^{-1}, the predicted radius of the tornado was around 250 m.* Furthermore, the low-level flow structure in the tornado vortex was shown to be independent of the vertical altitude and distribution of the convective forcing, but highly dependent on the horizontal scale of the convective updraft.

2.1.2 Maximum Horizontal Wind Speeds

Theoretical studies have attempted to place a lower limit on the maximum winds in tornado by Snow and Pauley (1984) and Fiedler and Rotunno (1986). Snow and Pauley (1984) discussed a "thermodynamic method" based upon the idea that surface pressure drops in the center of the tornado vortex result from the difference in weight between the column of air constituting the core, and that of the surrounding region. This pressure drop was determined by assuming an axisymmetric inviscid vortex flow and imposing a cyclostrophic balance constraint in either a single-cell vortex with a central updraft, or a two-cell vortex with a central downdraft surrounded by an updraft annulus (see section 2.2.1). *These constraints yielded estimated maximum pressure deficits of about 45 mb for a single cell vortex and 120 mb for a two-cell vortex.* This corresponded

with maximum tangential velocities of 65 m s^{-1} in the single cell case and 145 m s^{-1} in a two-cell vortex. While these values appeared to bracket theorized maximum speeds, it was acknowledged that the thermodynamic technique fails to account for significant frictional, asymmetric, and especially non-hydrostatic effects from rapid vertical accelerations just above the surface in the vortex core. Additional 20-30 mb pressure deficits in the single cell vortex were determined from vertical motions of 60-70 m s^{-1} above the surface.

Fielder and Rotunno (1986) expanded upon the thermodynamic method and recognized that the buoyancy effects helping drive vertical motions in a tornado are not confined to narrow cores, but rather, are on the scale of the thunderstorm updraft. They proposed a "thermodynamic speed limit" which was effectively the square root of the convective available potential energy (CAPE) (Moncrieff and Miller 1976),

$$U = \sqrt{CAPE} \tag{2.2}$$

where U is the thermodynamic speed limit. *For typical atmospheric values of CAPE in very unstable environments (around 4000 J kg^{-1}), the thermodynamic horizontal speed limit was about 65 m s^{-1}.* Recognizing the importance of nonhydrostatic effects (large vertical accelerations) resulting from a convergent swirling boundary layer in tornadoes, they described a vortex breakdown process commonly observed in tornado laboratory models. They discussed a laminar supercritical state upstream of a vortex breakdown to a turbulent subcritical state similar to a hydraulic jump downstream of the breakdown.

In the context of vortex flow the supercritical states were defined in terms of airspeeds exceeding the fastest centrifugal waves generated by radial displacements in the vortex. In matching the states between the upstream and downstream conditions it was

determined that the fastest tangential wind speeds could be achieved in the supercritical region just below (upstream) of the vortex breakdown point, and were about 1.7 times the peak tangential speed in the subcritical region predicted by the thermodynamic limit. *This placed peak tangential speeds around 110 m* s^{-1}. Furthermore, the matching of the conditions also predicted peak vertical motions of twice the peak tangential speeds or about 220 m s^{-1}.

2.2 Models of Tornado Dynamics

2.2.1 Laboratory Simulations of Vortex Breakdown

The first laboratory model studies of a tornado-like vortex were conducted by Ward (1972) where a rotating horizontal screen with an air intake hole along its sides was placed below an exhaust fan that simulated the updraft over the swirling boundary layer. Smoke was used a tracer to observe air motions and structures of the vortex. Ward noted the effects of both radial inflow depth and updraft radius on the appearance of the vortex structure. He also examined changes in the radial inflow angle (angle between radial wind component and full horizontal wind) as it affected the vortex structure. A common observation of the tornado vortex structure was a transition from a relatively narrow laminar vortex with a central updraft just above the boundary layer to a broader more turbulent vortex with a central downdraft at higher elevations. The elevation of this vortex breakdown appeared to be a function of a configuration ratio (inflow depth to updraft diameter) and the inflow angle. It was noted that the vortex breakdown region could be brought down to the surface resulting in a multiple vortex structure for small

inflow angles of less than 30° when the updraft diameter is about four times the inflow depth. This inflow angle must increase as the configuration ratio approached unity. If the ratio decreased further, no multiple vortices could be produced. Ward framed these structural attributes in terms of a necessarily large inward radial momentum flux that opposed a centrifugal force in order to form an intense vortex.

Davies-Jones (1973) placed the inflow angle and configuration ratio in a non-dimensional parameter know as the swirl ratio that is effectively the ratio of circulation to convergence at the vortex core edge,

$$S = \frac{R\Gamma_R}{2Q_R} = \frac{R(2\pi R v_g)}{2h(2\pi R u_g)} = \frac{R v_g}{2h u_g} = \frac{R}{2h}\tan\Phi \qquad (2.3)$$

where R is the updraft radius edge relative to the center of the vortex, Γ_R and Q_R are the circulation and inflow rate at R, u_R and v_R are the radial and tangential winds (relative to the vortex center) at R, h is the inflow depth, and Φ is the inflow angle relative to pure radial inflow.

Church et al. (1977) constructed a similar laboratory model for the purpose of studying tornado vortex structure under a variety of swirl ratios ranging from 0.01 to 30. Initial work from their efforts placed the phenomena of vortex breakdown in the range from 0.1 to 1.0. They were able to establish a single laminar vortex in low-swirl states with a vortex breakdown region developing aloft and descending to the surface (Fig. 2.1) (Fielder and Rotunno 1986). This evolution was followed by an increasing number of multiple vortices for ever-increasing values of the swirl above 1.0. Further studies by Church and Snow (1985) attempted to determine pressure distributions in the laminar (one cell) and turbulent (two cell) vortices. They discovered that the maximum pressure deficit in the one cell low-swirl cases appeared to reside above the surface and below the

breakdown region, and the deficit decreases (increases) at the surface (aloft) as the swirl number is increased until the breakdown region nears the surface. After breakdown reached the surface, the surface pressure deficit increased again. For high swirl cases where the breakdown reached the surface, the central pressure deficit appeared approach a more constant value and was about one-sixth of the peak value in the single-vortex laminar core.

2.2.2 Numerical Simulations of Corner Flow Region

Rotunno (1977, 1979) took the Ward (1972) laboratory model and implemented a computational equivalent while introducing a range of values for eddy viscosity starting with the molecular viscosity of air (1.39×10^{-5} $m^2 s^{-1}$) in order to study the effects of the frictional boundary layer on the tornado vortex structure. The result was similar to the conclusions drawn by Davies-Jones (1973) with the core flow size remaining a function of swirl ratio. *Furthermore, Rotunno established that core size does not change for decreasing values of eddy viscosity, and in the two-cell vortex, the core structure appears very stagnant with all vorticity confined to an increasingly narrow annulus between the core and an outer irrotational region.*

In continued simulations Rotunno (1979) examined the full transition of vortex structural states from no swirl to high swirl cases and numerically verified the initial observations of the laboratory models. For zero and low swirl cases (0.0 to 0.1), flow separates from the surface near the center of the vortex due to an adverse pressure gradient leaving a stagnant region near the surface and preventing the formation of an intense concentrated vortex as angular momentum is deflected upward into a jet in a

"corner-flow" region (Fig. 2.1b). For moderate swirls (0.4) the flow does not separate from the lower surface, and a strong low-level vortex forms with a breakdown developing aloft. Finally, as the swirl moves to high values (1.0) the vortex breakdown lowers to the surface and a two-cell vortex forms. *The maximum tangential velocity attained near the surface in the moderate swirl cases appeared to be strongly related to inflow layer thickness. The radial momentum flux in the boundary layer inflow was also noted to be inward toward the center of the vortex.*

Following this work, Rotunno (1984) examined the forcing for vertical motions in a tornado vortex and established that the introduction of tangential flow near the surface in a tornado vortex results in a lowering of pressure near the surface and downward pressure gradient force near the vortex center. He also established that for high-swirl flows where vortex breakdown occurs at the surface, the resulting structure is unstable and finite amplitude disturbances manifesting as multiple vortices developed near the edge of the core which moved at about half the speed of the axisymmetric tangential flow. These vortices acted in a manner similar to eddy viscosity by decreasing the sharp radial gradients of angular momentum in the axisymmetric flow.

Fiedler (1998) modeled high swirl vortices (swirl ratio > 1) in three dimensions that contained subsidiary vortices with maximum wind speeds that exceed the thermodynamic speed limit by a factor of 1.3 to 2.4. Furthermore, his study demonstrated that these subsidiary vortices were confined to a near-surface vertical layer about the size of the parent vortex radius and persisted for approximately one rotation period about the parent vortex. Generation and amplification of these subsidiary vortices was attributed to shearing instability in the parent vortex and differential vertical

stretching which promoted axial pressure gradients and permitted centrifugal waves to propagate downward along the axis of the subsidiary vortex.

More recent efforts to study tornado structure have been led by Lewellen et al. (1997, 2000) and Xia et al. (2003). These numerical modeling studies have employed advances in computer computational speed and storage capacity to simulate a tornado vortex with typical grid spacing as small as 1.5 m in the vertical and 2.5 m in the horizontal over a spatial domain of 1 or 2 km. Their model used a Local Eddy Simulation (LES) with subgrid turbulence parameterizations using an effective eddy viscosity (ν) in the sub-grid turbulent kinetic energy (TKE),

$$\nu = \sqrt{2\mathrm{TKE}}\,\Lambda/4$$
$$\Lambda = \min[0.65z,\ 0.3\max(dx,dy,dz)] \qquad (2.4)$$

where z is the vertical level in the model and (dx,dy,dz) are the model grid spacing in the horizontal and vertical directions. *Like previous modeling studies, they simulated a frictional swirling boundary layer of the tornado that contained a more laminar quasi-cylindrical region above about 300 m. The maximum tangential velocities were observed within 50 m of the surface and were about 110 m s^{-1} or approximately 60% higher than the maximum tangential velocities in the region above. Vertical velocity values reached about 50 m s^{-1} in an annular updraft region about 40 m from the core center, and about 30 m s^{-1} in the downdraft region of the core center.*

Similar to Rotunno (1984) and Fiedler (1998), Lewellen et al. (1997) also observed secondary vortices spiraling around the main vortex in the higher swirl cases which contained instantaneous velocities about one-third higher than the maximum time-averaged tangential velocity. These eddies appeared within the core flow region in areas where large vertical velocity gradients appeared, and they moved slower than the average

peak tangential velocity. Furthermore, they also noted that transport of angular momentum by the multiple vortices is inward at low levels and this enhanced the angular momentum of the core by about 30%. Pressure deficits reached a maximum value at about 30 m above ground level (AGL) and varied considerably from 70 to 130 mb. This LES simulation also tested the effect of a 15 m s^{-1} tornado translation which slightly increased the surface velocity by about 5 m s^{-1}. The LES simulation also addressed the variance in the velocity field as a function of time. Peak variance values resided in the core flow near the surface and were about 2000 m^2 s^{-2} (standard deviation of about 45 m s^{-1}) with the unresolved variance usually remaining at or below 10% of the total variance.

In some following work Lewellen at al. (2000) discussed the separation of scales associated with a tornado vortex and identified three distinct length scales namely, the storm scale on tens of kilometers which drives the outer flow, the outer tornado scale of a few kilometers, also known as the tornado cyclone in Rasmussen and Straka (2007), in which the flow is considered to be a converging swirling plume, and an inner tornado scale of tens to hundreds of meters containing the tornado core, boundary layer, and corner flow regions. It is within this smallest scale that they prescribe a local corner-flow swirl ratio as a measure to describe the corner flow structure of a tornado vortex interaction with the surface. This local swirl ratio was defined as the ratio of a characteristic tangential velocity in the surface core flow to a characteristic flow-through radial velocity,

$$S_c = \frac{v_c}{u_c} \tag{2.4}$$

where S_c is the corner-flow swirl ratio, and u_c and v_c are the characteristic radial and tangential velocities respectively. The characteristic tangential velocity was defined as

the velocity realized from an initial angular momentum value at a large distance away from the tornado vortex in the boundary layer that has converged to the core radius, while the characteristic radial velocity is related to the loss of angular momentum at the corner flow edge compared to that at large distances away. The local swirl ratio is decreased by anything that increases the inflow of low angular momentum air, and increased by increases in the core radius.

An axisymmetric numerical model implemented by Nolan and Farrell (1999) focused on the relationship between tornado vortex structure and the "vortex Reynolds number",

$$\mathrm{Re}_v = \frac{\Omega R^2}{\nu} = \frac{\Gamma_\infty}{\nu} \tag{2.5}$$

where Re_v is the vortex Reynolds number, Ω, R and Γ_∞ are the far field angular rotation rate, radius and angular momentum respectively, and ν is the turbulent eddy viscosity. The relationship between the vortex maximum tangential velocity and far field angular momentum appeared to change as a function of the eddy viscosity. Furthermore, the vortex aspect ratio, defined as the ratio between the radius of maximum tangential velocity and the height of those maximum velocities appeared to increase from around 0.5 to 1.5 as the vortex transitioned from a supercritical low-swirl state to one that was high-swirl.

The important dynamic process in the intensification of the near surface tangential wind was related to the depletion of angular momentum flux towards the tornado core in the boundary layer (Lewellen et al. 2000). The two sources for the depleted flux were frictional loss from the outer swirling flow to the surface, and an influx of low angular momentum fluid from large distances outside the outer swirling flow. Low angular

momentum could also be advected downward from higher regions in the core or turbulently removed from the upper core. Conceptually Lewellen et al. (2000) describe an inertial overshoot of air in the frictional boundary that remains out of cyclostrophic balance, and the air converges toward the central axis past the point where the angular momentum reached a maximum value in the cylindrically symmetrical region above the surface layer. It is this overshoot that produces the maximum tangential velocities and lowest pressure deficits in a horizontal jet that is forced upward as air converges toward the center of the vortex.

Work by Xia et al. (2003) briefly examine the compressibility effects of tornado-like flows that may reach a half Mach. The results appear to indicate that density changes from the high velocities do not change the dynamics of the corner flow region. The compressibility effect did appear to increase the maximum vertical velocity and the height of the vortex breakdown in the low-swirl cases.

More recently, Lewellen and Lewellen (2007a,b) have examined other mechanisms supporting rapid intensification of a tornado-scale vortex. They focused on nesting a developing vortex within a larger scale swirling flow characteristic of an intense low-level mesocyclone and achieved an interior vortex intensification by reducing the inflow of low-swirl air near the surface from the larger scale vortex. This reduction of low-swirl air (in a variety of manners) produced a frequent response termed a "corner-flow collapse" which involved a reduction in the corner flow radius as high angular momentum air from aloft descended in a downdraft and entered the strong convergence near the surface in the radial overshooting region. The time scale for this process was related to the time for low-swirl air to be exhausted through the corner-flow region of the

interior vortex. The resulting amplification often reached an order of magnitude greater than the conditions aloft but was very transient in nature. This model has provided a possible mechanism for the formation of concentric velocity maxima although the outer vortex in these simulations, with a shallow low-swirl corner-flow and a vortex breakdown aloft in a high-swirl flow, does not resemble that of many observed low-level mesocyclones.

Most numerical and laboratory simulations describe tornado-like vortex structures as having a relatively shallow frictional boundary layer with small vertical pressure gradients, and an inflow region that transported initially low angular momentum values from great distances toward the central axis due to a radial pressure gradient driven by a central pressure deficit from the swirling tangential velocity. This air attained a vortex-wide maximum tangential velocity as it was turned upward in a jet before reaching a vortex breakdown interface. Above the interface there exists an axisymmetric quasi-cylindrical region with a radius of maximum tangential winds (upper core radius) that was up to four times larger than the lower-core radius below the breakdown region. When the swirl ratio was increased towards a value of unity, the breakdown descends to the surface and a multiple-vortex structure develops. All of the numerical models stressed the importance of properly characterizing the low-level angular momentum transport from an unsteady outer region well away from the tornado vortex.

2.2.3 Numerical Simulations of Tornadogenesis

On the outer tornado scale several other numerical modeling studies have examined the vorticity budget during the tornadogenesis stage in a parent supercell thunderstorm. Typical horizontal and vertical grid spacing on this scale ranged from 250 m to 1 km, and the spatial domain ranged across many tens of kilometers. Klemp and Rotunno (1983) and Rotunno and Klemp (1985) performed a trajectory and circulation analysis of low-level rotation that develops in a supercell thunderstorm (Fig. 2.2).

These model results indicated that horizontal vorticity is generated from horizontal buoyancy gradients along the upstream edge of a rain-cooled forward-flank downdraft region relative to the updraft region (Fig. 2.2). This horizontal vorticity is then tilted vertically before being stretched as it enters the updraft region. Their results indicate that circulation values on the order of $1x10^5$ m^2s^{-1} and vertical vorticities of about 0.01 s^{-1} can develop within a 15 min period at low levels about 250 m AGL. Vertical vortex tilting values were slightly above $5x10^{-5}$ s^{-2} while vertical stretching values appeared to be about an order of magnitude higher around 5 $x10^{-4}$ s^{-2}. They also describe the formation of an occlusion downdraft on the order of several 100 m that resulted from a downward directed pressure gradient force due to the strongest rotation near the surface. This downdraft produces an annulus of higher vorticity bearing some similarity to the multiple vortex structure in a tornado.

Walko (1993) used a regional atmospheric model with telescoping nested grids of grid spacing as small as 100 m in the horizontal and 20 m in the vertical to study the effects of horizontal vorticity present in the near surface environment prior to tornado

formation. This work concluded that vertical vorticity must be present in the ambient winds, or it must be tilted from horizontal vorticity by motions that include a downdraft (significant upward vertical motion is precluded very near the ground surface) in order to produce a tornado vortex extending to the ground. He also found circulations on the order of 5 x10^4 m^2s^{-1} could be produced within 15 min from tilting of pre-existing shear in the low to mid levels of the domain in which baroclinic effects actually reduced the circulation unlike the Rotunno and Klemp results.

Grasso and Cotton (1995) also used the same non-hydrostatic atmospheric model at an even smaller grid spacing of 25 m near the surface to produce a tornado vortex with similar structural attributes of other model simulations. Maximum updraft strengths exceeded 60 m s^{-1} less than 400 m AGL along with pressure deficits of 30 mb and tangential wind speeds in excess of 50 m s^{-1}. Unique to this model result was the formation of a vortex near the edge of an updraft where there were large horizontal gradients in the upward motion. This vortex appeared to build downward toward the surface as preexisting vertical vorticity at the surface was drawn into the vortex thereby helping to enhance the pressure deficits and drawn the vortex closer to the surface in a so-called "dynamic pipe effect (DPE)." The source of the low level vorticity appeared to result from air passing through a large downdraft thereby tilting vorticity into the vertical prior to entering the updraft near the developing vortex aloft. Concerns were raised about the initiation of the tornado vortex shortly after spawning a higher mesh grid that may have contributed to artificial changes in the flow structure.

Another numerical modeling approach was conducted by Wicker and Wilhelmson (1995) using a two-way interactive adaptive grid system where a high mesh grid was

introduced 10-15 min prior to peak low-level rotation formation. Their observations reinforced a conceptual model of tornadogenesis that had some similarities to that of Klemp and Rotunno (1983). They also noted that mid-level rotation in the parent mesocyclone first increased (producing a tornado vortex signature) thereby enhancing both the strength of the low-level updraft through vertical pressure gradients to 20 to 30 m s^{-1}, and convergence near the surface. Following this intensification, horizontal vorticity that was generated along the forward edge of the rain-cooled region was tilted into the vertical by downdrafts and then stretched in the convergent flow creating the tornado vortex. Decay of the tornado vortex was observed when the vertical pressure gradient relaxed and the updraft weakened followed by the occlusion downdraft surrounding the tornado vortex. Again, typical values of dynamical terms such as $1x10^{-4}$ s^{-2} for vertical vorticity stretching, and $1x10^{-5}$ s^{-2} for vorticity tilting into the vertical at 100 m AGL were seen near the developing tornado vortex. Peak ground relative winds exceeded 60 m s^{-1} in the tornado vortex, although they acknowledge the need to improve the resolution in the swirling boundary layer to address the vortex interaction with the surface as addressed by Lewellen et al. (1997).

Likewise a "pseudostorm" model of a tornado-like vortex by Trapp and Fiedler (1995) were unable to produce a vortex of any intensity greater than that predicted by the thermodynamic speed limit. While their model did not explicitly simulate the morphology of a tornadic thunderstorm, they did emulate the storm-relative flow of horizontal vorticity into an updraft. Critical to their results was the observation that their tornado vortex vorticity intensification strengthened uniformly in the vertical from stretching of tilted low-level vorticity, and there did not appear to be a need for the DPE.

They also established a relatively small parameter space of vertical velocity gradients, baroclinically generated horizontal vorticity, and eddy viscosities that would result in the formation of a tornado vortex. The most supportive conditions for vortexgenesis included strong downdrafts near baroclinic vorticity generation, limited storm-relative flow, and a thin viscous boundary layer.

Trapp and Davies-Jones (1997) presented two modes of tornado-scale vortex development that were dependant upon the vertical distribution of angular momentum and horizontal convergence near the axis of the developing vortex (Fig. 2.3). Using a two-dimensional, axisymmetric forced convection model with a closed impermeable cylinder rotating at constant rate, they demonstrated that in cases where the highest angular momentum air first approached a central axis aloft, a positive feedback developed. Angular-momentum conserving air increased in rotation lowering the central pressure and enhancing mass convergence at the base of the developing vortex where streamlines are modified in response to the vertical pressure gradient force. Air does not enter the sides of the vortex where cyclostrophic balance is attained. This "boot-strapping" process (DPE) results in a progressively downward building intense tornado-scale vortex (Fig. 2.3a,b). The model also demonstrated a second mode of vortex development where high angular momentum air approaches a central axis both near the surface and aloft and resulted in simultaneous development of an intense tornado-scale vortex through a deep layer of 1-2 km (Fig. 2.3c). In this mode there is no modification of streamlines by the developing vortex as convergence is constant with height and the vortex is simply stretched in the vertical.

The Regional Atmospheric Modeling System (RAMS) used by Gaudet and Cotton (2006) further examined vortex development within a simulated supercell thunderstorm and examined the effects of both horizontal and vertical forcing on preexisting vorticity through the use of convergence tendency equations. Assuming incompressibility and ignoring diffusive and surface frictional effects, the model results showed a process where vorticity concentration could occur in the absence of horizontal convergence. Both modes of vortex development discussed by Trapp and Davies-Jones (1997) focus on an essentially two dimensional axisymmetric vortex concentration where a central pressure deficit was driven by vertical evacuation of mass and the feedback results in increased horizontal convergence tendency. The pressure deficit causes this increase in horizontal convergence. Gaudet and Cotton (2006) consider vortex concentration in three dimensions which is nonaxisymmetric and horizontal evacuation of mass is the dominant forcing mechanism. Vertical vorticity is first generated by nonaxisymmetric horizontal convergence and then concentrated by horizontal advective processes. The resulting pressure deficit is a result of the concentrated vortex rather than a cause for its formation. Furthermore, the horizontal convergence tendency tends to be negative in this case so the convergence is decreasing with time.

Common to these larger scale numerical modeling simulations of tornadogenesis was the presence of horizontal vorticity at low levels in the pre-storm environment and/or generated by baroclinic effects in a thunderstorm. This horizontal vorticity was then tilted into the vertical by horizontal gradients of vertical motion (updrafts and downdrafts) and then stretched in the vertical by an updraft. While these model simulations place similar values on the advection, tilting, stretching, and baroclinic

generation leading to vertical vorticity, most of the work acknowledges that each simulation is effectively a single event and the values of these various forcing terms likely vary from storm to storm and tornado to tornado.

2.3 Observations of Tornadoes

2.3.1 Damage Survey Climatologies

Initial observational studies of tornadoes were dominated by damage surveys where inferences into tornado structure were made through various damage patterns produced by tornado passage through building structures or vegetation. Fujita et al. (1970) performed aerial surveys of 24 tornado damage paths from the Palm Sunday tornado outbreak on 11 April 1965. Cycloidal damage swaths were an occasional indirect observation of suction-spots that provided evidence of multiple-vortex structure in a translating parent vortex. Fujita et al. (1970) estimated the surface peak tangential speed of a tornado via a cycloidal curve analysis where he used the spacing of the cycloid tracks on the ground as a function of the translation to tangential flow ratio. Implicit in this assumption was that suction spot features in the tornado rotated at the tangential flow speed. They estimated the translational speed of one tornado from path length and tornado observation times, and this resulted in an estimated translational motion of about 28 m s^{-1}, peak tangential speeds of about 51 m s^{-1} and total ground-relative speeds of about 80 m s^{-1}.

Following this work, Fujita (1971) proposed the Fujita-Pearson-scale (FPP-scale), which became more commonly referred to as the Fujita-scale (F-scale), as a metric for

estimating tornado intensity from damage indicators. The scale initially ranged from F0 to F12 connecting the Beaufort and Mach airspeed scales before a later revision reduced the scale to an F0 through F5 range with maximum wind speeds believed to be around 140 m s^{-1}. A range of wind speeds were associated with each rating category where wind speeds were arbitrarily defined as the fastest quarter mile of wind at structure level (10 m AGL). This path-length relationship was developed to account for a decreasing duration of wind speeds necessary to produce equivalent amounts of damage as the wind speed increased. Refinements to the scale were discussed in Fujita (1992) to account for varying structural integrity.

A new damage-based intensity scale has been established for use by both research and operational communities known as the Enhanced Fujita Scale (EF-scale). This new scale addresses the variability in vegetative and structural integrity more thoroughly than the previous F-Scale and introduces degrees of damage associated with about 30 different structure types (Marshall 2004). These degrees of damage are associated with three-second wind gust speeds at 10 m that are believed necessary to produce the observed damage. The result of the EF-Scale work has been to compress the tornado wind speed range associated with the original F-Scale, raising the minimum speed associated with damage from the weakest of tornadoes (EF0) and reducing the wind speeds necessary to produce the most severe damage associated with the strongest classification of tornadoes (EF5). Work continues in this area with ongoing discussions and efforts to relate damage with various metrics of tornado intensity in an attempt to account for wind duration, accelerations and higher moments of the velocity field (Wurman and Alexander 2005).

The climatology of tornado frequency and intensity distribution was developed in

the 1960s and 1970s including work by Thom (1963) and Kelly et al. (1978) where the National Severe Storm Forecast Center (NSSFC) tornado logs were used to construct a climatology of 14409 tornadoes in the United States from 1950 to 1976. About 62% of the tornadoes were classified as weak (F0-1), 36% of the tornadoes were strong (F2-3) and only about 2% were considered violent (F4-5). The diurnal tornado frequency peaked in the late afternoon (local time) with a minimum just before sunrise (local time). Similar results were found from work by Grazulis (1993) for damage intensity estimates of reported tornadoes from 1950 to 1994 with an even higher percentage of weak tornadoes at 74% when compared to strong (25%) and violent tornadoes (1%).

The frequency of weak tornadoes across bimonthly periods throughout the year exhibited a single complete oscillation with a maximum frequency in the summer months of July and August and a corresponding minimum in November and December. The frequency of strong tornadoes also exhibited a single full oscillation throughout a year but was 180 degrees out of phase with the weak tornado cycle, exhibiting a minimum frequency in July and August and a maximum in November and December. When combining the two frequency climatologies, the maximum frequency for any tornado intensity occurs in the four month period from March through June.

The geographic distribution of weak and strong tornadoes exhibited a maximum frequency in the central and southern plains of the United States including Kansas, Oklahoma and northern Texas. There was also a larger fraction of weak tornadoes comprising the total tornado population in the plains (65%) than the corresponding weak tornado fraction in both the Midwest and southeast when compared to their respective tornado populations (58% and 50%). There was a corresponding increase in the strong

tornado percentages in the Midwest (39%) and southeast (47%) when compared to the plains (34%).

Brooks et al. (2003) constructed daily tornado probabilities using an updated Storm Prediction Center (SPC) tornado report database that is archived in the National Oceanic and Atmospheric Administration (NOAA) publication *Storm Data*. These tornado probabilities were constructed from tornado reports across the United States from 1980-1999 and exhibited a maximum in tornado probability near 2% (within 25 nautical miles of a point) in the central and southern plains during the late spring (late May and early June) along with separate regions in northeastern Colorado and Florida at different times of the year.

Additional work by Dotzek et al. (2003), Brooks (2004) and Feuerstein et al. (2005) have attempted to characterize reported tornado intensities, path lengths and widths using a more generalized Weibull distribution of which the exponential distribution is a specific case. The Weibull distribution has the form

$$p(x) = \left(\frac{a}{b}\right)\left(\frac{x}{b}\right)^{a-1} \exp\left[-\left(\frac{x}{b}\right)^{a}\right] \tag{2.6}$$

where p(x) is a probability density function of x, and a and b are the shape parameter and scale factor respectively. When the shape parameter is equal to unity, the distribution takes the form of the more familiar exponential distribution.

$$p(x) = \left(\frac{1}{b}\right)\exp\left[-\left(\frac{x}{b}\right)\right] \quad , \; a \equiv 1 \tag{2.7}$$

The use of the Weibull distribution refined previous distributions of tornado characteristics by matching physical boundary conditions of zero tornadoes with zero wind speeds and an upper limit of tornado intensities derived from energy budget

calculations. Furthermore, the Weibull distribution appeared to better match the tail-end of the reported tornado distribution for the infrequent high-intensity tornadoes.

Tornado path lengths and widths in the Storm Prediction Center (SPC) database comprising tornado reports in the United States from 1950-2001 showed median path lengths ranging from near a kilometer for F0 tornadoes to almost 45 km for F4 tornadoes. Median path widths ranged from near 25 m for F0 tornadoes to about 450 m for F4 tornado reports. While path length and width can provide a reasonable estimate for the lower bound on the reported tornado intensity, there remains a significant probability of a range of possible F values. Therefore, the observation of length or width is insufficient to make an accurate estimate of the F scale intensity (Brooks 2004).

It is well known, as discussed by Doswell and Burgess (1988), that current climatological distributions of tornado frequency and intensity are based upon damage observations, and are necessarily biased toward populated areas with greater densities of potential damage descriptors.

2.3.2 In-situ Near Surface Measurements

Direct observations of tornado structure from within or in very close proximity to such vortices have been extremely difficult to obtain for obvious safety reasons and due to the catastrophic damage usually imparted on instrumentation by direct tornado impacts. Several organized efforts to sample tornadoes with in-situ measurements resulted in failure due to placement of instrument packages that were missed by the translating tornado (Bedard and Ramzy 1983; Bluestein 1983). However, a few

observations from fixed platforms near a tornado passage have yielded a few pieces of information.

One of the most promising observations was wind measurements collected near Tecumseh, Michigan at an airport on 11 April 1965 during the Palm Sunday tornado outbreak (Fujita et al. 1970). The wind observations were collected along the southern edge of a damage track. Peak velocities recorded by the instrument were about 67 m s^{-1}. Fujita performed a time to space conversion of the wind trace, and determined the translational velocity of the tornado as 27 m s^{-1} based upon motion of the parent thunderstorm cell. The damage path width of about 4.8 km implied a core radius of about 800 m. The inferred profile of the wind field in the tornado yielded a belief that solid body rotation was present in the core with an irrotational flow outside the core. He estimated a circulation of about $4x10^5$ m^2 s^{-1}.

In the past few years, renewed efforts to place instrument packages in a tornado's path have yielded more success, and analysis of these observations is now underway (Samaras 2004, Wurman and Samaras 2004). Pressure traces from passage of tornadoes over these packages have revealed pressure deficits between 20 and 100 mb. Another in-situ observation platform is the Tornado Intercept Vehicle (TIV), which is an armored truck with a set of standard meteorological instruments capable of measuring air pressure, temperature, humidity and wind speed mounted to the roof of the vehicle. While penetration to and inside the radius of maximum winds of a mature tornado has only been achieved a few times to date, measurements also have been collected just outside the core of a tornado on 12 June 2005 near Jayton, TX (Wurman et al. 2007a). The measurements were made at 3 m AGL from the TIV and compared to simultaneous mobile radar

Doppler-velocity observations collected at 18 to 150 m AGL over the TIV location. The peak wind speed measured at 3 m was about 38 m s^{-1} which represents a 20 to 25% reduction in wind speed from peak Doppler-velocities at 18 m AGL and higher, where the variability in peak Doppler-velocities decreases to about 10%. This small variation in peak tornado Doppler velocities near and above 20 m AGL is also observed in a violent tornado near Spencer, SD on 30 May 1998 (Alexander and Wurman 2005) and indicates that measurements at 30 m AGL may be reasonably representative of conditions at 10 m AGL, at least in some tornadoes, in some terrain conditions.

2.3.3 Photogrammetry

A common technique for analyzing visual observations of tornado structure involved the tracking of passive tracers such as cloud tags or small debris in a tornado flow from movies or photographs, and is known as photogrammetry. The first detailed photogrammetric analysis was performed on the Dallas, Texas tornado of 2 April 1957 (Hoecker 1960). In this study, 19 minutes of a tornado movie were analyzed and three-dimensional attributes of the apparent tornado structure were derived from cloud and debris motions. The largest tangential wind speeds of about 76 m s^{-1} were estimated at a radius of 40 m from the apparent center at an elevation of 70 m AGL. Wind speeds as high as 55 m s^{-1} were estimated as low as 20 m AGL at 30 m from the vortex center. Also of note was the radius of the maximum tangential winds which appeared to increase from about 20 to 80 m over a vertical distance from 20 to 360 m AGL.

Other estimated structural attributes included similarities to a Rankine combined tangential velocity profile with solid body rotation in the core. The tangential velocity region outside the core appeared to decrease more sharply with radius than irrotational

flow at low-levels between 50 and 90 m AGL. The rate of decrease was inversely proportional to radius raised to the 1.6 power. At a higher level of 300 m AGL the vortex appeared irrotational outside the core. Vorticity values estimated in the core at several elevations varied around 2 s^{-1} with maximum values near 4 s^{-1} in the core at 50 m AGL. Radial motions were also estimated and reached maximum inflow values of 35 m s^{-1} at 60 m AGL before reversing to outflow above 150 m AGL. Vertical motions were estimated to attain a maximum value of 70 m s^{-1} in a jet structure near the center of the tornado at about 40 m AGL. These vertical motions appeared to decrease in speed above this level to about zero by 260 m AGL.

The edge of the condensation funnel appeared to reside very close to the estimated zero vertical velocity isotach. The debris cloud at and near the surface always appeared to be larger than the condensation funnel width, and both appeared to widen as the funnel approached the ground. Errors in this analysis were acknowledged from both the non-simultaneous observations of motions in different tornado regions and variations of the tornado opacity. Furthermore, debris motion may have had considerable deviations from the actual air motion.

These observations remained the only direct low level tornado speed estimates until Golden and Purcell (1977, 1978) observed tornadoes near Union City, Oklahoma on 24 May 1973 and Great Bend, Kansas on 30 August 1974. Motion picture film revealed that the Great Bend tornado moved toward 120° (southeast) at about 8 m s^{-1}. During much of the tornado's life a dust column extended from the ground to cloud base around the tornado condensation funnel. The diameter of the dust cloud at the ground ranged from 200 to 250 m. Golden and Purcel (1977) also observed asymmetric vertical motion

around the vortex column with weak sinking motion observed above 130 m AGL on the west side of the vortex with strong rising motions on the east side below 130 m AGL. These differential motions appeared to shift around the axis with time. Of great significance was a band of dust about 35 m deep that was being drawn into the vortex base before rising and then centrifuging outward and sinking back into the surface inflow.

Horizontal accelerations in the inflow band at about 10 m AGL appeared rather significant with air speeds of 25 m s^{-1} at 120 m from the edge of the vertical dust column increasing to 55 m s^{-1} at points within 60 m of the edge. Rising motions near 75 m AGL also appeared to increase from 10 to 20 ms^{-1} between 225 and 20 m from the vortex column edge. Maximum values of horizontal velocities in the Great Bend tornado were estimated to be about 85 m s^{-1} at 80 m AGL and a corresponding core radius of 150 m. The horizontal wind speeds increased rapidly from tree top level of 50 m s^{-1} to 75 m s^{-1} at 80 m AGL. Above 80 m AGL the horizontal wind speeds appeared to decrease to 45 m s^{-1} by about 200 m AGL. Likewise vertical motions appeared to increase towards 60 m s^{-1} at 60 to 100 m AGL implying vertical accelerations of 3 g within this layer. As with the horizontal winds, the vertical motions also appeared to decrease above 100 m AGL to around 20 m s^{-1}. Their work concludes that cyclostrophic balance and a Rankine-combined structure were probably violated within 200 m of the surface from frictional effects and radial motions.

The Union City tornado observations (Golden and Purcell 1978) also included similar characteristics during the tornado's mature stage with maximum tangential velocities of 80 m s^{-1} near 90 m AGL at a radius of 200 m. Upward vertical velocities also reached a maximum value at this same location of 30 m s^{-1}. Both the horizontal and

vertical velocities decreased above this level to around 30 and 15 m s^{-1} respectively between 300 and 700 m AGL while the core radius expanded to about 400 m. Between the mature and decay stages of the tornado, the estimated debris-cloud circulation decreased from 6 $x10^4$ to 1.6 $x10^4$ m^2 s^{-1}. During the decay stage, when the tornado had a rope-like appearance, the radius of maximum winds collapsed to about 25 m with peak tangential winds about 65 m s^{-1}. They estimated wind speed errors on the order of 10% from tracking uncertainties.

Fujita also conducted many photogrammetric studies including the Xenia, Ohio tornado (Fujita 1975) where he estimated peak winds of about 118 m s^{-1}. In the Parker, Indiana tornado, Forbes (1976) estimated peak winds of and 123 m s^{-1}. Both of these studies also contained the first movies of multiple vortices where visual observations were reconstructed in individual vortex-fixed frames of reference. Tangential velocities in these suction vortices were estimated in the range from 40 to 61 m s^{-1}.

Photogrammetric measurements of tornado air speeds appeared to confirm the ranges produced in many of the numerical model simulations except near the surface. However, due to the opaque nature of most tornadoes, only very limited regions around the periphery of the tornado vortex could be characterized, and Fujita (1992) comments on substantial temporal variations in vortex structure during photogrammetric studies thereby leaving considerable uncertainty in the observations. However, the visual observations of the tornadoes appeared to reveal a very shallow inflow layer that is not more than 50 m, and possibly as small as 20 to 30 m in depth, and the most pronounced horizontal and vertical motions close to the surface.

2.3.4 Single-Doppler Radar

One of the most useful observational tools for studying tornadoes and parent mesocyclones has been the Doppler weather radar. Doppler radar measures phase shifts from consecutive backscattered radiation pulses to determine the average motion of the backscattering targets either forward or backward along the line from the radar to the region being sampled (sample volume). The total power returned to the radar receiver is range-corrected to compensate for energy spreading, and the derived product is called reflectivity. Phase ambiguities do result from large motions exceeding a threshold (Nyquist) value that is dependant upon the frequency of transmitted pulses, and the wavelength of the transmitted radiation. For the first time, remote measurements of the wind field throughout the entire structure of a tornado and parent circulations could be achieved. Some of the first pulsed Doppler measurements in a tornado or mesocyclone were estimated by Zrnic et al. (1977, 1985) and Zrnic and Istok (1980). Zrnic et al. (1977) estimated maximum speeds between 85 and 92 m s^{-1} in two tornadoes. However these measurements were derived from a radar transmitter with a maximum unambiguous velocity of only 34 m s^{-1}.

A second transmitter was later used in Zrnic and Istok (1980) and Zernic et al. (1985) with a maximum unambiguous velocity of 91 m s^{-1}. This radar had a beamwidth (angular distance to half-power output) of 0.81° with 10 cm wavelength and a receiver sample spacing of 300 m. Two supercell storms observed at ranges of 130 km and 34 km had Doppler velocity differences of about 55 to 60 m s^{-1} across the mesocyclone as inferred from peak values in the Doppler power spectra. The second storm, observed near Del City, Oklahoma on 20 May 1977 produced a weak tornado that was close

enough to the radar (34 km) to sample a tornado vortex feature. While the resolution of the radar data was still not sufficient to completely resolve the tornado, the power spectrum was fitted to a least-square model with a high reflectivity donut structure. These assumptions retrieved a maximum (rotational) velocity of 35 m s^{-1} which became 65 m s^{-1} when considering the added effect of storm motion. The estimated radius of maximum tangential winds was between 65 and 125 m. Considerable variation of Doppler velocities existed in each sample volume with standard deviations (spectral width) values from 12 to 15 m s^{-1}. The observed tornado damage width ranged between 200 and 500 m and had a maximum damage in the F2 range (50 to 70 m s^{-1}) which agreed with the radar observations. However, given the range to the tornado observations, the height of the Doppler observations was around 2 km.

A more damaging tornado was observed with the same radar on 22 May 1981 near Binger, Oklahoma. While the radar radial resolution (300 m) was unchanged, the azimuthal spacing of beams was decreased to 0.2°, which corresponded to 560 m at the tornado range, effectively increasing the resolution of the observations. However, there were still only about a dozen radar sample volumes centered in and around the tornado. Furthermore, a single beamwidth encompassed the entire tornado condensation funnel (radar was at 70 km range) and debris cloud, as determined from photographs of the tornado. The maximum tangential velocity at the lowest observation about 500 m AGL was estimated to be about 80 m s^{-1} or 90 m s^{-1} when the translational effects were included. The tornado damage was rated in the F4 range which is just above the intensity measured by the Doppler observations. The diameter of the large core flow appeared to be about 1000 m at 500 m AGL and this increased to about 1700 m aloft. This diameter

was again consistent with a damage survey path width. The distribution of the Doppler power spectra in different sample volumes around the tornado appeared skewed so that a divergent signature was a significant component of the rotational wind field. From this skewed structure, an inferred 20 m s^{-1} of radial outflow from centrifuging debris was estimated.

While these radar observations provided further evidence for some typical values of maximum tornado wind speeds and sizes, their resolution was insufficient to truly resolve the details of the tornado scale flow, and the lowest 500 m in a tornado were usually below the elevation of the lowest radar scan. Rather than waiting for tornadoes to form near radars, radars were constructed which could be brought to the location of the tornadoes.

On such radar was placed onboard an aircraft called the Electra Doppler Radar (ELDORA). This radar was used in a field project to study tornadoes in 1994 and 1995 called VORTEX (Rassmusen et al. 1994). ELDORA had two radars, and the 3 cm radar on the tail of the plane could scan in conical sections both forward and aft permitting two observations of the same region from different viewing angles at slightly different times and thereby permitted a pseudo-dual-Doppler analysis. With two Doppler observations of sufficiently different crossing angles (usually greater than 20° and less than 160°) and an dynamical constraint like mass conservation, all three components of the wind field could be estimated. This radar's beamwidth was about 1.35 across and 1.90 along the sweep angle. Effective horizontal spacing between pseudo-dual-Doppler observations was initially about 600 to 700 m.

Observations of a tornado were made with ELDORA near Newcastle, Texas on 29 May 1994 (Wakimoto and Atkins 1996). While this tornado was of F3 intensity, it did not appear to be directly associated with a mid-level mesocyclone in the parent thunderstorm, but rather with a developing convective tower on the flanking line of the supercell. Preexisting vertical vorticity is speculated to have existed in a lateral shear region at the surface along the gust front interface which was simply stretched by the developing updraft. The mesocyclone of the mature supercell did not produce a tornado. ELDORA did observe a vertically oriented minimum reflectivity (weak-echo hole) on the size of several km that extended from the cloud base to the mid levels of the storm in which the observed tornado was located. A low level circulation was evident in the Doppler data with a width of slightly larger than 4 km and was classified as a low-level mesocyclone. The formation of a strong tornado without the presence of a mid-level circulation presented yet another possible mode for tornado formation.

In the following year, ELDORA observed several tornadoes including an F3 near Friona, Texas on 2 June 1995, an F4 near Kellerville, Texas and one near McLean, Texas on 8 June 1995 (Wakimoto et al. 1996). ELDORA was about 10 km from the Kellerville tornado which had a condensation funnel diameter and damage path width of about 1 km. ELDORA also employed a faster scanning technique where they achieved near 300 m along-aircraft-track resolution with range-gate spacing of 150 m and a maximum unambiguous velocity of 79 m s^{-1}. They observed peak velocity differences across the tornado region of 139 m s^{-1} implying an azimuthal shear of 0.46 s^{-1}. The tornado was again observed to be within a weak-echo hole in vertical reflectivity scans.

While the ELDORA and fixed surface Doppler observations were valuable observational tools used to probe the evolution of the three dimensional structure of low and mid-level circulations in supercell thunderstorms, their resolution of 4-5 min updates and several 100 m spacing between observations precluded detailed resolution of the tornado structure. Furthermore, due to either range limitations from the fixed radars or ground clutter returns in the airborne radars, the region below about 300 to 500 m AGL remained unobserved. In an effort to remotely sample this low-level region at high resolution, mobile ground-based Doppler radars were constructed to be placed in close proximity to tornadic regions of supercell storms. The first such mobile ground radars to be extensively used for the purpose of scanning tornadoes was a 3 cm continuous wave (CW) Doppler radar with a beamwidth of 5° and peak power of 1 Watt that had no ranging capability (Bluestein and Unruh 1989).

During the early 1990s Bluestein et al. (1993) observed six tornadoes of various intensities from F1 to F4 with this CW radar. The tornadoes were observed at ranges between 1.6 and 11.3 km with cross section sizes through the tornado between 140 and 980 m across. These values were usually on the order of the width of the condensation funnel at cloud based or debris cloud size at the ground. Maximum Doppler velocities inferred from the power spectra ranged from 55 to 60 m s^{-1} to between 120 to 125 m s^{-1} in the strongest tornado and were probably the first radar measured winds in an F5 tornado. Uncertainties in these observations were estimated to be about 5 to 10 m s^{-1}. The thermodynamic speed limit predicted by Fiedler and Rotunno (1986) and estimated from proximity soundings was exceeded in most of the data sets leading to more support for near surface intensification of a tornado vortex due to frictional interaction with the

ground (Lewellen and Lewellen 1997). They performed a comparison of actual power spectra with simulated spectra in an axisymmetric Rankine vortex with a Gaussian radial reflectivity profile. The results indicated that the maximum radar reflectivity in supercell tornadoes resided well outside the radius of maximum winds. Since Doppler velocity measurements are power-weighted, this lead to the possibility that the true maximum Doppler velocities may be unobserved in the apparently less reflective core of the tornado.

The CW radar also observed the Northfield, Texas tornado of 25 May 1994 (Bluestein et al. 1997) and they measured wind speeds of at least 60 m s^{-1} with smaller areas in the tornado vortex possibly reaching 75 m s^{-1}. Again, the cross-sectional area of the radar beam in the tornado was on the scale of the funnel cloud width (500 m). However, no clear separation was observed between the region representing the tornado and its parent low-level mesocyclone.

The CW radar introduced remote radar observations into the lowest 500 m of tornadoes, although its beamwidth (5°) still severely limited the spatial resolution of measurements in the tornado to usually one or two observation points. Therefore, a pulsed Doppler-radar was constructed in the late 1990s with an operating wavelength of 3 mm which decreased the beamwidth to 0.18° producing sample volume spacing values on the order of 15 to 30 m in space and resampling periods as small as 10-15 s (Bluestein and Pazmany 2000). They also employed a polarization diversity pulse pair technique to yield a maximum unambiguous velocity of 79 m s^{-1}. Tornadoes observed on 3 May 1999 in Oklahoma contained wind speeds approaching 80 m s^{-1}. The reflectivity structure in the tornadoes appeared to contain a minimum in reflectivity (or eye) near the center of

the vortex, and spiral bands wrapping around the periphery of the vortex into a disk of high reflectivity outside the eye. Furthermore, multiple vortices or wavelike perturbations in the reflectivity field appeared on the edge of the eyewall. This was the first direct observational evidence of multiple vortex structure in a tornado.

Tornadoes were also observed near Stockton, Kansas on 15 May 1999 (Tanamachi et al. 2007), Bassett, Nebraska on 5 June 1999 (Bluestein et al. 2003a, b) Happy, Texas on 5 May 2002 (Bluestein et al. 2004) and Attica, Kansas on 12 May 2004 (Bluestein et al. 2007) with the 3 mm radar. Most of these tornadoes exhibited a velocity structure similar to a Burgers–Rott vortex especially during the most intense phases. The near-surface reflectivity structure near the mesocyclone in the Bassett, Nebraska supercell prior to tornadogenesis included a horizontal hook-like appendage of high reflectivity that separated warm inflow air from cold downdraft air. This feature was commonly observed at coarser resolutions from other radars in supercells. However, a small kink and bow about 400 m across formed along the hook echo axis that was followed by a closing off the bulging bow into a small echo free region. A 500 m scale cyclonic circulation was also observed to develop along the bow which over the course of several minutes attained a Doppler velocity difference of 50 m s^{-1}. At the same time, smaller 100 m scale vortices were observed along the rear-flank gust that interacted and were often absorbed into the larger scale cyclonic shear region. It is the large-scale circulation that appeared to develop into a tornado within a 5 min period.

A Fourier analysis technique was applied to the Doppler velocity data in the Stockton, Bassett and Attica tornadoes to decompose the tangential flow into averaged and wavenumber one, two, and three perturbations (Lee et al. 1999). The maximum

azimuthally averaged azimuthal wind speed increased while the radius of maximum wind decreased slightly during the intensification phase of the Stockton tornado. In addition, the maximum azimuthally averaged azimuthal wind speed, the radius of maximum winds, and the circulation about the vortex center all decreased simultaneously as the tornado decayed (Tanamachi et al. 2007). This analysis revealed a persistent and stationary wavenumber two feature across the vortex that may be the result of deformation or surface stresses from translation acting on the vortex during radar scanning periods.

In the Bassett tornado, the analysis also revealed that the radius of maximum averaged tangential wind decreased from 200 m to 100 m as the tornado intensified from a Doppler velocity difference of 44 to 94 m s^{-1}. This observation was consistent with model results of significant stretching dominating the tornado vortex formation at low levels. The radius began to increase again as the tornado vortex weakened. The vorticity value across the core flow ranged between 0.18 and 0.94 s^{-1}. It was suggested in this work that a metric for tornado intensity should include the core vorticity values that are Galilean invariant, but translation effects need to be included for damage potential.

The tornado observed near Attica, Kansas contained vorticity in the core of about 1 s^{-1} with a core diameter of about 250 m. Maximum Doppler velocity in the tornado is about 77 m s^{-1} between 25 and 75 m AGL and it was noted the wind speed decreased by 25% in the lowest 25 m inside the core to about 60 m s^{-1} at the surface. Peak radar reflectivity values were noted to reside within the radius of maximum winds which in turn were outside the observed condensation funnel. Furthermore, divergence is noted in the interior of the vortex with outward radial wind speeds of 15 m s^{-1} very near the

surface. Radial inflow was noted outside the radius of maximum winds. Circulation values increased and leveled off between 40000 and 53000 m^2s^{-1} several radii outside the radius of maximum winds. A reflectivity weak-echo hole was observed in the interior of the tornado which closed off in a bowl-shaped structure within 10 m of the surface and grew to about 600 m in diameter above 400 m AGL which was 100 to 200 m outward from the edge of the observed condensation funnel and near the edge of the debris cloud. Peak averaged tangential wind speeds were slightly less at about 50 m s^{-1} at a radius of 110 m. A tornado observed immediately following the Attica, Kansas tornado had maximum Doppler velocities around 40 m s^{-1} with peak average tangential winds around 37 m s^{-1} at a radius of 70 m. Divergence was also noted near the surface in the core of this tornado with outward radial motion of 7 m s^{-1}.

While the observations in the Bassett tornado were collected at only one elevation, the Happy, Texas and Attica, Kansas tornado observations (Bluestein et al. 2004, 2007) were collected in vertical planes to further examine the vertical structure of a tornado vortex. Again sample volume sizes were on the order of 15 m x 15 m x 30 m. In the Bassett tornado, the vertical cross-sections revealed a pear-shaped weak-reflectivity hole from about 60 m above the ground up to the top of the domain at about 800 to 1000 m AGL. The hole was about 40% wider at 100 m AGL than it was above this level. The condensation funnel appeared much narrower than the width of the weak-echo hole, and the debris cloud near the ground was about as wide as the hole above 150 m. The depth of the debris cloud was estimated to be about 200 m. The broadening of the reflectivity hole aloft was attributed to either outward centrifuging of scatterers or a secondary circulation above the surface layer that was advecting the scatterers outward. Also of

significance was an inflow jet with peak Doppler velocities as high as 35 to 40 m s^{-1} in a narrow band observed at 200 to 400 m AGL. This jet was speculated to have resulted from lifting of a surface layer inflow jet over cold air near the tornado, an asymmetric distribution of the surface-layer jet, or a horizontal roll in a wavelike structure extending outward from the edge of the vortex. In the Attica tornado, horizontal vortices are observed near the outside edge of the vortex in several vertical cross-sections.

In addition to the 3 mm "w-band" radar, an additional radar operating at 3 cm wavelength with a half-power beamwidth of 1.25 degrees, range sampling of 150 m and dual-polarization capability, collected data in supercell tornadoes observed near Attica and Harper Kansas on 12 May 2004.

These mobile ground-based Doppler radars were the first to fully resolve and examine the tornado scale structure and flow in the lowest levels below 200 m AGL. A minimum in reflectivity was a common attribute in the core of tornadoes. However, the high-resolution 3 mm radar often suffered from severe attenuation in moderate precipitation, and a lack of signal in scatterer-sparse regions including tornado cores. These limitations usually prevented the collection of a complete Doppler velocity field in and within 1 to 2 km of the tornado core. Furthermore, this instrument usually scanned tornadoes in only two-dimensions due to slow scanning speeds necessary to process the polarization diversity velocity measurement. There was also some uncertainty in the elevation of observations since the mobile radar was not able to take level measurements.

However, another mobile ground-based radar was developed in the mid 1990s called the Doppler On Wheels (DOWs) (Wurman et al. 1997). After initial prototype development, two 3 cm radars were constructed with a peak power of 250 kW, and fully

capable of three-dimensional volumetric scanning with load-levelers for precise measurements. While the beamwith of this radar (0.93°) was larger than the mm radar, typical data spacing of 50 m x 50 m x 50 m and as high as 13 m x 15 m x 15 m for very close observations would still be able to fully resolve the tornado scale flow (Wurman et al. 1996).

Initial observations with the prototype DOW were collected in 1995 with the first significant tornado (rated F3) observed near Dimmitt, Texas on 2 June 1995 during project VORTEX (Wurman and Gill 2000). Scanning repetition intervals were 100 s in this tornado. The tornado moved at forward speed of between 5 and 7 m s^{-1}. Peak ground relative wind speeds were estimated at 95 m s^{-1} with the maximum Doppler observations of 74 m s^{-1} at 60 m AGL. Implied vertical vorticities across the core were near 1.3 s^{-1}. Corrections were applied to the Doppler velocity measurements for the aspect viewing ratio of the tornado as derived from Burgess et al. (1993). Again, a ring of high reflectivity about 400 m in radius and 200 to 300 m deep surrounded the tornado at the surface. The outer edge of the observed debris ring was in the region of 35 m s^{-1} Doppler velocities. Concentric rings and spiral bands of high reflectivity also appeared as transient features around the tornado. A small scale eye or reflectivity minimum was again apparent in the center of the tornado vortex embedded within the higher reflectivity disk, and may have been the first such observation of this structure on the scale of 50 to 100 m.

The velocity structure of the Dimmitt tornado appeared to contain multiple maxima in the radial direction away from the tornado at ranges between 500 and 1000 m from the tornado center. It was suggested that these areas were evidence of parcels

containing characteristic but differing initial angular momentums causing an "onion-skin-like" structure as they converged toward the tornado center. Also of note was a central downdraft region of about 150 m in diameter near 1 km AGL with relatively constant motions of 7 to 10 m s^{-1} toward the radar at 10° elevation indicating an estimated downdraft strength of 30 m s^{-1}. This downdraft did not appear below 300 m AGL and this structure was consistent with a partial two-cell vortex model with a downdraft penetrating to about 400 m AGL (Ward 1972; Rotunno 1977; Church et al. 1979).

The velocity field outside the core did not appear to contain constant angular momentum and appeared to decay more slowly than the Rankine model (inversely proportional to radius from the center) yielding a gradient in angular momentum away from the tornado core region. Furthermore, as the tornado vortex weakened, the core circulation decreased in size (area decreased by 70%) while maintaining relatively constant speeds (decrease of 15%) in the core implying a loss of angular momentum. The tornado vortex also appeared to be tilted by about 20° from the vertical below 450 m AGL and about 10° from the vertical above this level early in the observation period.

Additional analysis of the Dimmitt tornado event is performed by Rasmussen and Straka (2007). Angular momentum budgets were derived using DOW observations where axisymmetric retrievals of Doppler velocity data produced estimates of horizontal and vertical flux convergence of mean (axisymmetric) angular momentum including viscous dissipation,

$$\frac{\partial \overline{M}}{\partial t} + \frac{\partial \overline{uM}}{\partial r} + \frac{\partial \overline{wM}}{\partial z} = R \tag{2.8}$$

where $\overline{M}$ is the axisymmetric angular momentum (product of axisymmetric tangential velocity and radius from the center of rotation), $\overline{u}$ and $\overline{w}$ are the axisymmetric radial and

vertical components of the flow, and R is the residual of the terms. The study focused on the axisymmetric tangential and radial velocity components as a function of radius from circulation center. The maximum radius of their analysis domain was determined by degree to which the retrieved axisymmetric tangential velocity fit the observed data to within a fraction of the mean absolute error. When the ratio of the mean absolute error to the tangential velocity exceeded 0.35 the flow was determined to lack sufficient axisymmetry. The analysis focused on a concentric circulation larger than the tornado in Wurman and Gill (2000) and termed the "tornado-cyclone". This scale is defined as a radius larger than the tornado's radius of maximum winds where angular momentum continually increases with increasing radius.

The retrieved axisymmetric observations showed maximum angular momentum values at about 1 km radius at 800 m AGL which descended during intensification at larger radii near the surface. During the intensification period the secondary circulation, induced by the nonhydrostatic vertical pressure gradient force, exhibited an inward-upward-outward flow structure. The swirl flow was higher aloft during intensification, about the same during maturity and higher near the ground during the weakening phase.

During intensification, within a radius of 400 m and within 200 m AGL the mean inflow was advecting higher angular momentum values towards the vortex center which was offset almost entirely by loss of angular momentum to the ground. Above 200 m AGL, the mean transport was outward but the residual was positive along with the mean angular momentum tendency indicating eddy transport was more than offsetting mean transport. As the tornado cyclone progressed through maturity and into a weakening phase the secondary circulation reversed direction with downward and outward flow at

lower levels and the concomitant lowering of the maximum swirl from aloft towards the surface leading to negative vertical advection of angular momentum which replaces the positive inward angular momentum flux from earlier in the lifecycle. The cause-and-effect relationship of the descending maximum swirl with development of the downward secondary circulation cannot not be determined but it is concluded that for long duration tornado cyclone, the maximum swirl must remain elevated less the destruction of the tornado cyclone becomes inevitable.

In successive years more strong and violent tornadoes were observed with the DOWs at close range including Spencer, South Dakota on 30 May 1998 (Alexander and Wurman 2005; Wurman and Alexander 2005), and Moore and Mulhall, Oklahoma on 3 May 1999 (Burgess et al. 2002; Wurman 2002). Key observations in the Spencer, South Dakota tornado included the detection of a surface circulation of weak tornado strength 35 m s^{-1} and scale of 150 m about 3 min prior to any visual indication of a tornado vortex. Variations of wind speed with height appeared to be most pronounced in the lowest 200 m AGL with extreme Doppler velocities over 100 m s^{-1} confined to the lowest 50 to 100 m AGL (Alexander and Wurman 2005) (Fig. 2.4). Comparison of Doppler velocity wind estimates with observed damage in the town agreed reasonably well in the context of the maximum observed Fujita scale rating. However, the peak Doppler-velocity-derived wind speeds appeared displaced by 50 to 100 m from the peak damage observed in the town leading to the conclusions that debris centrifuging or vortex core slope in the lowest 30 m AGL may account for the disparity between these observations (Wurman and Alexander 2005).

The thermodynamic wind speed limit accurately predicted the tornado vortex strength above 200 m AGL. Oscillations in the core vorticity and Doppler velocity difference across the vortex were noted within 500 m AGL with periods of about 120 s. These oscillations contained magnitudes of 20 to 30 m s^{-1} for the velocity difference and core vorticity varied between 0.2 and 2.0 s^{-1}. The oscillations may have been indirect evidence of a multiple vortex structure.

Tornadoes observed on 3 May 1999 included a F5 tornado in Moore and Oklahoma City, Oklahoma which was observed by the DOWs. As with the Dimmitt observations, the tornado vortex appeared as a single-cell structure at the surface with a fairly axisymmetric Doppler velocity rotational couplet. A truncated reflectivity eye was again visible near the center of the vortex above 300 m AGL. Both Bluestein (2004) and Wurman and Gill (2000) suggest the lack of an eye near the surface may result from concentration of scatterers by horizontal convergence and generation of new scatterers. The diameter of the reflectivity minimum increased from near 100 m at 300 m AGL to over 500 m at 1.5 km AGL. The minimum reflectivity eye often had values more than 40 dB lower than the surrounding high reflectivity annulus. The eye's sharp reflectivity gradients were therefore about 20-40 dB over a few hundred meters of horizontal distance. The diameter of the reflectivity minimum also corresponded well with the diameter of the maximum tornado velocity. Furthermore, concentric horizontal wind maxima were again observed in the DOW Doppler-velocity field in and away from the tornado vortex core. The high resolution DOW observations peaked with a velocity difference of 160 m s^{-1} when the sampling of the same circulation by a radar with a coarser resolution revealed a velocity difference of only 80 m s^{-1}. This difference in

observations was an indication of the limitations of current operational radars (WSR-88Ds) which only resolve the low-level mesocyclone or outer wind maxima surrounding a tornado. There was some evidence that the wind speeds associated with the tornado intensity damage ratings were slightly higher than the actual observed tornado velocities from the DOW. This difference again raised the question of biases in tornado intensity estimates from damage.

The most dramatic observations of multiple vortex structure were taken in the Mulhall, Oklahoma tornado on 3 May 1999 (Wurman 2002). The diameter of the estimated core flow region in this large tornado was about 1200 m which compared with average diameters of 200 m for the Dimmit, Texas tornado, 300 m for Spencer, South Dakota tornado, and 400 m for Oklahoma City, Oklahoma tornado.

While the Oklahoma City tornado contained peak Doppler velocities of a record 130 m s^{-1}, the Mulhall tornado peak velocities were around 109 m s^{-1}. The Mulhall tornado had a slightly faster translational velocity near 13.5 m s^{-1}, than previously observed tornadoes. Given the size of this tornado, and the small 4 to 5 km range from the DOW radar, the core region was well resolved and clearly exhibited solid body rotation. However, the region outside the core was again observed to decay more slowly ($R^{-0.6}$) than a Rankine vortex. It was estimated that the region of about 4500 m in diameter which contained winds greater than 30 to 40 m s^{-1} was roughly coincident with the debris cloud. Furthermore, the outer edge of the high reflectivity disk was located in regions of Doppler velocities around 80 m s^{-1}. The absence of high reflectivity outside this range where damaging velocities of 50 to 80 m s^{-1} existed indicate that strong winds

in the lowest 70 m contained little upward motion and transported debris inward below the lowest radar observation level before rising.

Embedded within the main tornado flow were many smaller scale shear couplets with Doppler velocity differences over 100 m s^{-1} across a distance of 100 to 200 m which represented about 50% of the total azimuthal shear across the tornado. Peak Doppler velocities in the vortices of 110 m s^{-1}, and about 1.5 times the estimated peak tangentially averaged velocities, were consistent with modeling results of Lewellen et al. (1997). Vertical vorticity values in the vortices were estimated to be as high as 8 s^{-1}. The vortices appeared to translate at speeds about half the background tangential flow of the primary vortex suggesting a possible propagation mechanism (Ward 1972, Rotunno 1984). The multiple vortices appeared to persist at the edge of the high reflectivity core as multiple minima (eyes). This suggested the vortices were embedded within a corner-flow region or updraft annulus of a two-cell vortex (Davis-Jones 1973), although Lewellen et al. (1997) simulations produced multiple vortices well within the core flow region. The spacing between vortices appeared to be about 2 to 4 times the scale of the vortices, and this yielded a dominant wavenumber 6 structure around the tornado, although wavenumbers as high as 10 were observed when the scale of the vortices decreased.

Lee and Wurman (2005) performed a ground-based velocity track display (GBVTD) analysis (Lee et al. 1999) of this same tornado where they retrieved a maximum primary circulation of 84 m s^{-1} with a radius of maximum winds between 500 m and 1000 m and a peak axisymmetric vertical vorticity value of 0.36 s^{-1} at 50 m AGL. The tornado was moving at about 13 m s^{-1}. A secondary two-cell central downdraft structure in the interior of the tornado with an annular updraft near the radius of

maximum winds was also observed. The maximum pressure deficit was estimated to be about 80 mb with respect to pressure at 3 km from the center. Additionally, the maximum vertical vorticity was identified inside the radius of maximum winds and the vorticity profile satisfied the necessary condition of barotropic instability with swirl ratios between 2 and 6. Peak convergence values of 0.06 s^{-1} were retrieved with an average inflow layer of 600 m. Peak outflow velocities were 14 m s^{-1}, inflow 23 m s^{-1} and downdraft speeds of 32 m s^{-1} at 400 m radius.

The observations in this multiple vortex tornado were unprecedented, and the scale of all features in this tornado were about an order of magnitude larger than most other observed tornadoes. Typical multiple vortex scale structures would more likely be confined to scales around 10 m, and remain unresolved in most cases (Bluestein and Pazmany 2000). Furthermore, the very rapid temporal evolution of these features is on the order of 5 to 10 s, and their close proximity generally leads to aliasing problems with most current radar scanning technologies. However, efforts are underway to improve the scanning speed and help improve the temporal resolution of such features (Wurman and Randall 2001; Wurman 2003; Shapiro et al. 2003). A similar GBVTD analysis was performed with DOW single-Doppler observations of the Spencer, SD tornado on 30 May 1998 which also revealed a two-cell vortex structure with a very strong axial downdraft throughout the observation period (Kosiba and Wurman 2010).

Remote measurements of tornado velocity structures are not without errors since Doppler velocity measurements are heavily biased towards the motion of larger scatters, and gradients in reflectivity will alter the Doppler velocity structure from the true wind field structure in the tornado. Estimates of departures between large scatterer (debris)

motions and air motions in regions of a tornado where centrifugal effects are large was recently conducted by Dowell et al. (2005) which yielded differences of 10 to 30 m s^{-1}.

These high resolution radar tornado observations have common attributes including high reflectivity disks with minima (except near the surface) that increase in diameter with height near the center of tornado circulations. However, the location of maximum tangential winds relative to the inner eye edge or outer reflectivity disk appeared variable. Evidence also existed that flows outside the tornado cores do not contain constant angular momentum and often contain one or more concentric Doppler velocity maxima. Solid-body rotation was present in the core region where vorticities typically range between 0.1 to 1.0 s^{-1}. Vertical gradients of maximum tangential velocity also appeared most extreme decreasing up to 200 m AGL. The depth of surface inflow layer was inferred to be very shallow and possibly less than 50 or even 30 m AGL. Finally, both single-cell and two-cell structures have been observed in tornado core flows.

2.3.5 Dual-Doppler Radar

When two or more radars are able to simultaneously observe a region from sufficiently different perspectives (crossing angles usually between 20° and 160°) it is possible to retrieve the three dimensional wind field using a dynamical constraint such as mass conservation for the third component (usually the vertical wind). The Doppler velocity field from each radar can be combined along coplanar surfaces between the radars (Armijo 1969) or in a Cartesian coordinate system (Heymsfield 1976; Brandes 1977). In the Cartesian framework, the Doppler velocity data from each radar are first

interpolated to horizontal grids. Using the mass conservation equation, the vertical motion is initially estimated and then iterated with equations for the horizontally interpolated wind components until convergence of solutions for all three components is achieved at each point in the domain.

A pseudo-dual-Doppler analysis of ELDORA observations in the McLean, Texas storm was performed by Dowell and Bluestein (2002a,b). In this study, a unique observation of the multiple tornado genesis process was established. Bulges along a gust-front or wind shift line developing to the right of a mature tornado's forward motion helped enhance a vertical velocity gradient and updraft ahead of the tornado from increased low-level convergence. This was followed by localized tilting along the leading edge of the updraft producing a new vorticity maximum that developed a profile of increasing rotation with height from both the tilting and stretching of horizontal vorticity. The developing storm-scale circulation was horizontally advected to the rear side of the updraft where low-level trajectories into the vorticity maximum passed through regions along the left edge of the primary updraft (and near a rear downdraft) relative to its forward motion. These trajectories contained vorticity that was oriented so that it was easily tilted into the vertical and stretched along the back side of the updraft where a new tornado strength circulation developed at the surface. This was followed by a bulge in the gust-front to the right of the tornado, and the process repeated itself several times resulting in the production of a family of tornadoes.

The key finding in Dowell and Bluestein (2002a,b) was that cyclic tornado formation may result if the horizontal motion of tornadoes repeatedly does not match the horizontal motion of the main storm-scale updraft and downdraft. Also of critical

importance was the weak updraft-relative flow in the tornadic region, which implied that the gust-front did not surge ahead of the main updraft. Storm-scale evolution consistent with this conceptual model was documented via single and dual-Doppler observations obtained in tornadic supercells in the Texas Panhandle on 15 May 2003 (French et al. 2008) and near Greensburg, KS on 4 May 2007 (Bluestein 2009).

Again consistent with other observational and modeling studies were the magnitudes of various vertical vorticity forcing terms including values of $3x10^{-4}$ s^{-2} for horizontal advection, $1x10^{-4}$ s^{-2} for vertical advection, $4x10^{-4}$ s^{-2} for stretching, and $5x10^{-5}$ s^{-2} for tilting in the lowest km (Dowell and Bluestein 2002a,b). Convergence at 500 m AGL around the strongest tornado vortex was estimated to be between 0.8 to $1.4x10^{-2}$ s^{-1} with circulations values of $2x10^{5}$ m^{2} s^{-1}. Furthermore, low-level vertical shear of the horizontal flow in the environment was substantial at about $8x10^{-3}$ s^{-1}, which continued to raise the question of how much horizontal vorticity eventually incorporated into the tornado circulations was derived from the environment as opposed to storm-scale processes of baroclinic generation. This ELDORA analysis was the highest resolution pseudo-dual-Doppler case to its date with 4-5 min updates and spatial resolution on the order of several 100 m (Dowell and Bluestein 2002a,b).

Two other dual-Doppler observations from two stationary 10-cm ground-based radars were constructed by Brandes (1984) of the Del City tornadic storm on 20 May 1977, and Dowell and Bluestein (1997) of the Arcadia, Oklahoma tornadic storm observed on 17 May 1981. Brandes dual-Doppler analysis of the Del City storm and tornado revealed environmental low-level horizontal vorticity values of about $3.5x10^{-2}$ s^{-1} that was slightly higher than the McLean storm. Vertical vorticity values in the low-level

mesocyclone were on the order of $3x10^{-2}$ s^{-1} with convergence values on the order of $1x10^{-3}$ s^{-1}. The analysis revealed that mid-level mesocyclone formation above 3 km in the supercell was dominated by tilting of horizontal vorticity into the vertical along the edge of the primary updraft, while low-level mesocyclone formation was dominated by near-surface convergence of vertical vorticity ($1x10^{-4}$ s^{-2}). Tornado formation resulted from multiplicative growth of tilted horizontal vorticity that was stretched in an enhanced convergence zone that developed as a rainy downdraft near the rear of mesocyclone interacted with the inflow region.

The dual-Doppler analysis of the Arcadia supercell observed at about 45 km range (Dowell and Bluestein 1997) contained a horizontal grid spacing of 800 m and a vertical spacing of 500 m with the lowest observations at about 500 m AGL. The evolution of the low-level and mid-level mesocyclones appeared very similar to the Del City storm. Again, tornadogenesis was observed when vorticity and convergence were increasing in the low level mesocyclone, and was nearly coincident with the development of a downdraft region spreading around the backside of the mesocyclone. Vertical velocities in the updraft of the storm were estimated to be about 20 m s^{-1}. A synergistic relationship was also proposed to describe the interaction of the low-level mesocyclone with the downdraft. A strengthening downdraft may enhance low-level convergence and downward momentum transport while mesocyclone intensification may enhance the downdraft by wrapping precipitation into the downdraft and increasing a downward directed perturbation pressure gradient force. An instrument tower also sampled the inflow region into the supercell and measured 1.5 x 10^{-2} s^{-1} of vertical shear between the surface and 444 m AGL that increased by a factor of two as the supercell updraft passed

by the tower. This enhancement of horizontal vorticity may have been an indication of storm-scale processes that enhance low-level horizontal vorticity. The demise of tornadoes observed in both the Del City and Arcadia storms resulted when the tornado vortex became surrounded by a downdraft that prevented the ingestion of additional vertical vorticity and eliminated the stretching of existing vertical vorticity.

Several dual-Doppler tornado observations were also collected with DOW observations including tornadoes near Kiefer, OK and Glenpool, OK on 26 May 1997, Bridgeport, NE on 20 May 1998 (Wurman et al. 2007b,c) and Crowell, TX on 30 April 2000 (Marquis et al. 2008). In the Kiefer case, repeated storm mergers were observed with repeated tornadogenesis of brief tornadoes that were attributed to enhancement of convergence in association with the merging storms. The peak velocity difference across the Kiefer tornado was observed to be about 90 m s^{-1} at 400 m AGL with an estimated vertical vorticity of 0.8 s^{-1}, an associated core diameter of 220 m and Doppler velocity of 47 m s^{-1}. A double eyewall of reflectivity was observed along with a double-gust front feature about 3 km east of the tornado, which may have enhanced vertical vorticity near the tornado.

The Glenpool tornado was observed to have multiple iterations of scale contraction with velocity difference values increasing to 50 m s^{-1}, a core diameter contracting to 200 m and vertical vorticity increasing to 0.7 s^{-1}. Peak velocity value was 37 m s^{-1} at 86 m AGL. The Bridgeport tornado showed sudden intensification near the surface with a velocity difference of 61 m s^{-1} over 235 m and implied vertical vorticity near 0.52 s^{-1}. Convergence of 0.05 s^{-1} was analyzed north of the tornado with values of 0.03 s^{-1} well to the east along a gust front. Peak stretching near the tornado from the

dual-Doppler synthesis was about $4x10^{-4}s^{-2}$ with a similar magnitude for tilting resulting in combined values near $1x10^{-3}s^{-2}$. This combined forcing could produce the tornado-scale vorticity values on the time scale of hundreds of seconds. Circulation values were calculated as $3.4x10^{5}$ m^2s^{-1} at about 2 km from the tornado.

The Crowell tornado analysis (Marquis et al. 2008) had well documented concentric vortex structure, one at 0.5 km and one at 2 km from the tornado center. These concentric vortices consolidated into a single vortex which became multiple vortex in structure and contained a velocity difference of 70 m s^{-1}. Multiple gust-fronts were observed as with the Kiefer tornado, although in this case the convergence along the second gust front did make contact with the region of convergence associated with the tornado. Trajectories from this case showed streamwise horizontal vorticity in low-level inflow that was tilted and then stretched into the tornado region. Rear-flank trajectories rose and fell over the gust-front.

Unfortunately, two problems exist when attempting to apply this technique to the DOW tornado dataset when two DOWs are present. First, interpolations to a Cartesian system result in an degradation of spatial resolution. The lower resolution of the two radars is usually the limiting factor, and typical dual-Doppler observations for tornadoes with DOWs involve radar separations of at least 10 km with ranges to the tornado of at least 7 km and often larger. The asymmetrical position of most tornadoes relative to the radars yields sample volume spacing of the more distant radar on O(100 m). This spatial degradation is unacceptable in attempting to retrieve detailed structure of a tornado which is usually at or slightly larger than this scale especially if one radar has volume spacings at least two or three times smaller than this scale. Second, most radar tornado

observations in the DOW dataset are single Doppler (between 80 and 90%) either due to poor radar deployment geometry, redeployments during genesis and lifecycle, or general unavailability of a second radar. Therefore, there is not a sufficient sample size of dual-Doppler radar observations to construct a dual-Doppler tornado climatology.

2.4 Key Issues

While tornado theories and laboratory models appeared to provide some information about tornado structure and genesis dynamics, their applicability to real atmospheric vortices remained in question until numerical modeling studies and observational cases could better simulate or observe actual atmospheric structure. However, most of these numerical studies and observational cases were analyzed in isolation. There are common attributes in the structures and genesis dynamics of the mesocyclone or tornado structures in the numerical models when compared to observations, but some fundamental differences are still present. Furthermore, many questions remained unanswered about the variability of tornado and low-level mesocyclonic structures and genesis mechanisms across many cases. The questions most commonly posed in this area of research are, how does a tornado form, and what does the average tornado structure look like? Perhaps the more appropriate question is how do dynamical forcings in and structures of supercell tornadoes vary, and how are these forcings and structures related?

The motivation for this thesis stems from the abundance of observational case-studies and the opportunity to integrate a sufficient number of observations to examine

the variability of tornado kinematics and dynamics in much the same way modeling efforts have examined the tornado structure parameter space in simulated cases. Given the characteristic scales and intensities of mesocyclones in supercell thunderstorms that have been well observed and simulated, it is hypothesized that tornadoes produced in association with mesocyclones of parent supercell thunderstorms also contain a characteristic structure. This structure contains a preferred horizontal scale and tangential velocity. Additionally, it is hypothesized that the mode of horizontal scale contraction for most mesocyclonic tornadoes is also relatively uniform and depends upon the horizontal distribution of near-surface angular momentum as a necessary but not sufficient condition for significant tornadogenesis.

Chapter 3

Data

3.1 Doppler On Wheels Radar Observations

While the construction of theories and models to characterize tornado vortex structure and dynamics have provided important insights into this phenomenon, direct observations are needed to verify these theories and model results. The body of observations and modeling results place a tornado vortex on the scale of O(300 m) in space and O(300 s) in time. To resolve such a feature with a minimum of six observation points (Gal-Chen and Wyngaard 1982; Carbone et al. 1985) requires spatial and temporal spacing of O(50 m) and O(50 s). Resolving sub-tornado scale features such as multiple vortices requires an even higher observation spacing closer to O(10 m) and O(10 s). Only mobile radar observations dedicated to this purpose can provide such resolution.

Efforts to collect radar observations of tornadoes from the DOWs over the past decade during both the VORTEX and ROTATE field projects have yielded a large dataset covering about 150 tornadoes with observed Doppler velocities as high as 135 m s^{-1} (Wurman and Gill 2000; Burgess et al. 2002; Wurman 2002; Alexander and Wurman 2005, Wurman and Alexander 2005; Wurman et al. 2010a). The tornado scanning strategies employed by the DOWs usually include range-gate spacing between 13 and 60 m at ranges between 1 and 20 km from most tornado vortex centers. With a beamwidth (B) of 0.93° and typical azimuthal oversampling by a factor of two to three, azimuth data spacing usually lies between 10 and 60 m. The DOW radar volume scan typically

consists of 120° azimuthal sectors comprised of about 10 to 12 fixed elevation angles between 0.5° and 20° in a 60 s period which places the elevation of radar observations in a tornado vortex between 20 m and 4 km AGL. Each consecutive elevation scan usually requires about 4-6 s.

Data used for this study include DOW supercell tornado observations from 1995-2004. The DOW supercell tornado observations from 1995-2001 are used in the computation of values for DOW climatological tornado distributions and comprise about 6282 individual observations of 69 different mesocyclone-associated tornadoes. These tornado observations are all at ranges of less than 30 km from the radar. When focusing on the typical sub-cloud layer below about 500 m above ground level (AGL) the number of DOW tornado observations is reduced to about a third of the total number, namely about 2205 observations and comprise 52 distinct tornadoes. Almost two-thirds (63%) of all the DOW supercell tornado observations are collected while the radar is moving resulting in an additional Doppler velocity component that must be accounted for in the 3991 scans that contain mobile data.

The PIRAQ-II digital signal processor in the DOWs produces lagged autocorrelations of the input analog radar signal yielding three values p, a_1, and b_1 which represent the lag-0 (autocorrelation using the same transmitted pulse) and real and imaginary parts of the lag-1 (autocorrelation using two consecutive pulses) autocorrelation respectively. From these three autocorrelation values, six radar moments P, V, N, R, S, and C are calculated at each range-gate,

$$
\begin{aligned}
P &= 10\log|p| + P_c \\
V &= \frac{\lambda}{4\pi T_1}\tan^{-1}\left(\frac{-b_1}{a_1}\right) \\
N &= \frac{\sqrt{\left(a_1^2 + b_1^2\right)}}{p} \\
R &= P + R_c + 20\log r \\
S &= \frac{\lambda}{2\sqrt{2}\pi T_1}\sqrt{\ln\left|\frac{p - P_n}{\sqrt{\left(a_1^2 + b_1^2\right)}}\right|} \\
C &= 10\log\left|\sqrt{\left(a_1^2 + b_1^2\right)}\right| + P_c + R_c + 20\log r
\end{aligned}
\tag{3.1}
$$

where P is total received power (dBm), V is Doppler-velocity (m s^{-1}), N is normalized coherent power, R is reflectivity (dBz), S is spectral width (m s^{-1}), and C is coherent reflectivity (dBz). All other symbols represent constants specific to the radar hardware including transmitted wavelength (λ), radar constant (R_c), noise power (P_n), power correction (P_c), and pulse repetition period (T_1), except for beam-path range from the radar (r).

Occasionally the PIRAQ-II signal processor is operated in staggered pulse repetition period (SPRT) mode. This process involves the radar transmission of two distinct PRTs (T_1, T_2) that are interleaved in time during a pulse integration period where half the number of pulses are associated with each PRT. The signal processor produces five values including the lag-0 autocorrelation p from the smaller PRT (T_1), and the real and imaginary components of the lag-1 autocorrelation for each PRT namely, a_1, b_1, a_2, b_2. Ten radar moments are then calculated at each range-gate including P, N, R, C, a Doppler velocity and spectral width for each PRT (V_1, V_2, S_1, S_2) and a combined Doppler velocity and spectral width (V_s, S_s) which are defined as,

$$V_s = \frac{\lambda}{4\pi|T_1 - T_2|}\tan^{-1}\left(\frac{a_2 b_1 - a_1 b_2}{a_1 a_2 + b_1 b_2}\right)$$

$$S_s = \frac{\lambda}{2\sqrt{2}\pi|T_1 - T_2|}\sqrt{\ln\left|\frac{p - P_n}{\sqrt{(a_1 a_2 + b_1 b_2)}}\right|} \qquad (3.2)$$

While SPRT mode halves the number of samples available for the autocorrelations and resulting moment estimations, the obvious advantage of this mode is the greatly increased Nyquist interval allowing for reduction of Doppler-velocity ambiguities in the very strong wind fields of tornadoes. While the single PRT operating mode of the DOW system can yield Nyquist values of up to around +/- 32 m s^{-1}, SPRT modes with the DOW yield Nyquist values over +/- 128 m s^{-1}.

The extensive observational data contained in the DOW radar measurements are sufficient to resolve the tornado-scale flow, but inadequate to fully characterize smaller scales of motion, especially with respect to the temporal resolution constraint of approximately 60 s volume scans. Therefore, it is now possible to construct a tornado climatology based upon high resolution radar observations of actual tornado structures. Although this analysis will be limited necessarily to the observed cases, it avoids the biases and limitations of damage-only based statistics.

Each DOW tornado vortex observation is defined as a single quasi-horizontal scan through the entire tornado core-flow region (Fig. 3.1) which usually requires about 4-5 s with about 10-20 data points in the core, and this comprises the basic unit of observation. *A radar scanning volume is defined as a set of consecutive tornado observations at different elevation angles.*

For this database, the DOW tornado observations will have three independent variables namely tornado (n), time of observation (t), and radius from the tornado vortex

center (r) (Fig 3.1). Given the previously discussed DOW volume scanning strategy, the elevation of each tornado observation (z) is explicitly a function of time (t), and the database can be processed using either variable. This observational database contains about 69 tornadoes, O(n) = 69, with about 10 time observations (elevations) per volume spanning about 30 volumes O(t) = 300, and typical radial data-spacing in a 2 km domain of about 20 m, O(r) = 100. This yields a total database size of O(2 million). Assuming O(50 bytes) of attributes will be stored at each location in the database, this yields O(100 MB) of memory necessary to load the entire database for processing in real-time. Obviously, this is quite practical with current computer hardware.

The fundamental problem lies with how to retrieve a rapidly evolving three dimensional velocity field having only a portion of each velocity component (in the direction of the radar) observed by a radar across a spatial domain that is not sampled simultaneously.

Three assumptions will be applied to reduce the dimensionality of the tornado observation problem from five dimensions (n, t, r, θ, z) to three (n, r, z).

1. Assume axisymmetric flow relative to the tornado vortex center

The analysis is only concerned with tornado scale flow attributes, and not smaller scale transient features that introduce asymmetries in the flow such as multiple vortices. Comparisons between asymmetric and axisymmetric observations will evaluate the robustness of the axisymmetric assumption. This assumption simplifies the equations of motion (in cylindrical coordinates r and z for radial wind u, tangential wind v, vertical wind w, divergence δ, vertical vorticity ζ):

$$\frac{\partial u}{\partial t} = -u\frac{\partial u}{\partial r} - w\frac{\partial u}{\partial z} - \frac{v^2}{r} - \frac{1}{\rho}\frac{\partial P}{\partial r} + F_r$$
$$\frac{\partial v}{\partial t} = -u\frac{\partial v}{\partial r} - w\frac{\partial v}{\partial z} - \frac{uv}{r} + F_r$$
$$\frac{\partial w}{\partial t} = -u\frac{\partial w}{\partial r} - w\frac{\partial w}{\partial z} - g - \frac{1}{\rho}\frac{\partial P}{\partial z} + F_r$$
$$\vec{\nabla} \bullet \vec{U} = \frac{1}{r}\frac{\partial (ru)}{\partial r} + \frac{\partial w}{\partial z} \qquad (3.3)$$
$$\hat{k} \bullet \vec{\nabla} \times \vec{U} = \frac{1}{r}\frac{\partial (rv)}{\partial r}\hat{k}$$
$$\hat{h} \bullet \vec{\nabla} \times \vec{U} = \left(\frac{\partial u}{\partial z} - \frac{\partial w}{\partial r}\right)\hat{\theta} - \frac{1}{r}\frac{\partial (rv)}{\partial z}\hat{r}$$

where k is the unit normal vector in the positive z direction and h is the unit normal vector perpendicular to k in the θ-r plane.

2. Assume each tornado observation scan in a sub-domain is at a constant elevation and time of that of the vortex center

This analysis is only concerned with tornado scale evolution on O(60 s) or greater, and the duration of each tornado observation is an order of magnitude less at O(5 s). The elevation constraint results from Doppler velocity observations contributing to an axisymmetric value that varies symmetrically in elevation both above and below the elevation of the vortex center. Furthermore the average elevation deviation in a radar scan (from an average elevation scan of 7°) across a 1 km radius from the vortex center is O(100 m) which is near or less than the average elevation of the next closest tornado observation (assuming an average range of 7 km to the tornado center and 1° separation between elevation angles):

$$1000m \sin 7° = 121m \cong 7000m \sin 1° = 122m$$

This assumption avoids the need for data interpolation to a constant elevation which potentially smoothes information and deamplifies features.

3. Assume the evolution of the tornado velocity and reflectivity field is negligible compared to translation for time periods less than 60 s

This assumption permits the adjustment of the tornado vortex center position (and times) in different observations of a radar volume scan to a common time and position. While this assumption may be violated, this is the effective temporal resolution of three-dimensional scanning volumes. Analysis of higher temporal resolution two dimensional scanning volumes will be used to evaluate the robustness of the small evolution assumption.

3.2 Navigation Procedures

All DOW radar observations have several stages of both automated and manual navigation of radar-relative observations to a common ground-relative coordinate system. Unfortunately, no inertial navigation system was used during radar data acquisition for any of the DOW radar observations in this data set. Therefore, the navigation of the radar observations is attained through two alternate sources of information. The first source of information is radar operator and/or vehicle navigator logs collected during the real-time operations where the vehicle position and/or heading is recorded through the use of Global Positioning System (GPS) observations. Typical position error associated with these observations is on the order of 300 m prior to 2 May 2000 and is reduced to about 20 m after this date when "Selective Availability" (the intentional degradation of signal

for civilian use) was discontinued. The second source of navigational information originates from ground clutter targets such as road networks and buildings which can be an easily identified in the radar power, reflectivity and Doppler velocity fields. Knowledge of the approximate location of the radar from the operator logs can then be accurately adjusted using the ground clutter observations to improve radar position estimates to within the radar beamwidth and range-gate spacing, usually O(30 m) or less.

3.2.1 Date/Time and Lat/Lon Corrections

In observation cases where operator logs indicate that the PIRAQ-II radar data acquisition took place with an inaccurate system clock, date and/or time adjustments have been made to the final radar data set using the operator indicated time offsets to properly encode the date and time of each radar observation to within about 1 s accuracy. Additionally, for all radar observations, the truck position including latitude, longitude, elevation above sea level, and vehicle heading are encoded in the final data set. Typical accuracy of these measurements are on the order of O(30 m) for latitude and longitude and about one degree in heading. In cases where the radar truck is mobile during data collection, the approximate position and heading of the radar are encoded using the same navigational sources of information as during stationary periods, although the latitude, longitude, elevation, and vehicle heading are encoded as constant during the entire observation period (usually 4-5 s). Vehicle heading estimates during mobile periods are derived from the derivative the radar position estimate at consecutive observation times. The derivative of the radar position is constrained to time periods between significant turning (greater than a few degrees) of the vehicle.

3.2.2 Ranging Corrections

During early DOW1 operations in 1995, a small ranging error was diagnosed for the range to the first (and all subsequent) radar gates of each radar beam. This ranging error was determined to be 220 m and the corrected range to all gates in all beams is encoded into the final data set.

3.2.3 Pointing Angle Corrections

During early DOW2 and DOW3 operations in 1997 and 1998, an antenna elevation angle error was diagnosed for both radars. DOW2 elevation angles for all beams were reported as -1.7 degrees too low while DOW3 elevations angles were 0.6 degrees too high. The corrected elevation angles were encoded into the final data set for both radars.

In observations where the reported elevation angle (ϕ_r) is less than the radar beamwidth (B), a Gaussian-weighted elevation correction factor is applied whereby an effective elevation angle (ϕ_{eff}) is computed assuming that all of the primary lobe of the radar beam below the radar horizon (zero elevation) does not contribute to the illumination pattern and is effectively blocked by the ground (Fig. 3.2):

$$\phi_{eff} = \frac{\int_0^\infty \phi e^{-4(\ln 2)(\phi-\phi_r)^2/B^2} d\phi}{\int_0^\infty e^{-4(\ln 2)(\phi-\phi_r)^2/B^2} d\phi} \tag{3.4}$$

This correction factor has effectively no impact on reported elevation angles above about 0.5 degrees. However, for reported elevation angles between 0.5 degrees and 0.0 degrees (or less) the effective elevation angle asymptotes at around 0.3 degrees

for the DOW beamwidth. This correction factor will improve the estimate of the vertical position of features.

3.2.4 Rotation to Ground-Relative Position

Navigational field logs and/or ground clutter road patterns provide sufficient information to determine the orientation of the radar relative to true north. Automated application of data rotation to a specified angle can then be applied to the radar fields. Since only single-Doppler observations are being processed, exact orientation estimates on the order of 0.2° are preferred but not necessary. Using the radar heading information encoded in the data during the navigation procedure in 3.2.1 all radar beam azimuth angles for each observation are rotated by an amount equal to the radar heading at the time of the observation. This rotation completes the transformation from radar-relative to a common ground-relative coordinate system. The antenna pitch and roll angles are assumed to be zero for all stationary and mobile data collection. During stationary data collection, radar vehicle load-levelers are usually deployed and are designed to level the truck bed and radar antenna to within 0.2 degrees of a horizontal plane. By definition, the drift angle is zero for all ground-based radar observations such as the DOW, so the track and heading angles of the vehicle are always identical. The ground-relative azimuth angles are encoded into the final data set.

In order to quantify the uncertainty in ground-relative position of sample volumes in mobile radar data, two Cartesian coordinate systems are defined in x, y, z space. Azimuth angles are measured clockwise in the x-y plane from the positive y-axis to the direction of the radar beam, and elevation angles are measured as the departure of the radar beam from the x-y plane along the positive z-axis.

The first coordinate system is the position of the radar sample volume relative to the radar antenna. The antenna-relative system is defined with the x-y plane containing the rigid truck bed upon which the radar antenna pedestal is mounted. The positive y-axis is oriented towards the front of the truck with the positive x-axis located at 90 degrees azimuth, and the positive z-axis is oriented perpendicular to and pointing above the truck bed and antenna.

The second coordinate system is ground-relative where the x-y plane is locally parallel to the ground, the positive y-axis points toward true north, the positive x-axis points toward true east, and the positive z-axis points upward toward the local zenith.

These coordinate systems are similar to those described in Lee et al. (1994b), but contain a few important differences due to antenna pedestal orientation on a truck bed as opposed to a plane fuselage. Following from Lee et al. (1994b), it is possible to start with antenna-relative coordinates of range, azimuth, and elevation (r, θ_a, ϕ_a) and perform three successive coordinate rotations to account for the roll, pitch and heading (P, R, H) of the radar antenna and yield ground-relative coordinates in range, azimuth, and elevation (r, θ, ϕ) for the radar sample volume. Pitch is defined as the rotation angle of the truck bed and antenna pedestal about a positive x-axis with positive angles when the front of the truck is raised above the back. Roll is defined as the rotation angle of the truck bed and antenna pedestal about a positive y-axis with positive angles when the right side of the truck is lower than the left. Heading is defined as the rotation angle of the truck bed and antenna pedestal about the positive z-axis with the same sign convention as azimuth angle. Since the truck is effectively fixed to the surface of the earth in all but the most extreme weather conditions, no drift angle needs to be accounted for, and the heading of the truck is identical to its track.

The antenna-relative Cartesian position of a radar sample volume located at (r, θ_a, ϕ_a) is given by

$$\vec{X}_a = \begin{bmatrix} x_a \\ y_a \\ z_a \end{bmatrix} = r \begin{bmatrix} \sin\theta_a \cos\phi_a \\ \cos\theta_a \cos\phi_a \\ \sin\phi_a \end{bmatrix} \tag{3.5}$$

This antenna-relative system can then be rotated into ground-relative coordinates using three transformation matrices (M_H, M_R, M_P) to rotate through roll, pitch and then heading angles

$$\vec{X}_g = \begin{bmatrix} x_g \\ y_g \\ z_g \end{bmatrix} = M_H M_P M_R \vec{X}_a$$

$$\vec{X}_g = \begin{bmatrix} \cos H & \sin H & 0 \\ -\sin H & \cos H & 0 \\ 0 & 0 & 1 \end{bmatrix} \begin{bmatrix} 1 & 0 & 0 \\ 0 & \cos P & -\sin P \\ 0 & \sin P & \cos P \end{bmatrix} \begin{bmatrix} \cos R & 0 & \sin R \\ 0 & 1 & 0 \\ -\sin R & 0 & \cos R \end{bmatrix} \vec{X}_a \tag{3.6}$$

When the radar truck is stationary and the load-levelers are deployed to reduce the pitch and roll angles (P and R) to approximately zero (within 0.2°), the ground-relative coordinates reduce to

$$\vec{X}_{gstationary} = \begin{bmatrix} x_{gs} \\ y_{gs} \\ z_{gs} \end{bmatrix} = r \begin{bmatrix} \sin(\theta_a + H)\cos\phi_a \\ \cos(\theta_a + H)\cos\phi_a \\ \sin\phi_a \end{bmatrix} \tag{3.7}$$

When the radar truck is in motion the heading, pitch and roll angles are very rarely zero, and the radar system does not record such angles during operations. However, scale analysis can be employed to estimate errors in the position of sample volumes. The underlying assumption in this scale analysis is that typical values for radar truck pitch and roll angles are O(1°). This estimate is typical for pitch and roll as most road surfaces are within a few degrees of being level with respect to the earth's surface, except in regions of significant terrain (large hills or mountains) where ground-based radar operations are unlikely due to blockages of the radar beam. During stationary data

collection the radar heading angle can usually be determined to within O(1°) based upon ground clutter returns or other external information such as field notes or GPS measurements. A more precise orientation estimate is occasionally possible if the data is used for dual-Doppler synthesis. During mobile data collection the vehicle heading is more tightly constrained along the direction of roads and the heading estimate improves to within O(0.1°).

Typical values for the antenna-relative position of a sample volumes and radar truck orientation are listed in Table 3.1. Neglecting terms in equation set 3.6 that are an order of magnitude or more smaller than the largest term using the typical values provided in Table 3.1, an estimate of the positional error when assuming a zero pitch or roll angle is O(10 m) in the horizontal and O(100 m) in the vertical for mobile operations. The horizontal position error is larger for stationary operations and is near O(100 m) since the radar heading is not necessarily parallel to a particular road when it is stationary and deployed. The vertical position error is smaller at around O(10 m) for stationary data collection when the load-levelers are deployed. The positional error will remain constant during an entire stationary deployment while small variability in positional error will take place during mobile data collection.

3.3 Quality Control Procedures

Following the navigation procedures, all DOW radar observations have several stages of both automated and manual quality control (QC) applied to the Doppler velocity measurements. The QC operations include thresholding of Doppler velocities by a signal quality field, removal of isolated low signal quality values, retrieval of Doppler velocities

collected in staggered pulse repetition mode, dealiasing of folded Doppler velocities and removal of non-meteorological target Doppler velocity measurements.

3.3.1 Normalized Coherent Power Thresholding

The first stage of QC involves the automated removal of V values where the value of N (ranging from 0 to 1) is below a user-specified criteria. Since N represents the fraction of total returned power that is coherent and comprises the estimate for the detection algorithm, a typical value of 0.20 is specified (reference) and is typical with DOW data. However, V values within tornado core regions are preserved with a lower NCP threshold of about 0.10.

3.3.2 Removal of Low-NCP Speckles

Following the thresholding, there is an automated two-pass removal of isolated V values which are surrounded by less than 50% coverage of unthresholded V values within a two-gate square patch. This step removes highly isolated V values that were not removed during the thresholding (Fig. 3.3a).

3.3.3 Removal of Staggered Pulse Repetition Period Velocity Glitches

Much of the tornado observations collected by the DOWs have employed a staggered-pulse-repetition-period (PRT) velocity processing technique, thereby yielding a high unambiguous velocity and greatly limiting the number of cases (about 30%) where significant folding of Doppler velocities occurs. However, velocity "glitches" still appear in staggered-PRT data, and an automated algorithm has been established to appropriately

unfold these "glitched" gates based upon iterated comparisons with surrounding data using a limited number of Nyquist adjustments derived from the two known PRTs.

In general, this algorithm identifies V glitches where the velocity value is at a given gate exceeds a user-specified difference in velocity from the median value of surrounding gates. For most cases in the data set, a two-gate square patch and a velocity threshold of 20 m s^{-1} are used. For each glitch that is identified, the algorithm attempts to find a V value using Nyquist multiples of the V values from the two individual PRTs that produces the closest match to the median of the surrounding values. If the closest match exceeds the threshold, the V value is deleted and is deemed irretrievable (Fig. 3.3b).

3.3.4 Dealiasing of Doppler Velocity

Another algorithm is employed to unfold single PRT velocity data in regions where ground clutter is not present. Generally speaking it is not possible to automatically dealias all DOW tornado data given the available moment data. However, automated algorithms are applied to dealias data following some manual editing of the data. Following the manual dealiasing of a single radar volume, an automated algorithm is applied to use the manually dealiased volume as a reference field to dealias successive volumes of data. The algorithm identifies each radar gate in the successive volume that is within a user-specified azimuth, elevation and range of a gate in the manually dealiased volume. If the V value exceeds a user-specified fraction (usually about 0.8) of a Nyquist velocity from the reference data, the algorithm then attempts to adjust the V value based upon iterated comparisons and minimization with the reference data using a limited number of Nyquist adjustments derived from the known PRT. Typical settings for this

algorithm included an azimuth and elevation search tolerance of 0.5 degrees and a Nyquist threshold of 1.0. An ambiguity in this algorithm develops when the temporal evolution of the V field between successive radar observations of nearly the same point in space exceeds the Nyquist velocity. This ambiguity is most common when observing a strong tornado that is moving rapidly through the field of view of the radar either due to the tornado translation, the vehicle motion or a combination of both. In cases where the ambiguity develops, manual dealiasing of the V field is necessary.

3.3.5 Removal of Ground Clutter

Ground clutter is manually removed in regions of data where high R values appear from non-meteorological sources coincident with near-zero V values. Approximately 20% of the observations require manual removal of ground clutter. All other regions containing incoherent velocities i.e. low N returns below about 0.20 are removed except within the tornado core-flow region. This N thresholding is performed by an automated algorithm. Ground clutter, multiple trip echoes, and low signal-to-noise (clear-air) data in the V and R fields are removed through the automated and manual QC procedures.

3.3.6 Removal of Radar Velocity

For cases with mobile radar observations, removal of truck velocities (speed V_{DOW} and heading φ) must be incorporated into the data processing by first determining the motion vector of the radar based upon measured Doppler velocities of ground-clutter along the direction of the truck motion. Road grids often provide a suitable target for

ground clutter return, and must necessarily lie in the direction of the vehicle motion. In observations without sufficient ground clutter return, the time derivative of the vehicle position is used to estimate the vehicle motion. Mobile data is typically recorded in a radar-relative orientation so no estimation of radar heading is necessary to remove truck velocities. In all cases of mobile data collection, the vehicle velocity estimate is encoded into the final radar data. The following trigonometric relationship can then be applied to the V_d field to remove the vehicle motion assuming a constant vehicle velocity for the observation period of 4-5 s (Fig. 3.4):

$$V_{dg} = V_d + V_{DOW}\cos(\theta - \varphi)\cos\phi_{eff} \tag{3.8}$$

The typical error of truck velocity estimates is O(1 m s^{-1}) which is also the typical error in the estimate for the final ground-relative Doppler velocity (V_{dg}) as reported in Table 3.1.

3.4 Analysis Algorithms

Following all navigation and quality control procedures, the final V field can be used to uniquely identify, track, and extract measurements in and near tornadoes from DOW radar observations. An additional suite of automated algorithms are implemented to accomplish these tasks. These algorithms provide an objective filter through which the observations are processed.

3.4.1 Tornado Detection

The first step in the processing of the tornado observations is to detect features of

interest in the radar data. *About 25% of the DOW supercell scans (observations) contain features that are classified as a detection by an algorithm that requires at least 40 m s^{-1} of V difference across no more than 2 km of horizontal distance at constant range from the radar (pure rotation).* This detection sequence begins by searching across all gates of an observation beginning at a range closest to the radar and at the earliest azimuth in the observation. The search proceeds azimuthally at each range whereby the velocity difference is first measured between the given gate and the two azimuthally adjacent gates. This difference calculation is then repeated using the two gates on either azimuthal side of the given gate. This sequence is repeated at more azimuthally adjacent gates centered about the given gate until the distance between gates reaches the specified threshold of 2 km. If a velocity difference of 40 m s^{-1} or more is identified in the azimuthal search around a given gate, then the gate position is recorded as the first-guess center point of a possible tornado vortex along with other information including the velocity difference and horizontal scale of the difference (Fig. 3.5). It is important to note that the horizontal scale of the difference is associated with the largest difference value in the 2 km search diameter. While it is possible and not entirely uncommon to observe concentric vortices, the stronger vortex (higher velocity difference) will have precedence in the detection of scale. More than one feature can be identified as a possible tornado in the same observation field but they must be separated by more than about one diameter associated with the stronger vortex. Both cyclonic and anti-cyclonic features are detected with the same criteria.

Following the first guess center-point detection, a refined center-point detection is executed by ranking all velocity values within one first-guess diameter (two radii) of the

first guess center and then finding the median coordinate position of the lowest and highest values using a user-specified threshold of the 90th percentile (Fig. 3.6a,b). This threshold will identify the median position of the lowest 10% (most negative/least positive) and highest 10% (most positive/least negative) velocity values in the search domain. The gate nearest the midpoint of the two median coordinate positions is recorded as the refined vortex center point (Fig 3.7). It should be noted that in extreme cases of the threshold value (0% or 100%) the refined center point will either be the midpoint between the two maximum values (100%) or the midpoint between the median coordinate position of the upper half and the lower half of all values in the search domain (0%). The refined center point can be located asymmetrically closer to either the maximum or minimum value with this algorithm, although the exact location will depend on the positional distribution and sample size of the more extreme velocity values, which for typical scanning strategies and observation geometries will usually be less than ten values in total. The refined center point radar-relative and ground-relative positions are also recorded.

While the selection of 40 m s^{-1} difference and 2 km diameter is arbitrary, these thresholds are grounded in the existing body of research associated with tornado structure. Both the original F-scale and the revised EF-scale estimate low-end tornado wind speeds between 18 and 29 m s^{-1} respectively. Synoptic-scale horizontal wind speeds are characterized at about 10 m s^{-1}. A 40 m s^{-1} velocity difference for a stationary tornado would imply ground-relative wind speeds of about 20 m s^{-1} which is very close to the original low-end estimate of tornado intensity and is below the current EF-scale threshold. Ideally, the detection of dynamical features such as a corner-flow region or

vertical motion exceeding that of the near-field horizontal motion would provide a more definitive detection of a tornado, however, neither of these attributes can be identified from single-Doppler observations.

Based on existing damage surveys, tornado diameters have not been inferred to be larger than about 2 km, which is also the low-end threshold for meso-gamma scale phenomena including larger-scale structures such as mesocyclones within thunderstorms.

3.4.2 Tornado Isolation

After all possible tornado detections are compiled for a given case, the detections are collated into unique persistent events. This step is necessary to separate multiple tornadoes that are observed simultaneously and provides information for additional algorithms to track the evolution of vortex features. The isolation algorithm searches all detections for a given case and groups the detections into sequential observations whereby the location of temporally adjacent detections cannot imply a translational speed of more than about 25 m s^{-1}. *Furthermore, the feature is considered a tornado if it can be tracked in two or more scans (observations) assuming the feature is moving at ground-relative speeds of less than about 25 m* s^{-1}. There is inherent ambiguity with this algorithm if multiple tornadoes are observed simultaneously and a large gap in time occurs between successive observations. This problem is analogous to tracking multiple-vortices within a single parent vortex where aliasing of features can occur. Whenever such ambiguity arises, manual inspection of the radar observations can provide sufficient pattern recognition to track tornado features across the large gap in observations. No manual inspection of observations revealed translation values greater than 25 m s^{-1}.

3.4.3 Tornado Tracking

After each tornado is uniquely identified in the isolation step and all observations are grouped sequentially, the next step involves automated tracking of the tornadoes. This tracking is performed for each tornado by stratifying all observations of a given tornado into four quartiles based upon the elevation of the refined vortex center point of each observation. This stratification permits identification of differential vortex motion between various elevation layers while ensuring sufficient observation sample sizes within each layer. The motion vector of the refined tornado vortex center is recorded with each observation using a centered-in-time difference scheme comparing the previous and next position of the refined vortex center in the same elevation layer. In addition to the motion vector, an estimate of the vortex tilt is recorded as measured by the horizontal and vertical displacement of the next higher vortex center observation. The directional heading of the tilt and departure from the vertical axis are both recorded. Finally, a corrected tilt and heading of the tilt are calculated after compensating for vortex motion between the times of the consecutive observations.

3.4.4 Patch Extraction

Once each tornado has been detected, isolated and tracked the retrieval of kinematic and dynamic quantities are executed. For each tornado observation a series of values are recorded that effectively provide single-point estimates of tornado structure based upon a "patch" of data values surrounding each center point. These data values include distributions of V, P, R and S within about four core radii (half the distance

between maximum velocity values) of the refined center point. The statistical values include sample size, average, standard deviation relative to the average, mode, median, minimum, maximum, range, tenth and ninetieth percentiles, and first and third quartiles.

In addition to these statistical values, for the V field, several additional quantities are extracted (Table 3.1). These quantities include the coordinate positions of the minimum and maximum V values in the search domain around the refined center, the distance between the refined center-point and each maximum value, the average distance between each maximum V value and the refined center point, and the distance and orientation angle of the axis between the maximum values. The distance between the maximum values is defined as the tornado core diameter. For the two maximum velocity values, the difference between the values, the average magnitude of the values, and the difference between the magnitudes are recorded.

Dynamical quantities computed include the radius from the refined center where the ratio of the velocity difference and the distance is maximized (radius of maximum bulk vertical vorticity). Additionally, this bulk vertical vorticity, horizontal divergence, angular momentum and stretching of vorticity are computed at 0.25, 0.50, 0.75, 1.0, 1.5, 2.0, 3.0 and 4.0 times the core radius. Mean circulation over the entire search radius is also computed along with cyclostrophic pressure deficit from the vortex center to the maximum radius.

Ground-relative wind speed estimates are also estimated using an aspect ratio correction factor (Wurman and Gill 2000) to account for reduction in velocity measurements (V_{dg}) as the radar beamwidth (B) becomes large relative to the size of the vortex core (D) (Fig. 3.8). This correction factor is limited to no more than about a 14%

increase in the maximum V value at which point the radar beamwidth is about 50% of the radius (25% of the diameter).

For B < 0.25D:

$$V_{corr} = V_{dg} \frac{1}{1 - 0.48(B/D)} \tag{3.9}$$

For B > 0.25D:

$$V_{corr} = V_{dg} * 1.14 \tag{3.10}$$

Following application of the aspect ratio correction to both the minimum (most negative) and maximum (most positive) V values, the unobserved component of the tornado translation velocity (component of tornado movement perpendicular to the radar beam) is added to both V values,

$$V_{\max} = V_{corr} + C\sin(\beta - \theta) \tag{3.11}$$

The resulting aspect-corrected ground-relative maximum values are then compared and the magnitude of the largest value is mapped to both the F-Scale and the EF-Scale using fractional scale values. While the F-scale provides an analytic function for the mapping, a linear interpolation between category bins is used for the EF-Scale.

3.4.5 Cross-section Extraction (1-D)

In addition to point-value extraction from the observations, one-dimensional sets of V, R, P and S values are also extracted from each observation containing all gate values on azimuthal arcs through the refined center point of each tornado observation (Fig. 3.9a). Along these psudo quasi-horizontal cross sections, shear vorticity, curvature vorticity, vertical vorticity, angular momentum, circulation and cyclostrophic pressure

deficit are also computed using a centered-difference scheme over each gate along the arcs.

3.4.6 Single-Doppler Velocity Retrieval Extraction (2-D)

Assuming axisymmetry, a 2-D single-Doppler retrieval technique is applied to concentric annuli around each refined tornado center point for each observation (Fig. 3.9b). The width of each annulus is set to be the smaller of either the range or azimuthal data spacing in the observation field. Each annulus provides an axisymmetric value of tangential and radial velocity along with estimates of azimuthally averaged values of angular momentum, circulation, cyclostrophic pressure deficit, and inflow angle as a function of radius from the refined center point.

The algorithm estimation of the azimuthally averaged tangential and radial velocity components is achieved with a least-squares minimization of all observed V values within the annulus around the refined vortex center, first applied by Alexander in Dowell et al. 2005. The minimization involves the following cost function where D_i is the Doppler velocity observation at gate i in the annulus, θ_i is the ground-relative azimuth angle of gate i with respect to the radar, α_i is the ground-relative azimuth of gate i with respect to the refined vortex center point, C is the translation speed of the tornado vortex center, B is the ground-relative azimuth direction in which the tornado is moving and u and v are the azimuthally averaged radial and tangential velocity components of the flow at a distance r from the best guess vortex center point.

$$
\begin{aligned}
J &= \sum_i [D_i - u\cos(\alpha_i - \theta_i) - v\sin(\alpha_i - \theta_i) - C\cos(\beta_i - \theta_i)]^2 \\
a &= \sin(\alpha_i - \theta_i) \\
b &= \cos(\alpha_i - \theta_i) \\
c &= D_i - C\cos(\beta_i - \theta_i)
\end{aligned}
\tag{3.12}
$$

By taking the derivative of the cost-function with respect to both u and v and setting the resulting equations to zero, the analytic expressions for u and v are obtained.

$$
\begin{aligned}
u(r) &= \frac{\sum_i a_i^2 \sum_i b_i c_i - \sum_i a_i b_i \sum_i a_i c_i}{\sum_i a_i^2 \sum_i b_i^2 - \left(\sum_i a_i b_i\right)^2} \\
v(r) &= \frac{\sum_i b_i^2 \sum_i a_i c_i - \sum_i a_i b_i \sum_i b_i c_i}{\sum_i a_i^2 \sum_i b_i^2 - \left(\sum_i a_i b_i\right)^2}
\end{aligned}
\tag{3.13}
$$

It is important to note that this procedure assumes no functional shape to these velocity profiles as function of radius from the vortex center and the results are relatively robust to the selection of the vortex center point (Fig. 3.10).

3.4.7 Single-Doppler Velocity Retrieval Extraction (3-D)

When possible, the 2-D axisymmetric retrievals can be aligned vertically and 3-D fields can be computed assuming mass conservation. Typically this is only possible in well-resolved tornadoes with little temporal evolution between observations. In these cases, 4-D (time varying) terms can be evaluated from consecutive 3-D retrievals.

Once the detection, isolation, tracking, and extraction/retrieval algorithms are

applied to all the DOW radar tornado observations, the distribution of the results are analyzed to test the hypotheses related to common kinematic tornado structures and genesis evolution discussed in section 2.4.

Chapter 4

Analysis

4.1 Kinematic Tornado Structures

The analysis algorithms discussed in Chapter 3 are applied to DOW radar tornado observations for all cases from 1995 to 2001 with selected cases from 2003 and 2004 used in comparison with WSR-88D radar observations, but not incorporated in the overall climatology. These observations total 69 different tornadoes observed within 30 km range of the DOWs and are comprised of 6282 individual observations (scans). The total number of scans processed by the algorithms was 25,789, and therefore, tornado observations are detected approximately 25% of the time when DOW radar data are being recorded regardless of whether the radar was moving between deployments or stationary and level.

4.1.1 Data Sampling Statistics

Given the typical duration of the observed tornadoes (540 s) and the scanning frequency of the DOW, most tornadoes in this dataset have around 10-20 individual observations/scans each (Fig. 4.1a,b,c,d). Only seven tornadoes have more than 100 observations/scans. Ideally, all tornadoes would be sampled with the same number of observations, but this constraint is neither practical nor realistic and all observations are given equal weight considering that this phenomenon is significantly under-observed in time and space and has a high degree of variability with a short decorrelation time on the

order of several minutes. This sample size frequency distribution is more even more skewed when considering only observations within 500 m AGL (Fig. 4.1b,d) where only five tornadoes have more than 100 observations.

The data sampling statistics indicate the estimated center of the tornadoes are observed at ranges between 1 km and 30 km with the most frequent values around 5 km (Fig. 4.2a). Correspondingly, the elevation of these observations are between 20 m and about 7000 m AGL with a majority of observations below 500 m AGL (Fig. 4.2b). The scanning strategies employed during operations place the data resolution across the tornadoes at a typical value of about 50 m in the radial direction for the gate spacing (parallel to the radar beam) and slightly larger, around 60-70 m, in the azimuthal direction for the beam spacing (normal to the radar beam) (Fig. 4.3a,b). The time period between observations is usually about 5-10 s, both throughout the column and within the lowest 500 m AGL (Fig. 4.3c,d). This resolution depended not only on the range to the tornado, but varied depending on signal processing parameters and other hardware characteristics of the radar, which evolved with time as the DOWs evolved (Table 1.1, 1.2, 1.3).

The ability to resolve tornado-scale features is predicated upon a data sampling scale that is closer to an order of magnitude smaller than the scale of features being observed. The DOW scanning and signal-processing strategies typically place the data sampling scale between 0.1 to 0.3 times the inferred scale of the tornado core diameter, as described in section 3.4.4, which is sufficient to resolve between 60% and 90% of the amplitude of the features (Carbone et al. 1985) (Fig. 4.3e,f).

4.1.2 Tornado Intensity Distribution

Applying the velocity aspect correction factor from section 3.4.4 and accounting for the unobserved component of tornado motion normal to the radar beam, the largest amplitude velocity measurement for each of 52 tornadoes observed is mapped to both the F-scale and EF-scale. These mappings are then compared to the storm-report tornado intensities from the Storm Prediction Center (SPC) OneTor database (Schaefer and Edwards 1999) for these same tornadoes (Fig. 4.4a,b). In addition to the set of 52 common tornadoes, an additional 17 tornadoes are observed by the DOWs but not reported in OneTor and 13 tornadoes in OneTor are not detected by the DOWs, assuming the reported locations and times are accurate (Fig. 4.4c,d).

The most frequently observed intensity falls within the F2/EF2 intensity category when using the velocity mapping to damage potential for either scale. Furthermore, the DOW-inferred intensities appear to be normally distributed as opposed to the exponential decay distribution from storm-report intensities.

The same comparison is made between the DOW observations and tornado storm reports for the maximum width of each tornado (Fig. 4.5a). Again, there is a tendency to have storm reports produce a distribution that is favored towards the smallest values which are diameters less than 200 m. The maximum DOW tornado width, as defined by distance across the tornado core (distance between peak inbound and outbound Doppler velocities), appears to be much larger, in excess of 1800 m. When considering the DOW tornado width at the time of peak tornado intensity (maximum aspect-corrected ground-relative velocity) the values are clustered towards the smaller scales (Fig. 4.5b). Additional filtering of the tornadoes to include only stronger (EF2 rated/detected or

greater) tornadoes continues to show a skewed distribution towards smaller values. The largest DOW observed tornado core at peak intensity was detected near Mulhall, OK on 03 May 1999 (Wurman 2002).

A discussion of these findings as they relate to DOW random-sampling of supercell tornadoes, radar sampling biases, and the larger population of OneTor tornado reports (Fig. 4.6, 4.7) is presented in section 5.1.1.

4.1.3 Kinematic Distributions

When transforming Doppler velocities into ground-relative wind speeds, it is necessary to include both the component of unobserved translation of the tornado vortex as well as a compensation for smoothing of the cusp region at the radius of maximum winds due to radar beam broadening of the velocity signature discussed in section 3.4.4. Ideally, an elevation correction of the wind speed observations to the standard 10 m AGL height would be included. However, it is shown in section 4.1.5 and discussed in section 5.1.4 that the vertical profile of peak intensity below O(100 m AGL) is relatively constant and no obvious correction factor is apparent. *Applying the ground-relative and aspect correction factors, the median ground relative velocity across all tornado observations below 500 m AGL is about 65 m s^{-1} (Fig. 4.8a) with a very similar median value for all observations below 200 m AGL (Fig. 4.8b). The median value decreases slightly for all observations below 50 m AGL to about 59 m s^{-1} (Fig 4.8c) although the sample size is much smaller. When considering only the maximum value from each tornado, this median value is also about 59 m s^{-1} (Fig. 4.8d) which implies that the stronger tornadoes are observed for longer periods. The minimum value is about 23 m s^{-1} and the maximum is*

137 m s^{-1} which was observed near Bridgecreek, OK on 03 May 1999 (Burgess et al. 2002) . This maximum ground-relative velocity is 2 m s^{-1} higher than previously reported for this case (Glenday 2005), and while this difference is well within the observation error for this measurement, it is the result of the aspect correction factor applied to this particular radar scan. A peak ground-relative velocity of 23 m s^{-1} is associated with a very weak nearly stationary tornado near Medicine Park, OK on 03 May 1999.

The DOW tornado maximum ground-relative velocity distribution for all 52 tornadoes is transformed into a box plot showing minimum, 25th percentile, median, 75th percentile and maximum F-scale and EF-scale values (Fig. 4.9a,b) where the median F2/EF2 ranking is apparent (equal to the 25th percentile for the EF-scale). The DOW tornado database is then filtered to consider only tornadoes observed within 10 km range (Fig. 4.9c) and 5 km range (Fig. 4.9d). In both range-limited cases with reduced sample sizes, the distribution remains similar with a median EF2 value.

The translation of tornadoes appears to have a median value near 13.5 m s^{-1} with values near 9 m s^{-1} on the lower end of the distribution and 18 m s^{-1} near the upper end. Extreme values of nearly stationary and 25 m s^{-1} were also observed (Fig. 4.10a) with the maximum value associated with a tornado observed near Bassett, NE on 05 June 1999. A similar peak speed was been observed in a tornado not included in this work (Wurman et al. 2010b) of about 25 m s^{-1} near Stuttgart, AR on 10 May 2008. It should be noted that the tornado-tracking algorithm limits the upper end of translation speed to near 25 m s^{-1} as positional aliasing of features begins to occur with typical DOW update frequencies when this speed is exceeded. The observed duration of the DOW tornadoes range from about one min to 50 min with the longest duration observations in tornadoes observed

near Bridgecreek, OK on 03 May 1999 and Alama, KS on 03 June 1999 with about nine min for a median value (Fig. 4.10b). Assuming constant linear motion, the product of the translation and duration distributions (not shown) implies path lengths ranging from near zero to a maximum of 77 km with a median value near 7 km (4.3 miles). The DOW observations do not always capture the complete lifecycle of the each tornado and the duration estimates will have a low bias. Approximately 30% of the DOW-observed tornadoes have an incomplete lifecycle observation period based upon the velocity difference across the tornado core remaining above the detection threshold discussed in section 3.4.1 at the time of the first and/or last available DOW scan.

The inclination (tilt from the vertical) for adjacent segments of each vortex ranges from nearly vertical (0 degrees) to about 80 degrees from the vertical in the most sheared cases when compensating for vortex motion between observations (Fig. 4.11a). The typical inclination angle is around 40 degrees for all observations below 10 km. When focusing on the lowest 500 m AGL the tornado structure tends to be more vertical with most values within 10 degrees of vertical (Fig. 4.11b). These lower tilt angles are consistent with observations from other studies including Bluestein et al. (2004, 2007) and Alexander and Wurman (2005).

The peak velocity difference across the core of each tornado appears to have a median of just over 100 m s^{-1} with extreme values observed around 220 m s^{-1} for all observations below 500 m AGL and 200 m AGL (Fig. 4.12a,b). The median value decreases to about 90 ms s^{-1} for values less than 50 m AGL (Fig. 4.12c). The median value of the velocity difference as a maximum for each tornado is around 85 m s^{-1} with the algorithm specified minimum cutoff of 40 m s^{-1} (Fig. 4.12d).

The DOW radar observations of mesocyclonic tornadoes support a median diameter of the core region at about 300 m at peak tornado intensity when the diameter is defined as the distance between maximum inbound and outbound Doppler velocities for all observations below 500 m AGL (Fig. 4.13a). This distribution appears nearly identical for observations below 200 m AGL (Fig. 4.13b) but the median value increases slightly for observations below 50 m AGL to around 400 m (Fig. 4.13c). The maximum diameter of 2000 m is a constrained upper limit in the detection algorithms. The median diameter is much smaller, near 100 m, when considering the radius of maximum axisymmetric vertical vorticity (the distance from the best-guess tornado center where the ratio of velocity difference to distance reaches a maximum) (Fig. 4.13d). The discussion of the implication of this difference is in section 5.1.2.

The axisymmetric vertical vorticity across the tornado core can be estimated by taking twice the velocity difference divided by the distance of the velocity difference. This value has a range between about 0.2 s^{-1} to 1.2 s^{-1} (Fig. 4.14a) although extreme values approaching 3.0 s^{-1} have been observed in the Bridgecreek, OK tornado on 03 May 1999 and Spencer, SD tornado on 30 May 1998 (Burgess et al. 2002, Alexander and Wurman 2005). The algorithm lower limit for the vorticity value is about 0.04 s^{-1}. When considering the rotation of the Doppler velocity couplet and zero isoDop line away from pure rotation to include a convergent component, a majority of the tornado observations appear to be slightly divergent (Fig. 4.14b) with 75th percentile values near 0.15 s^{-1}.

It is also possible that the convergent inflow region is extremely shallow and not well sampled by most DOW observations, although this convergent region would need to be confined to within a few tens of meters of the surface as observed in tornadoes near

Spencer, SD on 30 May 1998 and Stuttgart, AR on 10 May 2008 (Alexander and Wurman 2005, Wurman et al. 2010). To this end, the horizontal divergence is computed for DOW tornado observations over an increasingly small layer above the surface including 200 m AGL (Fig. 4.14c), 100 m AGL (Fig. 4.14d) and 50 m AGL (Fig. 4.14e). For all cases there appears a bias towards divergent signatures and this is discussed in section 5.1.2. Additional filtering of the observations below 50 m AGL is performed by estimating the centripetal acceleration (Table 3.2) at the edge of the tornado core and removing all observations where this value exceeds 40 m s^{-2}. This filtering effectively removes observations of strong narrow tornadoes including about 74 scans below 50 m AGL. The resulting distribution of horizontal divergence appears almost symmetric with respect to non-divergence (Fig. 4.14f).

The circulation and angular momentum values retrieved from the tornado observations have median values near 50000 m^2s^{-1} and 9000 m^2s^{-1} respectively (Fig. 4.15a,b). The median value for centripetal acceleration is around 15 m s^{-2} with a 75^{th} percentile value of 40 m s^{-2} (Fig. 4.15c) which is used as a threshold for filtering observations for estimates of horizontal divergence (Fig. 4.14f).

4.1.4 Rates Of Change

Given the rapid update frequency of the DOW tornado observations it is also possible to examine the distribution of time-rate-of-change for many of the same kinematic quantities. The rate of change of ground-relative aspect-corrected velocity shows extreme values near +/- 4 m s^{-2} although most accelerations or decelerations of the flow are within +/- 1 m s^{-2} (Fig. 4.16a,b). When considering only near-surface (< 50 m

AGL) tornado observations, the change is less pronounced with acceleration typically within +/- 0.5 m s^{-2} (Fig. 4.16c,d). For a sustained acceleration over a time period of 50 s or more, the most extreme changes in ground-relative aspect-corrected velocity are observed to be about +/- 30 m s^{-1} with values typically bounded by about +/- 10 m s^{-1}. Velocity values increased by about 30 m s^{-1} over a 5 min period at 250 m AGL in a tornado near Seward, KS on 05 May 2007. The rate of change of velocity difference (Fig. 4.17) exhibits a nearly identical distribution to that of the change in peak ground-relative velocity with typical values of +/- 1 m s^{-2} and extreme values near +/- 5 m s^{-2}.

The scale contraction or expansion rate for tornado core diameter is typically on the order of 10 m s^{-1} although values around 90 m s^{-1} have been observed within 500 m AGL (Fig. 4.18a,b). For the near surface layer less than 50 m AGL the contraction/expansion rates appear smaller and are about half of those observed in the 500 m AGL layer (Fig. 4.18c,d). The intensification/weakening of axisymmetric vertical vorticity appears to be confined to within about +/- 0.03 s^{-2} with extreme values near +/- 0.2 s^{-2} (Fig 4.19a,b). As with the core diameter change rates, the vertical vorticity rates of change near the surface (< 50 m AGL) are about half as large as those observed over the deeper layer (Fig. 4.19c,d).

4.1.5 Vertical Profiles

The vertical structure of the DOW observed tornadoes is viewed through a scatter plot of velocity difference across the core and elevation of the vortex center AGL that encompasses all DOW observations (Fig 4.20). Layer-averaged values are fit to the scatter plot (solid black line) along with one standard deviation above and below the

layer-averaged values (dashed lines). *This scatter plot shows the envelope of tornado intensity observations with a marked decrease in peak vortex strength above the near surface region. However, the profile for all DOW observations using time (and tornado) averaged values in 500 m layers (Fig. 4.20a), 100 m layers (Fig. 4.20b), 50 m layers (Fig. 4.20c), 20 m layers (Fig. 4.20d), and 10 m layers (Fig. 4.20e,f) shows relatively constant values with height even as close as 20 m AGL before the sample size decreases drastically.* Layer-averaged velocity difference values remain around 110 m s^{-1} in the lowest km with a relatively uniform standard deviation of about +/- 40 m s^{-1}. The negative correlation of intensity with height over a deep layer (10 km) is significant at any confidence level with an R value of -0.15, a z-value of -41.96 and a p-value of zero. The negative correlation with height decreases by about an order of magnitude (and becomes slightly positive in some cases) when examining layers within 1 km AGL.

Removing inter-tornado intensity differences by normalizing all velocity differences observed in each tornado relative to the maximum velocity difference for each particular tornado yields a time averaged vertical velocity profile for all tornadoes (Fig. 4.21). Again, a slight negative correlation between velocity difference and height AGL is apparent, especially when focusing on the lowest km AGL (Fig. 4.21b). The layer and time averaged velocity difference values generally reside around 0.7 times the peak velocity difference value with a standard deviation of about +/- 0.15. For the layers within the lowest 100 m AGL (Fig. 21e), no maximum in the time averaged velocity difference is apparent with values near 100 m AGL very similar to those at or below 30 m AGL.

This same relationship holds true for ground-relative velocities as a function of height AGL with an R value of -0.12, a z-value of -44.12 and a p-value of zero for values over the deepest 10 km layer (Fig. 4.22). The layer-averaged ground-relative velocity values reside around 65 m s^{-1} in the lowest km with a standard deviation of about +/- 25 m s^{-1}. Ground-relative velocities for each tornado are normalized relative to the maximum value observed for each tornado and the resulting vertical profile also exhibits a very weak negative correlation with increasing height AGL (Fig. 4.23). Again, the layer and time averaged ground-relative velocity values reside around 0.7 times the peak velocity value with a standard deviation of +/- 0.15 throughout the lowest km AGL. *Additionally, as with the normalized velocity differences, no maximum in the layer averaged velocity values is apparent within the lowest 100 m AGL (Fig. 4.23e).*

The correlation of velocity difference and core diameter while also statistically significant at any confidence level with an R value of -0.23, a z-value of -60.52 and a p-value of zero, exhibits a maximum intensity value (as measured by velocity difference) around a core diameter of 250 m for smaller tornadoes (Fig 4.24a,b). A second maximum in intensity is apparent around the 1000 m core diameter although not as strong as the maximum for the smaller tornadoes (Fig 4.24a,c). Additionally, the difference in magnitude between the outbound (positive) and inbound (negative) Doppler velocities appears to be very slightly skewed towards larger outbound velocities (Fig. 4.25a) that is attributed to the tendency to observe tornadoes moving away from rather than towards the radar (Fig. 4.25b). This relationship is also true for the subset of observations collected during times when the radar is stationary and deployed (Fig. 4.25c).

In estimating peak ground-relative velocities for DOW tornado intensities, the "peakness" of the Doppler velocity distribution in and near the tornado core has implications for the duration of the highest speeds that would be experienced in a Eulerian reference frame. In other words, does the average of several adjacent DOW data points (gates) closely match the maximum Doppler velocity value? Examining all DOW tornado scans below 500 m AGL within about two core radii of the refined center, and filtering the observations on cases with peak Doppler velocities greater than 40 m s^{-1}, it is possible to determine the number of data points (gates) that are below/above the $10^{th}/90^{th}$ percentile of velocity values. Additionally the relationship of the $10^{th}/90^{th}$ percentile to the maximum Doppler magnitude can then be compared with the number of observations (Fig. 4.26). The $10^{th}/90^{th}$ percentile tends to lie within about 10% of the peak Doppler velocity, especially for cases where very few data points (less than five) exist between the $10^{th}/90^{th}$ percentile and the peak value. Therefore, in most cases, averaging the value of several gates including the maximum value will produce a value within a few percent of the peak value which would correspond to about 2-5 m s^{-1} less than the peak value for extreme velocity values. It is extremely rare when the Doppler velocity values below/above $10^{th}/90^{th}$ percentile are not adjacent when the number of data points in these percentiles are less than about 10.

4.1.6 Horizontal Profiles

Using the 1-D cross-sections through each DOW tornado observation below 500 m AGL described in section 3.4.5, a composite of horizontal velocity profiles is constructed by placing all cross sections into a normalized space where the radius is

measured as the distance from the detected tornado center (0.0) with a value of 1.0 at the radius of maximum Doppler velocity. Additionally, the Doppler velocities are normalized with a value of 1.0 assigned to the maximum Doppler velocity magnitude in each scan (Fig. 4.27).

The result of this compositing shows a distinct upper-envelope to the velocity profile particularly outside the radius of maximum velocity. *The envelope shows velocities decreasing in a power-law profile where the velocity decreases to about half of the maximum value at about 3.0 core radii.* While the number of observations inside the radius of maximum winds is necessarily less and not as well resolved, the slope of velocity increase appears greater than the slope of the velocity decrease outside the core and even greater than that characterized by solid body rotation. The implication of this structure is discussed in sections 5.1.2 and 5.1.4.

Given the constrains of V(0.0) = 0.0, V(1.0) = 1.0, V(2.0) = 0.7 and V(3.0) = 0.5, a velocity profile can be fitted as:

$$V(r) = \frac{V_o}{R_o} r, \;\; r < R_o$$
$$V(r) = V_o \left(\frac{R_o}{r} \right)^{0.63}, \;\; r \geq R_o \qquad (4.1)$$

Outlying values above the main velocity envelope are attributed to secondary velocity maxima at larger radii that appear on occasion and are not addressed here.

4.2 Comparison with 88D Observations

It is of practical importance to evaluate the impact of vertical intensity differences on the detection of mesocyclonic features from the operational WSR-88D radar network

with much more limited observational coverage at low levels. To this end, 10 strong/violent tornadoes observed by the DOW(s) were selected from 1995-2004 to compare with velocity signatures and detection algorithms from the nearest WSR-88D (Table 4.1).

4.2.1 Comparison with 88D Algorithms

The WSR-88D Mesocyclone Detection Algorithm (MDA) (Stumpf et al. 1998) and Tornado Vortex Signature/Tornado Detection Algorithm (TVS/TDA) (Mitchell et al. 1998) output from the nearest 88D radar is matched with the closest DOW observation time (usually within a minute) and correlated with the algorithm output to compare velocity differences and shear (velocity difference over distance). The comparisons are made using the DOW observations and the TVS maximum velocity difference (Fig. 4.28a), TVS shear (Fig. 4.28b) and MDA shear (Fig. 4.28c) (Alexander and Wurman 2004).

Overall, the TVS shear and MDA shear provide little guidance in gauging the magnitude of the shear associated with the tornado produced by the parent mesocyclone. For a given TVS/MDA shear value, the DOW-observed shear value is shown to span almost two orders of magnitude (Fig. 4.28b,c). *The most significant correlation appears between the TVS maximum velocity difference and the DOW velocity difference (Fig. 4.28a) where the correlation appears linear with a slight increase in spread at larger values.* For the most extreme DOW velocity-difference values there appears to be about a 50% reduction in amplitude to the 88D value, although the sample size is quite small.

A dramatic example of this comparison is shown with the Spencer, SD supercell of 30 May 1998 where the observed Delta-V within 50 m AGL is nearly three times

higher than that observed in the lowest scan of the WSR-88D across the mesocyclone at about 900 m AGL. At the same elevation as the 88D, the DOW observes a Delta-V about twice as high as the 88D. This difference not only demonstrates the effect of increased range and decreased azimuthal sampling, but also the extreme variability of the tornado strength in the lowest kilometer.

An additional source of variability between the DOW and 88D observations results from large tornado intensity changes on small time scales when compared with the 88D update frequency of about five min. The time series for seven strong/violent DOW-observed tornadoes are shown comparing DOW Doppler velocity difference across the tornado for the lowest level observation of each volume when compared with the maximum, lowest-level and average TVS velocity difference from the corresponding 88D volume (Fig 4.29) (Alexander and Wurman 2004). Velocity difference increases are noted on the order of 60 m s^{-1} over a period of 60 s in Geary, OK on 29 May 2004 (Fig. 4.29g) with values near 50 m s^{-1} in 60 s for several other tornadoes while in similar rates of decrease seen in the Attica/Harper, KS tornado on 12 May 2004 (Fig. 4.29f).

Additionally, there are examples of strong DOW velocity differences in the absence of any TVS signature in Spencer, SD on 30 May 1998 (Fig. 4.29a), Mulhall, OK on 03 May 1999 (Fig. 4.29c), and Almena, KS on 03 June 1999 (Fig. 4.29d). In many of these cases, range-folding prohibited the 88D TVS algorithm from operating. It is also interesting to note that the TVS algorithm almost always begins reporting a TVS when the DOW velocity difference exceeds 40 m s^{-1} which is, by definition, the DOW tornado detection threshold described in section 3.4.1. DOW values less than 40 m s^{-1} in the time series are shown for reference but not reported by the DOW tornado detection algorithm.

4.2.2 Simulated Observations

To further examine the effect of increased range and decreased azimuthal sampling on tornado Doppler velocity signatures, a DOW3 Doppler velocity scan of a

violent tornado observed at 1.7 km range is resampled (Fig. 4.30a) using a Gaussian-beam weighted pattern with 1.0° beamwidth, 0.5° oversampling and 250 m range gates. The resampling uses only the velocity observations contained within the two dimensional quasi-horizontal scan and does not include effects from vertical gradients in the tornado velocity field. The simulated radar is first placed at the same 1.7 km range from the tornado center (Fig. 4.30a) followed by increasing the range to 10 km, 30 km, 60 km and 90 km (Fig. 4.30b). The simulated radar images are projected onto the same DOW polar observation grid, which results in some slight distortion as the simulated beamwidth grows large enough to encompass the entire near-field view from the DOW. Each resampling uses the original DOW field as the "truth" and a starting point.

The DOW-observed Doppler velocity difference is 206 m s^{-1} while the simulated radar at the same range reduces this velocity difference to 142 m s^{-1}, a 31% reduction. At progressively larger ranges the velocity difference is reduced to 111 m s^{-1}, 106 m s^{-1}, 103 m s^{-1} and 83 m s^{-1} which are 46%, 48%, 50% and 60% reductions. *Half of the amplitude reduction occurs within the first 10 km followed by another half at the range of 90 km which is a typical range of 88D velocity observations.* These reductions in amplitude are consistent with those observed between the DOW and the 88D observations in the previous section.

4.3 Tornado Evolution

4.3.1 Vortex Scale Contraction

The two modes of vortex scale contraction in Trapp and Davies-Jones (1997) and Figure 2.3 present two distinct methods of vortexgenesis as discussed in section 2.2.3. These two modes can be evaluated in the light of DOW observations where frequent pre-genesis observations through a relatively deep layer (> 2 km AGL) yield the evolution of axisymmetric vertical vorticity across the nascent vortex core. There were relatively few DOW tornado cases that contained sufficient pre-genesis observations through a deep-layer since the lack of any obvious vortex usually promoted a repositioning of the DOW or continued approach to a target storm that would reduce the depth of the observations.

Five tornadoes were observed prior to vortexgenesis and through a deep layer including Farmer, SD on 30 May 1998, Tarzan, TX on 1 May 1999, Thedford, NE on 4 June 1998, and Crowell, TX on 30 April 2000. The axisymmetric vertical vorticity values are gridded in time-height space (Fig. 4.31) and color coded by increasing intensity. *In all five cases the vortex horizontal-scale contraction and associated vertical development occur rapidly within a few volume scans, which span a few minutes at most. Additionally, the scale contraction appears to develop simultaneously through a deep layer of O(1-2 km) in all of the tornadoes (Alexander and Wurman 2005). This mode of scale contraction was observed by the Rapid-Scan DOW in a tornado near Jayton, TX on 12 June 2005 where the DOW was able to simultaneously observe the tornado contract at six different elevations (Wurman et al. 2008). The time-height vorticity cross sections*

also highlight an apparent lack of any vortex intensification above about 2 km AGL. Additional discussion of this finding is presented in section 5.1.5.

4.3.2 Angular Momentum Evolution

Expanding upon a study by Rasmussen and Straka (2007) to diagnose angular momentum budgets in a tornado cycle, this analysis is focused on the tornado scale itself where equation 2.8 for flux-divergence of axisymmetric angular momentum of section 2.3.4 is expanded:

$$\frac{\partial \overline{M}}{\partial t} + \overline{u}\frac{\partial \overline{M}}{\partial r} + \overline{M}\frac{\partial \overline{u}}{\partial r} + \overline{w}\frac{\partial \overline{M}}{\partial z} + \overline{M}\frac{\partial \overline{w}}{\partial z} = R \qquad (4.2)$$

where $\overline{M}$ is the axisymmetric angular momentum (product of axisymmetric tangential velocity and radius from the center of rotation), $\overline{u}$ and $\overline{w}$ are the axisymmetric radial and vertical components of the flow, and R is the residual of the terms. The particular focus of this analysis are the first three terms (including local change of angular momentum, horizontal advection of angular momentum and divergence of angular momentum) when looking at observations grouped over the lowest 500 m AGL layer.

The retrieval of axisymmetric fields in DOW observed tornadoes is motivated to evaluate the characteristics of horizontal distribution of angular momentum in the vicinity of developing, mature and/or dissipating weak and strong tornadoes. Six weak tornadoes and six strong/violent tornadoes are preferentially selected to compare the horizontal structure of axisymmetric radial and tangential velocity along with angular momentum. The six weak tornadoes were observed near Tulia, TX on 10 April 1997, Bridgeport, NE on 20 May 1998, Kremlin, OK on 21 April 1999, Tarzan, TX on 1 May 1999, Jericho, TX on 20 May 1999 and Pyote, TX on 26 May 1999. The six strong/violent tornadoes

were observed near Dimitt, TX on 02 June 1995, Kellerville, TX on 08 June 1995, Spencer, SD on 30 May 1998, Moore, OK on 03 May 1999, Mulhall, OK on 03 May 1999 and Almena, KS on 03 June 1999.

The retrieval technique discussed in section 3.4.6 is applied to these twelve tornadoes with axisymmetric radial profiles retrieved at the time of the first scan through the tornado, the time of the highest tangential velocity, and/or the time of the last scan through the tornado. Some of the stronger tornadoes are already in progress when DOW observations begin. All axisymmetric profiles are placed in normalized space where the radius is measured as the distance from the detected tornado center (0.0) with a value of 1.0 at the radius of maximum axisymmetric tangential velocity. Radial velocity values are normalized by the magnitude of the maximum axisymmetric radial velocity in each scan, and the angular momentum values are normalized by the value observed at the radius of maximum axisymmetric tangential velocity.

The weak tornado cases predominantly exhibit initial tangential velocity values that decay more rapidly outside the radius of maximum tangential velocities than those in stronger tornadoes (Fig. 4.32a). Additionally, the radial velocity profile appears predominantly divergent (outward radial wind increasing with radius) with increasing radial outflow away from the radius of maximum winds (Fig. 4.32b). The initial angular momentum values are evenly distributed with nearly an equal number of values greater than and less than those that have converged to the radius of maximum winds (Fig. 4.32c).

During the peak intensity of the weak tornadoes, the tangential velocities still appear to drop off more sharply in the decay region than those observed in stronger

tornadoes (Fig. 4.33a). In fact, very little difference is apparent in the overall structure of the tangential velocity field at the peak intensity. The radial velocity profile still appears mostly divergent with radial outflow (Fig. 4.33b). The implication is that angular momentum is not getting advected inward but rather away from the tornado core and is likely being reduced in magnitude by the divergent field. This is apparent in the reduction in overall angular momentum values apparent outside the radius of maximum winds (Fig. 4.33c).

For the stronger tornadoes at the initial observation time, a tangential velocity profile with a shallower radial rate of decay when compared with the weaker tornadoes at the initial observation time, and this profile is indicative of the peak tangential velocity structure seen in the cross-sections in section 4.3.1. (Fig. 4.34a). The key difference between these stronger profiles and the weaker profiles is the greater number of observations of radial inflow and horizontal convergence (Fig. 4.34b). Angular momentum values at larger radii (three to four) appear to asymptote towards about twice the value converged at the radius of maximum tangential velocity (Fig 4.34c) and overall appear higher than those observed with the weaker tornado cases.

At the peak intensity the strong tornadoes continue to exhibit the same tangential velocity profile (Fig. 4.35a) but the trend in the radial profile is one from weak inflow and convergence to almost no convergence or inflow on average (Fig. 4.35b). The angular momentum profile continues to show an excess of values at larger radii similar to that observed at the initial observation time (Fig. 4.35c) indicating an environment supportive of sustained rotation if the forcing for radial convergence can be maintained.

At the final observation time, the tangential velocity profile has become more poorly defined with scale-contraction reaching a point that very few profile values can be retrieved within the core radius (Fig. 4.36a). Additionally, a large majority of observations now show divergent radial outflow as opposed to convergent radial inflow at the earliest observation times (Fig. 4.36b). The angular momentum profiles show almost uniform values at large radii that are similar to or even slightly larger than the values seen at the time of peak intensity (Fig. 4.36c). Similar to the observations with the weak tornado case at maturity, there is significant angular momentum that could be converged with sufficient forcing but the radial flow is both advecting this angular momentum away from the core and likely removing angular momentum through divergence.

Consistent with the axisymmetric vertical vorticity distribution shown in section 4.1.3, almost all radial velocity values retrieved inside the tornado cores represent divergent radial outflow.

Chapter 5

Discussion and Conclusions

5.1 Discussion of Analysis Results

5.1.1 Tornado Intensity Distribution

Given the differences between the DOW and OneTor tornado intensity distributions it is reasonable to consider how well, or if, the DOW observations are randomly sampling the mesocyclonic tornado population. From a statistical perspective, the question is: Do the DOW and OneTor intensity reports represent different distributions where one is stochastically greater than the other?

To address this question we first examine the intensity distribution of all OneTor tornado reports in the same geographic region (Texas, Oklahoma, Kansas and Nebraska) and seasons (April-June 1995-2003) as the ROTATE field campaign that comprise most of the DOW tornado observations (Fig. 4.6a). A total of 2022 tornado reports were made over this region during these time periods. This distribution is normalized by the number of F0 reports (Fig. 4.6b) to highlight the exponential-decay shape of the distribution. The distribution of the 49 OneTor tornado reports for the DOW-observed tornadoes are constructed and normalized in the same manner (Fig. 4.7a,b). Three DOW-observed tornadoes, reported in OneTor, have been removed from this comparison since they occurred in South Dakota which is outside of the geographic region discussed here. The shape of both OneTor distributions are very similar with a slight increase in the number of stronger tornadoes for the DOW-observed cases.

For an objective comparison of the two observation distributions, the Mann–Whitney *U* test is executed to determine if the two sets of OneTor samples have statistically identical distributions indicative of sampling from the same overall tornado population. The Mann–Whitney *U* test is appropriate in this case since the storm report distributions do not appear to be normal, they are independent of both other storm reports and DOW observations, and the measurements are ordinal and can be ranked (Wilks 1995).

Execution of this U-test reveals a U value of 58391.5 with a corresponding z value of 2.14 and a two-tailed p-value of 0.032. This p-value represents the probability of achieving this observed difference assuming the distributions are really identical. This p-value is not statistically significant at the 0.001 or 0.01 confidence level, but is significant at the 0.05 level. Therefore, it is concluded that the difference between the two intensity distributions is not significant and the null hypothesis (samples are from the same distribution) is accepted. This result is consistent with the interpretation of the shapes of the two distributions in that there are a slightly greater number of strong tornadoes sampled by the DOW when compared with pure random sampling, but the overall sampling has very little bias and cannot account for the large difference between the DOW and OneTor tornado intensity distributions.

When comparing the DOW and OneTor tornado intensity distributions for these same 49 tornadoes, the U-test produces a U value of 2040.5, z value of 5.97 and a two-tailed p-value less than 2×10^{-6} which is significant at even the 0.001 confidence level. Therefore the DOW and OneTor intensity distributions appear significantly different and the null hypothesis (same sampling distributions) is rejected in favor of the alternative

hypothesis that the intensity distributions are different even though they are both derived from the same set of tornadoes.

The difference between the F-scale and EF-scale DOW intensity distributions are much less than the OneTor distribution. The primary difference between the F-scale and EF-scale distributions results from the fact that the EF-scale has a smaller dynamic range of velocities (higher low-end threshold, lower high-end threshold) and finer velocity bins which result in more tornadoes being collected at the high end of the intensity spectrum. It is noteworthy that the range of peak ground-relative velocity values more closely approximate the upper and lower bounds of the F-scale rather than the newer EF-scale although no attempt is made here to associate a degree of damage with any particular wind speed.

Given the lack of weak tornadoes in the DOW intensity distribution, is there a systematic bias in observations where weak tornadoes tend to be small and not well resolved at larger ranges? Based on the filtering of tornadoes to those only within 10 km or even 5 km, the distribution (Fig. 4.9c,d) is preserved and therefore there does not appear to be any significant range bias to the DOW tornado intensity observations.

Additional considerations for bias of the radar Doppler velocity observations with respect to "true" wind speeds must be considered. There are several factors that can cause a departure of Doppler velocity measurements from actual wind speeds. These factors include ground clutter contamination within a radar sample volume, weighting of Doppler velocity measurements towards larger scatters such as rain, hail and debris, under-resolved regions of strong velocity gradients in the horizontal and/or vertical, discontinuous sampling of the same region and very small time integration periods with

respect to the standard duration of wind gust measurements, namely 3 seconds. With the exception of the time integration period, all other factors result in Doppler velocity measurements that are underestimates of the peak wind gust in a radar sample volume and is really an average motion within the volume. Given a typical DOW sample volume size of 50 m by 50 m, the space-to-time conversion for any Doppler-velocity measurement on the order of 50 m s^{-1} results in an estimated duration of 1 s per data point. With several adjacent data points (radar volumes) typically containing similar Doppler velocity values (Fig 4.26), it can be inferred that the duration of these velocity values at a fixed point in space is very close to the standard definition of a wind gust duration.

Finally, it must be stressed that the DOW tornado intensity distribution is focused on tornadoes produced from mesocyclones in supercell thunderstorms. These mesocyclonic tornadoes may have a different intensity distribution than tornadoes produced from non-mesocyclonic forcing that are not the primary focus of the targeted DOW observations.

Given the distribution of reported tornado intensities for the DOW observed cases, a hypothesis for this discrepancy in supercell tornado intensity distributions is the overestimate of the number of weak tornadoes (F/EF 0-1) due to a lack of damage surveys (not all tornadoes are surveyed even though an intensity is estimated) and/or damage indicators resulting in a persistent low bias to intensity estimates of strong tornadoes (F/EF 2-3) (Doswell and Burgess 1988). Violent tornadoes (F/EF 4-5) may be infrequent enough and are usually well documented to permit an accurate characterization of the upper end of the intensity distribution.

For the 13 tornadoes in OneTor that were not observed by the DOW (Fig. 4.4c,d) nearly all of the reports were listed with no tornado duration (identical start and end times), a zero path length and no damage was noted. Furthermore, many of these storm reports were associated with high precipitation storms in low visibility conditions and/or after dark. In addition, for all these tornadoes, the DOW(s) were scanning the reported region at the reported time and no tornadoes were detected or identifiable in manual inspection of the data. Therefore, the basis for these reports is highly questionable with a probable high false alarm rate. Examples of mobile radar observations being used to validate and/or refute tornado reports have been performed by others including French et al. (2009).

When adding the non-reported but DOW detected tornadoes (Fig. 4.4c,d) to those both detected and reported (Fig. 4.4a,b) the expected value of a mesocyclonic tornado intensity is in the F2/EF2 range with almost 60% of these tornadoes classified as strong, 30% classified as weak, and about 10% violent (using the F-scale). Using the EF-scale these percentages are 55% strong, 20% weak and about 25% violent. An average of the two scales yields about 25% weak, 60% strong and 15% violent. These percentages are a significant departure from those reported by Grazulis (1993), Dotzek (2003) and Brooks (2004) and represent a shift towards a normal distribution of mesocyclone tornado intensities from an exponential or Weibull distribution.

Mesocyclonic tornadoes have a characteristic intensity and scale. A hypothesis for this characteristic state emerges from modeling, theoretical and observational studies of tornado-scale vorticies discussed in chapter 2 that have documented dynamical non-linearity involving multiple-scale interactions and feedback mechanisms for tornado

formation and sustenance. These multi-scale non-linearities and associated feedback mechanisms are commonly observed in self-organizing systems (Ashby 1947). The mesocyclonic tornado may be yet another example of a naturally occurring self-organizing system.

Examples of the feedback mechanisms are discussed in Gaudet and Cotton (2006) where their analysis of the non-DPE vortex describes a vortexgenesis process initially driven by a vertical buoyancy gradient near the surface that induces horizontal convergence via a pressure deficit at the developing vortex core. The convergence intensifies the vortex and initiates a negative feedback whereby additional vortex intensification results in a negative horizontal convergence tendency until a cyclostrophic state is attained with no horizontal convergence. Rasmussen and Straka (2007) analyze the evolution of a tornado cyclone where the near-surface intensity exceeds that of the intensity aloft which results in an axial downdraft from the adverse vertical pressure gradient that advects lower angular momentum values from aloft towards the surface.

The characteristic tornado scale of O(300 m) and intensity of O(60 m s^{-1}) derived from these DOW observations are in relative agreement with theoretical studies of tornado structure including Nolan (2005) and Fielder and Rotunno (1986) which predicted an O(500 m) vortex diameter and O(65 m s^{-1}) horizontal speed limits given various scaling assumptions about the local thermodynamic and kinematic environment.

5.1.2 Tornado Diameter and Divergence Distribution

The discrepancy between the Storm Report damage width distribution and the maximum DOW tornado width is misleading in that the largest DOW tornado cores are

most frequently observed during the genesis stage prior to vortex intensification and a corresponding scale-contraction. Therefore, the largest DOW tornado core is most likely to occur at the weakest stage when the tornado is least capable of producing damage that could be reported. In general, the reported maximum damage width is a function of the damage descriptor density rather than the peak tornado intensity (Brooks 2004).

Constraining the DOW tornado diameter to values associated with the DOW peak intensities is another method for comparison. However, it is shown that peak intensity and core diameter are poorly correlated. Additionally, there is no guarantee that the reported damage width is also coincident with the time of greatest intensity. Finally, the DOW tornado core-diameter is an underestimate for the width of damage potential produced by the vortex. For these reasons, it is very difficult to make any meaningful comparisons between the reported damage width and maximum DOW tornado width.

The smaller median value of the diameter of maximum axisymmetric vorticity (Table 3.2, Fig. 4.13a,d) when compared with the median diameter of the velocity difference implies that the vorticity distribution across the tornado core region is not uniform and the bulk vorticity value increases in a non-linear fashion from the center of the tornado with a maximum value slightly inside the radius of maximum tangential velocity. This profile would also explain the non-solid body tangential velocity profile inside the tornado core (Fig 4.27). This structure would be consistent with the conceptual and simulated tornado models where an annulus of higher vorticity is contained within the radius of maximum winds that surrounds a central downdraft in a two-cell vortex structure seen in many tornado model simulations and other observational studies discussed in chapter 2 (Rotunno 1977, 1979, 1984; Fiedler 1998; Lewellen et al. 1997,

2000). It is important to note that this median core radius value is many times the size of the typical data sample spacing and is well resolved. Along these same lines, the divergent bias observed for axisymmetric horizontal divergence is also indicative of a two-cell structure with a central downdraft and annular updraft.

Alternative interpretations for the divergent bias are that either the DOW observations are slightly biased towards the latter stages of the tornado lifecycle or the convergent inflow layer is extremely shallow and is largely unobserved. Bias in the radar sampling introduced from debris centrifuging is also considered, and this seems a likely cause for the divergent bias in intense, small tornadoes given the impact of filtering divergence calculations using an upper threshold from the estimation of centripetal acceleration (Figs. 4.14e,f, 4.15c). Work by Dowell et al. (2005) estimated the effect of radar scatterer centrifuging which can impose a divergent signature on radar Doppler velocity measurements in small intense vorticies. Typical values of this divergence, assuming small raindrops are the dominant scatter type (DOWs typically don't operate in regions with high densities of large debris sources), yield about 5 m s^{-1} of outward radial motion from the tornado center over a core diameter of about 200 m which implies about 0.1 s^{-1} of divergence. This magnitude is almost exactly the amount by which the larger population of divergence calculations is skewed toward divergence (Fig. 4.14b). This result would imply that the DOW observations of tornadoes actually exhibit an equal frequency of divergence and convergence.

5.1.3 Kinematic Distributions

The median core width (300 m) and inferred path length (7 km) of the DOW-

observed tornadoes do fall within the ranges inferred from damage surveys over the broader period between 1950-2001 as reported in Brooks 2004. DOW-observed median circulation (50000 m^2s^{-1}), angular momentum (9000 m^2s^{-1}), vertical vorticity (0.5 s^{-1}) and horizontal divergence O(0.05 s^{-1}) values are consistent with numerical simulations of tornado-scale structures and other observational studies including radar an in-situ data (Fujita 1965; Wicker and Wilhelmson 1995; Wurman et al. 2007b).

5.1.4 Horizontal and Vertical Profiles

For the more intense tornadoes, the fact that the velocity profile outside the core doesn't decrease more rapidly, as with the inverse of distance within an irrotational vortex, is indicative of horizontal diffusion and lateral mixing of angular momentum that reduces the horizontal velocity gradient (Kundu 1990) (Fig. 4.27). The fact that vortex intensity and size are, in general, not positively correlated is also not surprising given well-documented examples of relatively small violent tornadoes. There is a common misconception in the broader community of a strong positive correlation between tornado size and intensity, but this is simply not the case. If anything, the DOW-observed tornado size and intensity are negatively correlated and it is likely that the class of broader weaker tornadoes is not well captured in damage surveys. In general, large (> 1.0 km core diameter) and strong (velocity difference > 140 m s^{-1}) tornado observations are rather uncommon and generally reside more than one standard deviation above the average size-intensity profile (Fig. 4.24). Additionally, public misconception of relationships between tornado size and intensity are likely due to the fact that the pressure deficit, and thus the diameter of the visible condensation funnel, are a function of intensity. An important

note is some signal of scale separation with the strongest tornadoes clustering around 250 to 300 m in diameter with a secondary cluster of tornadoes near 1000 m in diameter with generally weaker intensity (Fig. 4.24a).

As discussed in section 4.1.5, there appears to be no clear dependence of tornado velocity with height and this has also been documented in a few 2 m in-situ tornado observations from the TIV when compared with low-level DOW Doppler velocity measurements in the same tornado (Wurman et al. 2007a). TIV wind speed measurements exceeded DOW low-level Doppler velocity measurements in a tornado sampled near LaGrange, WY on 05 June 2009 (Wurman 2010b). Therefore, no speed bias is apparent between DOW observations at O(100 m AGL) with those near 10 m AGL. The lack of an apparent level of maximum horizontal velocity contradicts numerical studies, which depict a level near 30 m AGL for maximum horizontal wind speeds, such as Lewellen et al. (1997, 2000) and Xia et al. (2003).

5.1.5 Scale Contraction

Given that all tornadoes sufficiently sampled by the DOWs during genesis appear to contract and intensify simultaneously through a deep column reflects the second mode described by Trapp and Davies-Jones (1997) that does not include the dynamic pipe effect (i.e. descending vortex development). In order for this process to take place, convergence must be taking place through the entire column at the same time with radial inflow into the developing vortex at many levels. This mode of vortex intensification and vertical development appears to be even more frequent than those observed by Trapp et al. (1999) where they identified about 48% of 52 TVS cases that appeared to be non-

descending. The disconnect between lack of mid-level mesocyclone intensification and tornadogenesis in the lowest kilometer reinforces the importance of focusing on low-level forcing mechanisms for tornadogenesis including tilting of horizontal vorticity by downdrafts and stretching of vertical vorticity by intense low-level updrafts as depicted in Rotunno and Klemp (1985) and Wicker and Wilhelmson (1995).

5.1.6 Angular Momentum Evolution

While angular momentum values supportive of intensification are present at larger radii in the weak tornado cases, there is an apparent lack of convergence and associated radial inflow needed to contract the angular momentum. This mode of failure could be characterized by the presence of broader low-level rotation that persists but does not converge. This mode of failure also appears to characterize the eventual dissipation of stronger tornadoes where a horizontally homogeneous environment of high angular momentum values is achieved but ultimately removed through outward horizontal advection and divergence of angular momentum. Any tornado-scale vortex brought into this environment is likely to be short lived with negative horizontal flux-convergence (and diffusion) quickly removing the isolated source of rotation. This evolution in angular momentum is described conceptually as "in-up" radial flow reversing to "down-out" and is consistent with the analysis presented by Rasmussen and Straka (2007). The residence time of a tornado in a "in-up" flow regime may be modulated by the balance (or imbalance) between the storm-scale inflow and outflow as described in Dowell and Bluestein (2002).

5.2 Conclusions

In summary, several major findings are made about mesocyclonic tornadoes based upon the large sample size of observations from the DOWs. While some of these findings are consistent with previous research conducted by others, many points are in contrast with the previous understanding of mesocyclonic tornadoes.

- Our sample of mesocyclonic tornadoes have a median peak ground-relative intensity near 60 m s^{-1} which is an F2/EF2 on the intensity scale
- Mesocyclonic tornadoes have a median horizontal scale near 300 m in core diameter
- Mesocyclonic tornadoes core diameter and peak intensity are generally negatively correlated
- A secondary maxima in core diameter appears near 1000 m associated with a generally weaker class of tornadoes
- Strong mesocyclonic tornadoes peak intensity weakens rapidly with height AGL
- Time-averaged mesocyclonic tornado intensity remains relatively constant with height in the lowest several hundred meters AGL
- Strong mesocyclonic tornadoes tangential velocity tends to reduce by about 50% at three core radii from the tornado center in a power-law profile
- Mesocyclonic tornadoes develop through simultaneous horizontal scale contraction over the lowest 1 km AGL
- Mid-level mesocyclone intensity is not correlated with tornadogenesis

- WSR-88D amplitude of Doppler velocity difference signatures are reduced in amplitude by about 50% from those observed at close range (~ 5km)
- Weaker mesocyclonic tornadoes have similar relative angular momentum values at larger radii than what are observed with stronger mesocyclonic tornadoes but a lack of radial inflow/convergence appears to be unable to contract the higher angular momentum values

The semi-automated processing of the DOW radar data in this work incorporated two new techniques for dealiasing of mobile radar data. These techniques included restoration of isolated gates in staggered PRT Doppler velocity data where Nyquist multiples of the velocity fields from the individual PRTs are evaluated as possible substitutes for the staggered PRT velocity in isolated gates where one of the two PRTs produced an inaccurate velocity estimate for the staggered PRT velocity value. Dealiasing of single PRT fields was partially automated using manual dealiasing of a reference scan or radar volume which is then used as a weak constraint for automated dealiasing of successive scans or volumes.

5.3 Future Work

Many additional years of tornado observations have been collected from 2003-2010 that will be added to the existing DOW tornado climatology to further increase the sample size of the statistics presented here and enhance the analysis of the DOW observations from what was possible with the first seven years of the observations.

In addition, the analysis can be expanded to examine the DOW radar reflectivity structures of tornadoes to determine relationships between maximum Doppler velocity and the edge of reflectivity disks and any minimum present at the tornado center. A comparison of reported damage widths and DOW core width can be extended to DOW damage potential width, visible width, and associated reflectivity structures similar to Atkins et al. (2010) and Wakimoto et al. (2010).

The DOW observations can also be partitioned into the various stages of tornado lifecycle to extract kinematic characteristics at different stages of tornado evolution with particular interest in the evolution of vortex tilt with height and convergent signatures at low-levels that are external to the tornado core. This partitioning can also highlight the kinematic and dynamic structure of the near-field environment at the point in time when a tornado is first detected for cases containing the start of the tornado lifecycle. Higher-order kinematic quantities can be computed including time-integrated areas associated with particular tornado intensity metrics such as analysis of the Spencer, SD tornado on 30 May 1998 (Wurman and Alexander 2005) and other related work from Dotzek et al. (2003). Asymmetries in tornado structure can be evaluated by comparing simultaneous single-Doppler observations of tornadoes in cases where more than one DOW was collecting data.

Tornadogenesis remains a very complex multi-scale problem with numerous theories of storm-scale sources of horizontal and vertical vorticity production and the eventual concentration of this vorticity to the tornado-scale. Modeling efforts to reproduce tornadogenesis have yet to explain the observed variability in tornado production (or lack of) from one supercell to another. The axisymmetric retrievals

discussed in section 4.3.2 can be extended to three-dimensions in cases where the temporal and spatial resolution of the DOW data permits accurate single-Doppler retrieval of vertical motion. This analysis can more fully examine angular momentum flux-divergence terms with a research focus on why vortex tightening (horizontal scale contraction and intensification) occurs at some times and not others.

While the large number of tornado observations available for construction of this climatology have provided insight into supercell tornado structures and dynamics additional tornado observations are still needed, particularly those focused on more rapid scanning of tornado-scale features. The analysis of time rates of change of various kinematic attributes in tornadoes and dynamic processes such the vertical development and horizontal scale contraction of tornadoes are limited by the O(60 s) sampling rate common to much of this DOW tornado dataset. Mobile radar observations with O(10 s) sampling rates would effectively provide an order of magnitude increase in temporal resolution which would more closely match the spatial resolution of these observations given the characteristic flow speed of tornadoes. In addition, large arrays of in-situ surface observations in and near tornadoes could compliment mobile radar observations and provide critical observations of wind and pressure in the poorly sampled near-surface layer.

References

Alexander, C., and J. Wurman, 2004: Comparison between DOW observed tornadoes and parent mesocyclones observed by WSR-88Ds. Proceedings, *22nd Conf. on Severe Local Storms*, Hyannis, MA, Amer. Meteor. Soc, 13.4.

——, and J. Wurman, 2005: The 30 May 1998 Spencer, South Dakota storm. Part 1: The structural evolution and environment of the supercell tornadoes. *Mon. Wea. Rev.*, **132**, 72-96.

——, and J. Wurman, 2006: Mobile radar based climatology of tornado structure and dynamics. Proceedings, *23rd Conf. on Severe Local Storms*, St. Louis, MO, Amer. Meteor. Soc.

——, and J. Wurman, 2007: Mobile radar based dynamic climatology of tornadoes. Proceedings, *33rd Int. Conf. on Radar Meteorology*, Cairns, Australia, Amer. Meteor. Soc.

——, and J. Wurman, 2008: Updated mobile radar climatology of supercell tornado structures and dynamics. Proceedings, *24th Conf. on Severe Local Storms*, Savannah, GA, Amer. Meteor. Soc., 19.4.

Ashby, W.R., 1947: Principles of the self-organizing dynamic system. *J. Gen. Psych.*, **37**, 125-128.

Atkins, N., R. M. Wakimoto, A. McGee, R. Ducharme, and J. Wurman, 2010: The LaGrange, WY tornado during VORTEX II. Part II: Photogrammetric analysis of the tornado combined with dual-Doppler radar data. Proceedings, *25th Conf. on Severe Local Storms*, Denver, CO, Amer. Meteor. Soc., 6.3.

Armijo, L., 1969: A theory for the determination of wind and precipitation velocities with Doppler radars. *J. Atmos. Sci.,* **26**, 570-573.

Bedard, A. J., Jr., and C. Ramzy, 1983: Surface meteorological observation in severe thunderstorms. Part I: Design details of TOTO. *J. Climate Appl. Meteor.*, **22**, 911-918.

Bluestein, H. B., 1983: Surface meteorological observation in severe thunderstorms. Part II: Field experiments with TOTO. *J. Climate Appl. Meteor.*, **22**, 919-930.

——, and A. L. Pazmany, 2000: Observations of tornadoes and other convective phenomena with a mobile, 3-mm wavelength, Doppler radar: The spring 1999 field experiment. *Bull. Amer. Meteor. Soc.,* **81,** 2939–2951.

——, and W. P. Unruh, 1989: Observation of the wind field in tornadoes, funnel clouds, and wall clouds with a portable Doppler radar. *Bull. Amer. Meteor. Soc.,* **70**,

1514-1525.

——, C. H. Weiss, and A. L. Pazmany, 2003a: Mobile Doppler radar observations of a tornado in a supercell near Bassett, Nebraska, on 5 June 1999. Part I: Tornadogenesis. *Mon. Wea. Rev.,* **131,** 2954-2967.

——, C. H. Weiss, and A. L. Pazmany, 2004: The vertical structure of a tornado near Happy, Texas on 5 May 2002: High-resolution, mobile, w-band, Doppler radar observations. *Mon. Wea. Rev.,* **132,** 2325-2337.

——, C.H. Weiss, M. M. French, E. M. Holthaus, R. L. Tanamachi, S. Frasier, and A. L. Pazmany, 2007: The structure of tornadoes near Attica, Kansas, on 12 May 2004: High-resolution, mobile, Doppler radar observations. *Mon. Wea. Rev.*, **135**, 475–506.

——, J. G. LaDue, H. Stein, D. Speheger, and W. P. Unruh, 1993: Doppler radar wind spectra of supercell tornadoes. *Mon. Wea. Rev.,* **121,** 2200–2221.

——, W. C. Lee, M. Bell, C. H. Weiss, and A. L. Pazmany, 2003b: Mobile Doppler radar observations of a tornado in a supercell near Bassett, Nebraska, on 5 June 1999. Part II: Tornado-vortex structure. *Mon. Wea. Rev.,* **131,** 2968-2984.

——, W. P. Unruh, D. C. Dowell, T. A. Hutchinson, T. M. Crawford, A. C. Wood, and H. Stein, 1997: Doppler analysis of the Northfield, Texas tornado of 25 May 1994. *Mon. Wea. Rev.,* **125,** 212-230.

——, 2009: The Formation and Early Evolution of the Greensburg, Kansas, Tornadic Supercell on 4 May 2007. *Wea. Forecasting*, **24**, 899–920.

Brandes, E. A., 1977: Flow in severe thunderstorms observed by dual-Doppler radar. *Mon. Wea. Rev.,* **105**, 113-120.

——, 1984: Vertical vorticity generation and mesocyclone sustenance in tornadic thunderstorms: The observational evidence. *Mon. Wea. Rev.,* **112,** 2253-2269.

Brooks, H. E., and C. A. Doswell III, 2001: Some aspects of the international climatology of tornadoes by damage classification. *Atmos. Res.*, **56**, 191-201.

——, ——, and M. P. Kay, 2003: Climatological estimates of local daily tornado probability. *Wea. Forecasting*, **18**, 626-640.

——, 2004: On the relationship of tornado path length and width to intensity. *Wea. Forecasting,* **19**, 310–319.

Burgess, D W., R. J. Donaldson Jr., and P. R. Desrochers, 1993: *The Tornado: Its Structure, Dynamics, Prediction, and Hazards, Geophys. Monogr.*, No 79,

Amer. Geophys. Union, 203-221.

——, M. A. Magsig, J. Wurman, D. C. Dowell, and Y. Richardson, 2002: Radar observations of the 3 May 1999 Oklahoma city tornado. *Wea. Forecasting,* **17,** 456-471.

Carbone, R. E., M. J. Carpenter, and C. D. Burghart, 1985: Doppler radar sampling limitation in convective storms. *J. Atmos. Oceanic Technol.,* **2,** 357–361.

Church, C. R., and J. T. Snow, 1985: Measurements of axial pressures in tornado-like vortices. *J. Atmos. Sci.*, **42**, 576-582.

——, ——, and E. M. Agee, 1977: Tornado vortex simulation at Purdue University. *Bull. Amer. Meteor. Soc.*, **58**, 900-908.

——, ——, G. L. Baker, and E. M. Agee, 1979: Characteristics of tornado-like vortices as a function of swirl ratio: A laboratory investigation. *J. Atmos. Sci.*, **36**, 1755–1776.

Concannon, P. R., H. E. Brooks, and C. A. Doswell III, 2000: Climatological risk of strong and violent tornadoes in the United States. *Preprints*, 2nd Symposium on Environmental Applications, Long Beach, California, American Meteorological Society, 212-219.

Davis-Jones, R. P., 1973: The dependence of core radius on swirl ratio in a tornado simulator. *J. Atmos. Sci.*, **30**, 1427-1430.

Doswell, C. A., III, and D. Burgess, 1988: On some issues of United States tornado climatology. *Mon. Wea. Rev.,* **116,** 495–501.

Dotzek, N., J. Grieser, and H. E. Brooks, 2003: Statistical modeling of tornado intensity distributions. *Atmos. Res.*, **67-68**, 163-187.

Dowell, D. C., and H. B. Bluestein, 1997: The Arcadia, Oklahoma storm of 17 May 1981: Analysis of a supercell during tornadogenesis. *Mon. Wea. Rev.,* **125,** 2562-2582.

——, and ——, 2002a: McLean, Texas storm. Part I: Observations of cyclic tornadogenesis. *Mon. Wea. Rev.,* **130,** 2626-2648.

——, and ——, 2002b: McLean, Texas storm. Part II: Cyclic tornado formation, maintenance, and dissipation. *Mon. Wea. Rev.,* **130,** 2649-2670.

——, C. Alexander, J. Wurman, and L. Wicker, 2005: Centrifuging of scatterers in tornadoes. *Mon. Wea. Rev.*, **133***,* 1501-1524.

Feuerstein, B., N. Dotzek, and J. Grieser, 2005: Assessing a tornado climatology from global tornado intensity distributions. *J. Climate*, **18**, 585-596.

Fiedler, B. H., and R. Rotunno, 1986: A theory for the maximum windspeeds in tornado-like vortices. *J. Atmos. Sci.*, **43**, 2328–2340.

——, 1998: Wind-speed limits in numerically simulated tornadoes with suction vortices. *Quart. J. Roy. Meteor. Soc.*, **123**, 2377–2392.

Forbes, G. S., 1976: Photogrammetric characteristics of the Parker tornado of April 3, 1974. *Proc. Symp. On Tornadoes*, Lubbock, TX, Texas Tech University, 58-77.

French, M. M., H. B. Bluestein, D. C. Dowell, L. J. Wicker, M. R. Kramar, A. L. Pazmany, 2008: High-resolution, mobile Doppler radar observations of cyclic mesocyclogenesis in a supercell. *Mon. Wea. Rev.*, **136**, 4997–5016.

——, ——, L. J. Wicker, D. C. Dowell, and M. R. Kramar, 2009: An example of the use of mobile, Doppler radar data for tornado verification. *Wea. Forecasting*, **24**, 884–891.

Fujita, T. T., 1965: Formation and steering mechanisms of tornado cyclones and associated hook echoes. *Mon. Wea. Rev.*, **93**, 67-78.

——, D. L. Bradbury, and C. F. Van Thullenar, 1970: Palm Sunday tornadoes of April 11, 1965. *Mon. Wea. Rev.*, **98**, 29-69.

——, 1971: Proposed characterization of tornadoes and hurricanes by area and intensity. SMRP Research Rep. 91, University of Chicago, 15 pp.

——, 1973: Experimental classification of tornadoes in FPP scale. SMRP Research Rep. 98, University of Chicago, 15 pp.

——, 1975: New evidence from April 3-4, 1974 tornadoes. Preprints, *Ninth Conf. on Severe Local Storms*, Norman, OK, Amer. Meteor. Soc., 248-254.

——, 1992: *Mystery of Severe Storms.* The University of Chicago Press, 298 pp.

Gal-Chen, T., 1978: A method for the initialization of the anelastic equations: Implications for matching models with observations. *Mon. Wea. Rev.*, **106**, 587–606.

——, 1982: Errors in fixed and moving frame of references: Applications for conventional and Doppler radar analysis. *J. Atmos. Sci.,* **39**, 2279-2300.

——, and J. C. Wyngaard, 1982: Effects of volume averaging on the line spectra of vertical velocity from multiple-Doppler radar observations. *J. Appl. Meteor.,* **21,**

1881–1890.

Gao, J., M. Xue, A. Shapiro, Q. Xu, and K. K. Droegemeier, 2001: Three-dimensional simple adjoint velocity retrievals from single-Doppler radar. *J. Atmos. Oceanic Technol.,* **18,** 26-38.

Gaudet, B. J., and W. R. Cotton, 2006: Low-level mesocyclonic concentration by nonaxisymmetric transport. Part I: Supercell and mesocyclone evolution. *J. Atmos. Sci.*, **63**, 1113–1133.

Glenday, C., 2005: *Guinness Book of World Records 2007*. Guiness Ltd., 288 pp.

Golden, J. H. and D. Purcell, 1977: Photogrammetric velocities for the Great Bend, Kansas tornado of 30 August 1974: Accelerations and asymmetries. *Mon. Wea. Rev.,* **105,** 485-492.

——, and ——, 1978: Airflow characteristics around the Union City tornado. *Mon. Wea. Rev.,* **106,** 22-28.

Grasso, L. D. and W. R. Cotton, 1995: Numerical simulations of a tornado vortex. *J. Atmos. Sci.*, **52**, 1192-1203.

Grazulis, T.P., 1984: Violent tornado climatography, 1880-1982. Rep. NUREG/CR-3670 prepared for the U.S. Nuclear Regulatory Commission, Washington, DC p. A-38.

——, 1993: *Significant Tornadoes, 1680-1991.* Environmental Films, St. Johnsbury, VT, 1326 pp.

——, J. T. Schaefer, and R. F. Abbey Jr., 1993: Advances in tornado climatology, hazards, and risk assessment since Tornado Symposium II. *The Tornado: Its Structure, Dynamics, Prediction, and Hazards, Geophys. Monogr.,* No. 79, Amer. Geophys. Union, 409–426.

Hane, C.E., and B.C. Scott, 1978: Temperature and pressure perturbations within convective clouds derived from detailed air motion information: Preliminary testing. *Mon. Wea. Rev.*, **106**, 654–661.

Heymsfield, G. M., 1976: Statistical objective analysis of dual-Doppler radar data from a tornadic storm. *J. Appl. Meteor.,* **15**, 59-67.

Hoecker, W. H., 1960: Wind speed and air flow patterns in the Dallas tornado of April 2, 1957. *Mon. Wea. Rev.,* **88,** 167-180.

Kelly, D. L., J. T. Schaefer, R. P. McNulty, C. A. Doswell III and R. F. Abbey, Jr., 1978: An augmented tornado climatology. *Mon. Wea. Rev.* **106**, 1172-1183.

Klemp, J. and R. Rotunno, 1983: A study of the tornadic region within a supercell thunderstorm. *J. Atmos. Sci.*, **40**, 359-377.

Kosiba, Karen, Joshua Wurman, 2010: The Three-dimensional axisymmetric wind field structure of the Spencer, South Dakota, 1998 tornado. *J. Atmos. Sci.*, **67**, 3074–3083.

Kundu, P. J., 1990: *Fluid Mechanics*. Academic Press, 638 pp.

Lazarus, S. T., A. Shapiro, and K. Droegemeier, 1999: Analysis of the Gal-Chen-Zhang single-Doppler velocity retrieval. *J. Atmos. Oceanic Technol.,* **16**, 5-18.

Lee, W. C., and F. D. Marks Jr., 2000: Tropical cyclone kinematic structure retrieved from single-Doppler radar observations. Part II: The GBVTD-simplex center finding algorithm. *Mon. Wea. Rev.,* **128**, 1925-1936.

——, ——, R. E. Carbone, 1994a: Velocity track display – a technique to extract real-time tropical cyclone circulations using a single airborne Doppler radar. *J. Atmos. Oceanic Technol.,* **11,** 337-356.

——, B. J. Jou, P. L. Chang, S. M. Deng, 1999: Tropical cyclone kinematic structures retrieved from single-Doppler radar observations. Part I: Interpretation of Doppler velocity patterns and the GBVTD technique. *Mon. Wea. Rev.,* **127**, 2419-2439.

——, P. Dodge, F. D. Marks Jr., and P. H. Hildebrand, 1994b: Notes and correspondence mapping of airborne doppler radar data. *J. Atmos. Oceanic Technol.,* **11**, 572-578.

——, and J. Wurman, 2005: Diagnosed three-dimensional axisymmetric structure of the Mulhall tornado on 3 May 1999. *J. Atmos. Sci.*, **62**, 2373–2393.

Lemon, L. R., and C. A. Doswell III, 1979: Severe thunderstorm evolution and mesocyclone structure as related to tornadogenesis. *Mon. Wea. Rev.,* **107,** 1184-1197.

Lewellen, W. S., D. C. Lewellen, and R. I. Sykes, 1997: Large-eddy simulation of a tornado's interaction with the surface. *J. Atmos. Sci.,* **54,** 581–605.

Lewellen, D.C., W.S. Lewellen, and J. Xia, 2000: The influence of a local swirl ratio on tornado intensification near the surface. *J. Atmos. Sci.*, **57**, 527–544.

——, and ——, 2007a: Near-surface intensification of tornado vortices. *J. Atmos. Sci.*, **64**, 2176–2194.

——, and ——, 2007b: Near-surface vortex intensification through corner flow collapse. *J. Atmos. Sci.*, **64**, 2195–2209.

Marshall, T. P., 1992: Lessons learned from analyzing tornado damage. The Tornado: Its Structure, Dynamics, Prediction, and Hazards, Geophys. Monogr., No. 79, Amer. Geophys. Union, 495–499.

——, 2002: Tornado Damage Survey at Moore, Oklahoma. *Wea. Forecasting*, **17**, 582–598.

——, 2004: The enhanced Fujita (EF) scale. Preprints, *22d Conf. on Severe Local Storms*, Hyannis, MA, Amer. Meteor. Soc., CD-ROM, 3B.2.

Marquis, J., Y. Richardson, J. Wurman and P. Markowski, 2008: Single- and Dual-Doppler Analysis of a Tornadic Vortex and Surrounding Storm-Scale Flow in the Crowell, Texas, Supercell of 30 April 2000. *Mon. Wea. Rev.,* **136**, 5017-5043.

McDonald, J. R., and T. P. Marshall, 1984: Tornado damage documentation. Institute for Disaster Research Publ. 1984-20, Texas Tech University, 27 pp.

Mitchell, E. D., S. V. Vasiloff, G. J. Stumpf, A. Witt, M. D. Eilts, J. T. Johnson, and K. W. Thomas, 1998: The National Severe Storms Laboratory Tornado Detection Algorithm. *Wea Forecasting*, **13**, 352-366.

Moncrieff, M.W., and M.J. Miller, 1976: The dynamics and simulation of tropical cumulonimbus and squall lines. *Quart. J. Roy. Meteor. Soc.*, **102**, 373–394.

Nolan D. S., and B. F. Farrell, 1999: The structure and dynamics of tornado-like vortices. *J. Atmos. Sci.*, **56**, 2908–2936.

——, 2005: A new scaling for tornado-like vortices. *J. Atmos. Sci.*, **62**, 2639–2645.

Rasmussen, E. N., J. M. Straka, R. Davis-Jones, C. A. Doswell, F. H. Carr, M. D. Eilts, and D. R. MacGorman, 1994: Verification of the origins of rotation in tornadoes experiment: VORTEX. *Bull. Amer. Meteor. Soc.*, **75**, 995-1006.

——, and J. M. Straka, 2007: Evolution of low-level angular momentum in the 2 June 1995 Dimmitt, Texas, tornado cyclone. *J. Atmos. Sci.*, **64**, 1365–1378.

——, and D.O. Blanchard, 1998: A baseline climatology of sounding-derived supercell and tornado forecast parameters. *Wea. Forecasting*, **13**, 1148–1164.

Rotunno, R., 1977: Numerical simulation of a laboratory vortex. *J. Atmos. Sci.,* **34,** 1942–1956.

——, 1979: A study in tornado-like vortex dynamics. *J. Atmos. Sci.,* **36,** 140–155.

——, 1984: An investigation of a three-dimensional asymmetric vortex. *J. Atmos. Sci.,* **41,** 283–298.

——, and J. Klemp, 1985: On the rotation and propagation of simulated supercell thunderstorms. *J. Atmos. Sci.*, **42**, 271-292.

Samaras, T., 2004: Pressure Measurements in a Strong Tornado, Preprints, 22nd Severe Local Storms Conference, American Meteorological Society.

Schaefer, J. T., and R. Edwards, 1999, The SPC tornado/severe thunderstorm database. Preprints, *11th Conf. on Applied Climatology*, Dallas, TX, Amer. Meteor. Soc., 603-606.

——, and J. G. Galway, 1982: Population biases in the tornado climatology. *Preprints 12th Conf. on Severe Local Storms*, San Antonio, Amer. Meteor. Soc., 51-54.

Shapiro, A., S. Ellis, and J. Shaw, 1995: Single-Doppler velocity retrievals with Phoenix II data: Clear air and microburst wind retrievals in the planetary boundary layer. *J. Atmos. Sci.,* **52**, 1265-1287.

——, P. Robinson, J. Wurman, and J. Gao, 2003: Single-Doppler retrieval with rapid-scan radar data. *J. Atmos. Oceanic Technol.,* **20,** 1758-1775.

Snow, J. T. and R. L. Pauley, 1984: On the thermodynamic method for estimating maximum tornado windspeeds. *J. Climate Appl. Meteor.*, **23**, 1465-1468.

Stumpf, G. J., A. Witt, E. D. Mitchell, P. L. Spencer, J. T. Johnson, M. D. Eilts, K. W. Thomas, and D. W. Burgess, 1998: The National Severe Storms Laboratory Mesocyclone Dectection Algorithm for the WSR-88D. *Wea Forecasting*, **13**, 304-326.

Sun, J. and A. Cook, 1994: Wind and thermodynamic retrieval from single-Doppler measurements of a gust front observed during Phoenix II. *Mon. Wea. Rev.,* **1075**, 1075-1091.

Tanamachi, R. L., H. B. Bluestein, W. C. Lee, M. Bell, and A. Pazmany, 2007: Ground based velocity track display (GBVTD) analysis of w-band Doppler radar data in a tornado near Stockton, Kansas, on 15 May 1999. *Mon. Wea. Rev.*, **135**, 783–800.

Thom, H. C. S., 1963: Tornado probabilities. *Mon. Wea. Rev.,* **91,** 730–736.

Trapp, R. J., and B. H. Fiedler, 1995: Tornado-like vortexgenesis in a simplified numerical model. *J. Atmos. Sci.*, **52**, 3757-3778.

——, and R. P. Davies-Jones, 1997: Tornadogenesis with and without a dynamic pipe

effect. *J. Atmos. Sci.*, **54**, 113–133.

——, E. D. Mitchell, G. A. Tipton, D. W. Effertz, A. I. Watson, D. L. Andra, M. A. Magsig, 1999: Descending and nondescending tornadic vortex signatures detected by WSR-88Ds. *Wea. Forecasting*, **14**, 625–639.

Wakimoto, R. M., and N. T. Atkins, 1996: Observations on the origins of rotation: The Newcastle tornado during VORTEX 94. *Mon. Wea. Rev.,* **124,** 384-407.

——, W. C. Lee, H. B. Bluestein, C. H. Liu, and P. H. Hildebrand, 1996: ELDORA Observations during VORTEX 95. *Bull. Amer. Meteor. Soc.*, **77**, 1465-1481.

——, N. T. Atkins, and J. Wurman, 2010: The LaGrange tornado during VORTEX2. Part I: Photogrammetry analysis of the tornado combined with single-Doppler radar data. *25th Conf. on Severe Local Storms*, Denver, CO, Amer. Meteor. Soc., 6.2.

Walko, R. 1993: Tornado spin-up beneath a convective cell: required basic structure of the near-field boundary layer winds. *The Tornado: Its Structure, Dynamics, Prediction, and Hazards, Geophys. Monogr.*, No 79, Amer. Geophys. Union, 89-95.

Ward, N. B., 1972: The exploration of certain features of tornado dynamics using a laboratory model. *J. Atmos. Sci.*, **29**, 1194–1204.

Wilks, D. S., 1995: *Statistical Methods in the Atmospheric Sciences*. Academic Press, 467 pp.

Wicker, L. J., and R. B. Wilhelmson, 1995: Simulation and analysis of tornado development and decay within a three-dimensional supercell thunderstorm. *J. Atmos. Sci.*, **52**, 2675-2703.

Wood, V. T., and R. A. Brown, 1997: Effects of radar sampling on single-Doppler velocity signatures of mesocyclones and tornadoes. *Wea. Forecasting,* **12,** 928–938.

Wurman, J., 1999: Preliminary results from the Radar Observations of Tornadoes and Thunderstorm Experiment (ROTATE-98/99). Preprints, *29th Conf. on Radar Meteorology,* Montreal, QC, Canada, Amer. Meteor. Soc., 613–616.

——, 2001: The DOW mobile multiple-Doppler network. Preprints, *30th Conf. on Radar Meteorology*, Munich, Germany, Amer. Meteor. Soc., 95–97.

——, and M. Randall, 2001: An inexpensive, mobile, rapid-scan radar. Preprints, *30th Conf. on Radar Meteorology*, Munich, Germany, Amer. Meteor. Soc., 98–100.

——, 2002: The multiple-vortex structure of a tornado. *Wea. Forecasting,* **17,** 473–505.

——, 2003: Preliminary results from the Rapid-DOW, a multi-beam inexpensive alternative to phased arrays. Preprints, *31st Conf. on Radar Meteorology,* Seattle, WA, Amer. Meteor. Soc.

——, and C. Alexander, 2005: The 30 May 1998 Spencer, South Dakota storm. Part 2: Comparison of observed damage and radar-calculated winds in the supercell tornadoes. *Mon. Wea. Rev.*, **132**, 97-119.

——, C. Alexander, P. Robinson, and Y. Richardson, 2007a: Low-level winds and potential catastrophic impacts of tornadoes in urban areas. *Bull. Amer. Meteor. Soc.*, **88**, 31-46.

——, and S. Gill, 2000: Finescale radar observations of the Dimmitt, Texas (2 June 1995), tornado. *Mon. Wea. Rev.,* **128,** 2135–2164.

——, and M. Randall, 2001: An inexpensive, mobile, rapid-scan radar. Preprints, *30th Conf. on Radar Meteorology,* Munich, Germany, Amer. Meteor. Soc., 98–100.

——, and T. Samaras, 2004: Comparison of in-situ pressure and radar velocity measurements in a tornado, Preprints 22nd Severe Local Storms Conference, American Meteorological Society.

——, J. M. Straka, and E. N. Rasmussen, 1996: Fine-scale Doppler radar observations of tornadoes. *Science,* **272**, 1774–1777.

——, ——, ——, M. Randall, and A. Zahrai, 1997: Design and deployment of a portable, pencil-beam, pulsed, 3-cm Doppler radar. *J. Atmos. Oceanic Technol.,* **14,** 1502–1512.

——, Y. Richardson, C. Alexander, S. Weygandt, and P.-F. Zhang, 2007b: Dual Doppler and single-Doppler analysis of a tornadic storm undergoing mergers and repeated tornadogenesis. *Mon. Wea. Rev*., **135**, 736-758.

——, ——, ——, ——, and ——, 2007c: Dual-Doppler analysis of winds and vorticity budget terms near a tornado. *Mon. Wea. Rev*., **135**, 2392-2405.

——, W.C. Lee, C. R. Alexander, and K. A Kosiba, 2008: Rapid-Scan Mobile Radar 3D GBVTD and traditional analysis of tornadogenesis. Proceedings, *24th Conf. on Severe Local Storms*, Savannah, GA, Amer. Meteor. Soc.

——, K. Kosiba, P. Markowski, Y. Richardson, D. Dowell, and P. Robinson, 2010a: Fine-scale single- and dual-Doppler analysis of tornado intensification, maintenance, and dissipation in the Orleans, Nebraska, supercell. *Mon. Wea. Rev*., (in press).

——, ——, and P. Robinson, 2010b: In situ and radar observations of low-level winds in

tornadoes. Proceedings, *25th Conf. on Severe Local Storms*, Denver, CO, Amer. Meteor. Soc., P10.6.

Xia, J., W.S. Lewellen, D C. Lewellen, 2003: Influence of mach number on tornado corner flow dynamics.

Zhang, J. and T. Gal-Chen, 1996: Single-Doppler wind retrieval in the moving frame of reference. *J. Atmos. Sci.,* **53**, 2609-2623.

Zrnic, D. S. and R. J. Doviak, 1977: Probing tornadoes with a pulse-Doppler radar. *Quart. J. Roy. Meteor. Soc.*, **103**, 707-720.

——, and M. Istok, 1980: Wind speeds in two tornadic storms and a tornado, deduced from Doppler spectra. *J. Appl. Meteor.*, **19**, 1405-1415.

——, D. W. Burgess, and L. Hennington, 1985: Doppler spectra and estimated windspeed of a violent tornado. . *J. Climate Appl. Meteor.*, **24**, 1068-1081.

Table 1.1 Characteristics of the Doppler On Wheels (DOWs) mobile radar systems when scanning in convection during VORTEX and ROTATE (Wurman et al. 1997). Each radar maintained the same hardware configuration throughout the entire climatology except where noted in the table.

Characteristic	DOW1	DOW2	DOW3
Wavelength (cm)	3.2	3.2	3.2
Peak Power (kW)	50	250	250
Average Power (W)	40	200	200
3-dB Beamwidth (deg)	1.22 (1995) 0.93 (1996)	0.93	0.93
Rotation Rate (deg s^{-1})	40	40	40
Number of Samples	24-32	24-32	24-32
Pulse Repetition Frequency (Hz)	1000	2000	2000-4000
Staggered Pulse Repetition Frequency	No	After 1998	After 1998
Min Pulse Length (m)	75	25	12.5
Min Gate Length (m)	75	12.5	12.5

Table 1.2. History of DOW radar sampling characteristics including maximum unambiguous velocity and minimum attainable 3-dB sample volume dimensions in azimuth, elevation and range for features at three distances from the radars.

Year	Radar	Maximum Nyquist (m s^{-1})	Minimum Sample Volume Dimensions (m X m X m)		
			@ 1 km	@ 10 km	@ 30 km
1995	DOW1	16	21 X 21 X 75	213 X 213 X 75	639 X 639 X 75
1996	DOW1	16	16 X 16 X 75	162 X 162 X 75	487 X 487 X 75
1997	DOW2, DOW3	32	16 X 16 X 12.5	162 X 162 X 12.5	487 X 487 X 12.5
1998	DOW2, DOW3	32	16 X 16 X 12.5	162 X 162 X 12.5	487 X 487 X 12.5
1999	DOW2, DOW3	128	16 X 16 X 12.5	162 X 162 X 12.5	487 X 487 X 12.5
2000	DOW2, DOW3	128	16 X 16 X 12.5	162 X 162 X 12.5	487 X 487 X 12.5
2001	DOW2, DOW3	128	16 X 16 X 12.5	162 X 162 X 12.5	487 X 487 X 12.5
2003	DOW2, DOW3	128	16 X 16 X 12.5	162 X 162 X 12.5	487 X 487 X 12.5

Table 1.3. History of DOW radar typical data collection strategies including temporal updates and distance between nearest data points in azimuth, elevation and range for features at three distances from the radars.

Year	Radar	Typical Update Period (s)	Typical Data Spacing (m X m X m)		
			@ 1 km	@ 10 km	@ 30 km
1995	DOW1	60	21 X 17 X 75	213 X 175 X 75	639 X 524 X 150
1996	DOW1	60	16 X 17 X 75	162 X 175 X 75	487 X 524 X 150
1997	DOW2, DOW3	60	8 X 17 X 12.5	84 X 175 X 75	251 X 524 X 250
1998	DOW2, DOW3	60	8 X 17 X 12.5	84 X 175 X 75	251 X 524 X 250
1999	DOW2, DOW3	60	8 X 17 X 12.5	84 X 175 X 75	251 X 524 X 250
2000	DOW2, DOW3	60	8 X 17 X 12.5	84 X 175 X 75	251 X 524 X 250
2001	DOW2, DOW3	60	8 X 17 X 12.5	84 X 175 X 75	251 X 524 X 250
2003	DOW2, DOW3	60	8 X 17 X 12.5	84 X 175 X 75	251 X 524 X 250

Table 2.1. Fujita Scale used for estimating tornado intensity, defined as the fastest quarter-mile of wind at 10 m AGL, and based upon observed damage to structures.

F-Scale	Minimum Speed (m s^{-1})	Maximum Speed (m s^{-1})
0	17.8	32.6
1	32.7	50.3
2	50.4	70.3
3	70.4	91.9
4	92.0	116.6
5	116.7	142.5

Table 2.2. Enhanced Fujita Scale used for estimating tornado intensity, defined as the fastest three-second gust at 10 m AGL, and based upon maximum degree of damage to one or more damage indicators.

EF-Scale	Minimum Speed (m s^{-1})	Maximum Speed (m s^{-1})
0	29.1	38.0
1	38.4	49.1
2	49.6	60.4
3	60.8	73.8
4	74.2	89.4
5	> 89.4	None

Table 3.1. Order of magnitude estimates for variables relevant to ground-relative coordinate transformation.

Variable	Order of Magnitude
r	O(10 km)
θ_a	Highly Variable
ϕ_a	O(10°)
H error mobile/deployed	O(0.1°)/O(1°)
P error mobile/deployed	O(1°)/O(0.1°)
R error mobile/deployed	O(1°)/O(0.1°)
x error mobile/deployed	O(10m)/O(100 m)
y error mobile/deployed	O(10m)/O(100 m)
z error mobile/deployed	O(100 m)/O(10 m)
V_{DOW} error	O(1 m s^{-1})
φ error	O(0.1°)
V_{dg} error	O(1 m s^{-1})

Table 3.2. Kinematic quantities computed from the Doppler velocity observation patches.

Variable	Formula	Source
Ground-Relative Velocity	$V_{max}=V_{corr}+C\sin(\beta-\theta)$	Patch
Velocity Difference	$V_{diff}=V_{out}-V_{in}$	Patch
Velocity Asymmetry	$V_{asym}=\lvert V_{out}\rvert-\lvert V_{in}\rvert$	Patch
Average Velocity	$V_{av}=(\lvert V_{out}\rvert+\lvert V_{in}\rvert)/2$	Patch
Diameter (or Radius if in or out = center)	$D_{iam}=[d^2_{in}+d^2_{out}-2d_{in}d_{out}(\cos\phi_{in}\cos\phi_{out}\cos(\theta_{in}-\theta_{out})+\sin\phi_{in}\sin\phi_{out})]^{0.5}$	Patch
Average Radius	$R_{av}=(R_{out}+R_{in})/2$	Patch
Diameter of Maximum Vorticity	D_{iam} where $\mathrm{Max}[(2V_{diff}/D_{iam})*\sin(\alpha-\theta_c)]$	Patch
Bulk Vertical Vorticity	$\zeta_{bulk}=2(V_{diff}/D_{iam})*\sin(\alpha-\theta_c)$	Patch
Bulk Horizontal Divergence	$\delta_{bulk}=2(V_{diff}/D_{iam})*\cos(\alpha-\theta_c)$	Patch
Bulk Angular Momentum	$\Gamma_{bulk}=V_{av}R_{av}$	Patch
Circulation	$C=(\pi/2)*V_{diff}/D_{iam}$	Patch
Centripetal Acceleration	$F_a=V_{av}^2/R_{av}$	Patch

Table 4.1. List of strong or violent DOW-observed tornado cases including the available WSR-88D level II or III data. All radar data is classified by the height above ground level of the lowest beam in the tornado or parent mesocyclone. The * indicates ground-based Doppler velocity estimates of the tornado intensity where the official damage survey is either unavailable or indicates a weaker intensity due to a lack of damage descriptors.

Date	Location	F-Scale(s)	Radar Lowest Elevation			
			< 0.5 km	< 1 km	< 2 km	< 4 km
2 Jun 1995	Dimmitt, TX	F3*	DOW1		KLBB	
8 Jun 1995	Kellerville, TX	F4	DOW1		KAMA	KFDR
30 May 1998	Spencer, SD	F4	DOW3	KFSD		KABR
3 May 1999	Oklahoma City, OK	F5	DOW3, KTLX			KINX
3 May 1999	Mulhall, OK	F4	DOW3		KTLX	KICT, KINX
3 Jun 1999	Almena, KS	F3	DOW3		KUDX	KGLD
9 May 2003	Oklahoma City, OK	F3	DOW3, KTLX			KFDR, KINX, KVNX
15 May 2004	Stratford, TX	F3*	DOW3			KAMA
12 May 2004	Harper, KS	F4	DOW3	KICT, KVNX		KDDC
29 May 2004	Geary, OK	F3*	DOW3		KTLX, KVNX	KFDR

Figure 1.1. The WSR-88D radar network across the ROTATE domain of operations approximating regions of 88D radar coverage below 0.5 km AGL within green circles, below 1 km AGL within yellow circles and below 2 km AGL within the outermost red circles.

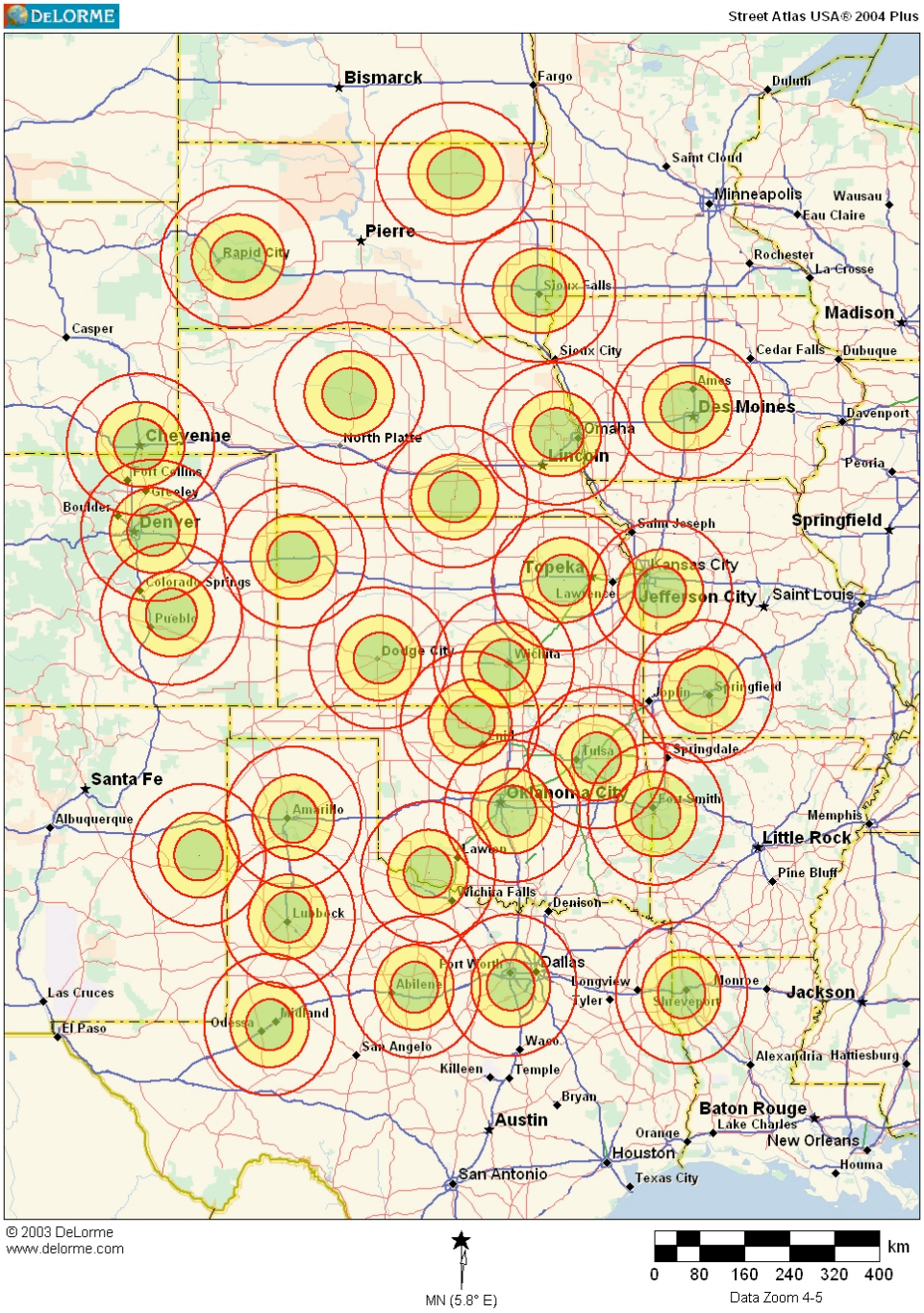

Figure 1.2. The locations of all mesocyclonic tornadoes observed by the DOWs from 1995 through 2001 and color-coded by storm-reported intensity (F0 = purple, F1 = blue, F2 = green, F3 = orange, F4 = red, F5 = black).

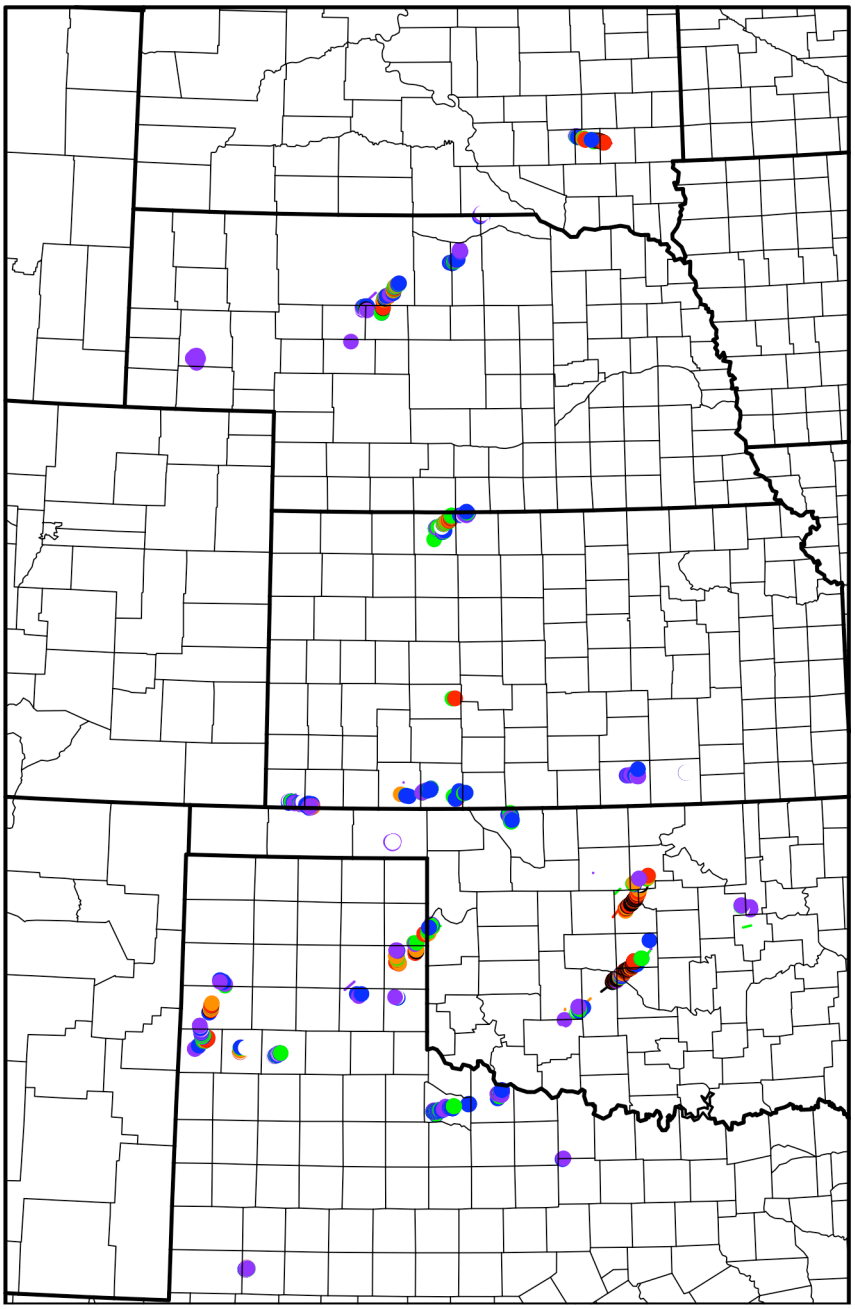

Figure 1.3. Frequency of dates when either (a) VORTEX or ROTATE field projects were conducted from 1995 through 2003 or (b) when DOW-observed tornadoes were present.

(a)

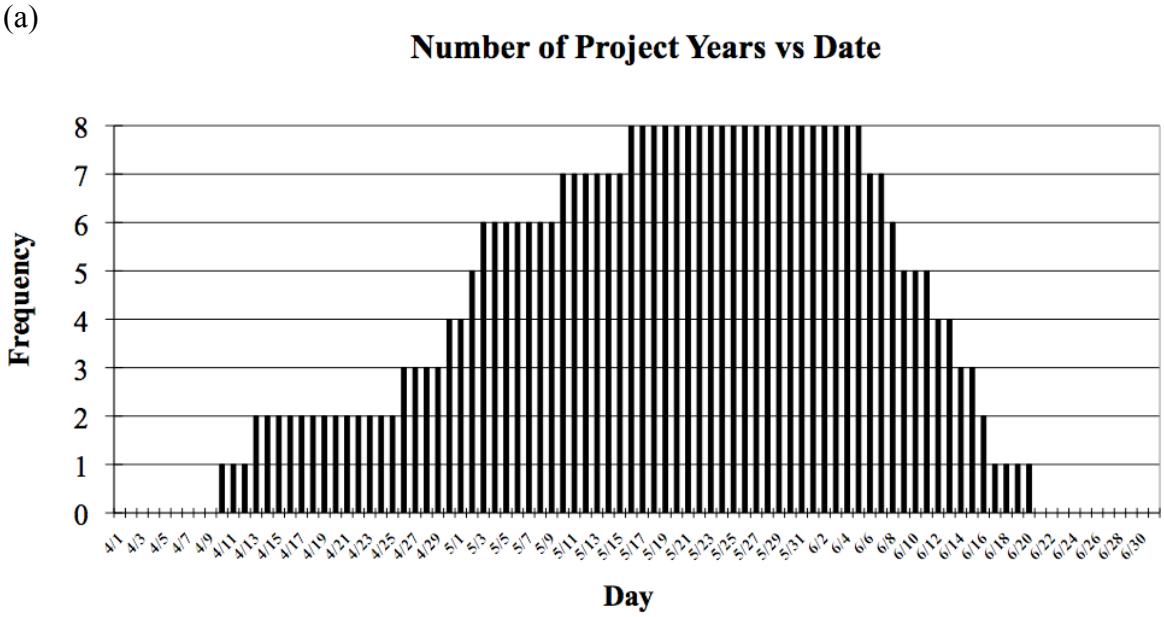

(b)

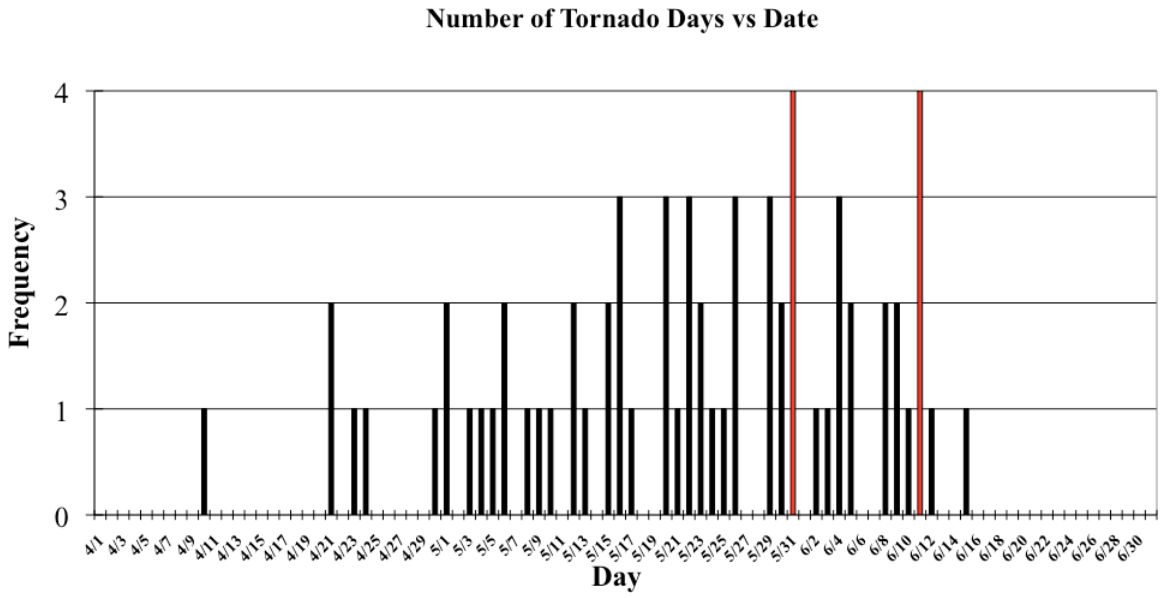

Figure 2.1. Change of vortex structure with increasing swirl ratio S in a vortex chamber. (a) At low S, the inflow boundary later separates and a confined vortex forms aloft. (b) As S increases, the boundary layer flow attaches and the vortex intensifies. There is vortex breakdown aloft which terminates the laminar core. (c) For S > critical value, the vortex breakdown has descended to the surface, the vortex intensity has decreased, and a downdraft penetrates into the turbulent core. (d) At high S, the downdraft has penetrated to the lower surface (Fiedler and Rotunno 1986).

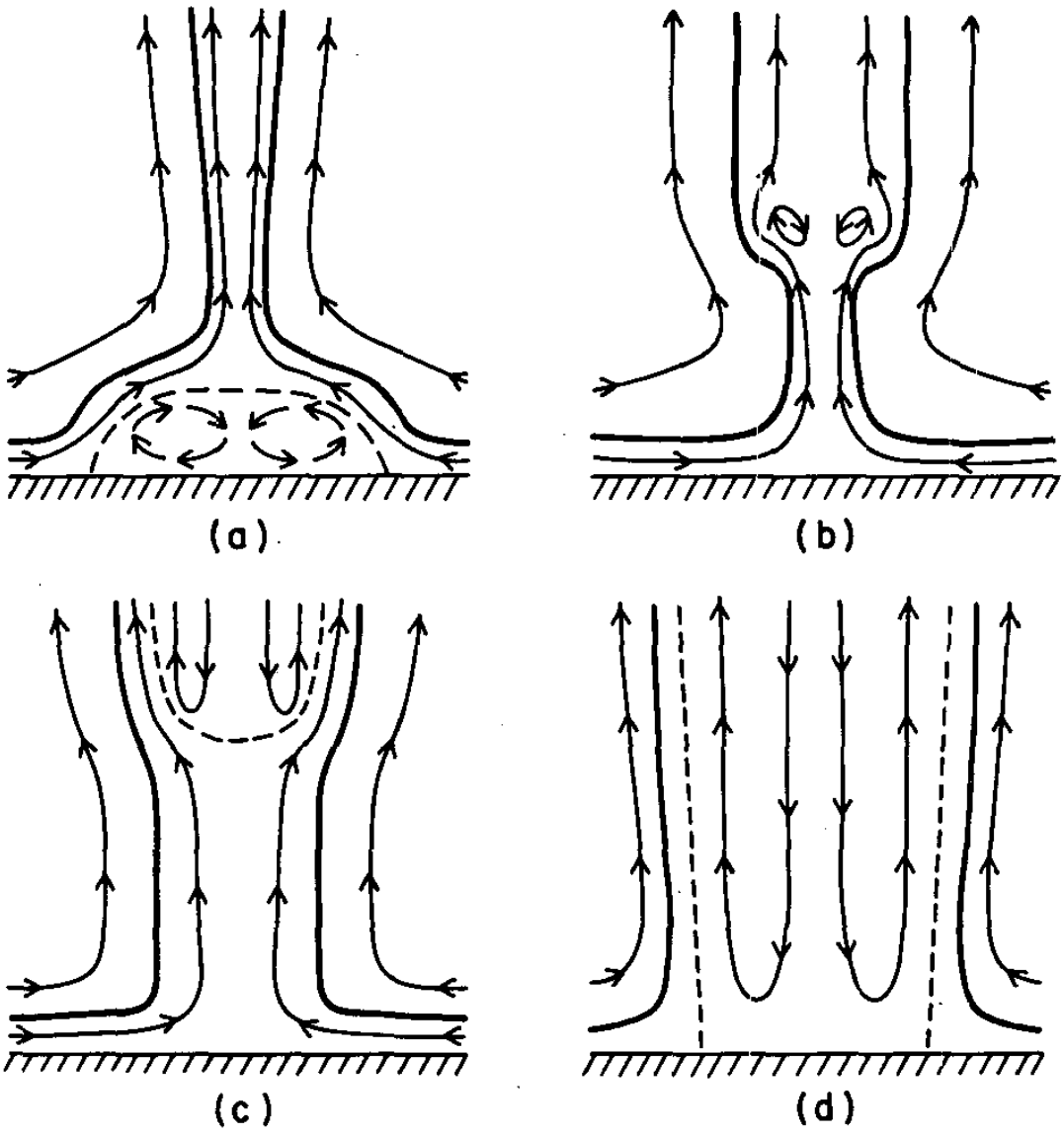

Figure 2.2. Conceptual model of a supercell thunderstorm including horizontal streamlines, regions of ascending air (UP) and descending air in the forward flank downdraft (FFD) and rear flank downdraft (RFD), and the location often associated with mesocyclone produced tornado (T) in a plan view (a) (Lemon and Doswell 1979) and in three dimensions (b) (Rasmussen et al. 1994).

(a)

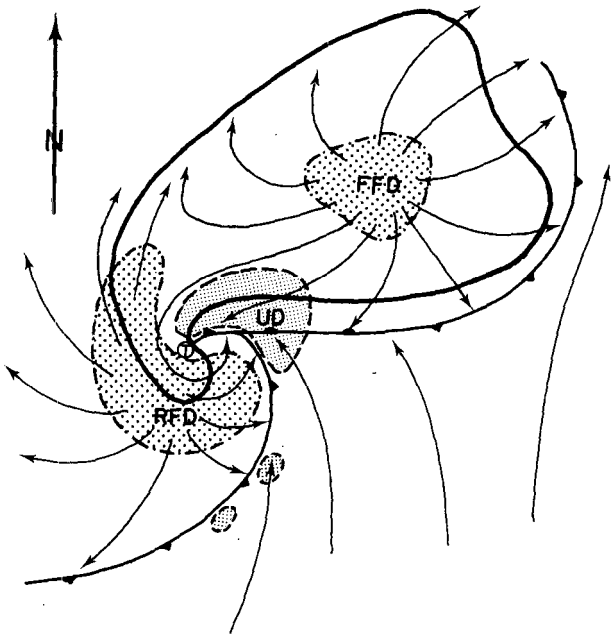

(b)

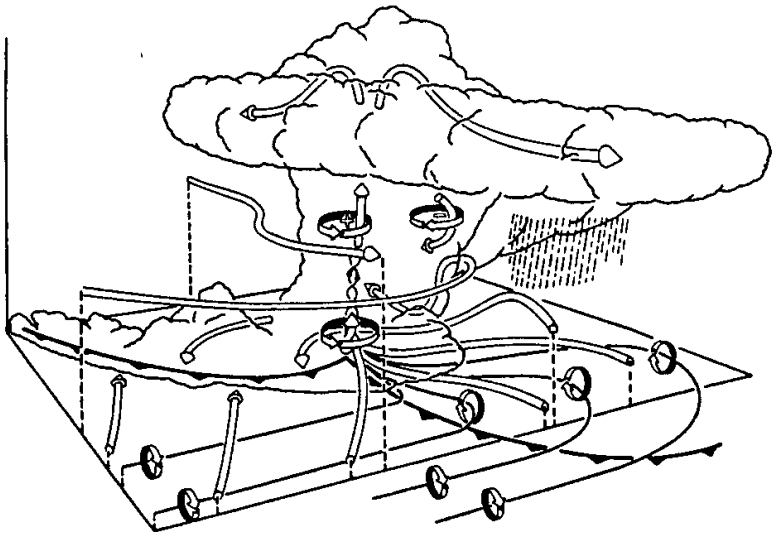

Figure 2.3. Vortex scale contraction conceptual models including the downward-building dynamic pipe effect (DPE) in (a) and (b) as opposed to simultaneous contraction in (c) (Trapp and Davies-Jones 1997).

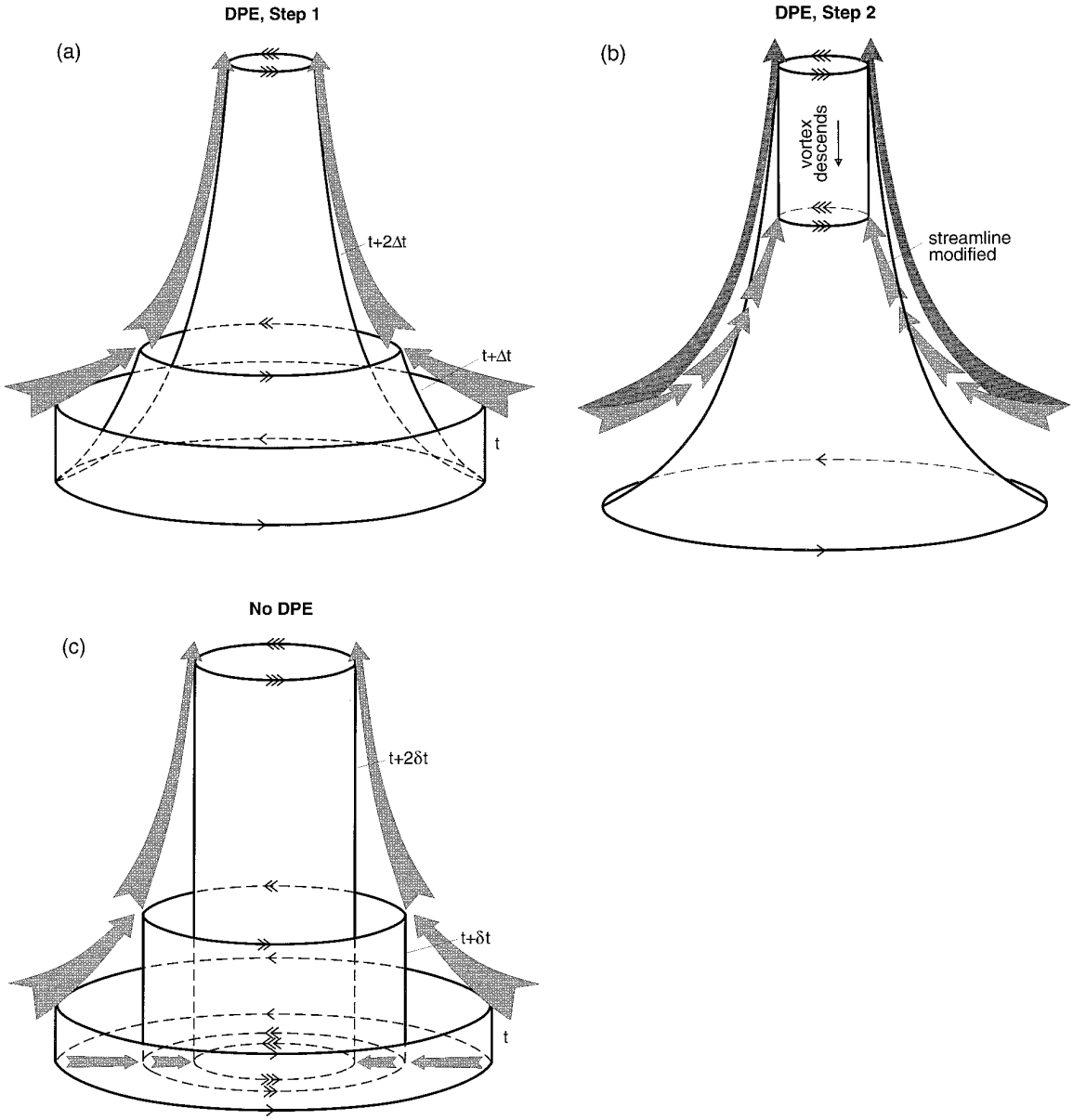

Figure 2.4. An example of a DOW radar observation showing the 1.4° elevation scan of the Spencer, SD tornado including Doppler velocities (m s^{-1}) on left and reflectivity (dB) on right. The tornado center is about 1.7 km from the radar (bottom center of each panel). A characteristic tornado rotational velocity couplet (left), and high-reflectivity disk are present.

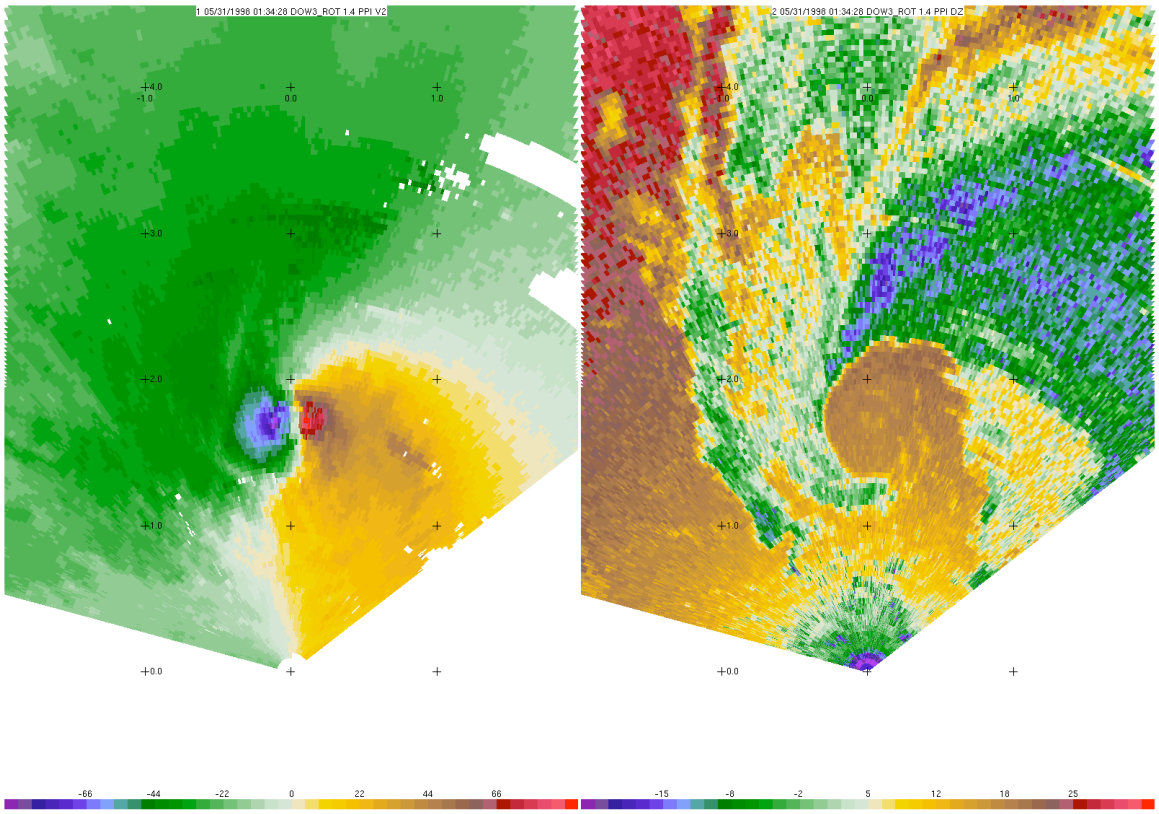

Figure 3.1. The typical geometry for a single tornado vortex observation. All quantities derived from data in each tornado observation will be associated with a fixed height and time of the vortex center observation, where (θ) is the radar azimuth angle measured clockwise from the front of the radar truck, (ϕ) is the radar elevation angle measured upward from the truck bed, (φ) is the radar tuck heading measured clockwise from true north, (V_{DOW}) is the radar truck speed, (d) is the slant-path distance to a sample volume point in space, (D) is the horizontal projection of the slant-path distance, (z) is the vertical projection of the slant path distance, (B) is the 3-dB beamwidth of the radar, (d_c, θ_c , ϕ_c) are the radar position coordinates of the center of the tornado vortex, (α) is the horizontal position angle in the tornado vortex relative to true north, (β) is the heading of the tornado vortex center measured clockwise from true north, (C) is the translational speed of the tornado vortex center, (V_{max}) is the maximum axisymmetric tangential velocity, (R_{mv}) is the radius of the maximum axisymmetric tangential velocity relative to the center of the tornado vortex, (r) is the horizontal distance to any point from the center of the tornado vortex, (V_{din} and V_{dout}) are the observed maximum inbound and outbound Doppler velocities, and (r_{in}, r_{out}) are the radii of the maximum inbound and outbound Doppler velocities relative to the center of the tornado vortex.

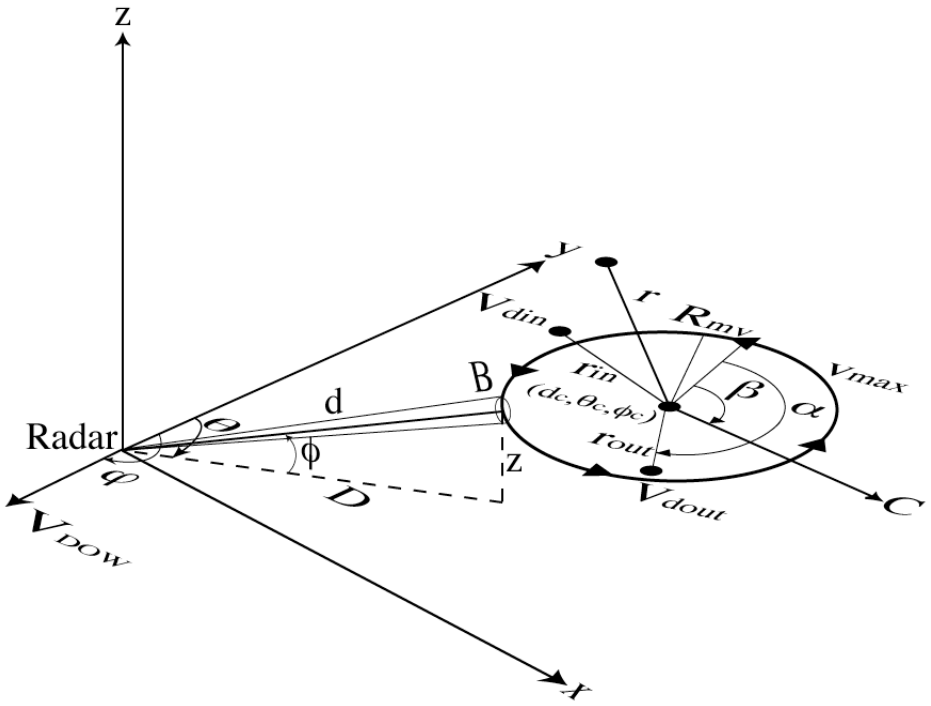
z
y
r
V_{din}
R_{mv}
V_{max}
B
r_{in}
(d_c, θ_c, ϕ_c)
d
Radar
θ
φ
ϕ
z
D
r_{out}
V_{dout}
C
V_{DOW}
x

Figure 3.2. The elevation angle correction used to account for partial beam blockage of the main radar lobe using the error function. The angle correction only impacts very low elevation angles where the reported elevation angle is less than about half a beamwidth (near 0.5 degrees) and the effective elevation angle reaches about 0.3 degrees in elevation for reported elevation angles at or just below zero degrees.

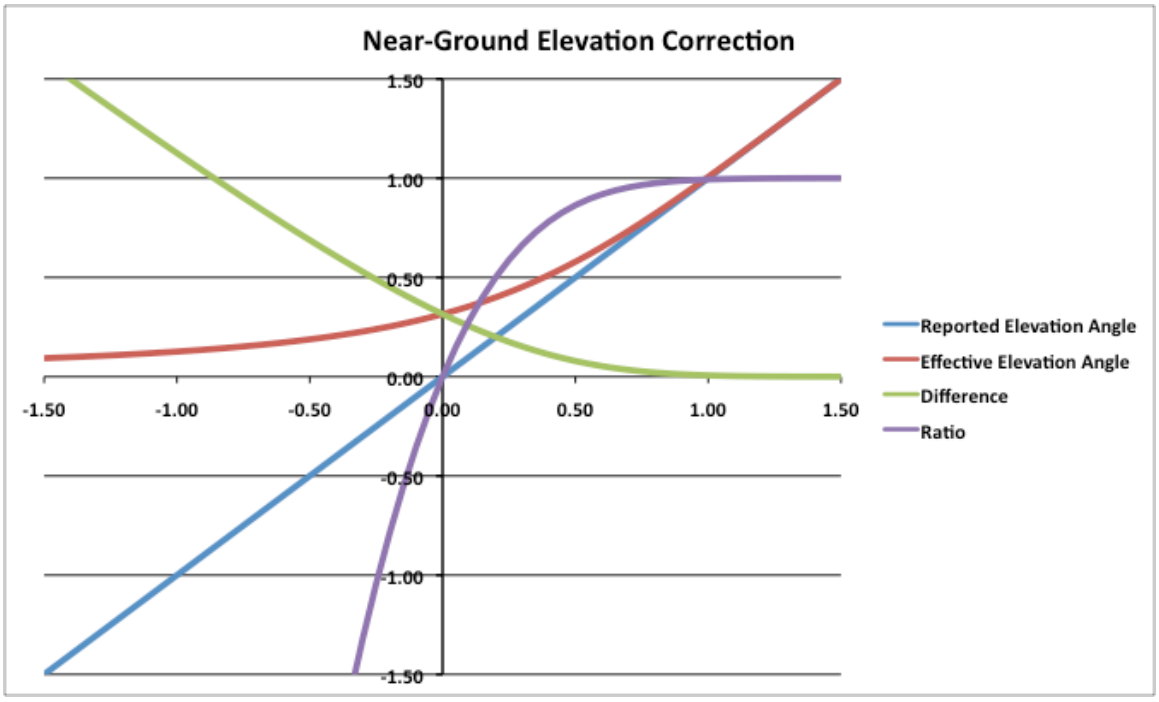

Figure 3.3. Example of automated quality control algorithms of Doppler velocity measurements (m s^{-1}) including (a) thresholding on NCP below 0.2 and two-pass despeckling within a 2-gate radius using 50% surrounding coverage minimum and (b) two-pass deglitching staggered-PRT Doppler velocity values using Nyquist multiples of the individual PRTs as guesses to match the median value of surrounding gates by less than 20 m s^{-1}. Original Doppler velocity values appear on left and final quality controlled fields are on the right. Cartesian tick marks are every 1 km.

(a)

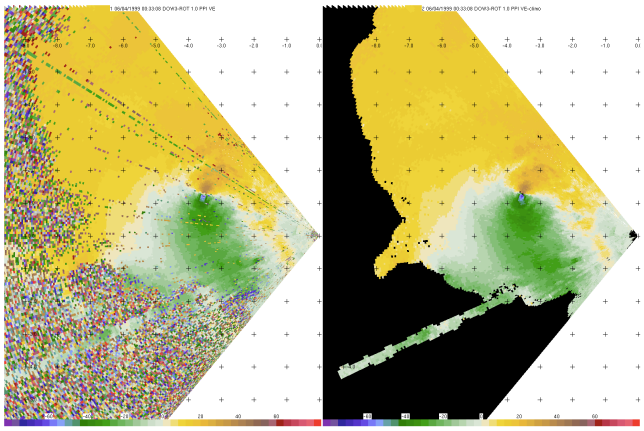

(b)

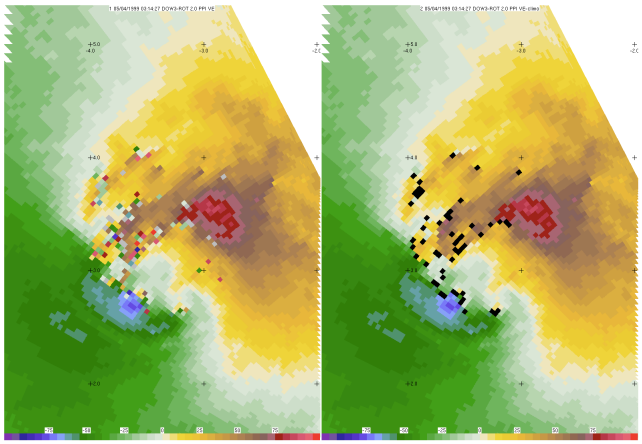

Figure 3.4. Example of automated quality control algorithms of DOW Doppler velocity measurements (m s^{-1}) including the thresholding on NPC below 0.2, a two-pass despeckling within a 2-gate radius using 50% surrounding coverage minimum, and removal of radar platform motion including rotation to ground-relative orientation. Original Doppler velocity values appears on left and quality controlled fields are on the right. Note that standard velocity dealiasing must still be implemented on the right. Cartesian tick marks are every 5 km.

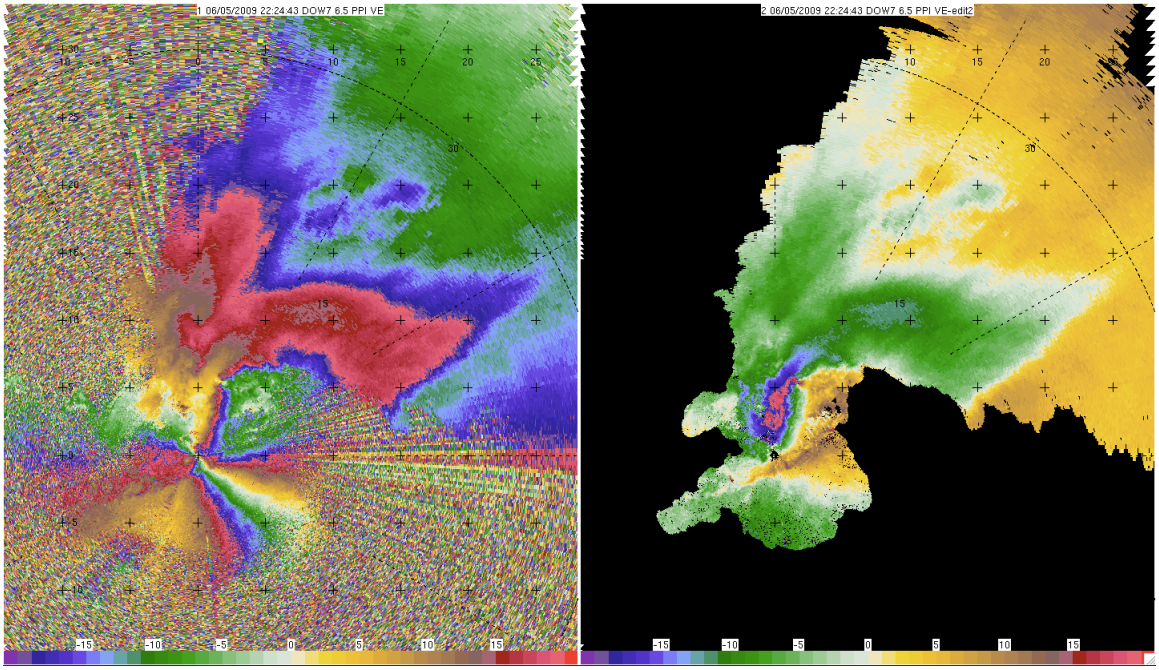

Figure 3.5. Example of tornado center identification showing a single DOW Doppler velocity field (m s^{-1}) through tornado at one degree elevation at about 3 km range. Cartesian tick marks are every 100 m. In the first step, the maximum Doppler velocity difference, at constant range from the radar, is identified and must be at least 40 m s^{-1} in magnitude over a horizontal distance of no more than 2 km. The Doppler velocity data point closest to the midpoint of the maximum inbound and outbound Doppler velocities (black circles), at constant rage, is the first-guess center point (hash mark on the line connecting the circles). The distance between the two maximum values is the first-guess core diameter (line connecting the circles). An intensive search domain is established using a sector of data that has dimensions in the azimuthal and radial directions that is twice the first-guess core diameter with a center point of the first-guess center (black polygon).

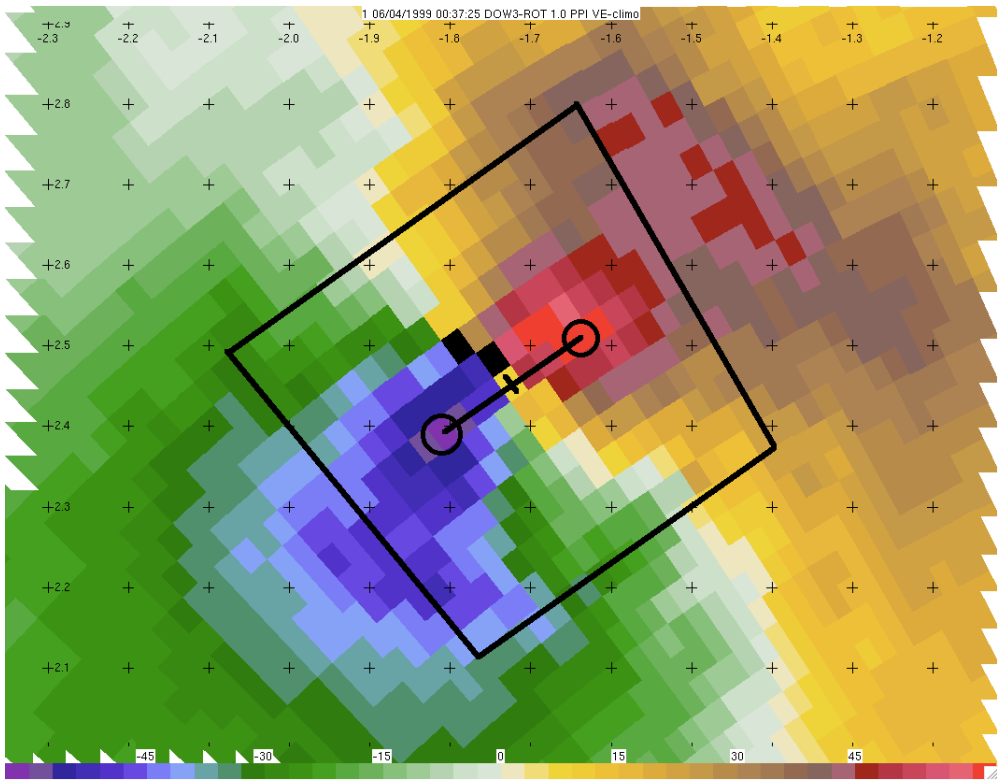

Figure 3.6. Example of tornado center identification showing a single DOW Doppler velocity field (m s^{-1}) through tornado at one degree elevation at about 3 km range. Cartesian tick marks are every 100 m. In the second step, the median velocity position (black circles) of the (a) lowest 10% of Doppler velocity values (magenta color) and (b) highest 10% of the Doppler velocity values (magenta color) in the intensive search domain (black polygon) are identified.

(a)

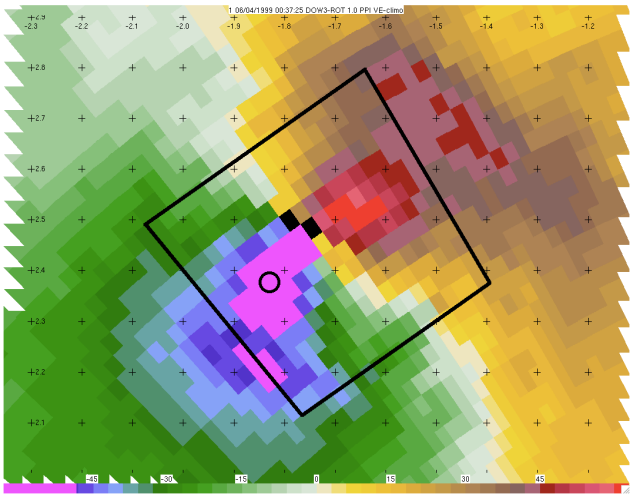

(b)

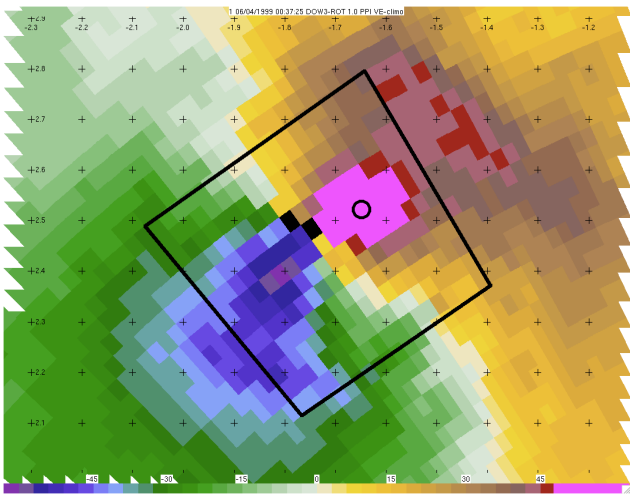

Figure 3.7. Example of tornado center identification showing a single DOW Doppler velocity field (m s^{-1}) through tornado at one degree elevation at about 3 km range. Cartesian tick marks are every 100 m. In the third step, the Doppler velocity data point nearest the midpoint of the two median positions identified in step two (black circles) is classified as the refined tornado center point and used as the best-guess tornado center (the hatch through the line connecting the circles).

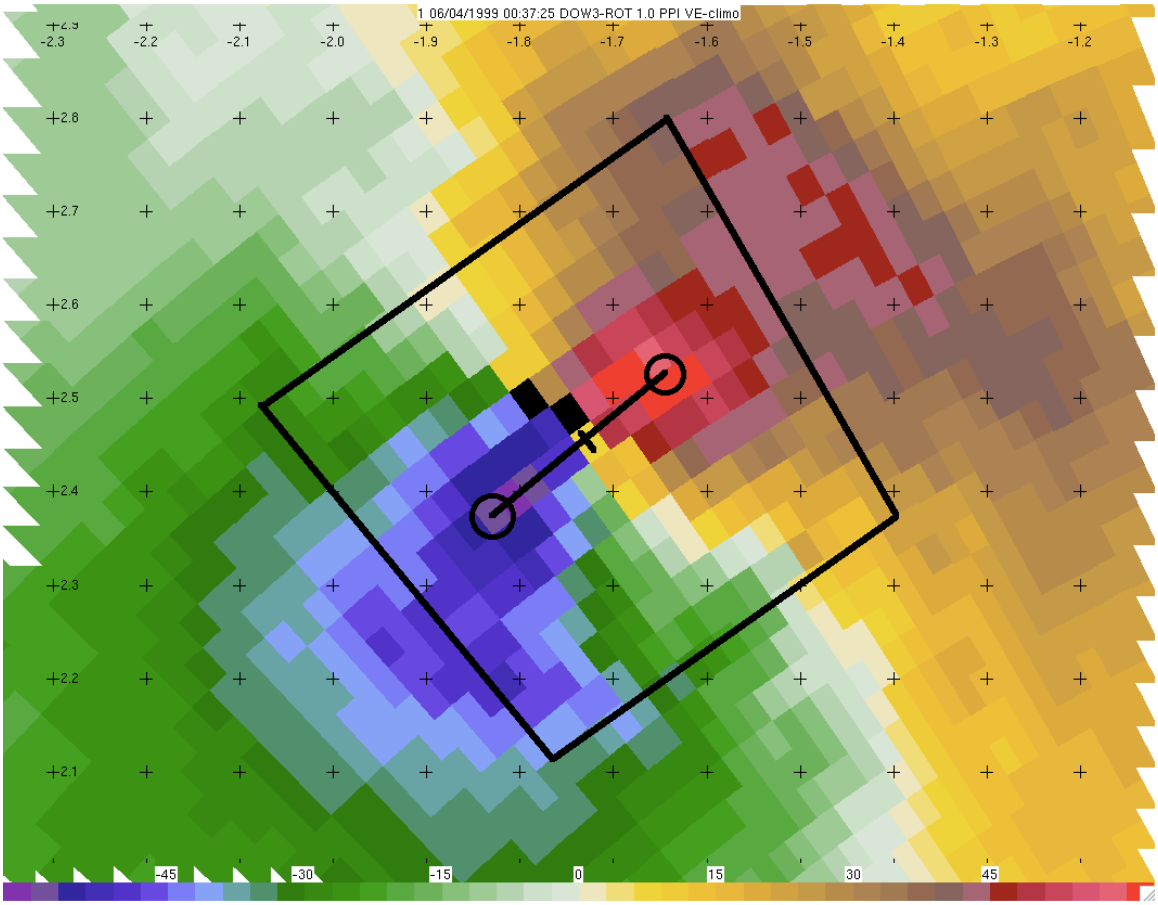

Figure 3.8. The aspect ratio correction factor used to account for reduction in Doppler velocity measurements when the radar beamwidth becomes large relative to the diameter of the tornado core. The correction factor is limited to a maximum value of 1.14 when the beamwidth reaches a quarter the inferred tornado diameter. The edge-case is reached when the beamwidth reaches half the diameter of the tornado and a gate-to-gate Doppler velocity signature results.

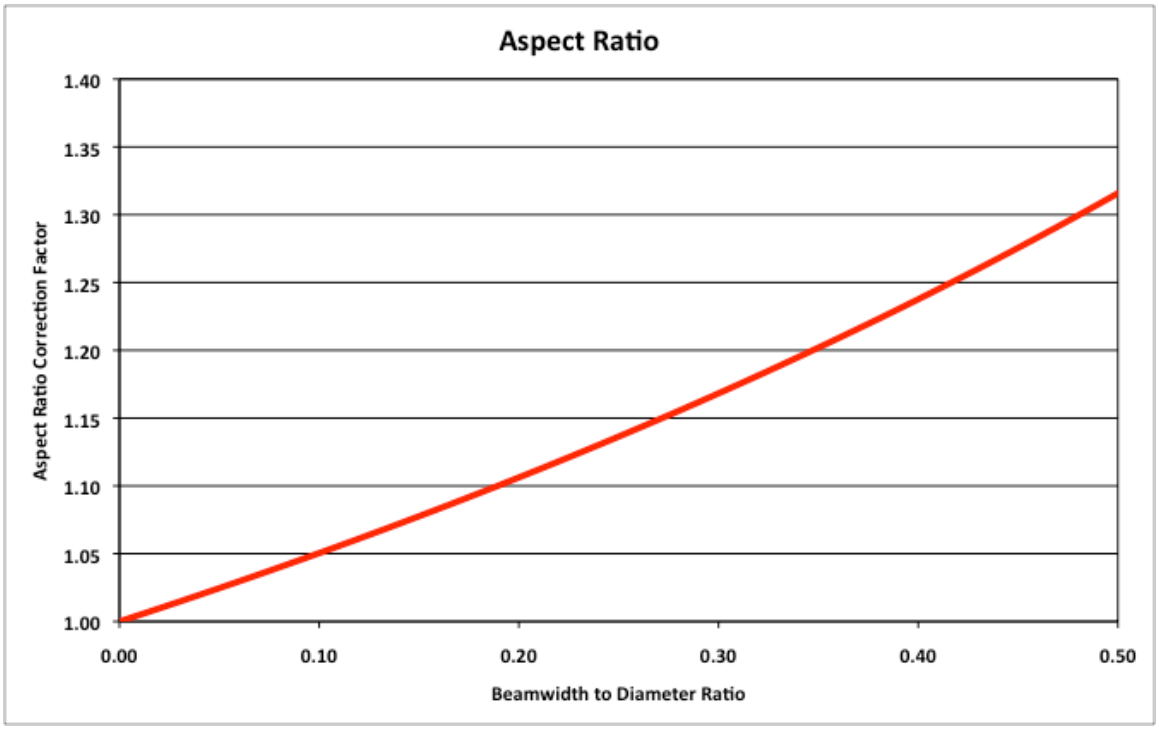

Figure 3.9. Example of tornado patch and cross-section extraction from the Doppler velocity field (m s^{-1}). The patch diameter in which attributes of the velocity field are collected and computed is set to three first-guess diameters (six radii) from the best-guess center point. The (a) azimuthal cross-section through the best-guess center to the edges of the patch are also extracted (black polygon) and (b) annuli (black dashed circles) in which axisymmetric tangential and radial components of the flow are retrieved relative to the best-guess center.

(a)

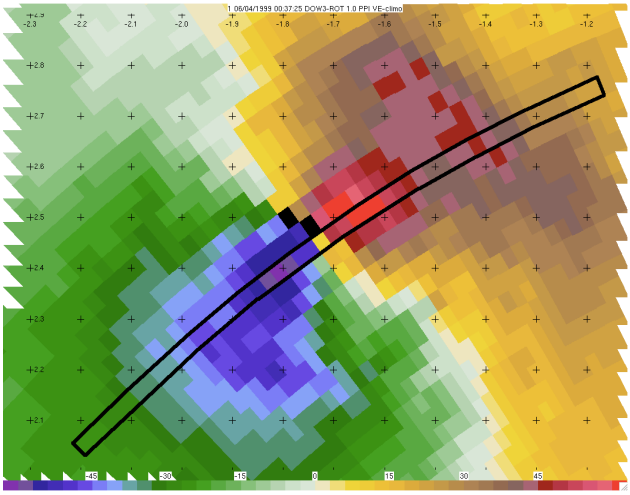

(b)

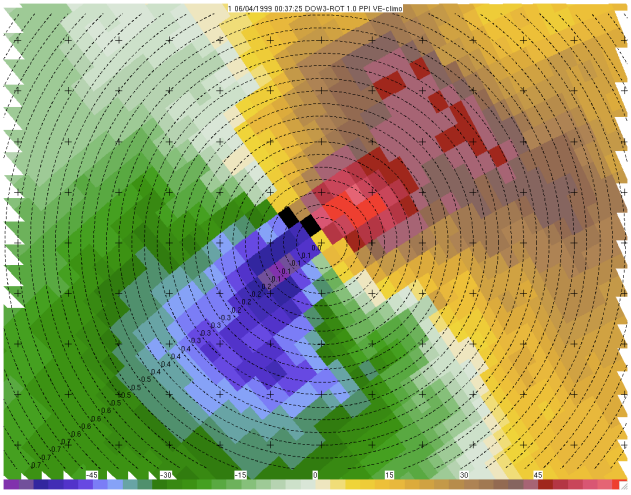

Figure 3.10. The sensitivity of the single-Doppler velocity retrieval technique to the selection of the vortex center point. The vortex center point is manually relocated 120 m in four directions from the refined center point and the resulting retrievals of axisymmetric tangential and radial velocities are compared with the retrieval from the algorithm identified center point (in bold black). The 120 m relocation represents a shift in center position by about 20% of the radius of maximum winds (700 m).

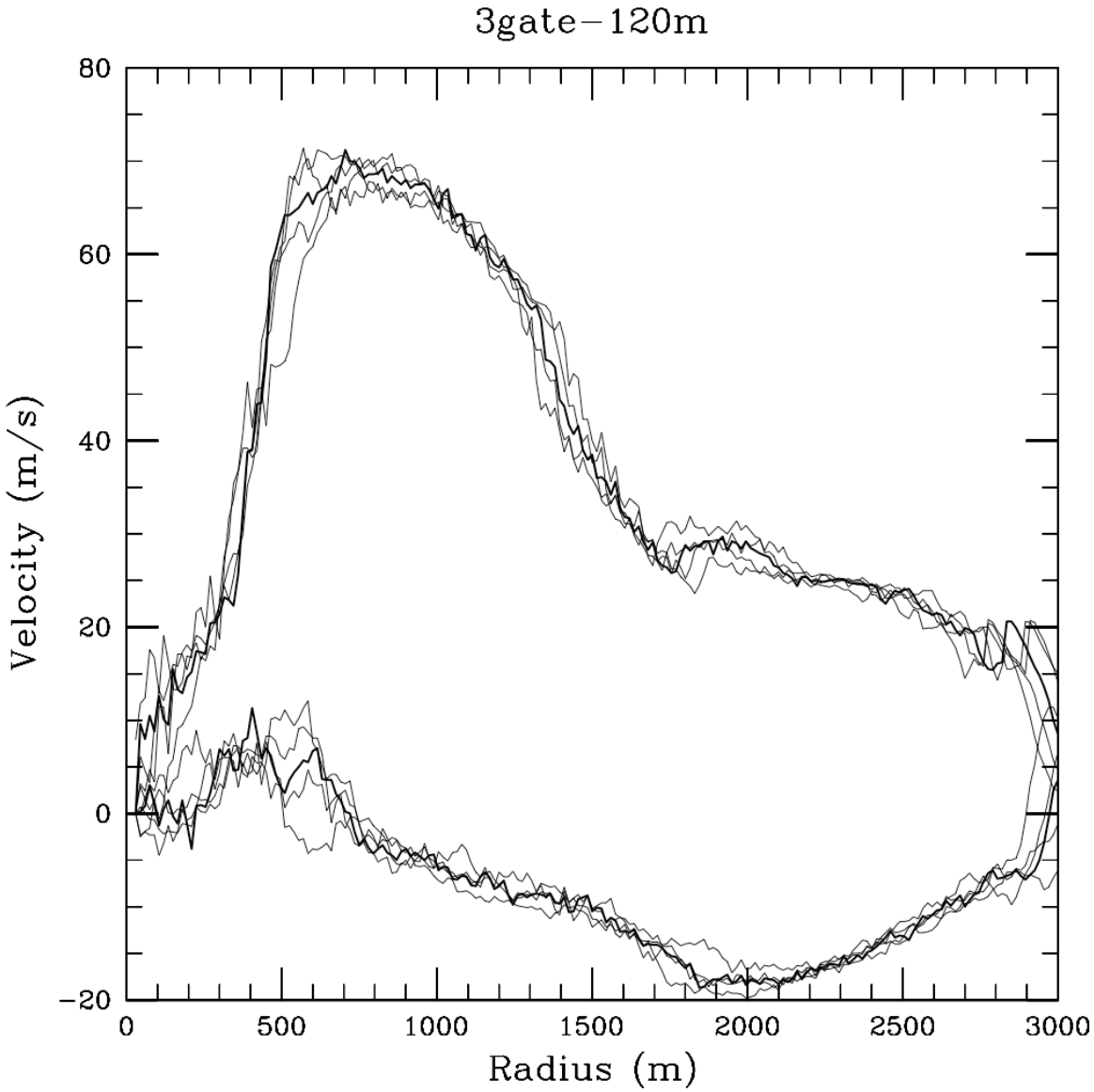

Figure 4.1. Frequency histogram of all DOW radar observations showing (a) number of observations for each DOW observed tornado at (a) all elevations and (b) all elevations below 500 m AGL. Observation counts less than 100 are expanded in (c) for all elevations and (d) all elevations below 500 m AGL.

(a)

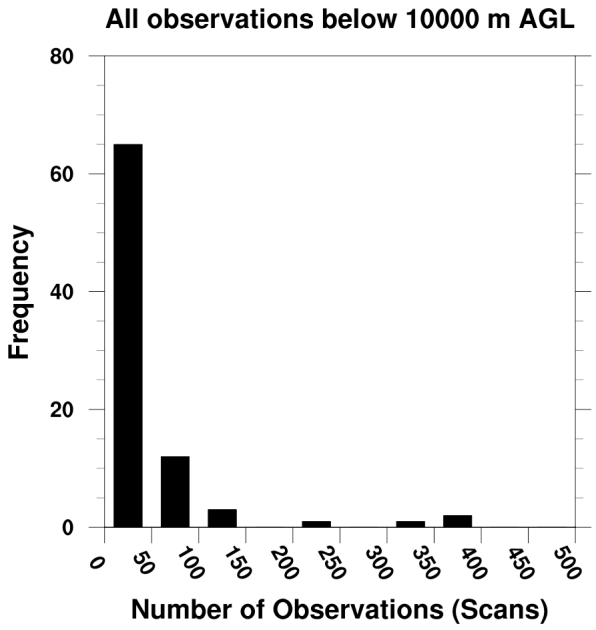

(b)

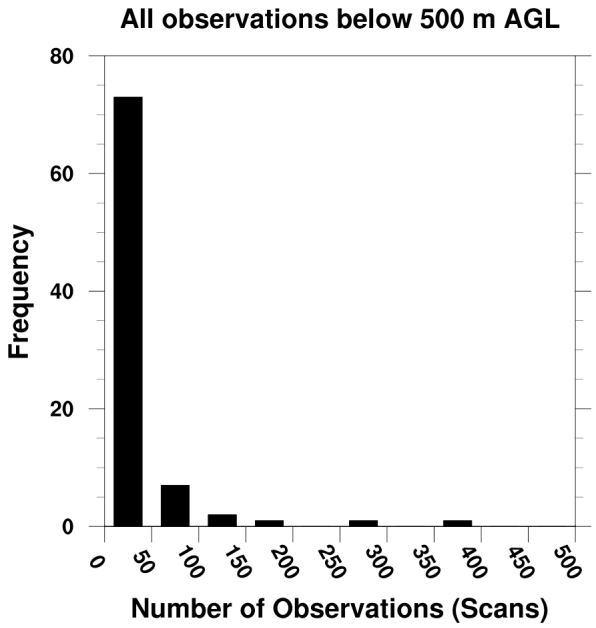

(c)

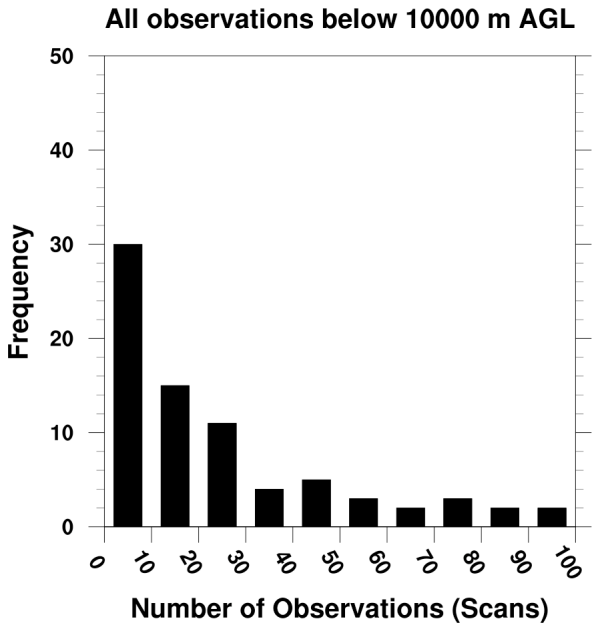
All observations below 10000 m AGL
Frequency
0
10
20
30
40
50
0
10
20
30
40
50
60
70
80
90
100
Number of Observations (Scans)

(d)

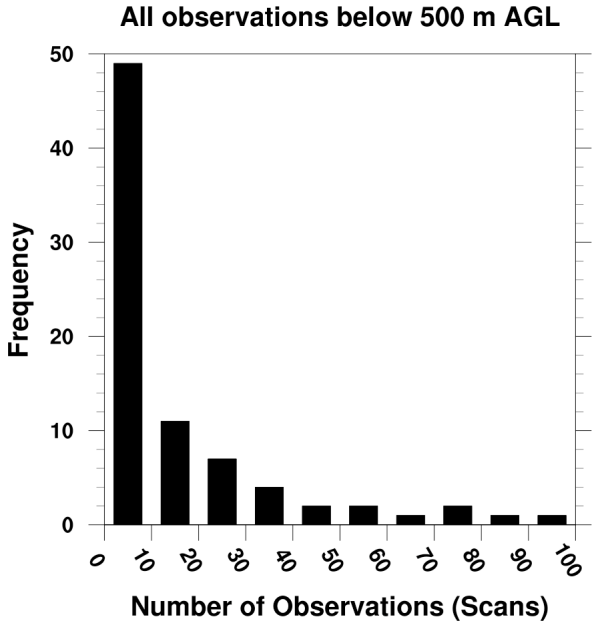
All observations below 500 m AGL
Frequency
0
10
20
30
40
50
0
10
20
30
40
50
60
70
80
90
100
Number of Observations (Scans)

Figure 4.2. Frequency histogram of all DOW radar observations showing (a) horizontal range to the center of the vortex and (b) elevation of the vortex center observation AGL.

(a)

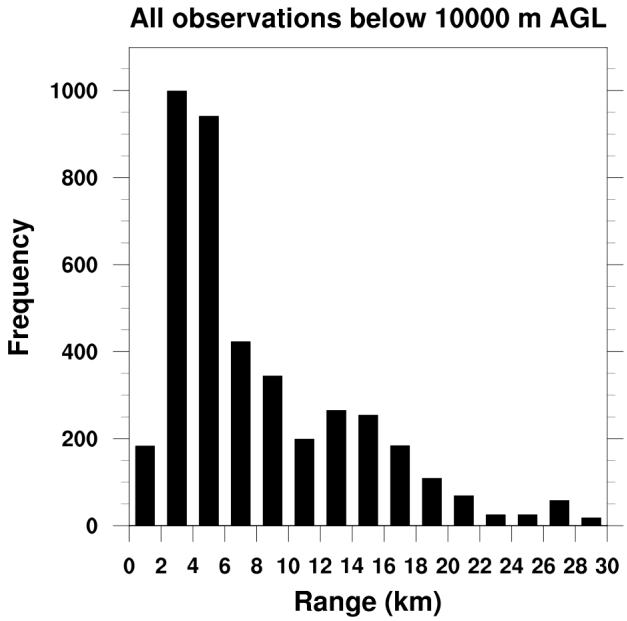

(b)

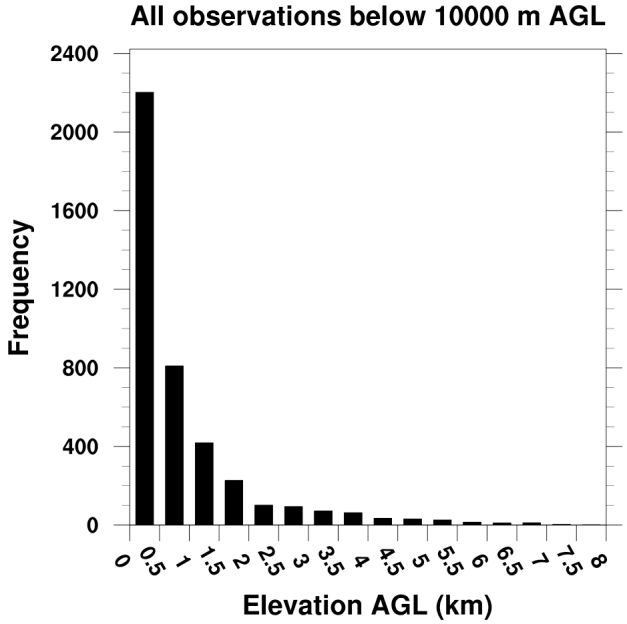

Figure 4.3. Frequency histogram of all DOW radar observations showing (a) gate spacing at the center of the vortex and (b) beam spacing at the vortex center.

(a)

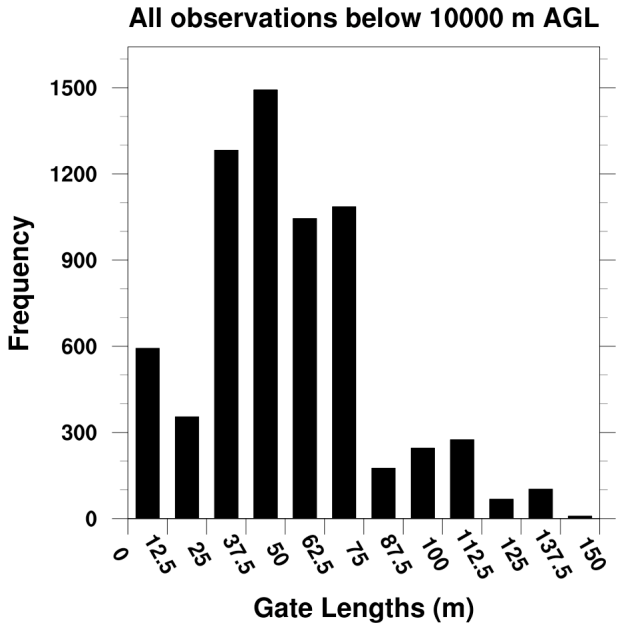

(b)

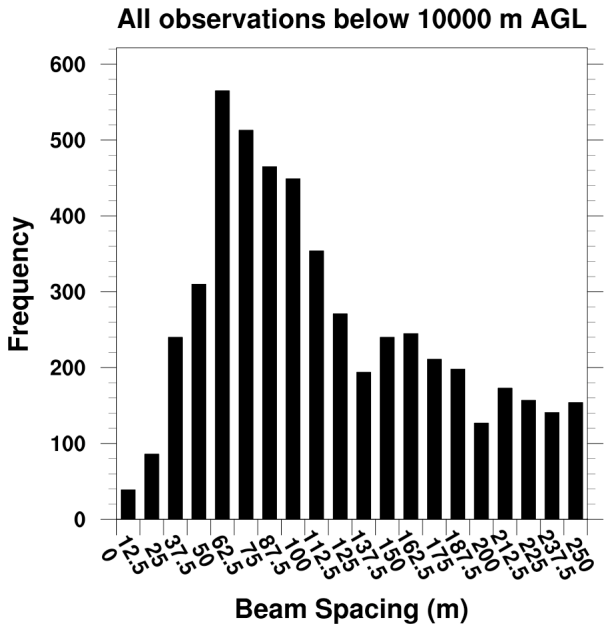

Figure 4.3. Frequency histogram of all DOW radar observations showing (c) period between successive observations of the vortex center and (d) period between successive low-level (< 500 m AGL) observations of the vortex center.

(c)

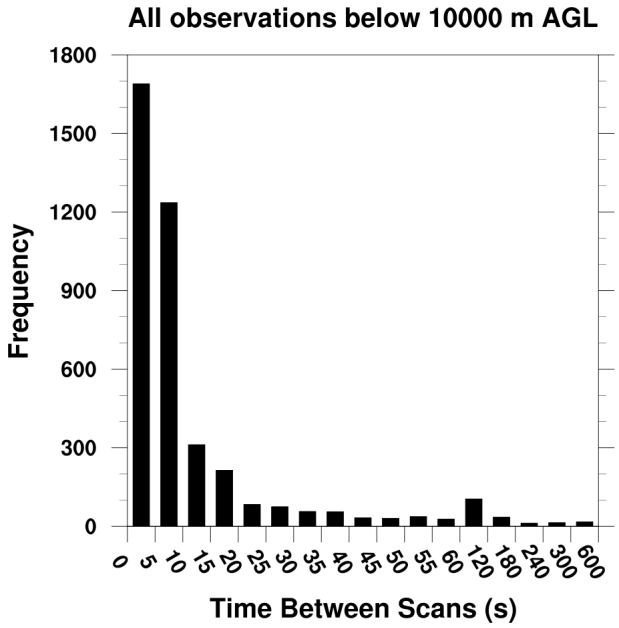

(d)

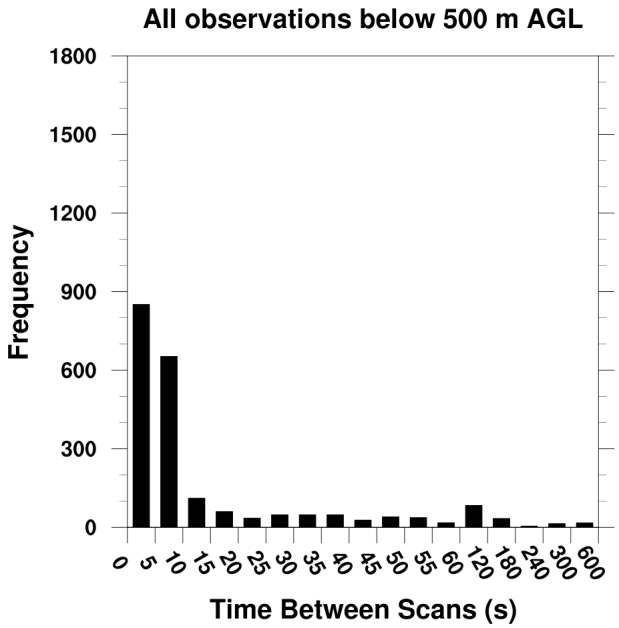

Figure 4.3. Frequency histogram of all DOW radar observations showing the ratio of (e) beam spacing at the vortex center and detected core diameter and (f) gate-spacing at the vortex center and the detected core diameter.

(e)

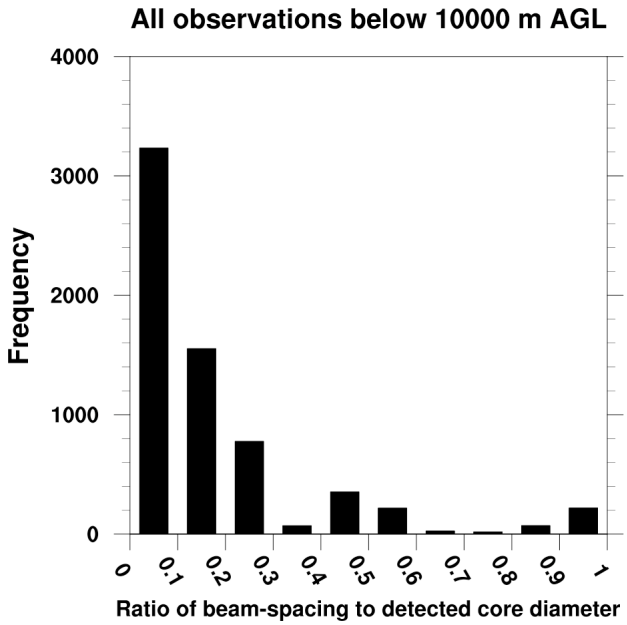

(f)

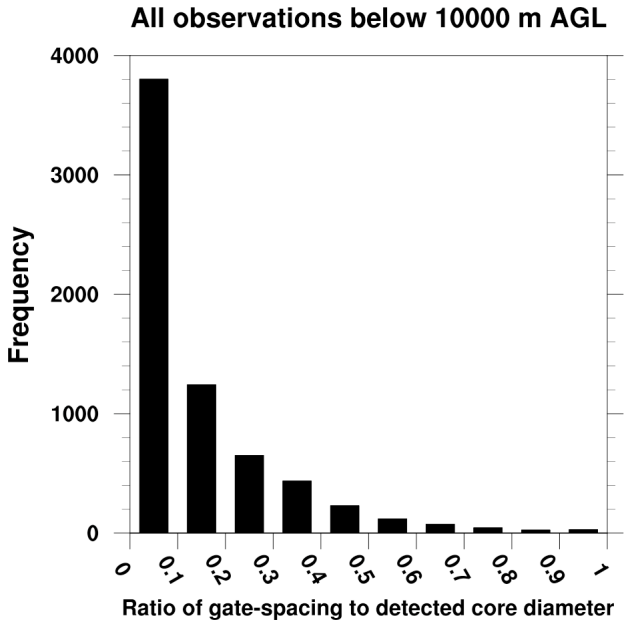

Figure 4.4. Frequency histogram of DOW observations (solid) containing the maximum ground-relative aspect-corrected velocity for each tornado observed as compared with OneTor tornado reports (hatched) for the same tornadoes using the (a) F-scale and (b) EF-scale mapping of the velocity.

(a)

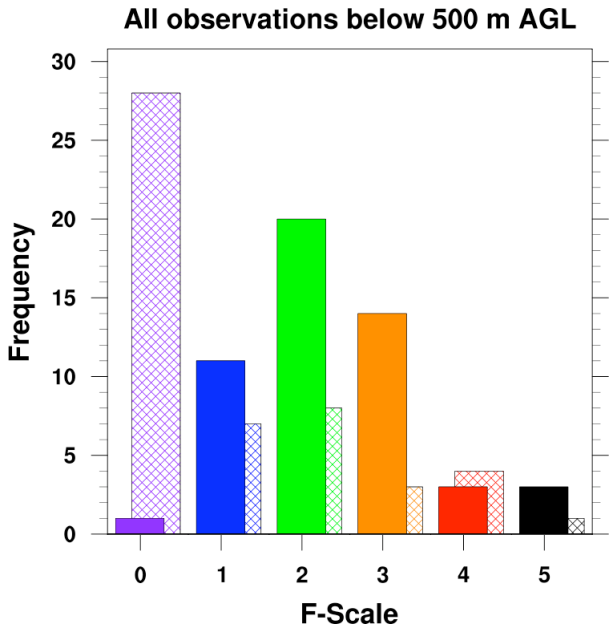

(b)

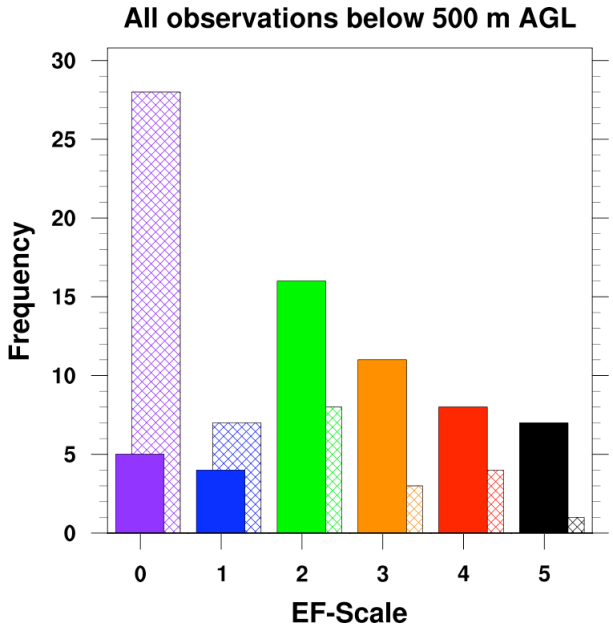

Figure 4.4. Frequency histogram of DOW observations (solid) containing the maximum ground-relative aspect-corrected velocity for each tornado that is not reported in OneTor and compared with OneTor tornado reports (hatched) not detected by the DOWs using the (c) F-scale and (d) EF-scale mapping of the velocity.

(c)

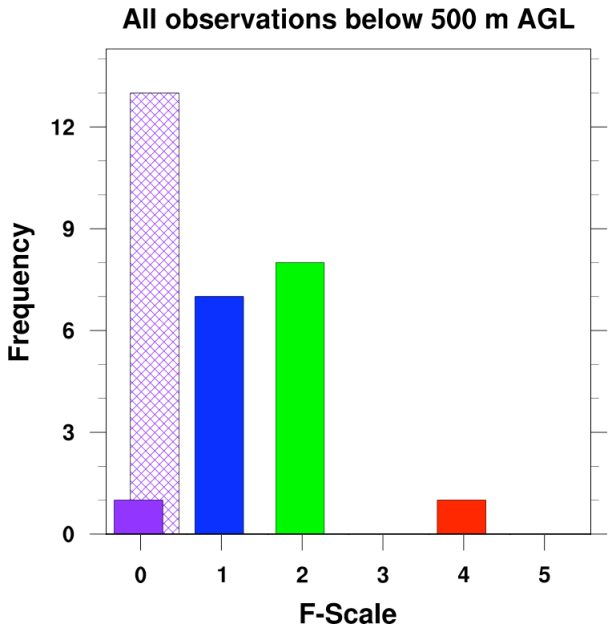

(d)

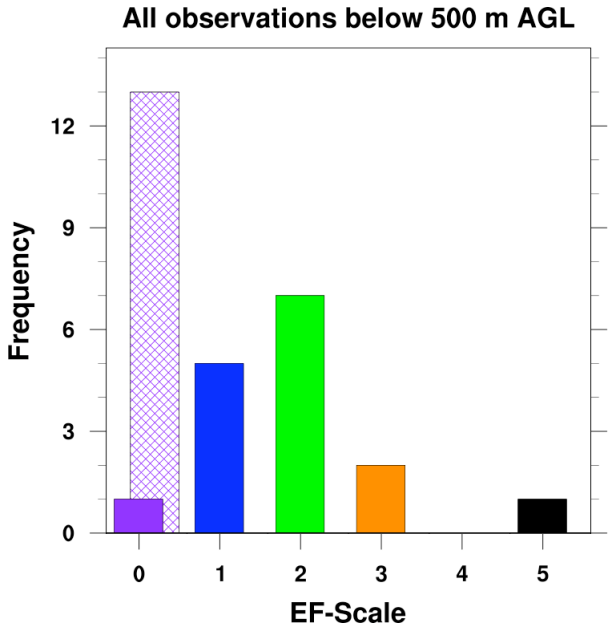

Figure 4.5. Frequency histogram of DOW observations (solid) containing the maximum core-diameter of each tornado as compared with OneTor tornado reports (hatched) for (a) maximum DOW core width, (b) DOW core width at peak intensity and (c) DOW core width at peak intensity for EF2 or greater ratings.

(a)

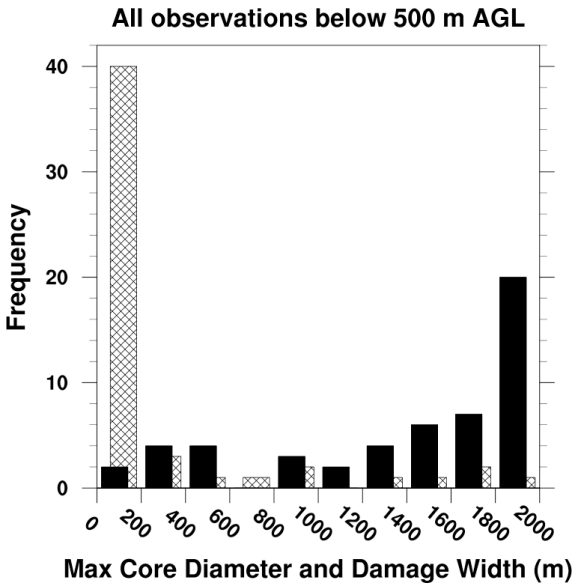

(b)

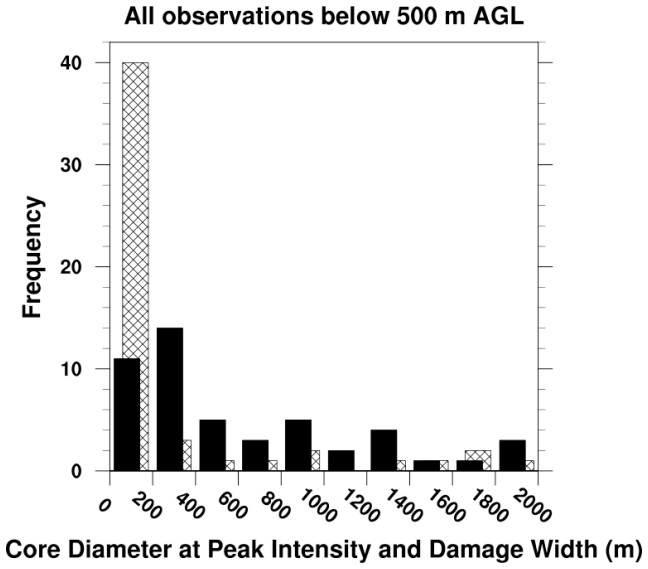

(c)

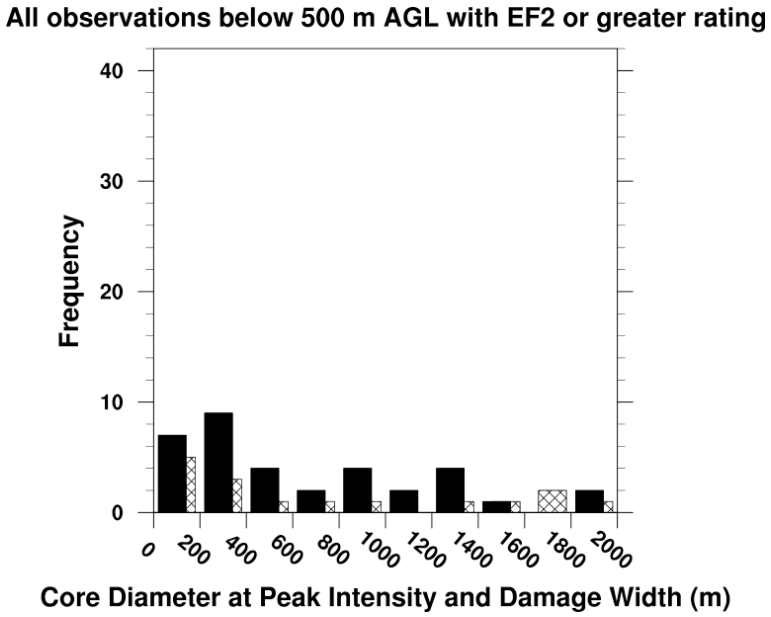
All observations below 500 m AGL with EF2 or greater rating
Frequency
0
10
20
30
40
0
200
400
600
800
1000
1200
1400
1600
1800
2000
Core Diameter at Peak Intensity and Damage Width (m)

Figure 4.6. Frequency histogram of OneTor tornado reports in Texas, Oklahoma, Kansas and Nebraska during April-June of 1995-2003 showing (a) F-scale intensity classification and (b) F-scale intensity classification normalized by F0 reports.

(a)

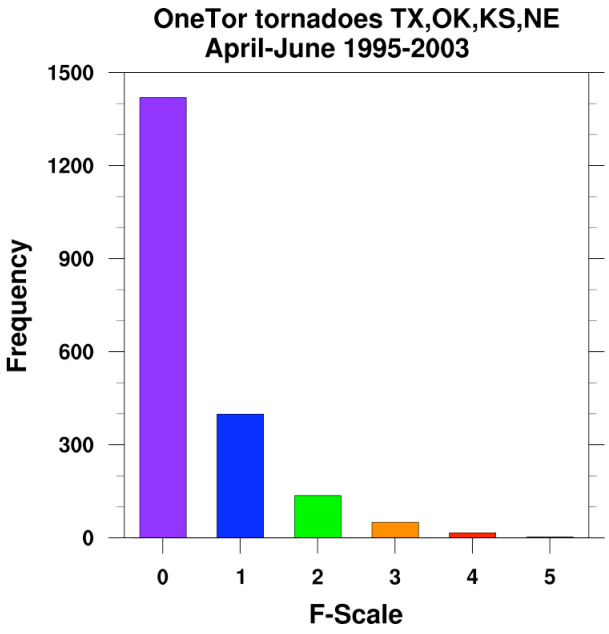

(b)

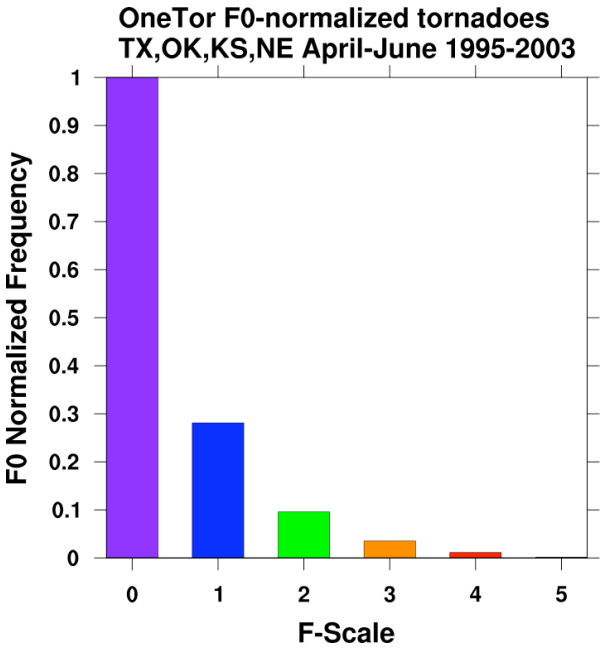

Figure 4.7. Frequency histogram of OneTor tornado reports in Texas, Oklahoma, Kansas and Nebraska during April-June of 1995-2003 for DOW-observed tornadoes showing (a) F-scale intensity classification and (b) F-scale intensity classification normalized by F0 reports.

(a)

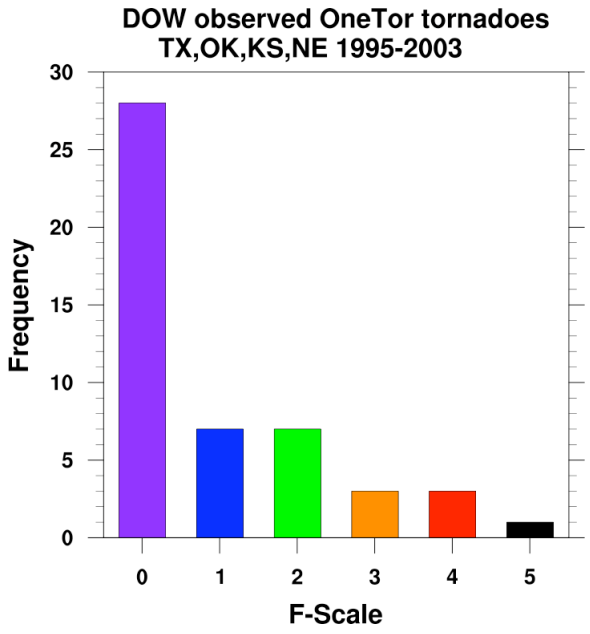

(b)

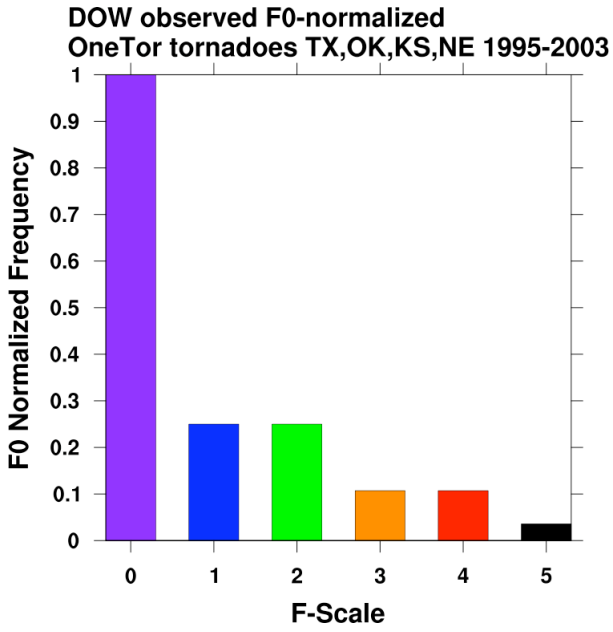

Figure 4.8. Box plots showing the distribution (minimum, 25th percentile, median, 75th percentile and maximum) of ground-relative aspect-corrected velocity for all DOW tornado observations below (a) 500 m AGL, (b) 200 m AGL, (c) 50 m AGL and (d) maximum value for each tornado below 500 m AGL. Sample sizes indicated for each distribution.

(a) Below 500 m AGL

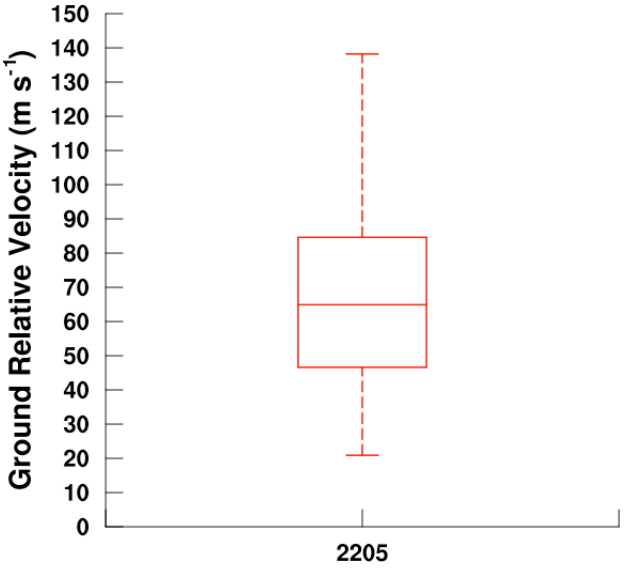

(b) Below 200 m AGL

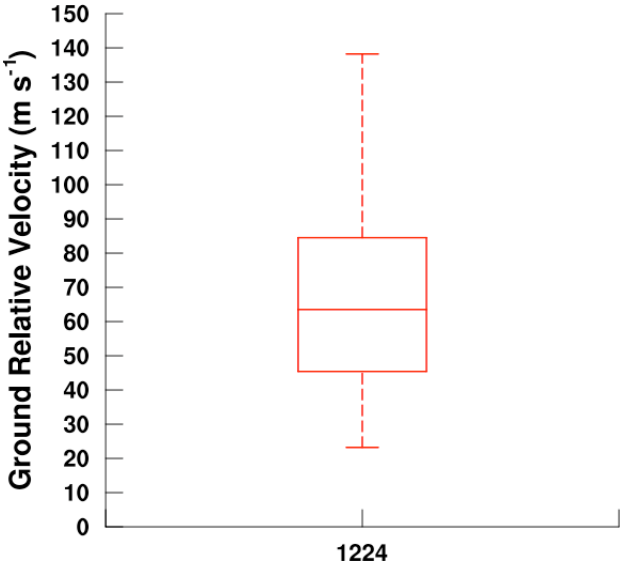

(c) Below 50 m AGL

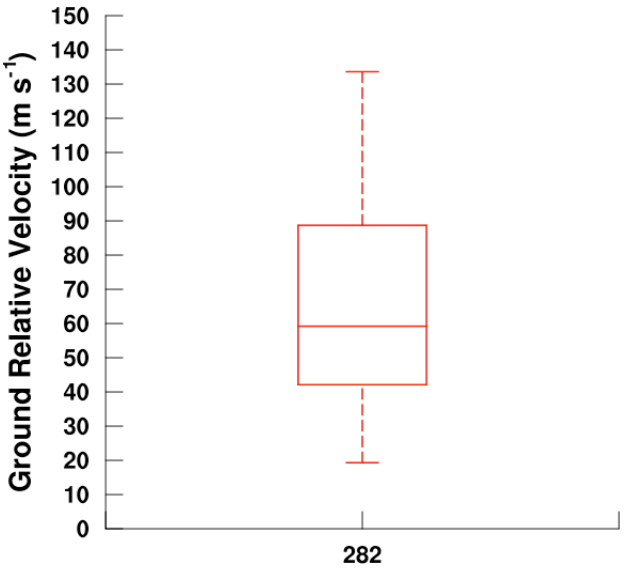

(d) Below 500 m AGL

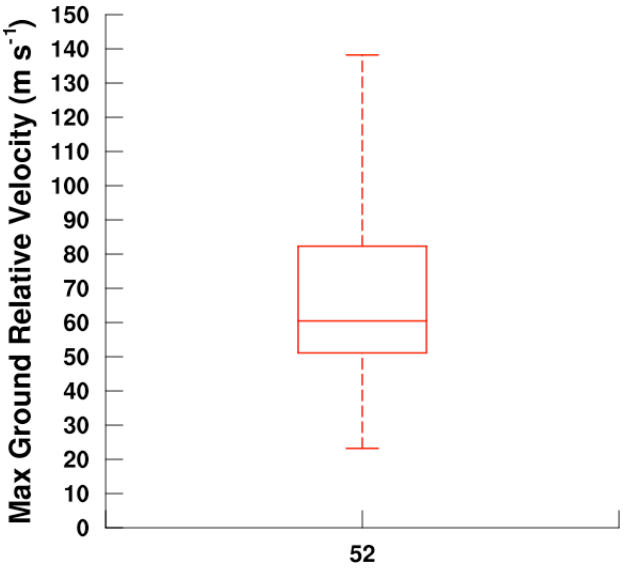

Figure 4.9. Box plots showing the distribution (minimum, 25th percentile, median, 75th percentile and maximum) of maximum ground-relative aspect-corrected velocity for each DOW tornado observed below 500 m AGL when mapped to the (a) F-scale and (b) EF-scale. Sample sizes indicated for each distribution.

(a) Below 500 m AGL

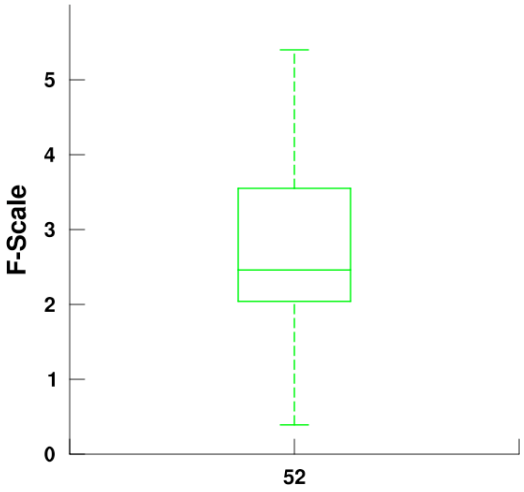

(b) Below 500 m AGL

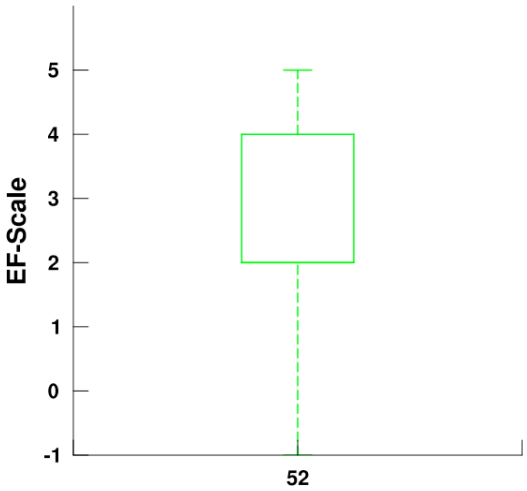

Figure 4.9. Box plots showing the distribution (minimum, 25th percentile, median, 75th percentile and maximum) of maximum ground-relative aspect-corrected velocity for each DOW tornado observed below 500 m AGL when mapped to the EF-scale for vortex centers within (c) 10 km and (d) 5 km of the DOW. Sample sizes indicated for each distribution.

(c) Below 500 m AGL and within 10 km range

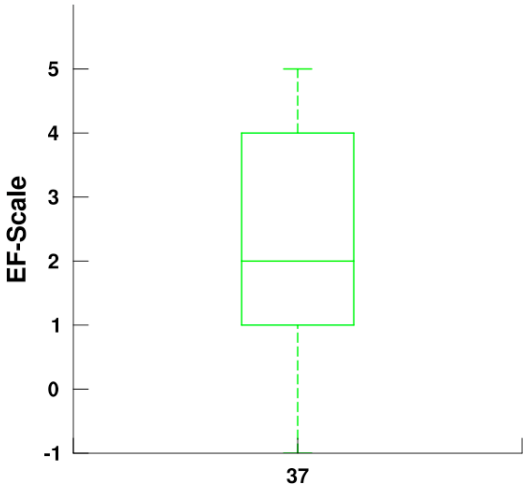

(d) Below 500 m AGL and within 5 km range

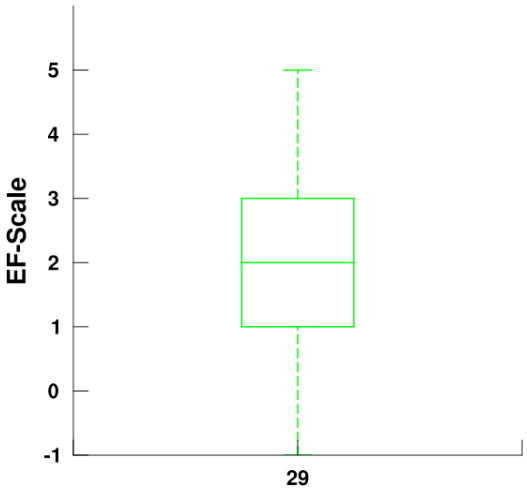

Figure 4.10. Box plots showing the distribution (minimum, 25th percentile, median, 75th percentile and maximum) of (a) translational speed for all DOW tornado observations below 500 m AGL and (b) duration of tornado observation for all DOW scans. Sample sizes indicated for each distribution.

(a) Below 500 m AGL

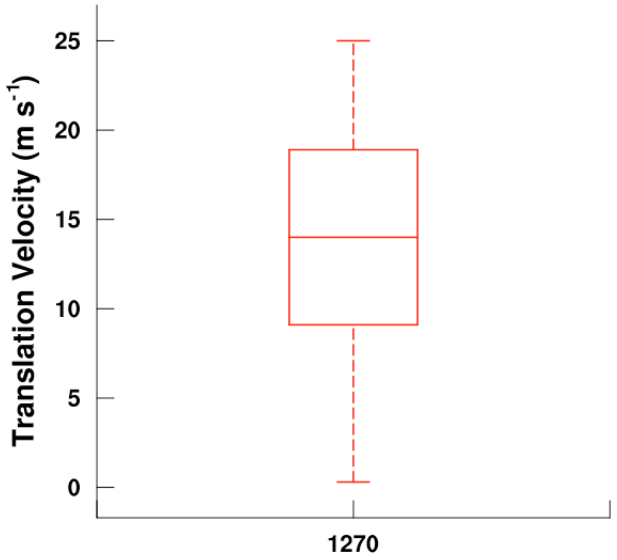

(b) Below 500 m AGL

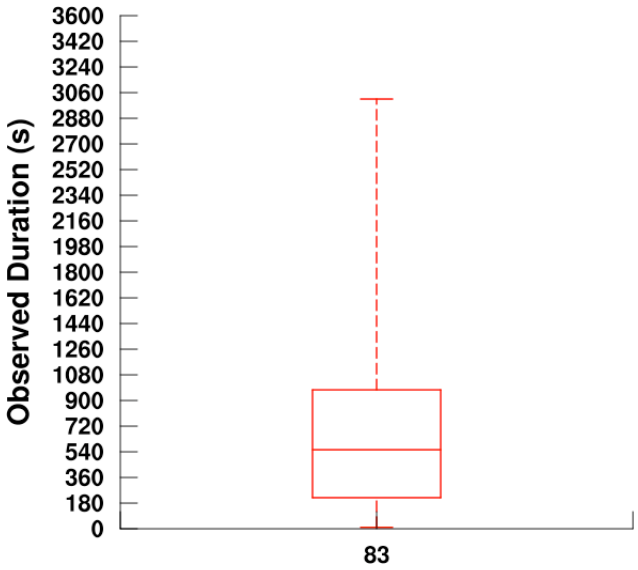

Figure 4.11. Box plots showing the distribution (5th percentile, 25th percentile, median, 75th percentile and 95th percentile) of all DOW observations of vortex tilt angle with respect to the vertical for (a) all observations and (b) observations below 500 m AGL. Sample sizes indicated for each distribution.

(a) Below 10000 m AGL

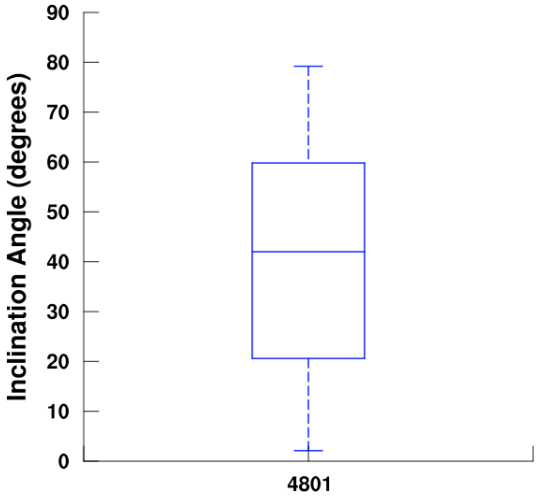

(b) Below 500 m AGL

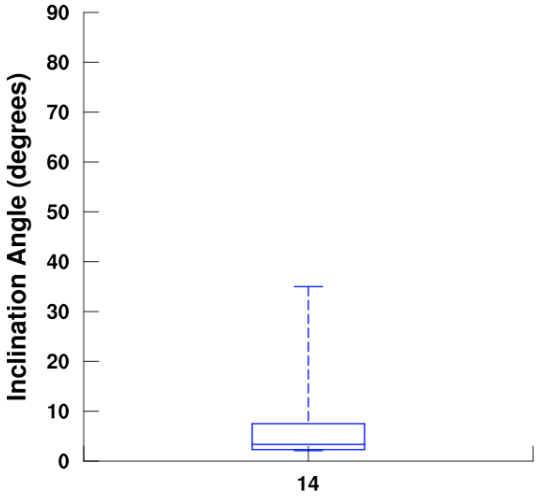

Figure 4.12. Box plots showing the distribution (minimum, 25th percentile, median, 75th percentile and maximum) of the velocity difference across the tornado core for all DOW tornado observations below (a) 500 m AGL, (b) 200 m AGL, (c) 50 m AGL and (d) maximum value for each tornado below 500 m AGL. Sample sizes indicated for each distribution.

(a) Below 500 m AGL

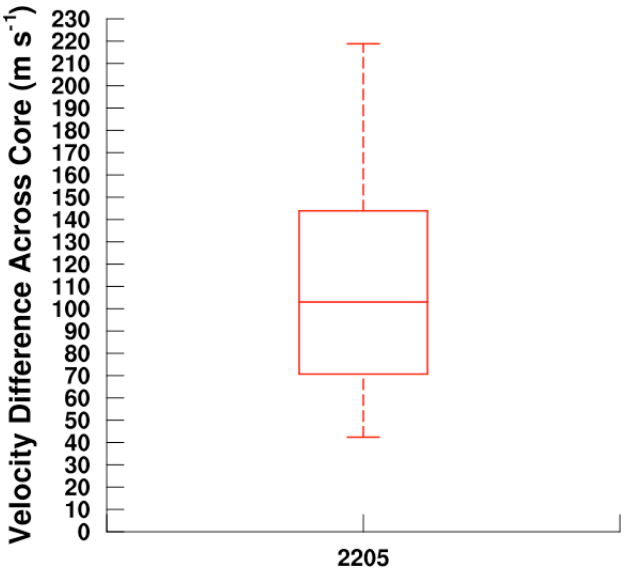

(b) Below 200 m AGL

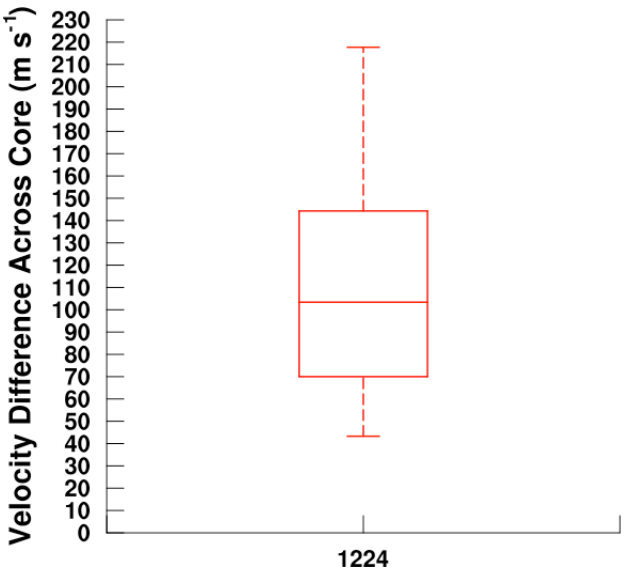

(c) Below 50 m AGL

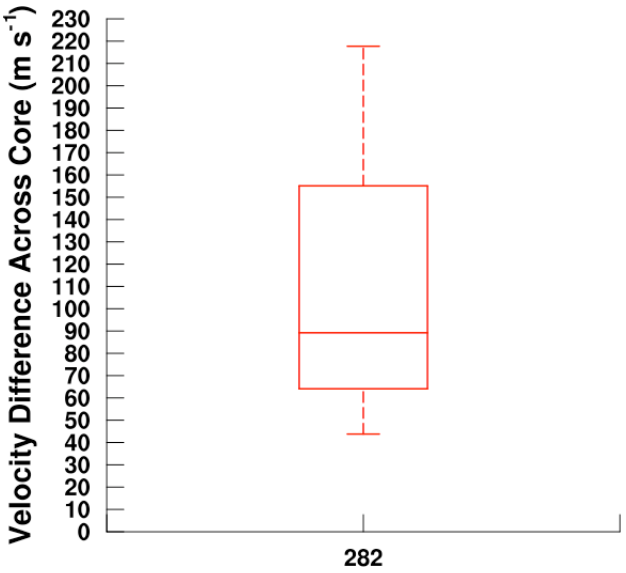

(d) Below 500 m AGL

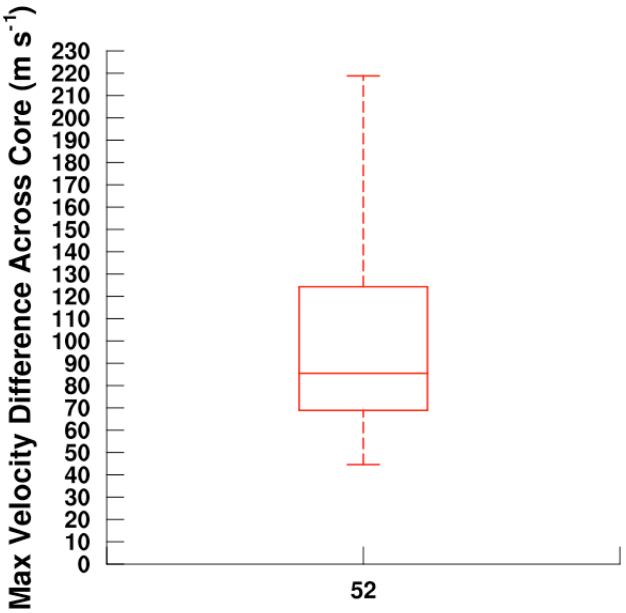

Figure 4.13. Box plots showing the distribution (minimum, 25th percentile, median, 75th percentile and maximum) of all DOW observations below (a) 500 m AGL, (b) 200 m AGL, (c) 50 m AGL and (d) diameter of maximum axisymmetric vertical vorticity below 500 m AGL. Sample sizes indicated for each distribution.

(a) Below 500 m AGL

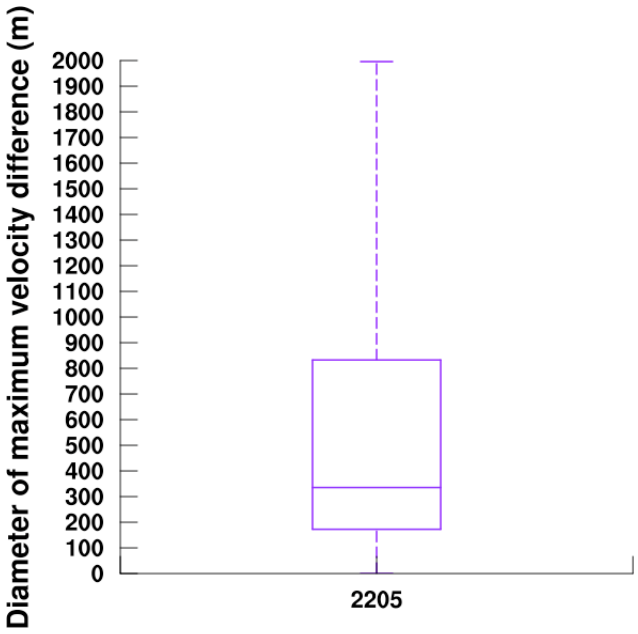

(b) Below 200 m AGL

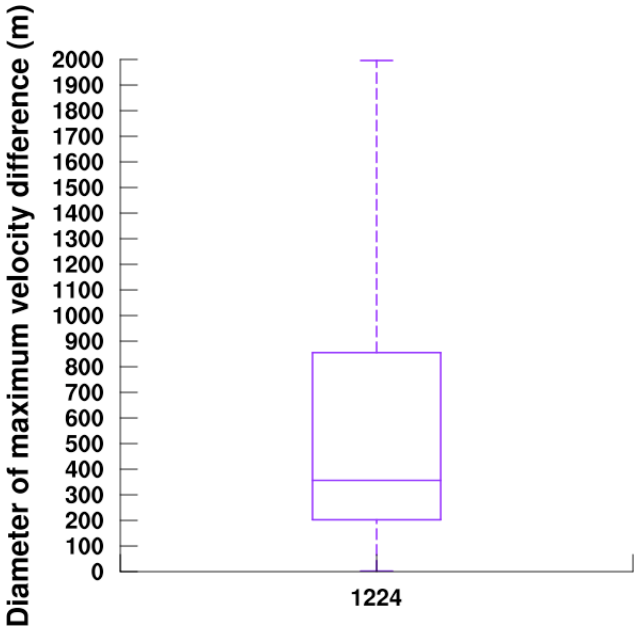

(c) Below 50 m AGL

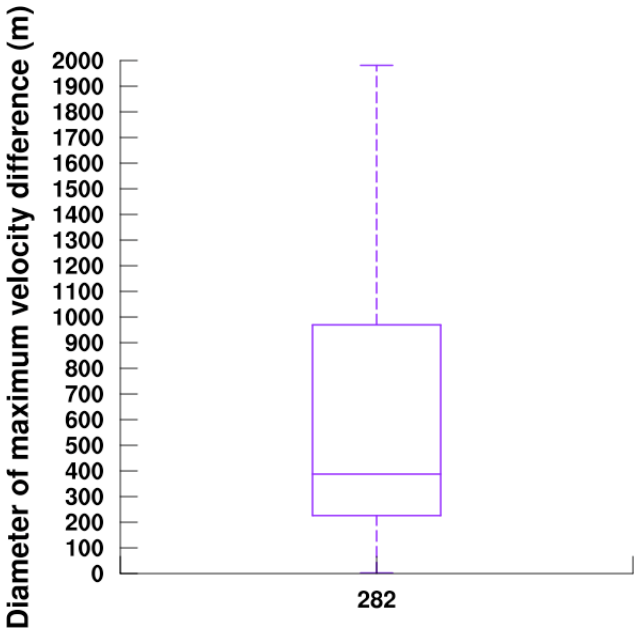

(d) Below 500 m AGL

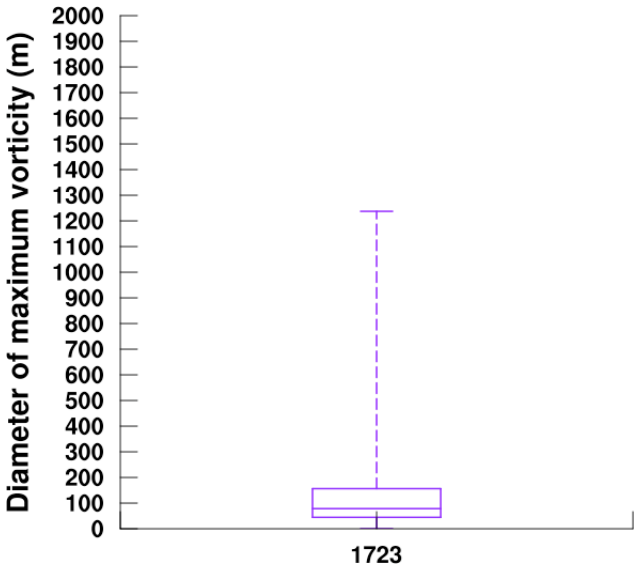

Figure 4.14. Box plots showing the distribution (5th percentile, 25th percentile, median, 75th percentile and 95th percentile) of all DOW observations below 500 m AGL for (a) axisymmetric vertical vorticity and (b) horizontal divergence across the core. Horizontal divergence is computed for tornado cores within (c) 200 m AGL, (d) 100 m AGL, (e) 50 m AGL and (f) 50 m AGL where observations with centripetal acceleration at core edge larger than 40 m s^{-2} are removed. Sample sizes indicated for each distribution.

(a) Below 500 m AGL

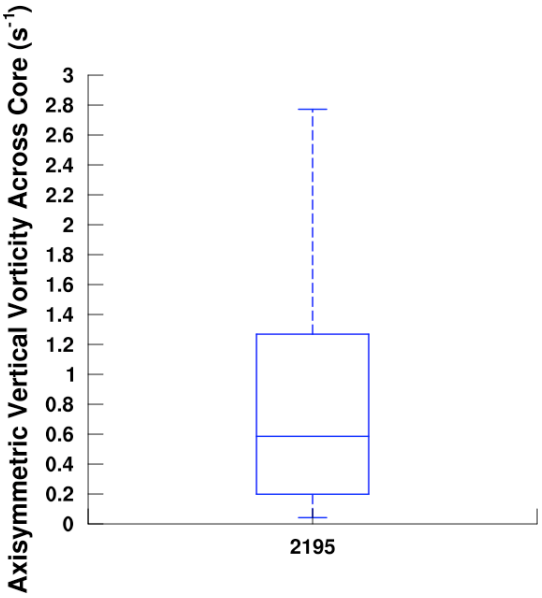

(b) Below 500 m AGL

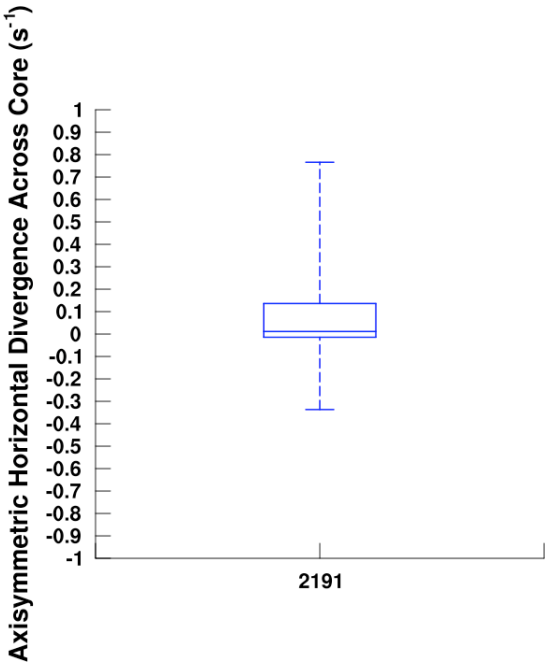

(c) Below 200 m AGL

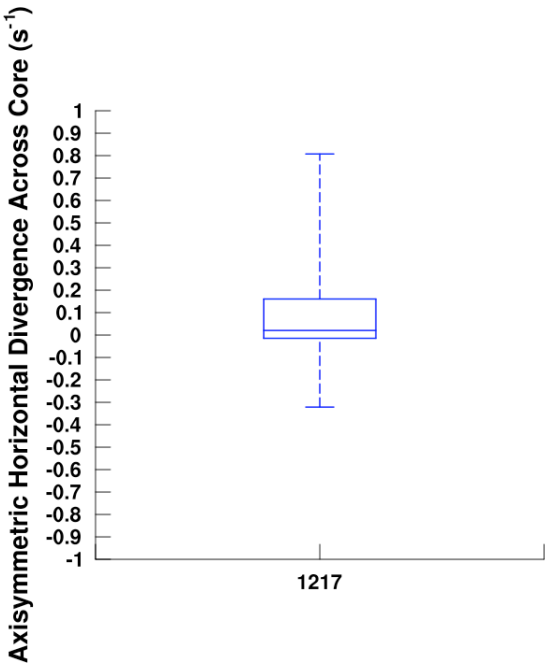

(d) Below 100 m AGL

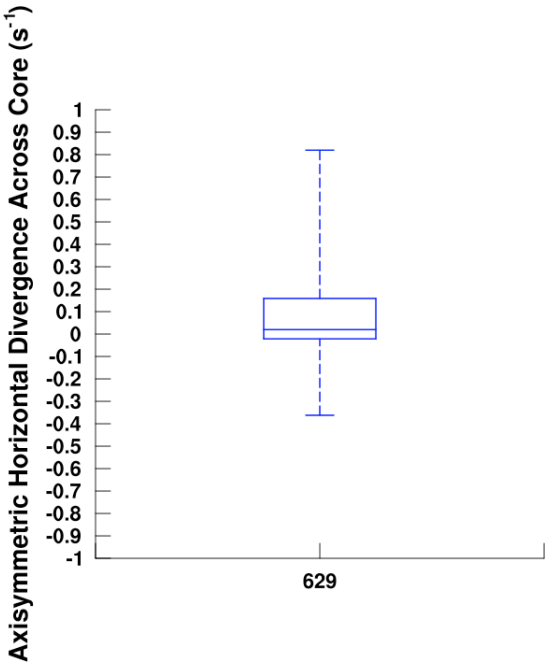

(e) Below 50 m AGL

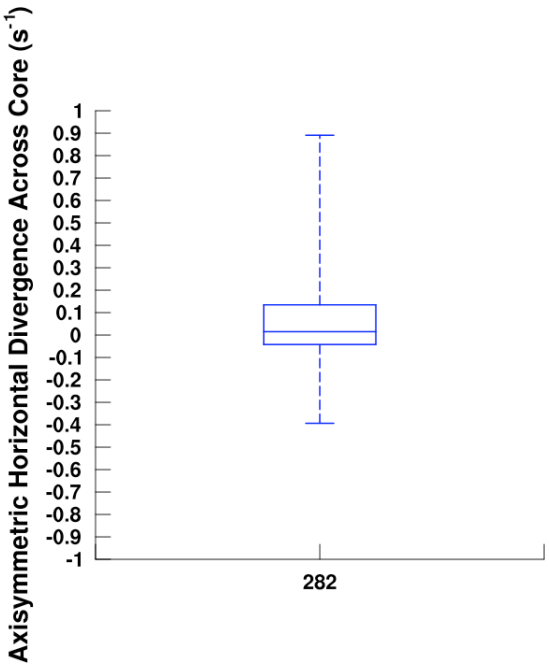

(f) Below 50 m AGL with centripetal accelerations greater than 40 m s^{-2} removed

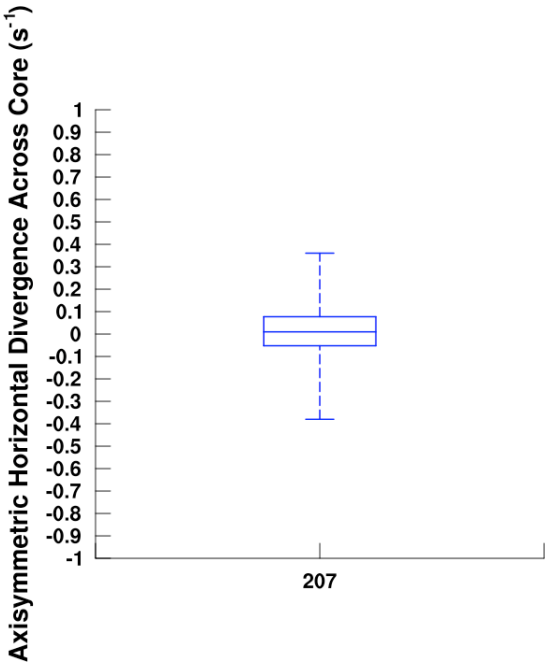

Figure 4.15. Box plots showing the distribution (5th percentile, 25th percentile, median, 75th percentile and 95th percentile) of all DOW observations below 500 m AGL for (a) circulation at the radius of maximum Doppler velocity, (b) averaged angular momentum at the core radius and (c) centripetal acceleration at the edge of the core. Sample sizes indicated for each distribution.

(a) Below 500 m AGL

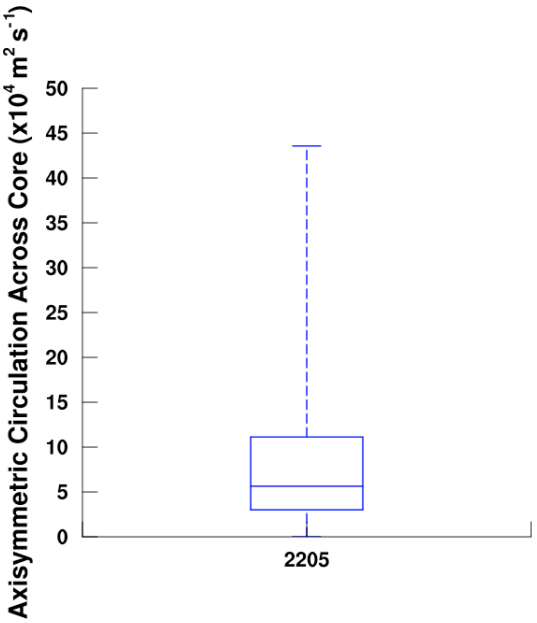

(b) Below 500 m AGL

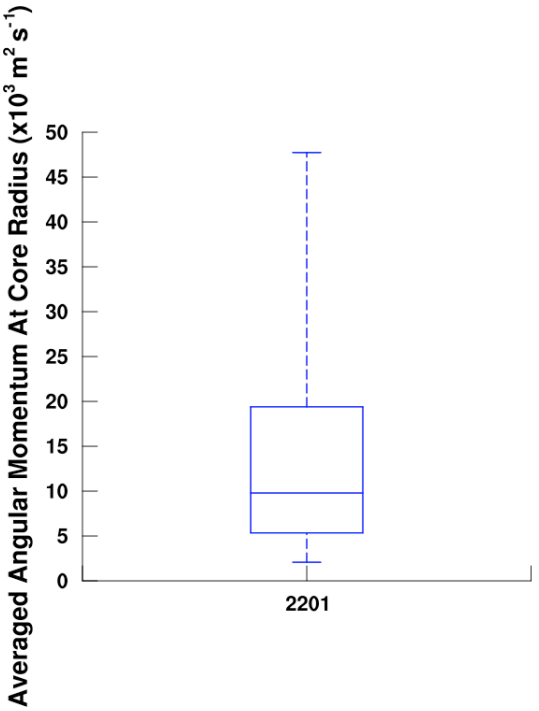

(c) Below 500 m AGL

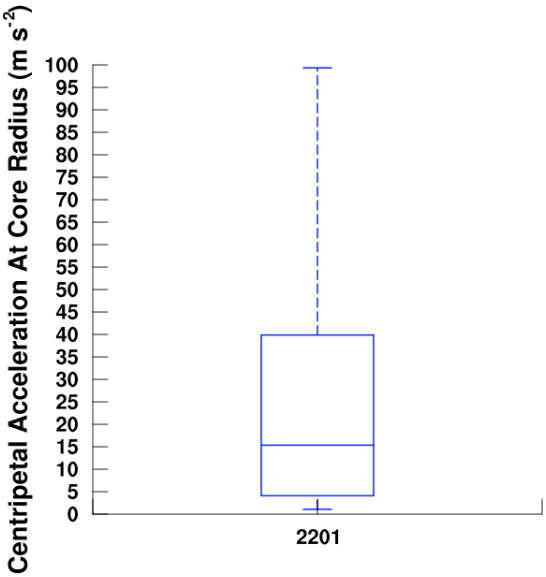

Figure 4.16. Box plots showing the distribution (5th percentile, 25th percentile, median, 75th percentile and 95th percentile) of (a) acceleration and (b) deceleration in ground-relative aspect-corrected velocity below 500 m AGL. Sample sizes indicated for each distribution.

(a) Below 500 m AGL

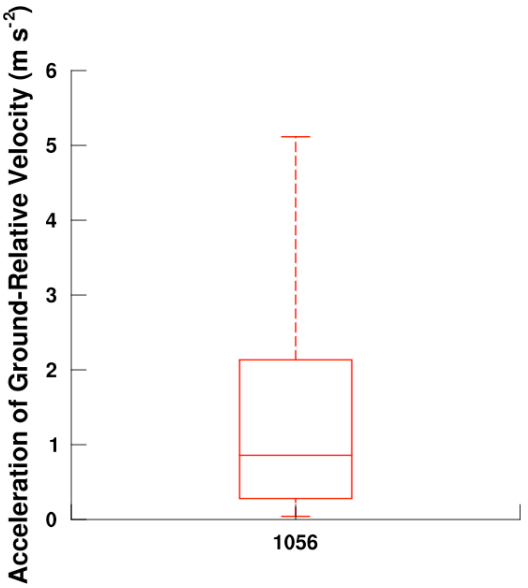

(b) Below 500 m AGL

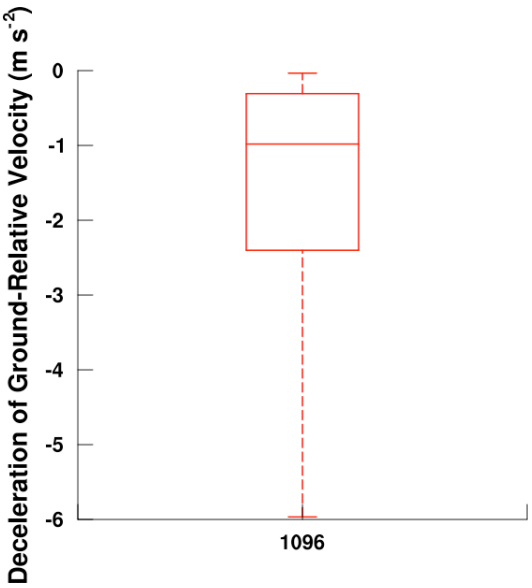

Figure 4.16. Box plots showing the distribution (5th percentile, 25th percentile, median, 75th percentile and 95th percentile) of (c) acceleration and (d) deceleration in ground-relative aspect-corrected velocity below 50 m AGL. Sample sizes indicated for each distribution.

(c) Below 50 m AGL

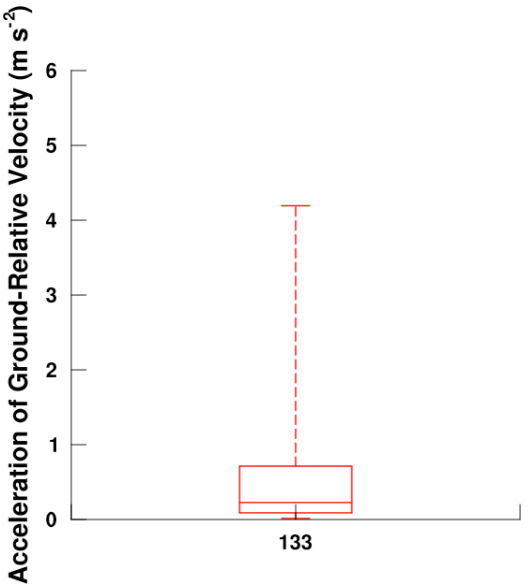

(d) Below 50 m AGL

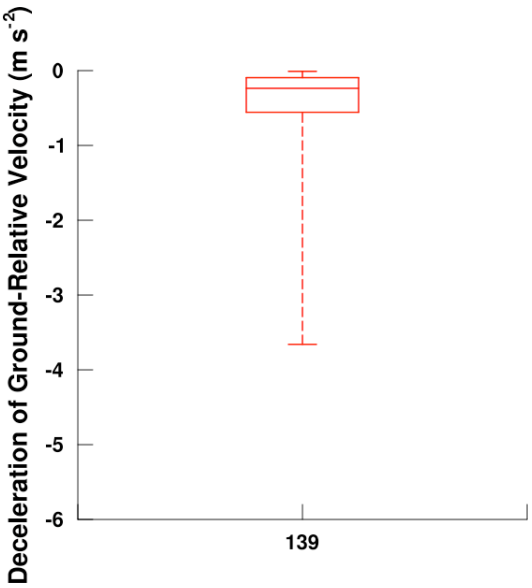

Figure 4.17. Box plots showing the distribution (5th percentile, 25th percentile, median, 75th percentile and 95th percentile) of (a) acceleration and (b) deceleration in velocity difference across the tornado core below 500 m AGL. Sample sizes indicated for each distribution.

(a) Below 500 m AGL

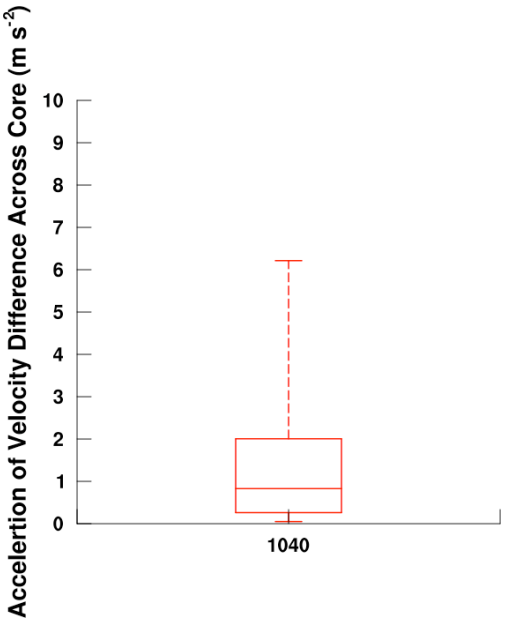

(b) Below 500 m AGL

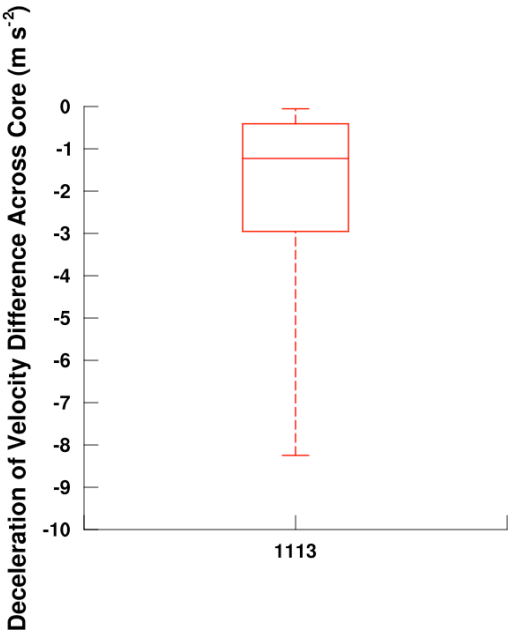

Figure 4.17. Box plots showing the distribution (5th percentile, 25th percentile, median, 75th percentile and 95th percentile) of (c) acceleration and (d) deceleration in velocity difference across the tornado core below 50 m AGL. Sample sizes indicated for each distribution.

(c) Below 50 m AGL

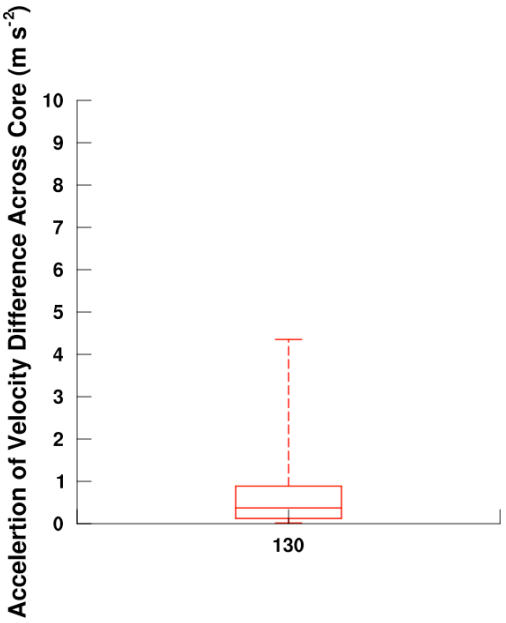

(d) Below 50 m AGL

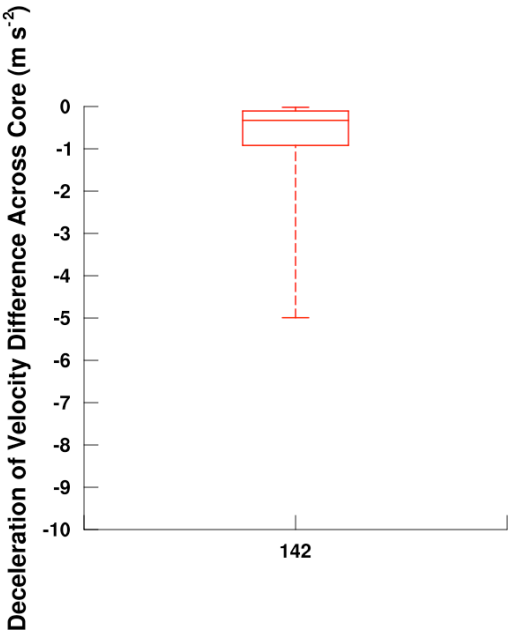

Figure 4.18. Box plots showing the distribution (5th percentile, 25th percentile, median, 75th percentile and 95th percentile) of (a) expansion and (b) contraction in tornado core diameter for all observations below 500 m AGL. Sample sizes indicated for each distribution.

(a) Below 500 m AGL

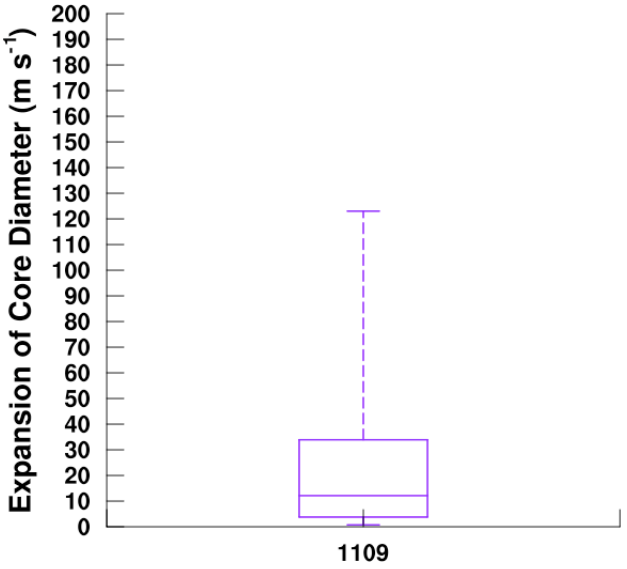

(b) Below 500 m AGL

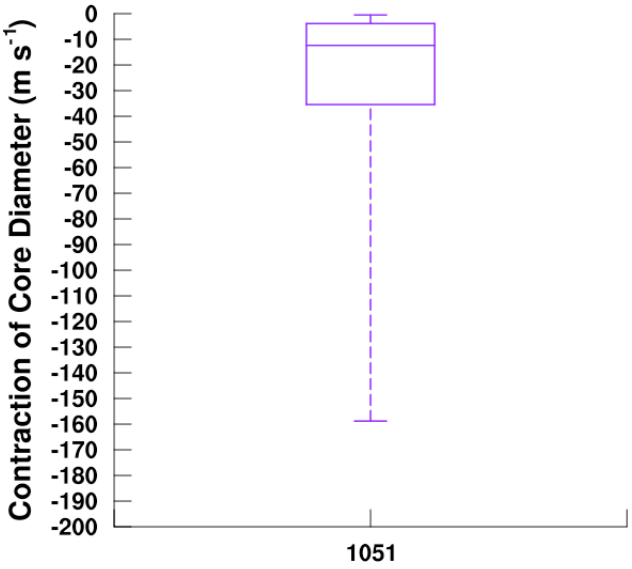

Figure 4.18. Box plots showing the distribution (5th percentile, 25th percentile, median, 75th percentile and 95th percentile) of (c) expansion and (d) contraction in tornado core diameter for all observations below 50 m AGL. Sample sizes indicated for each distribution.

(c) Below 50 m AGL

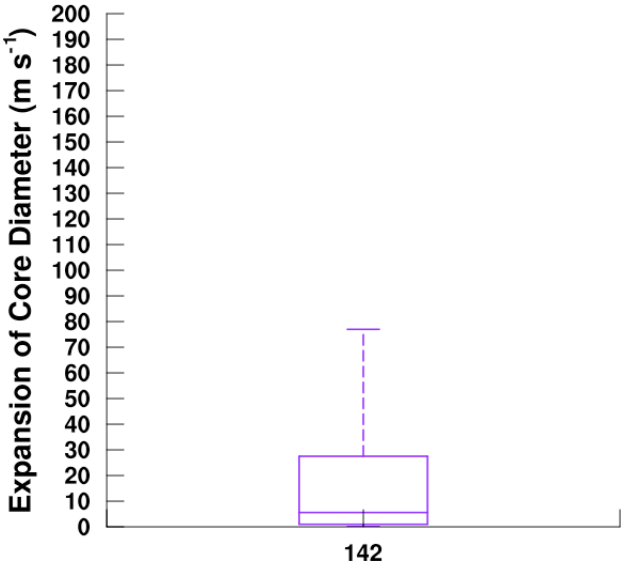

(d) Below 50 m AGL

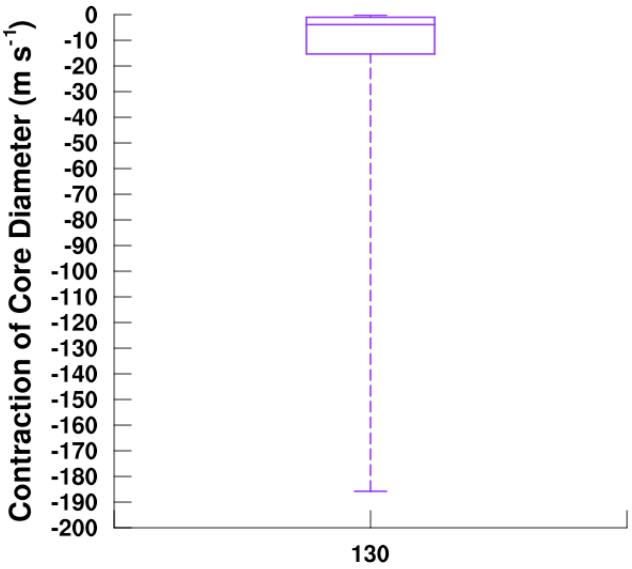

Figure 4.19. Box plots showing the distribution (5th percentile, 25th percentile, median, 75th percentile and 95th percentile) of (a) strengthening and (b) weakening axisymmetric vertical vorticity across the vortex core for observations below 500 m AGL. Sample sizes indicated for each distribution.

(a) Below 500 m AGL

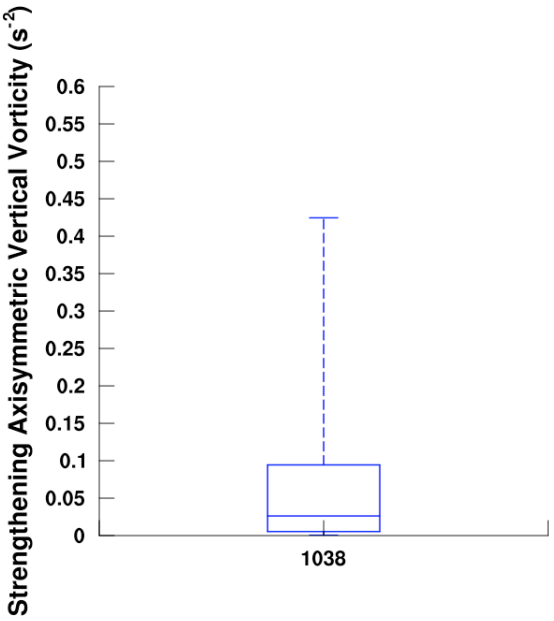

(b) Below 500 m AGL

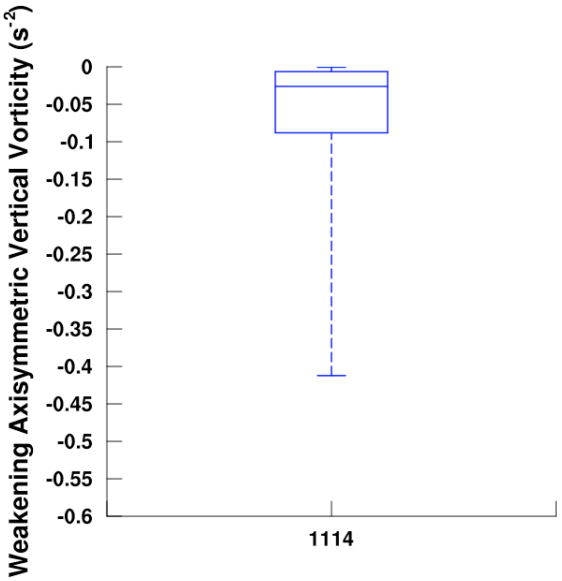

Figure 4.19. Box plots showing the distribution (5th percentile, 25th percentile, median, 75th percentile and 95th percentile) of (c) strengthening and (d) weakening axisymmetric vertical vorticity across the vortex core for observations below 50 m AGL. Sample sizes indicated for each distribution.

(c) Below 50 m AGL

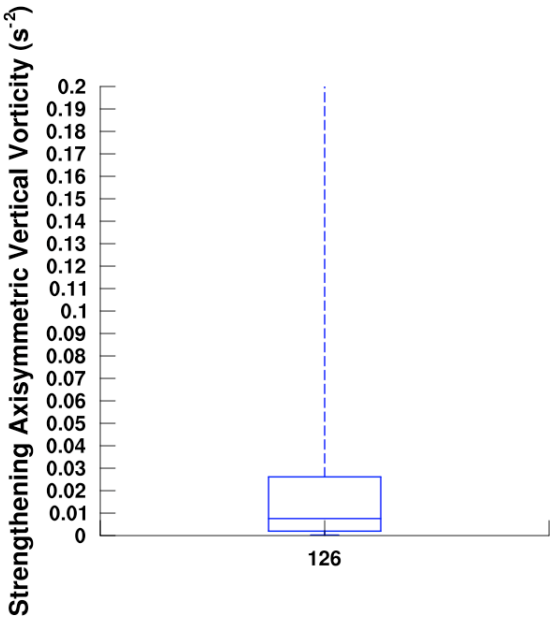

(d) Below 50 m AGL

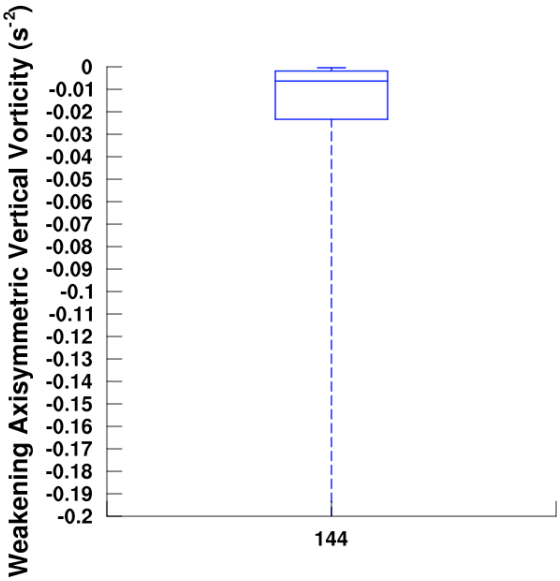

Figure 4.20. Scatter plots showing correlation between all DOW observations of velocity difference across core and elevation of vortex center AGL below (a) 10000 m, (b) 1000 m, (c) 500 m, (d) 200 m, (e) 100 m and (f) 50 m AGL. The average velocity difference in each layer (solid line) along with one standard deviation from the average (dashed lines) is overlaid. The correlation coefficients for linear fits are shown.

(a)

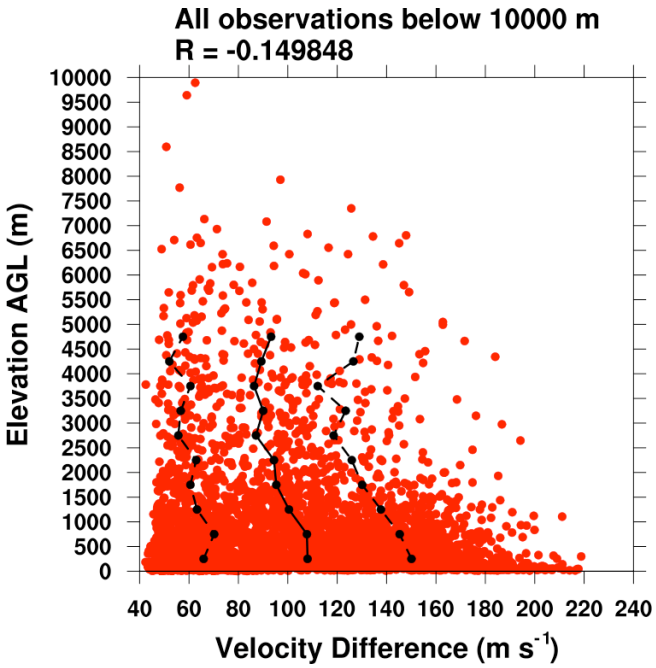

(b)

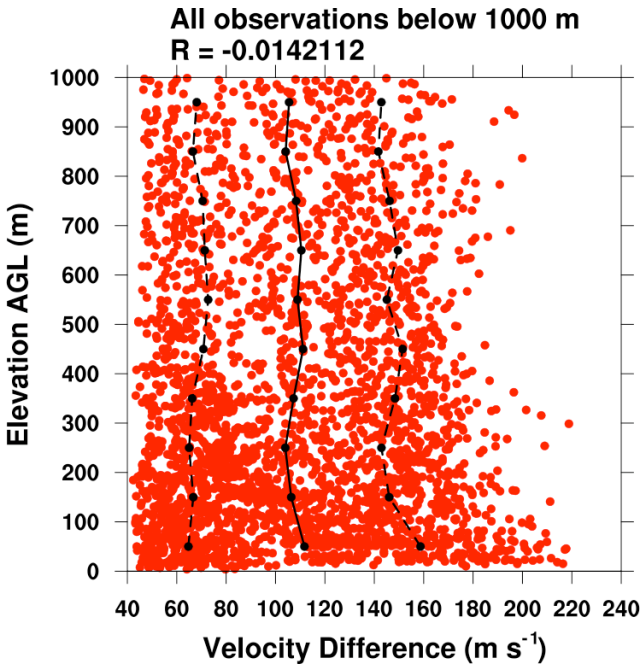
All observations below 1000 m
R = -0.0142112
Elevation AGL (m)
Velocity Difference (m s-1)

(c)

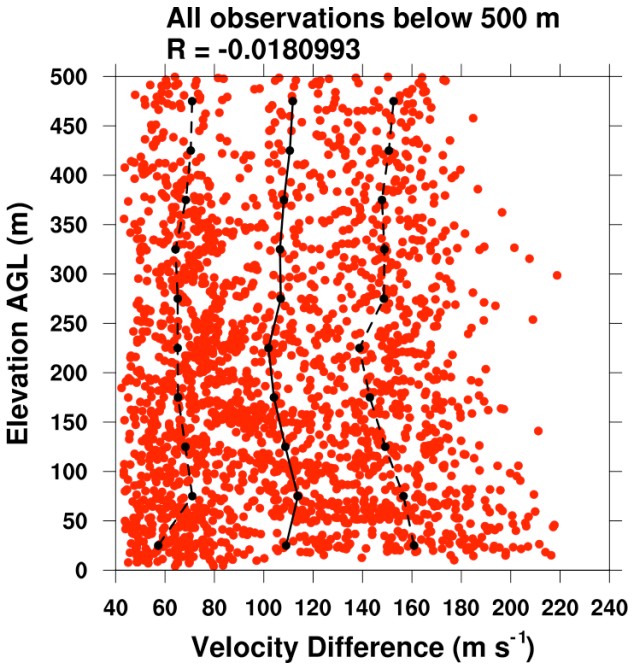
All observations below 500 m
R = -0.0180993
Elevation AGL (m)
Velocity Difference (m s-1)

(d)

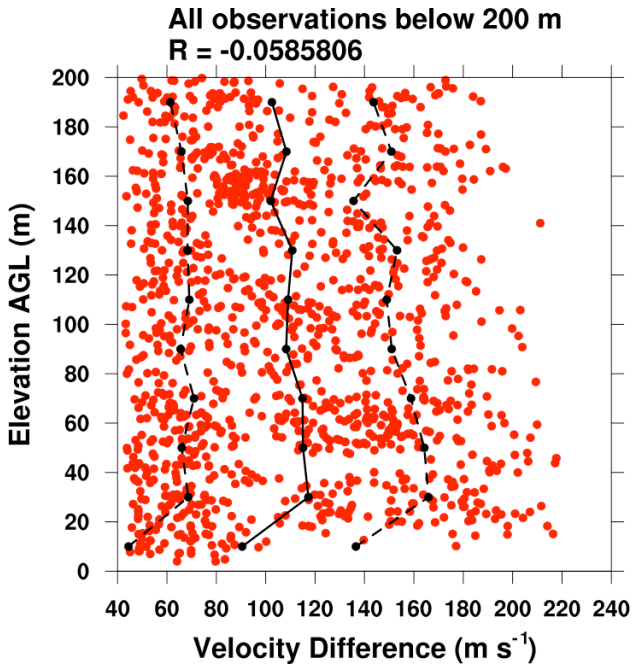
All observations below 200 m
R = -0.0585806
Elevation AGL (m)
Velocity Difference (m s-1)
0
20
40
60
80
100
120
140
160
180
200
40
60
80
100
120
140
160
180
200
220
240

(e)

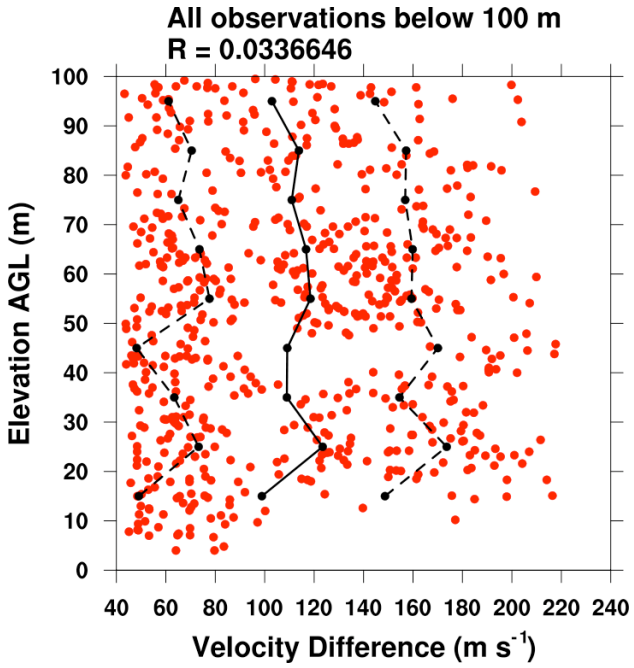
All observations below 100 m
R = 0.0336646
Elevation AGL (m)
Velocity Difference (m s-1)
0
10
20
30
40
50
60
70
80
90
100
40
60
80
100
120
140
160
180
200
220
240

(f)

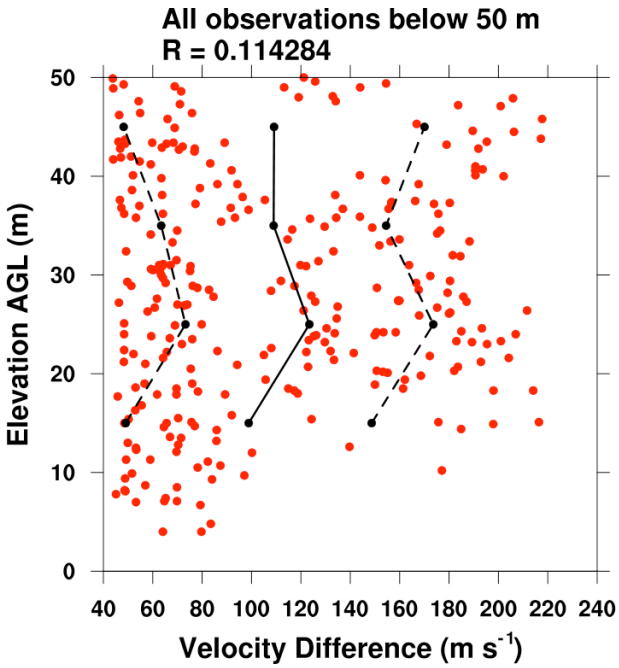
All observations below 50 m
R = 0.114284
Elevation AGL (m)
0
10
20
30
40
50
40 60 80 100 120 140 160 180 200 220 240
Velocity Difference (m s-1)

Figure 4.21. Scatter plots showing correlation between all DOW observations of normalized velocity difference across core and elevation of vortex center AGL below (a) 10000 m, (b) 1000 m, (c) 500 m, (d) 200 m, (e) 100 m and (f) 50 m AGL. Velocity difference values are normalized relative to the maximum observed velocity difference for a given tornado. The average normalized velocity difference in each layer (solid line) along with one standard deviation from the average (dashed lines) is overlaid. The correlation coefficients for linear fits are shown.

(a)

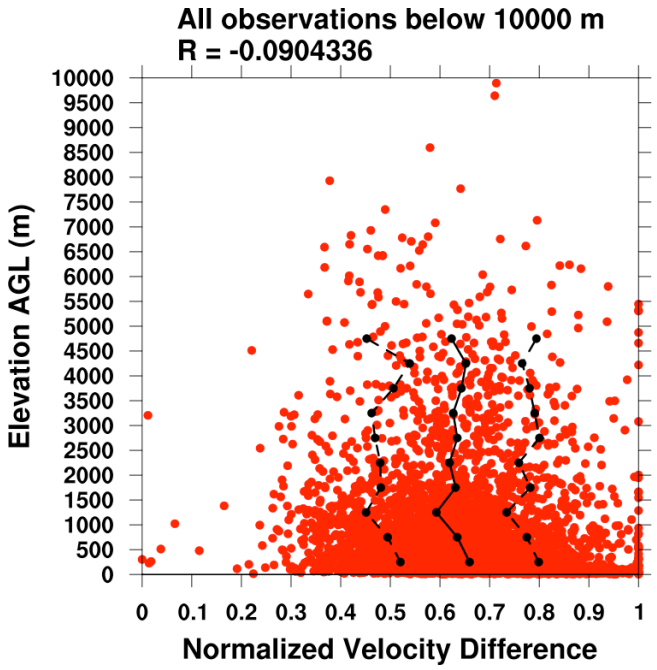

(b)

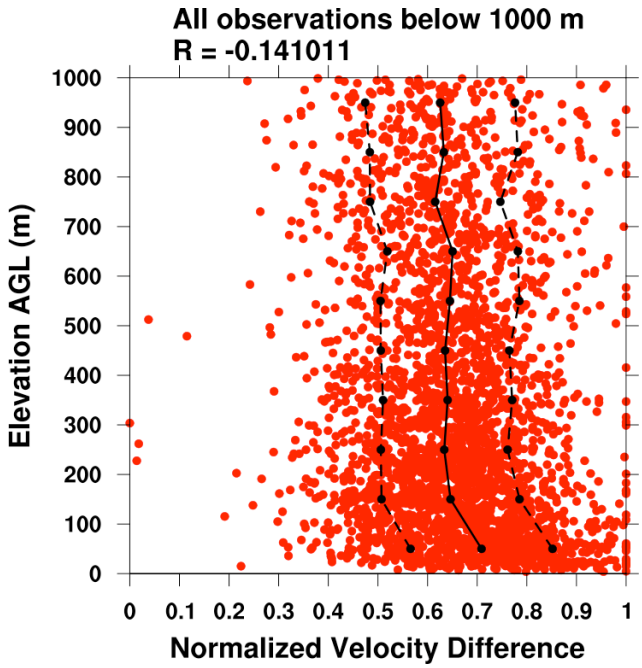
All observations below 1000 m
R = -0.141011
Elevation AGL (m)
1000
900
800
700
600
500
400
300
200
100
0
0 0.1 0.2 0.3 0.4 0.5 0.6 0.7 0.8 0.9 1
Normalized Velocity Difference

(c)

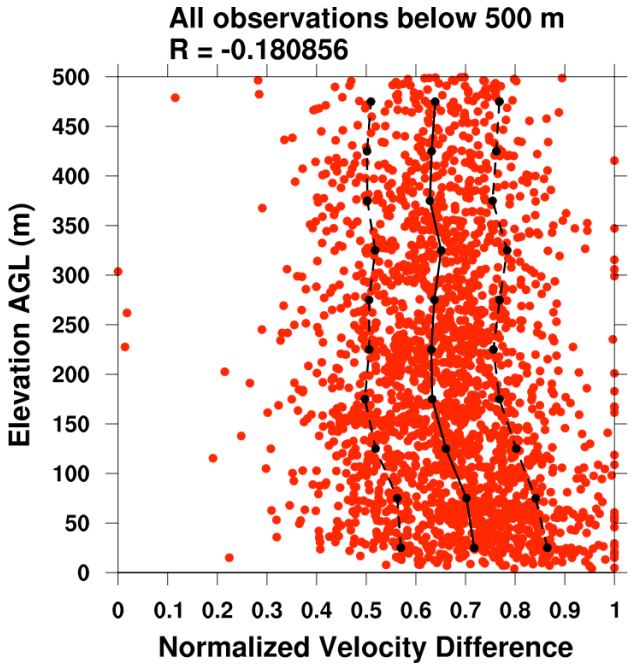
All observations below 500 m
R = -0.180856
Elevation AGL (m)
500
450
400
350
300
250
200
150
100
50
0
0 0.1 0.2 0.3 0.4 0.5 0.6 0.7 0.8 0.9 1
Normalized Velocity Difference

(d)

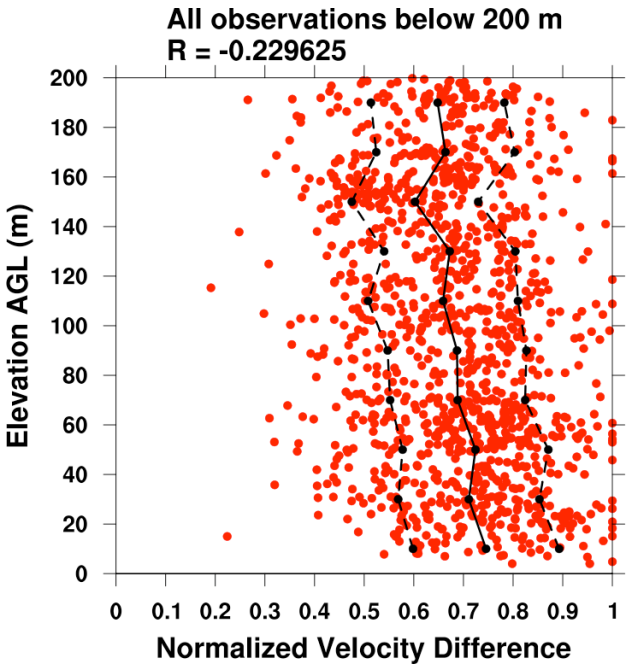
All observations below 200 m
R = -0.229625
Elevation AGL (m)
200
180
160
140
120
100
80
60
40
20
0
0 0.1 0.2 0.3 0.4 0.5 0.6 0.7 0.8 0.9 1
Normalized Velocity Difference

(e)

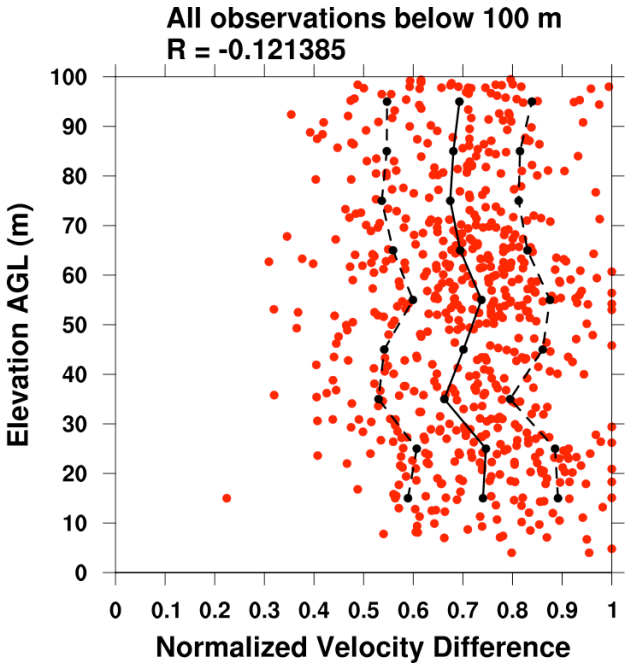
All observations below 100 m
R = -0.121385
Elevation AGL (m)
100
90
80
70
60
50
40
30
20
10
0
0 0.1 0.2 0.3 0.4 0.5 0.6 0.7 0.8 0.9 1
Normalized Velocity Difference

(f)

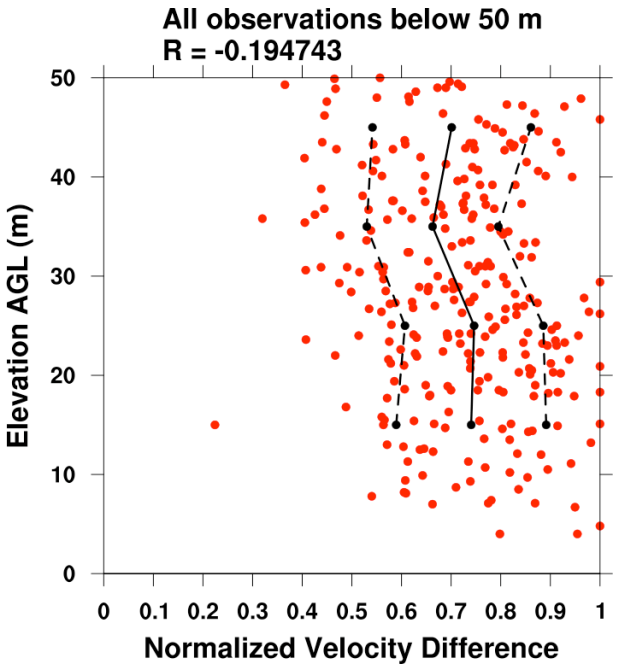
All observations below 50 m
R = -0.194743
Elevation AGL (m)
50
40
30
20
10
0
0
0.1
0.2
0.3
0.4
0.5
0.6
0.7
0.8
0.9
1
Normalized Velocity Difference

Figure 4.22. Scatter plots showing correlation between all DOW observations of aspect-corrected ground-relative velocity below (a) 10000 m, (b) 1000 m, (c) 500 m, (d) 200 m, (e) 100 m and (f) 50 m AGL. The average ground-relative velocity in each layer (solid line) along with one standard deviation from the average (dashed lines) is overlaid. The correlation coefficients for linear fits are shown.

(a)

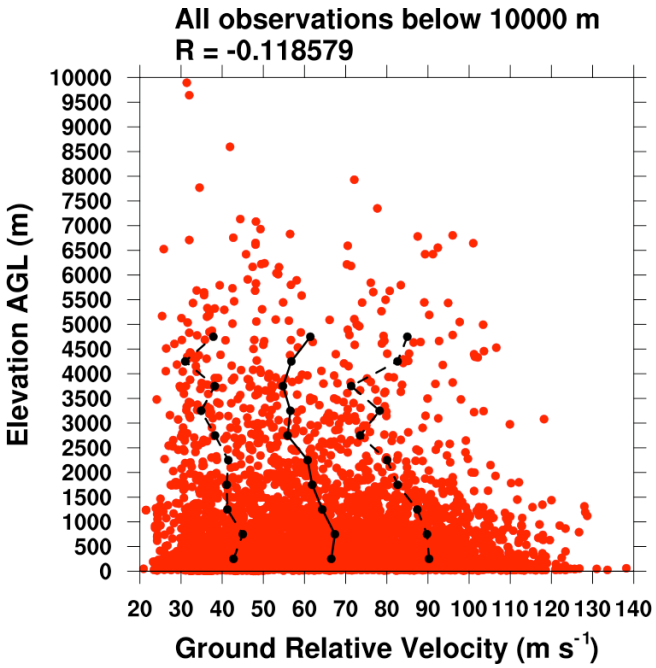

(b)

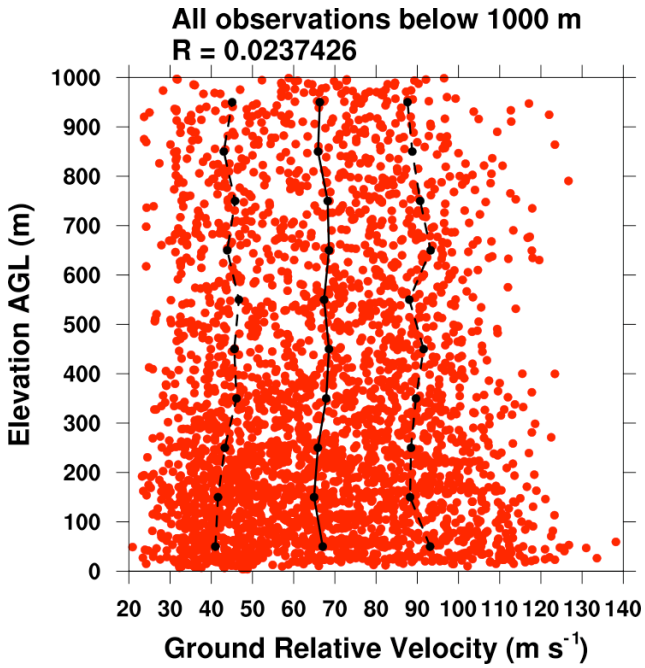
All observations below 1000 m
R = 0.0237426
Elevation AGL (m)
1000
900
800
700
600
500
400
300
200
100
0
20 30 40 50 60 70 80 90 100 110 120 130 140
Ground Relative Velocity (m s-1)

(c)

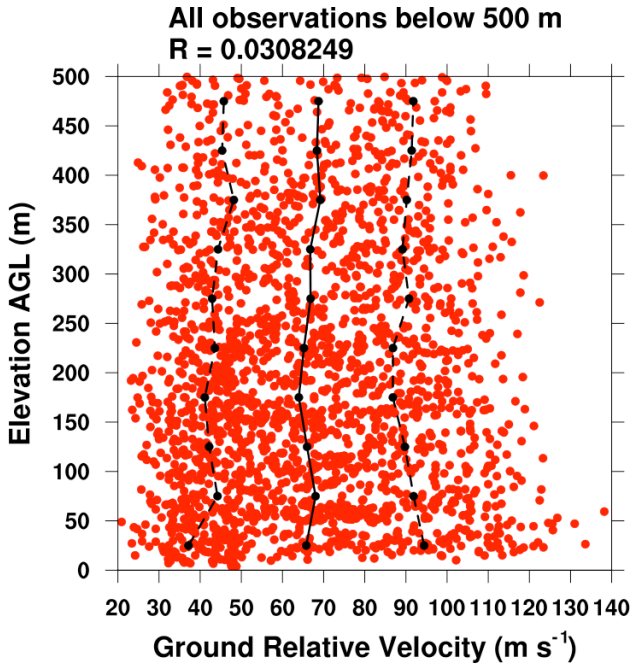
All observations below 500 m
R = 0.0308249
Elevation AGL (m)
500
450
400
350
300
250
200
150
100
50
0
20 30 40 50 60 70 80 90 100 110 120 130 140
Ground Relative Velocity (m s-1)

(d)

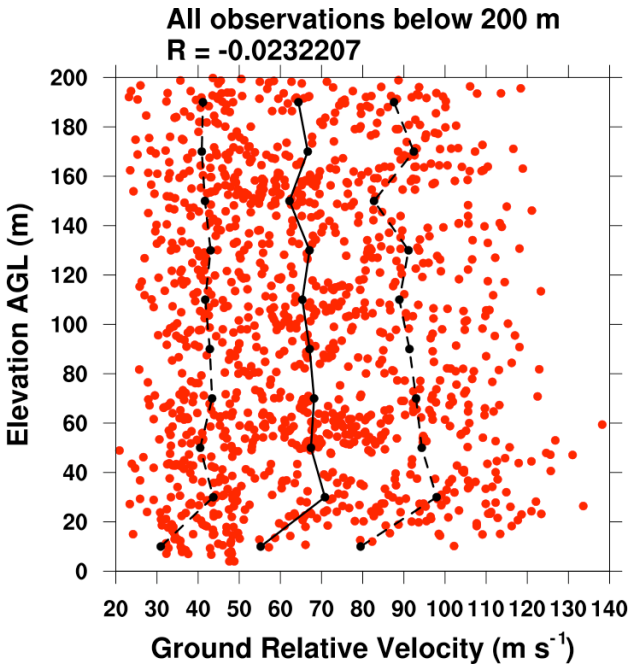
All observations below 200 m
R = -0.0232207
Elevation AGL (m)
0
20
40
60
80
100
120
140
160
180
200
20 30 40 50 60 70 80 90 100 110 120 130 140
Ground Relative Velocity (m s-1)

(e)

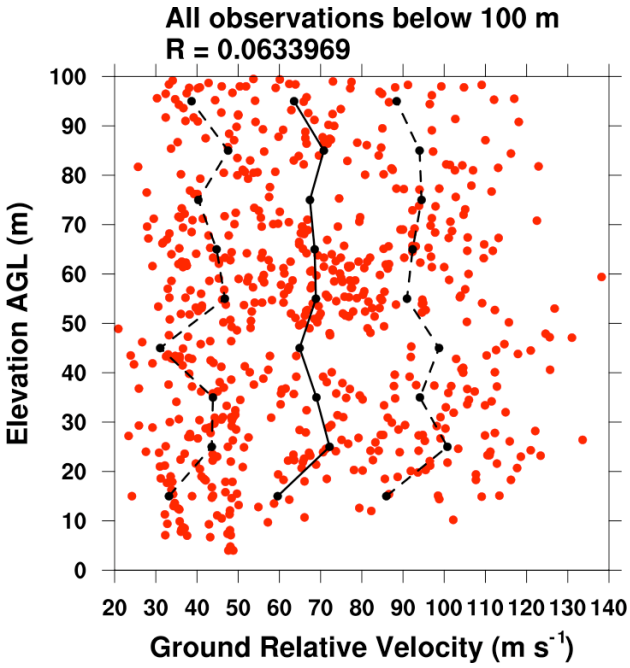
All observations below 100 m
R = 0.0633969
Elevation AGL (m)
0
10
20
30
40
50
60
70
80
90
100
20 30 40 50 60 70 80 90 100 110 120 130 140
Ground Relative Velocity (m s-1)

(f)

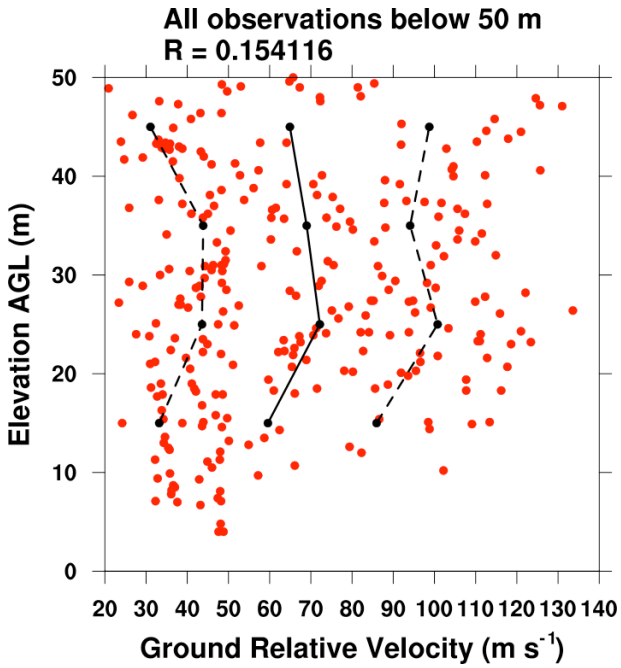
All observations below 50 m
R = 0.154116
Elevation AGL (m)
0
10
20
30
40
50
20 30 40 50 60 70 80 90 100 110 120 130 140
Ground Relative Velocity (m s-1)

Figure 4.23. Scatter plots showing correlation between all DOW observations of normalized aspect-corrected ground-relative velocity below (a) 10000 m, (b) 1000 m, (c) 500 m, (d) 200 m, (e) 100 m and (f) 50 m AGL. Velocity values are normalized relative to the maximum observed aspect-corrected ground-relative velocity for a given tornado. The average normalized ground-relative velocity in each layer (solid line) along with one standard deviation from the average (dashed lines) is overlaid. The correlation coefficients for linear fits are shown.

(a)

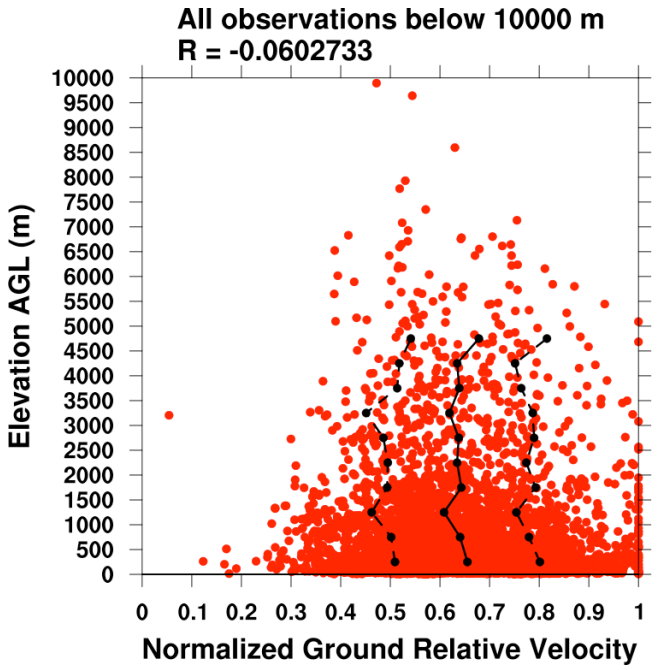

(b)

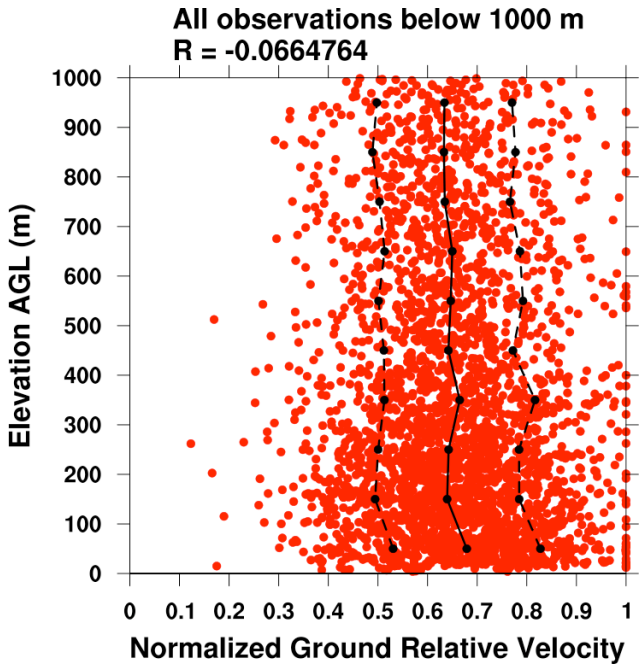
All observations below 1000 m
R = -0.0664764
Elevation AGL (m)
1000
900
800
700
600
500
400
300
200
100
0
0 0.1 0.2 0.3 0.4 0.5 0.6 0.7 0.8 0.9 1
Normalized Ground Relative Velocity

(c)

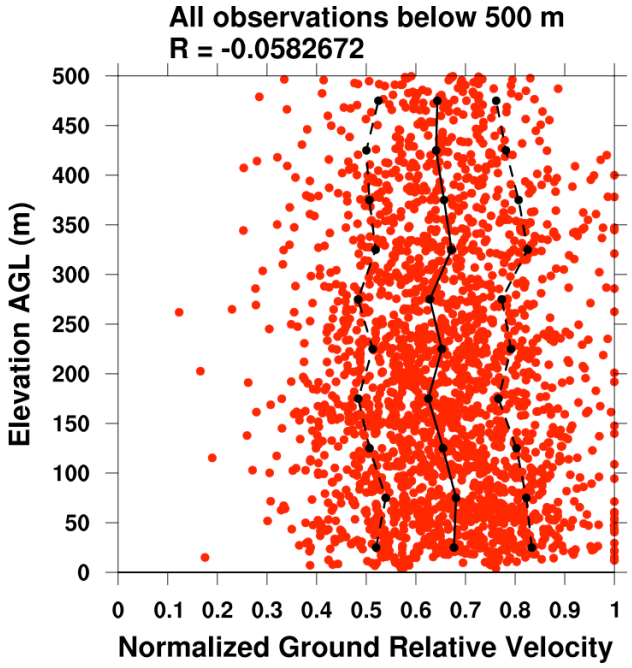
All observations below 500 m
R = -0.0582672
Elevation AGL (m)
500
450
400
350
300
250
200
150
100
50
0
0 0.1 0.2 0.3 0.4 0.5 0.6 0.7 0.8 0.9 1
Normalized Ground Relative Velocity

(d)

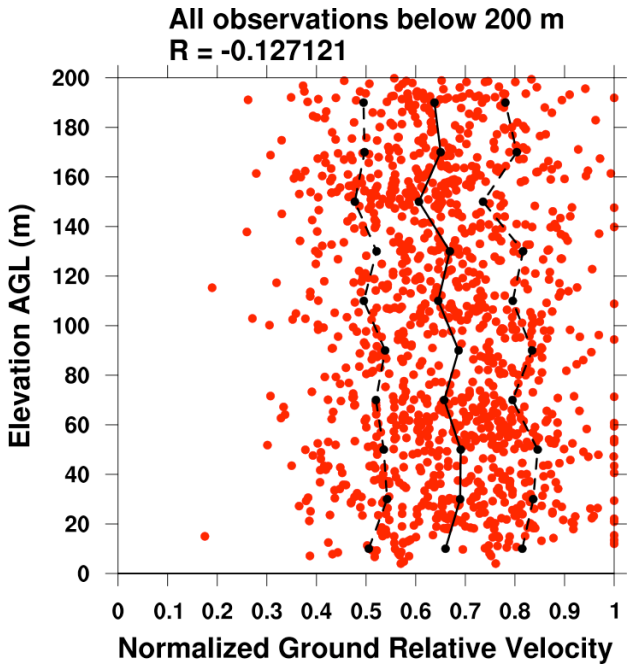
All observations below 200 m
R = -0.127121
Elevation AGL (m)
200
180
160
140
120
100
80
60
40
20
0
0 0.1 0.2 0.3 0.4 0.5 0.6 0.7 0.8 0.9 1
Normalized Ground Relative Velocity

(e)

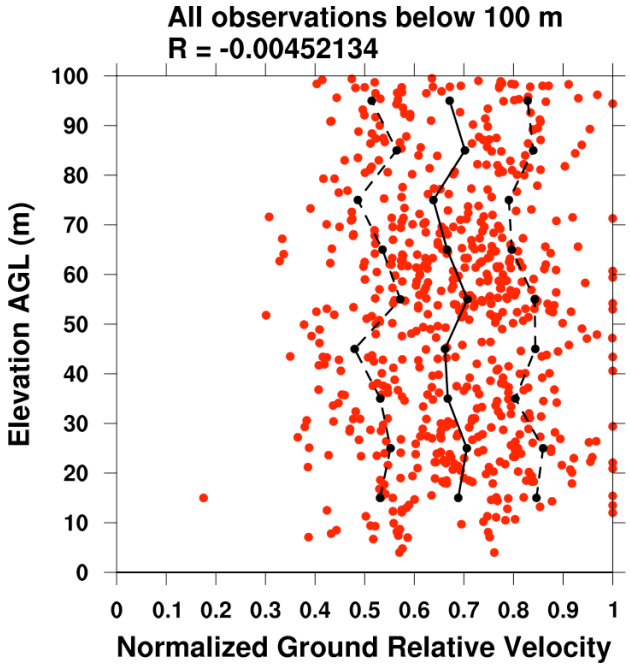
All observations below 100 m
R = -0.00452134
Elevation AGL (m)
100
90
80
70
60
50
40
30
20
10
0
0 0.1 0.2 0.3 0.4 0.5 0.6 0.7 0.8 0.9 1
Normalized Ground Relative Velocity

(f)

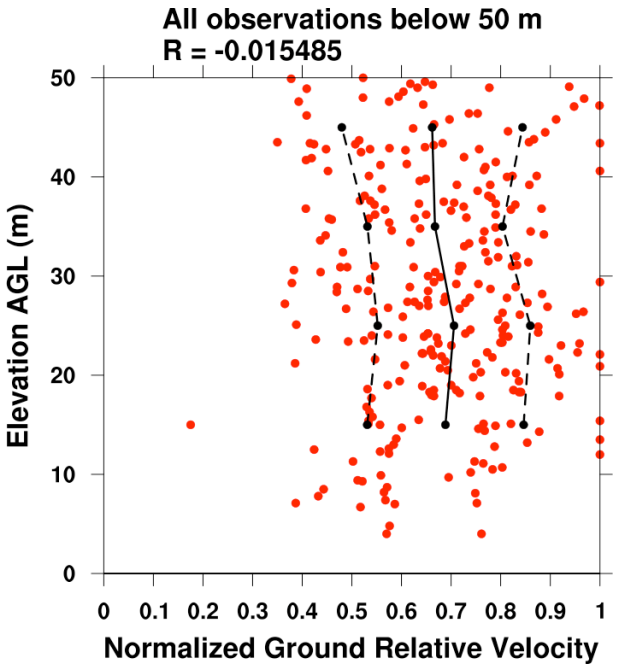
All observations below 50 m
R = -0.015485
Elevation AGL (m)
50
40
30
20
10
0
0
0.1
0.2
0.3
0.4
0.5
0.6
0.7
0.8
0.9
1
Normalized Ground Relative Velocity

Figure 4.24. Scatter plot showing correlation between all DOW observations of velocity difference across the core and core diameter for diameters between (a) 0-2000 m, (b) 0-700 m, and (c) 700-2000 m. The average velocity difference in each 100 m diameter bin (black solid line) along with one standard deviation from the average (black dashed lines) is overlaid. The diameter of the maximum averaged value is denoted (blue dashed vertical lines). The correlation coefficients for linear fits are shown.

(a)

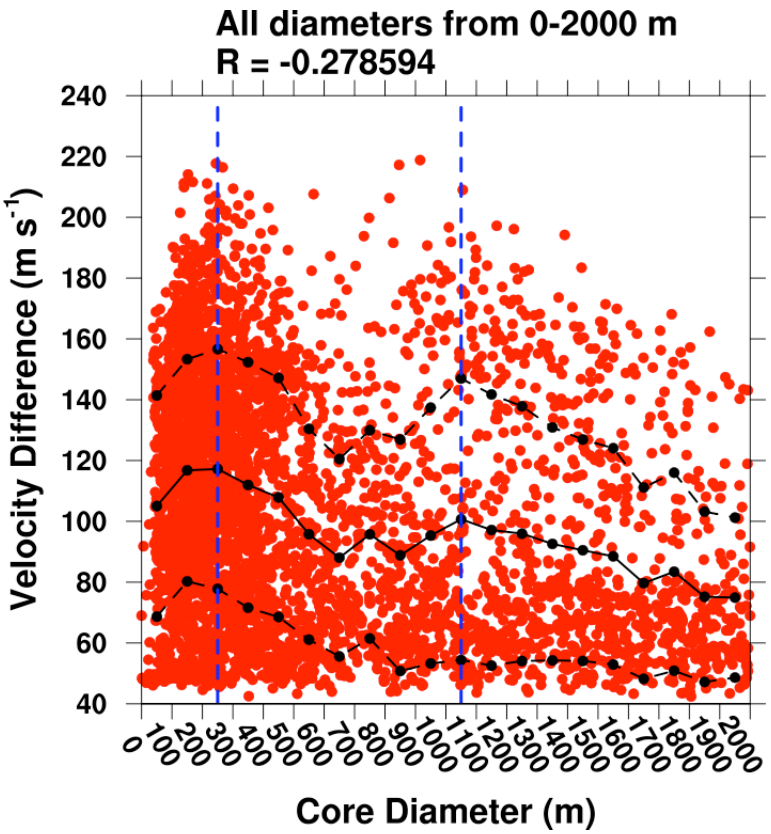

(b)

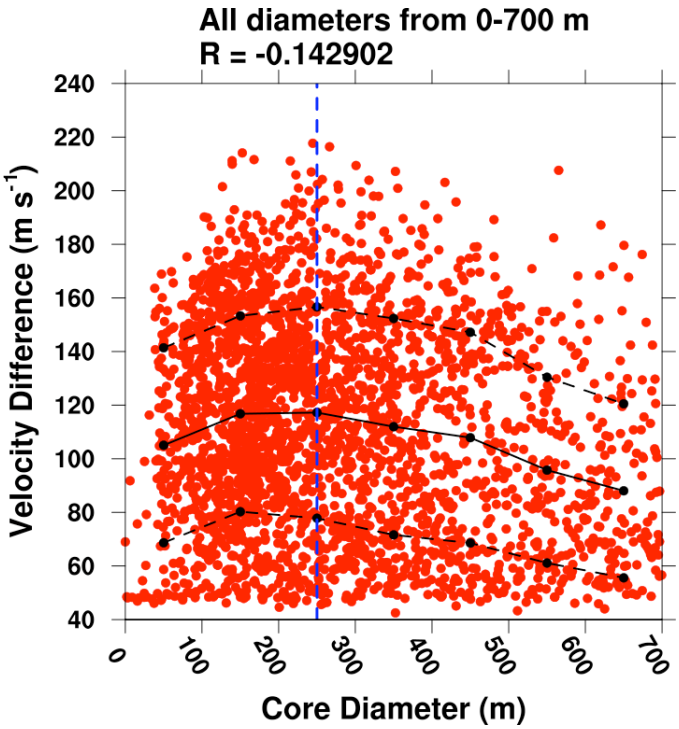
All diameters from 0-700 m
R = -0.142902
Velocity Difference (m s-1)
240
220
200
180
160
140
120
100
80
60
40
0
100
200
300
400
500
600
700
Core Diameter (m)

(c)

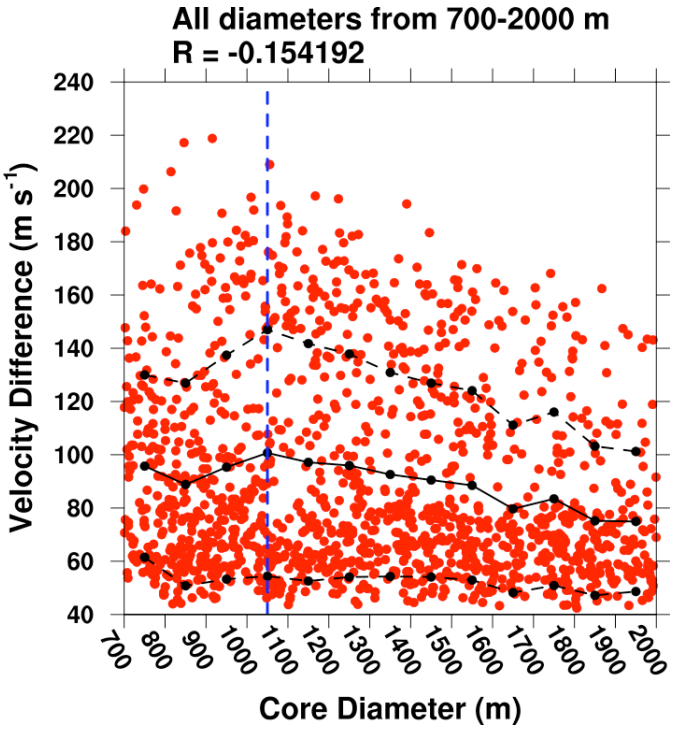
All diameters from 700-2000 m
R = -0.154192
Velocity Difference (m s-1)
240
220
200
180
160
140
120
100
80
60
40
700
800
900
1000
1100
1200
1300
1400
1500
1600
1700
1800
1900
2000
Core Diameter (m)

Figure 4.25. Scatter plot showing correlation between all DOW observations of (a) difference in magnitude between maximum outbound and maximum inbound Doppler velocity and elevation AGL, (b) tornado heading relative to azimuth angle and elevation AGL, and (c) tornado heading relative to azimuth angle and elevation AGL only for observations where the radar was stationary and deployed. All positive (negative) angles measured clockwise (counterclockwise) from true north. The correlation coefficient for linear fit is shown.

(a)

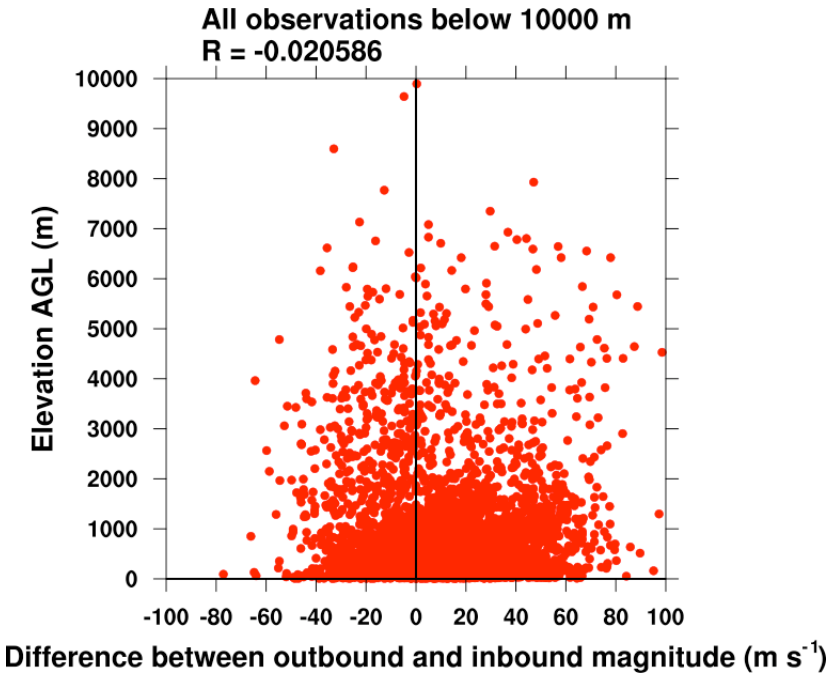

(b)

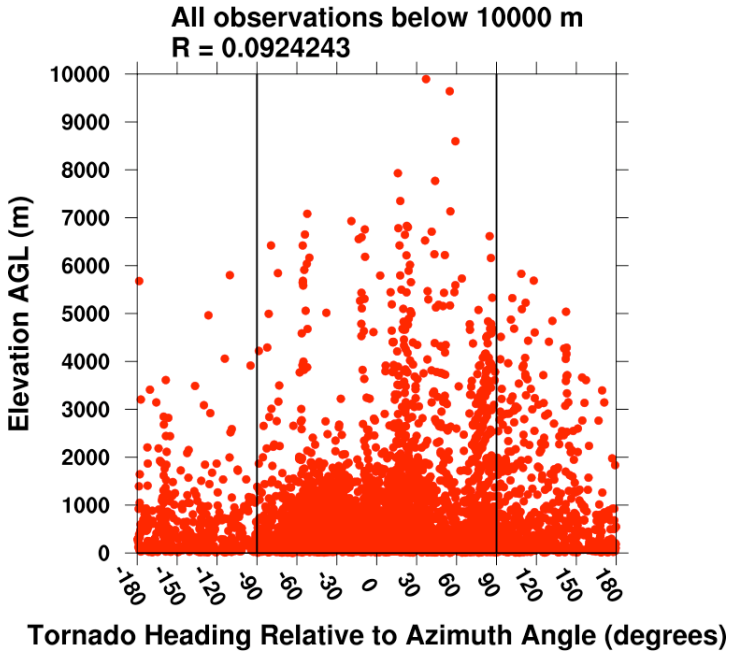
All observations below 10000 m
R = 0.0924243
Elevation AGL (m)
10000
9000
8000
7000
6000
5000
4000
3000
2000
1000
0
-180
-150
-120
-90
-60
-30
0
30
60
90
120
150
180
Tornado Heading Relative to Azimuth Angle (degrees)

(c)

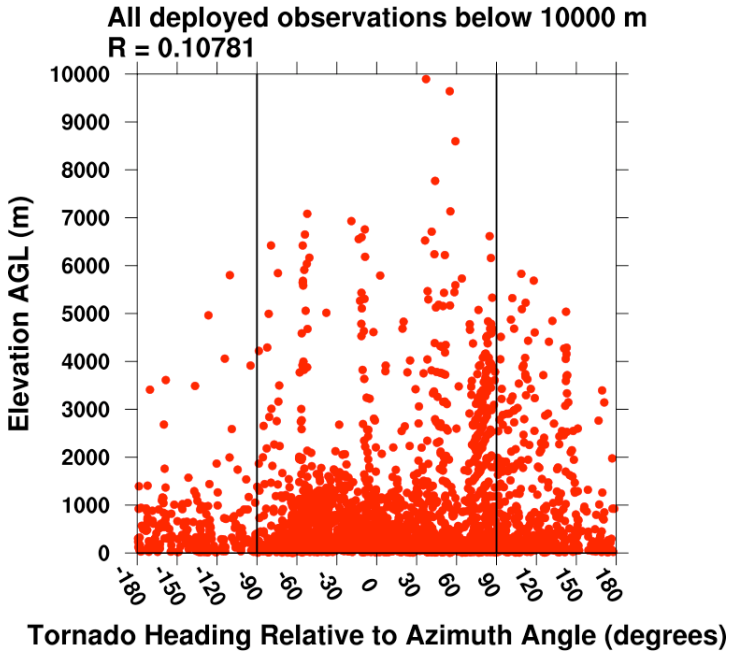
All deployed observations below 10000 m
R = 0.10781
Elevation AGL (m)
10000
9000
8000
7000
6000
5000
4000
3000
2000
1000
0
-180
-150
-120
-90
-60
-30
0
30
60
90
120
150
180
Tornado Heading Relative to Azimuth Angle (degrees)

Figure 4.26. Scatter plot showing the number of data points (gates) below/above the $10^{th}/90^{th}$ percentile within about two core radii of the vortex center when compared against the value of the $10^{th}/90^{th}$ percentile with respect to the maximum observed Doppler magnitude below 500 m ALG for (a) all observations and (b) maximum value for each tornado. Only Doppler magnitude values exceeding 40 m s^{-1} are shown.

(a)

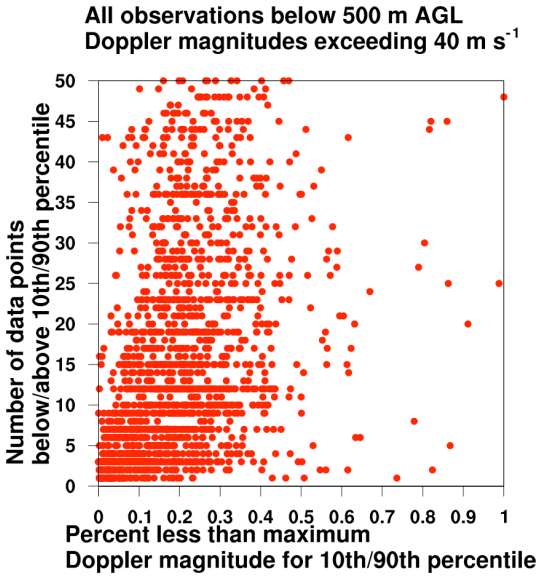

(b)

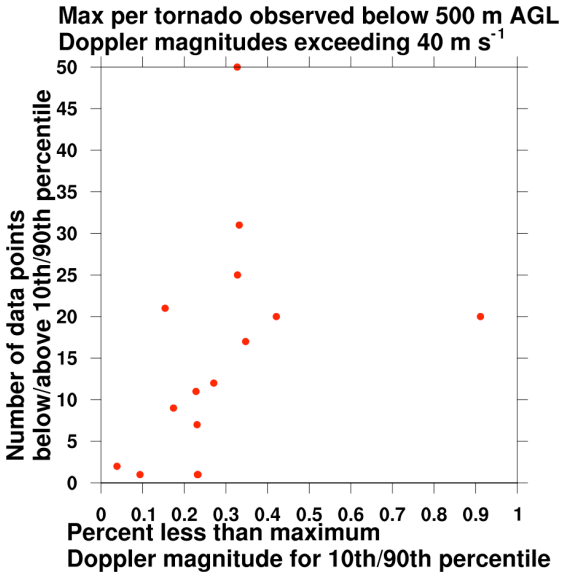

Figure 4.27. Doppler velocity radial profiles for the peak intensity observation of each tornado observed below 500 m AGL. Radius position from the vortex center are normalized relative to the radius of maximum Doppler velocity and velocity values are normalized relative to the maximum Doppler velocity for each observation. The solid body interior (not well-resolved) and decay region profiles are shown for reference. The large number of observations below the profiles result from asymmetries between the inbound and outbound sides of individual tornado cross-sections that are composited for this figure.

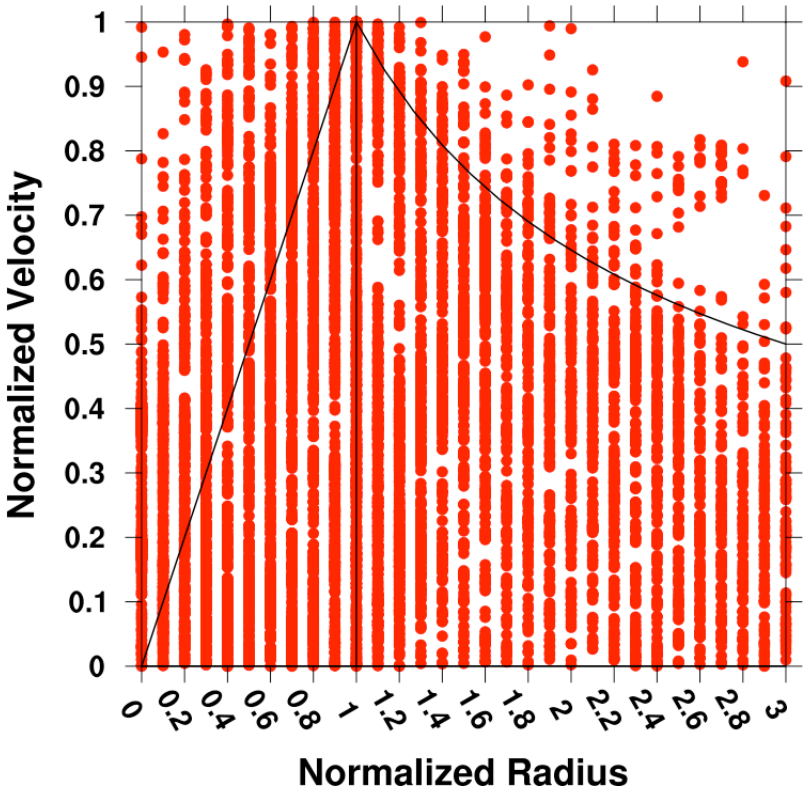

Figure 4.28. Scatter plot showing correlation between DOW observations from 10 strong/violent tornadoes and the closest WSR-88D radar time-matched (a) Tornado Vortex Signature (TVS) maximum velocity difference, and DOW velocity difference, (b) TVS shear vs DOW shear, and (c) mesocyclone shear vs DOW shear.

(a)

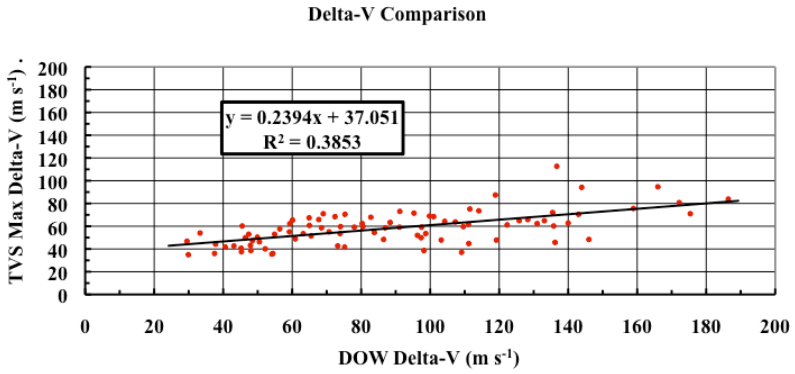

(b)

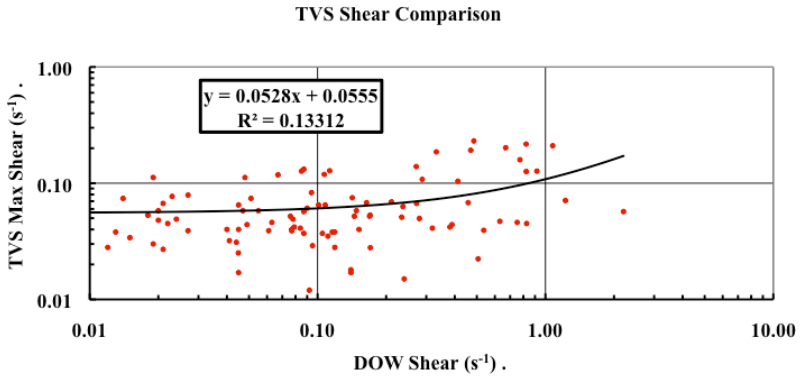

(c)

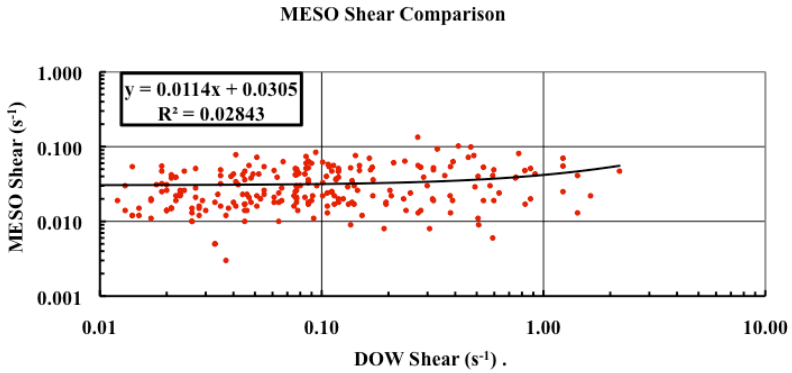

Figure 4.29. Line plots showing evolution of lowest-level DOW Doppler velocity difference observations (red/orange) from seven strong/violent tornadoes and the closest WSR-88D TVS algorithm maximum velocity difference (blue), lowest-level velocity difference (green) and average velocity difference (cyan) for tornadoes near (a) Spencer, SD 30 May 1998, (b) Moore, OK 03 May 1999, (c) Mulhall, OK 03 May 1999, (d) Alemena, KS 03 June 1999, (e) Oklahoma City, OK 09 May 2003, (f) Attica, KS 12 May 2004, and (g) Geary, OK 29 May 2004.

(a)

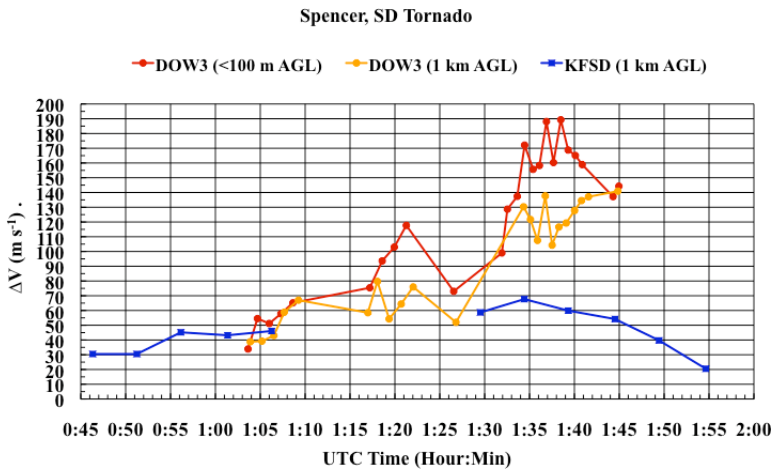

(b)

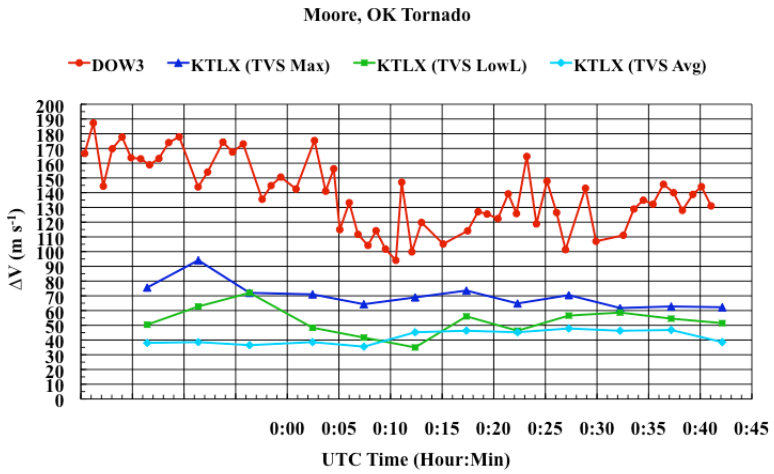

(c)

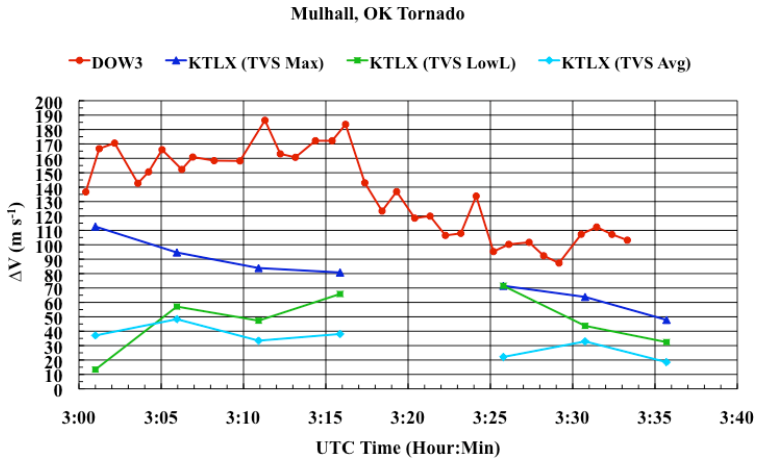
Mulhall, OK Tornado
DOW3
KTLX (TVS Max)
KTLX (TVS LowL)
KTLX (TVS Avg)
ΔV (m s-1)
UTC Time (Hour:Min)

(d)

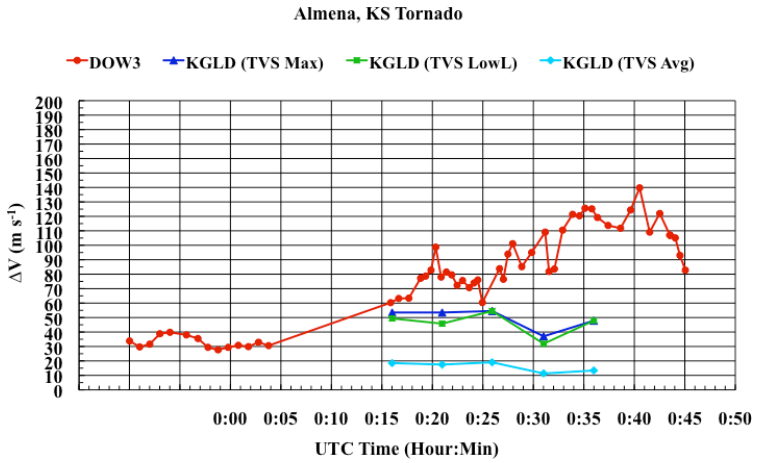
Almena, KS Tornado
DOW3
KGLD (TVS Max)
KGLD (TVS LowL)
KGLD (TVS Avg)
ΔV (m s-1)
UTC Time (Hour:Min)

(e)

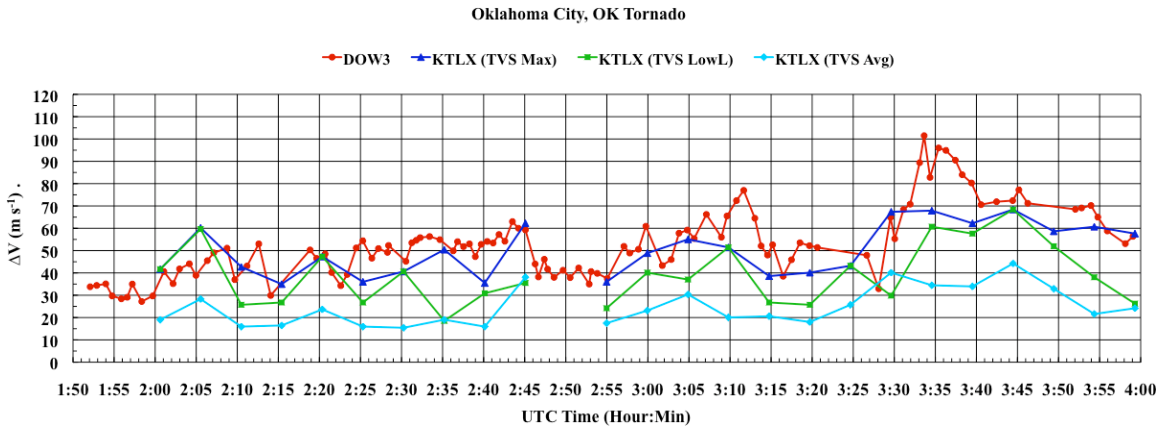
Oklahoma City, OK Tornado
DOW3
KTLX (TVS Max)
KTLX (TVS LowL)
KTLX (TVS Avg)
ΔV (m s-1) .
UTC Time (Hour:Min)

(f)

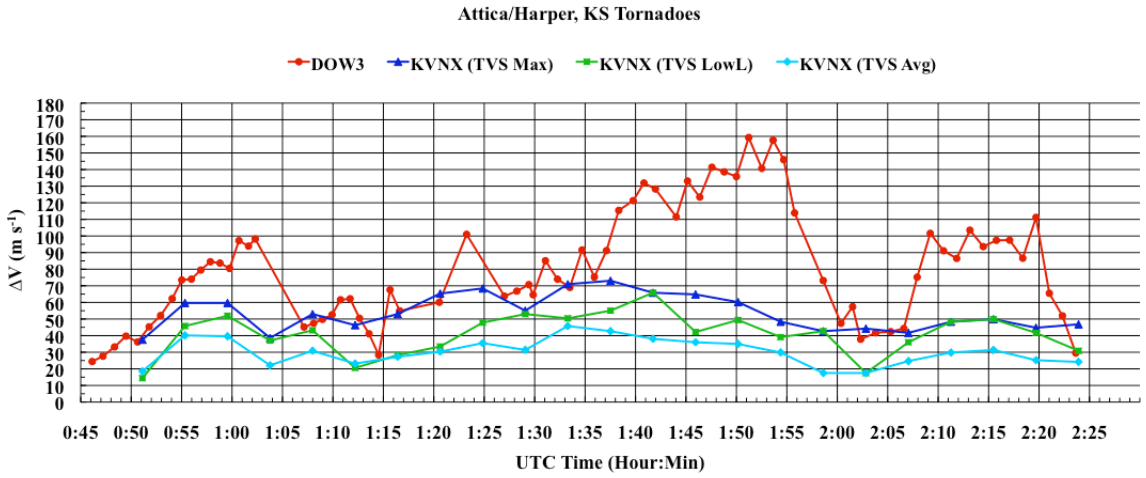
Attica/Harper, KS Tornadoes
DOW3
KVNX (TVS Max)
KVNX (TVS LowL)
KVNX (TVS Avg)
ΔV (m s-1)
UTC Time (Hour:Min)

(g)

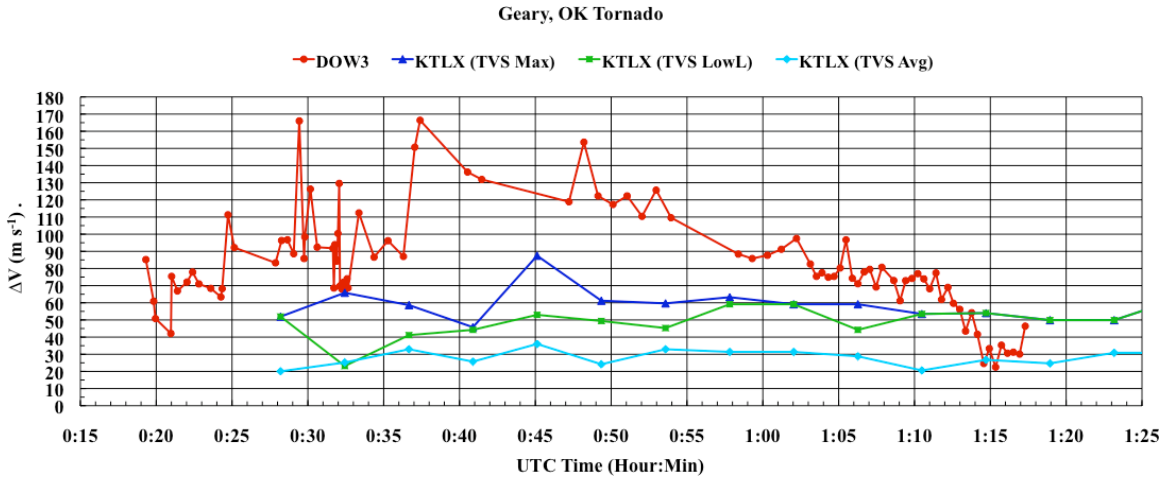
Geary, OK Tornado
DOW3
KTLX (TVS Max)
KTLX (TVS LowL)
KTLX (TVS Avg)
ΔV (m s-1) .
UTC Time (Hour:Min)

Figure 4.30. Doppler velocity fields for a tornado observed at (a) 1.8 km range from a DOW (left) and resampled using a Gaussian-weighted 0.5 azimuthal sampling with 250 m range gates (right). Resampling is then performed using 250 m range gates at increasing ranges in (b) including 10 km (upper-left), 30 km (upper-right), 60 km (lower-left) and 90 km (lower-right). Tick marks are spaced at 1 km intervals.

(a)

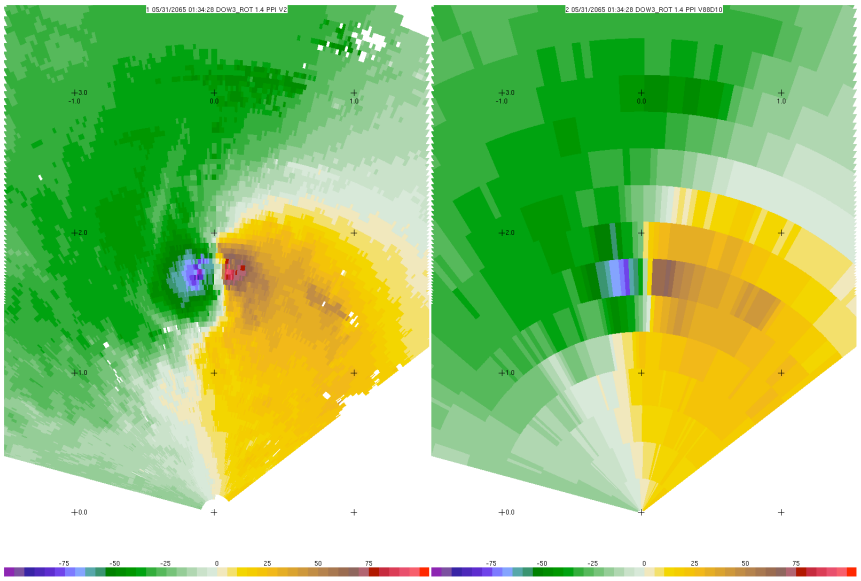

(b)

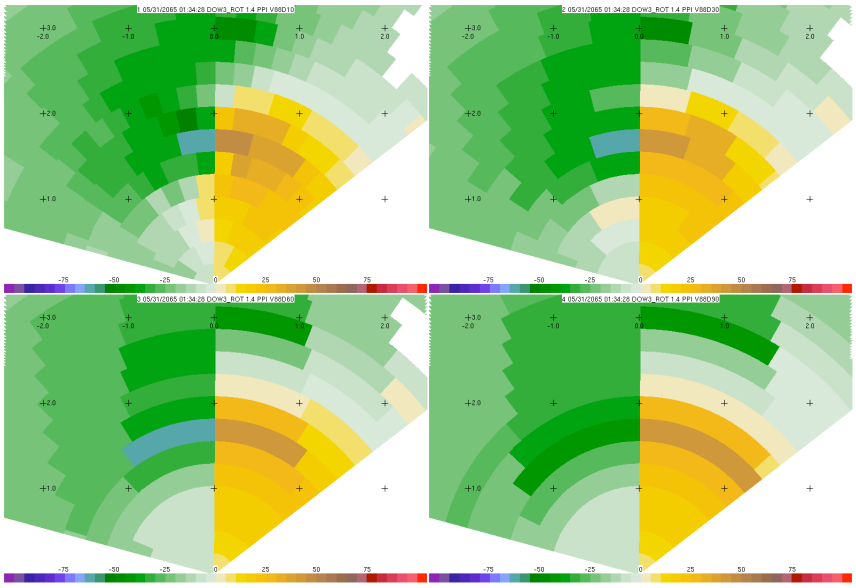

Figure 4.31. Time-height cross-sections of axisymmetric vertical vorticity across the vortex core for five cases where observations extend through at least the lowest 2 km AGL and capture tornadogenesis. Vorticity values are color-coded by magnitude where values less than 0.1 s^{-1} are blue, values 0.1 s^{-1} to 0.5 s^{-1} are green, values 0.5 s^{-1} to 1.0 s^{-1} are yellow, and values greater or equal to 1.0 s^{-1} are red. Cases include tornadoes observed near (a) Spencer, SD on 30 May 1998, (b) Tarzan, TX on 01 May 1999, (c) Thedford, NE on 04 June 1999, (d) Thedford, NE on 04 June 1999 and (e) Crowell, TX on 30 April 2000.

(a)

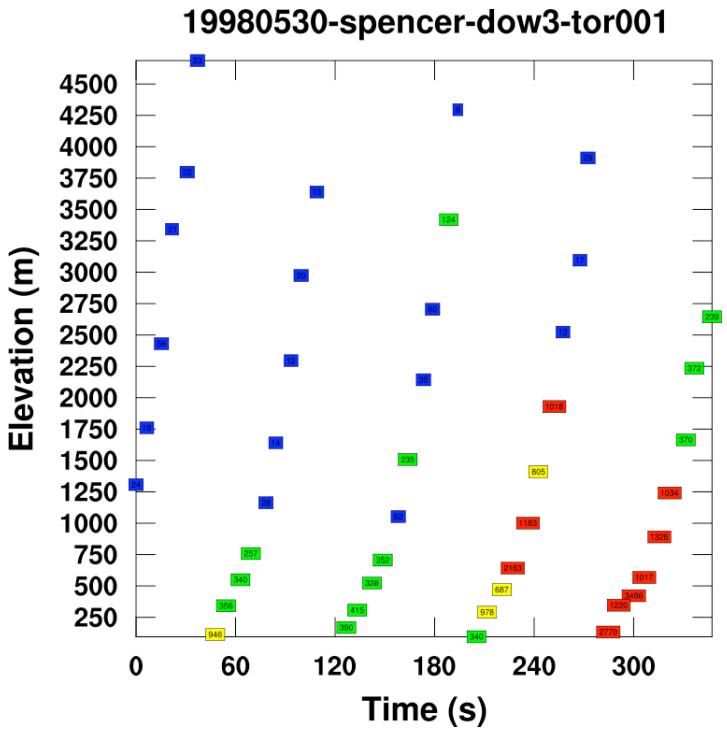

(b)

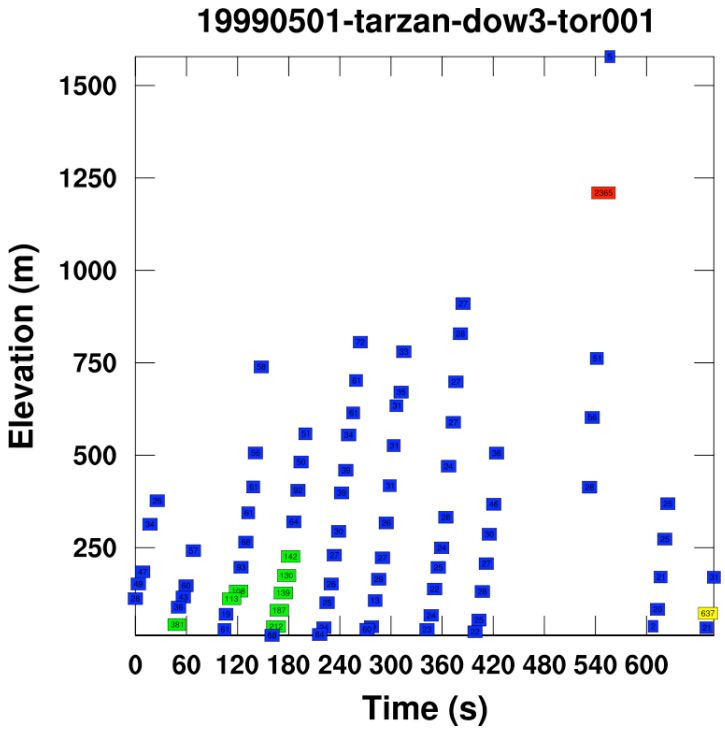
19990501-tarzan-dow3-tor001
Elevation (m)
1500
1250
1000
750
500
250
0 60 120 180 240 300 360 420 480 540 600
Time (s)

(c)

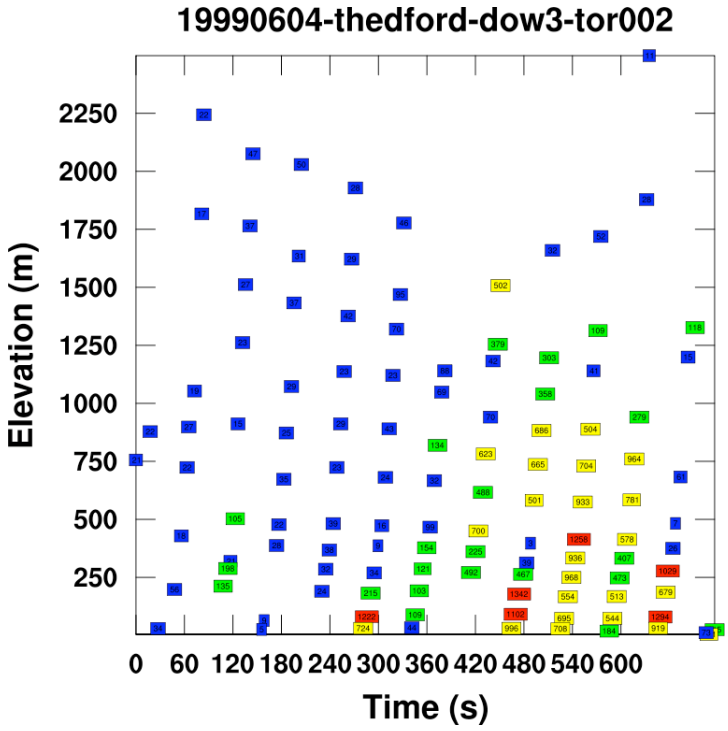
19990604-thedford-dow3-tor002
Elevation (m)
2250
2000
1750
1500
1250
1000
750
500
250
0 60 120 180 240 300 360 420 480 540 600
Time (s)

(d)

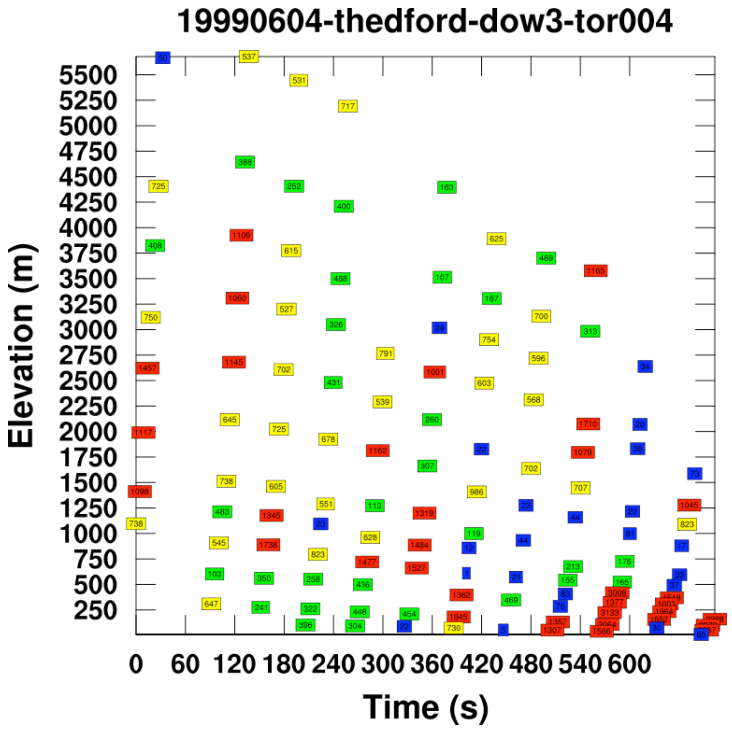
19990604-thedford-dow3-tor004
Elevation (m)
5500
5250
5000
4750
4500
4250
4000
3750
3500
3250
3000
2750
2500
2250
2000
1750
1500
1250
1000
750
500
250
0 60 120 180 240 300 360 420 480 540 600
Time (s)

(e)

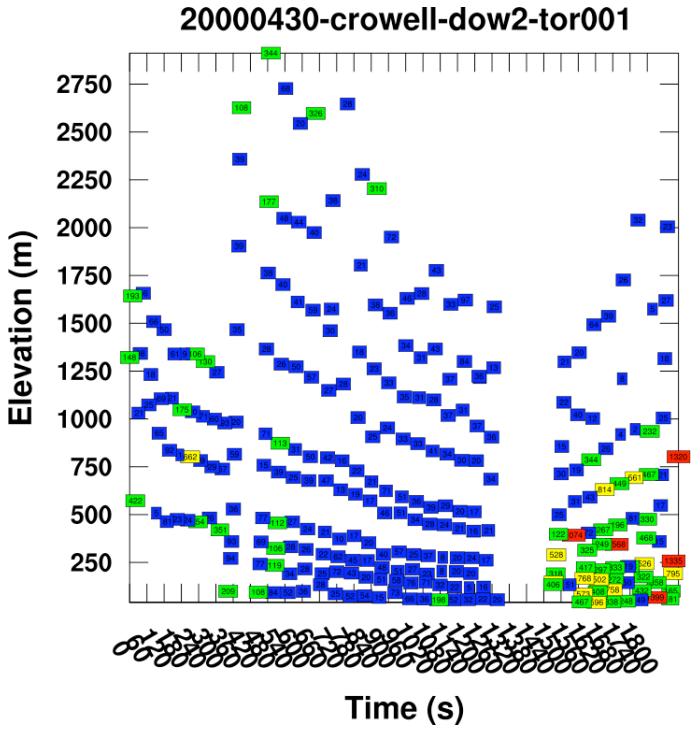
20000430-crowell-dow2-tor001
Elevation (m)
2750
2500
2250
2000
1750
1500
1250
1000
750
500
250
Time (s)

Figure 4.32. Retrieved horizontal profiles of axisymmetric (a) tangential velocity (b) radial velocity and (c) angular momentum for six weak tornadoes observed near Tulia, TX on 10 April 1997, Bridgeport, NE on 20 May 1998, Kremlin, OK on 21 April 1999, Tarzan, TX on 1 May 1999, Jericho, TX on 20 May 1999 and Pyote, TX on 26 May 1999. All radius values are normalized relative to the distance from the vortex center to the peak tangential velocity (1.0). All tangential velocities are normalized relative to the peak tangential velocity (1.0). All radial velocities are normalized relative to the peak radial velocity (1.0) with positive (negative) values indicating radial outflow (inflow). All angular momentum values are normalized relative to the value at the radius of maximum axisymmetric tangential velocity. The composite profiles show the six weak tornadoes at their initial observation time.

(a)

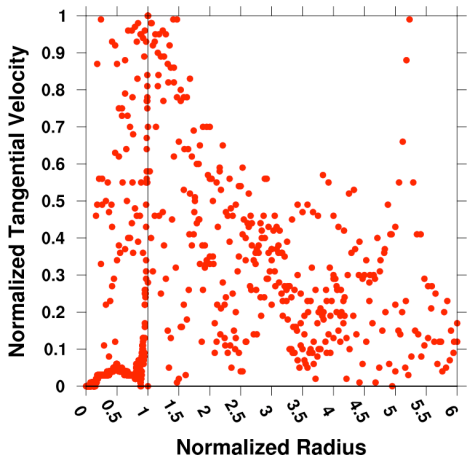
Normalized Tangential Velocity
Normalized Radius

(b)

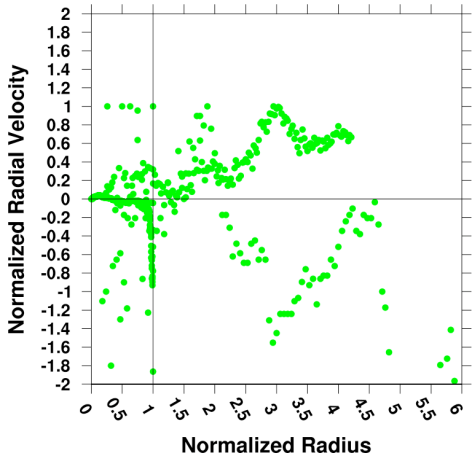
Normalized Radial Velocity
Normalized Radius

(c)

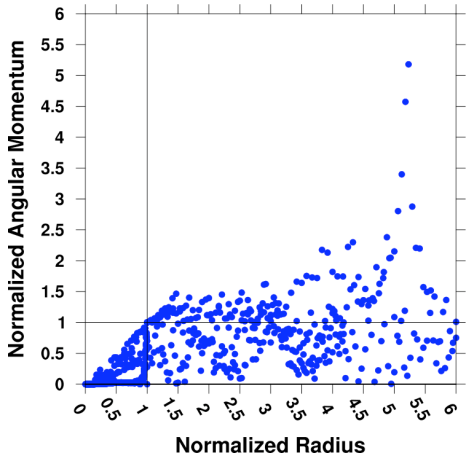
Normalized Angular Momentum
Normalized Radius

Figure 4.33. Same as Figure 4.32 except for mature stage of weak tornadoes.

(a)

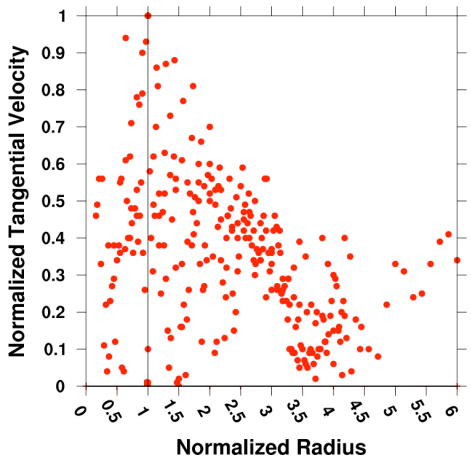

(b)

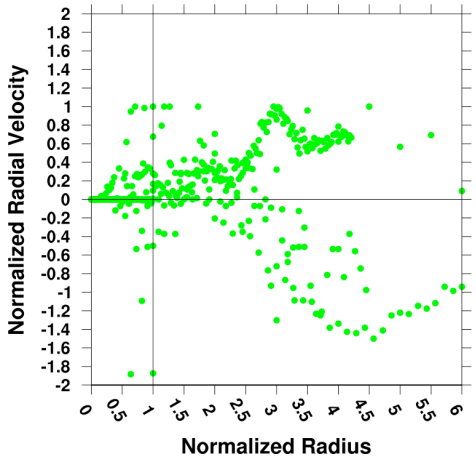

(c)

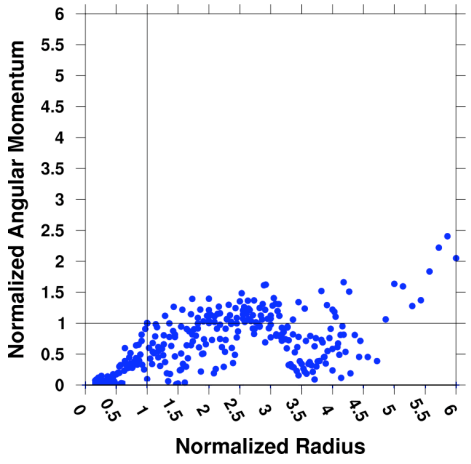

Figure 4.34. Same as Figure 4.32 except for the first observation time of six strong tornadoes observed near Dimitt, TX on 02 June 1995, Kellerville, TX on 08 June 1995, Spencer, SD on 30 May 1998, Moore, OK on 03 May 1999, Mulhall, OK on 03 May 1999 and Almena, KS on 03 June 1999.

(a)

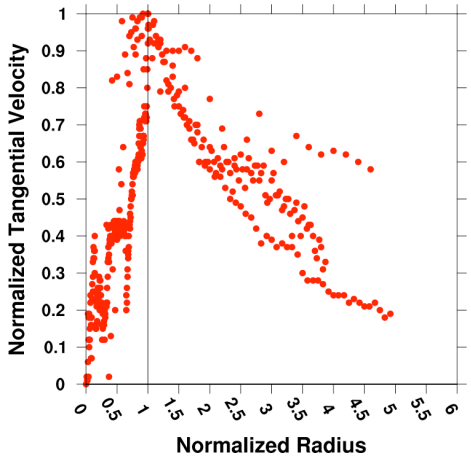
Normalized Tangential Velocity
Normalized Radius

(b)

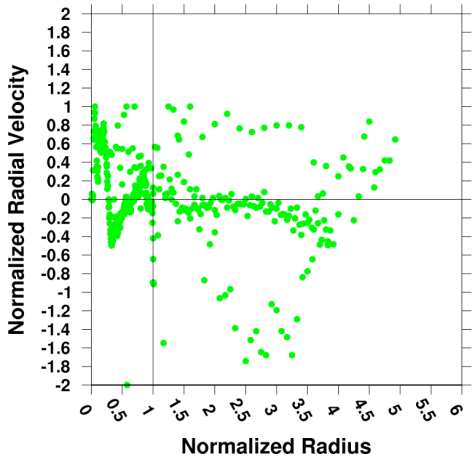
Normalized Radial Velocity
Normalized Radius

(c)

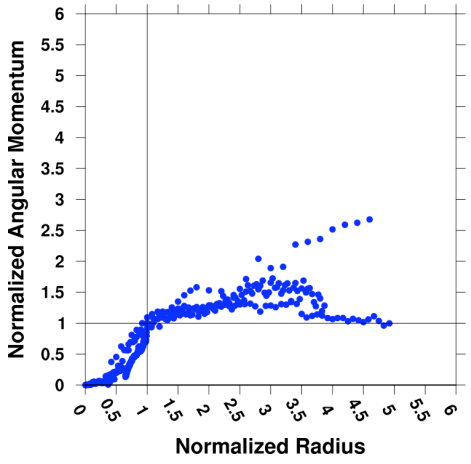
Normalized Angular Momentum
Normalized Radius

Figure 4.35. Same as Figure 4.34 except for mature stage of strong tornadoes.

(a)

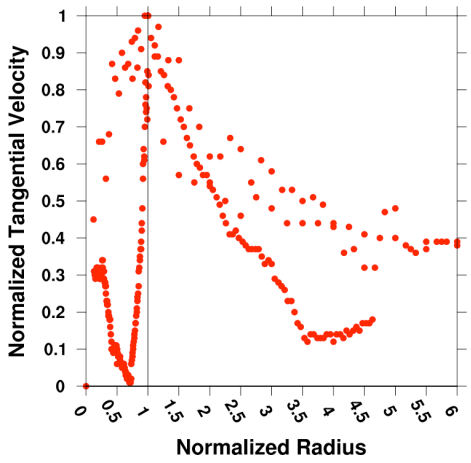

(b)

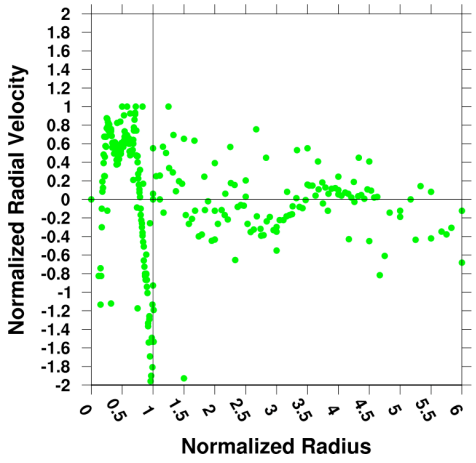

(c)

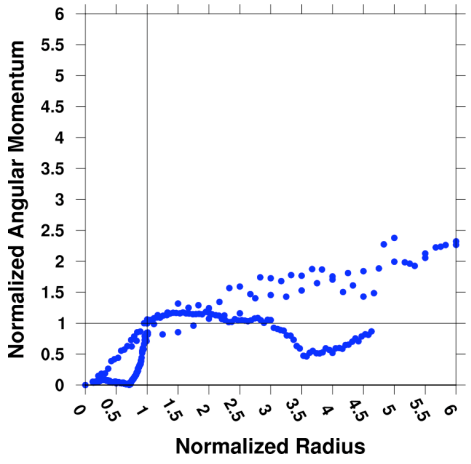

Figure 4.36. Same as Figure 4.35 except for last observation time of strong tornadoes.

(a)

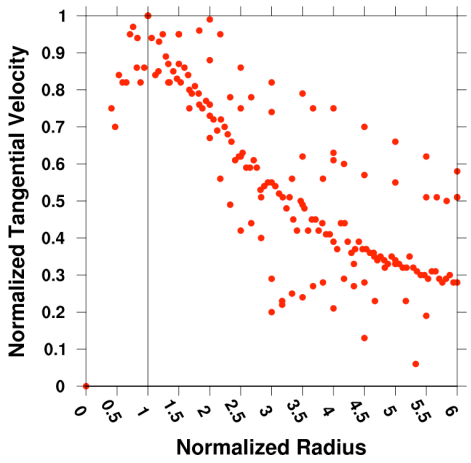

(b)

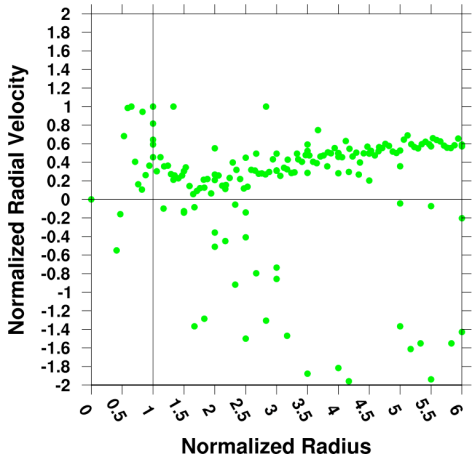

(c)